Faculteit Wetenschappen
Departement Fysica

Development and application of a non-local theory for the description of positron surface states

---

Ontwikkeling en toepassing van een niet-lokale theorie voor de beschrijving van positron oppervlakte toestanden

Proefschrift voorgelegd tot het behalen van de graad van
Doctor in de Wetenschappen: Fysica
aan de Universiteit Antwerpen te verdedigen door

Vincent Callewaert

Promotoren:
Prof. dr. Bart Partoens
Dr. Rolando Saniz

Antwerpen 2018

Members of jury:

Chairman
Prof. Dr. Jo Verbeeck, Universiteit Antwerpen, Belgium

Promotors
Prof. Dr. Bart Partoens, Universiteit Antwerpen, Belgium
Dr. Rolando Saniz, Universiteit Antwerpen, Belgium

Members
Prof. Dr. Nick Van Remortel, Universiteit Antwerpen, Belgium
Prof. Dr. Bernardo Barbiellini, Lappeenranta University of Technology, Finland
Dr. Stephan W. H. Eijt, Delft University of Technology, Netherlands
Prof. Dr. Stephen Dugdale, University of Bristol, United Kingdom

Abstract

Positrons are the anti-particles of electrons, and have the same mass but the opposite charge. As a consequence of the strong Coulomb repulsion with atomic nuclei, positrons are very sensitive to open volumes in materials, such as vacancies but also surfaces. The fact that electrons and positrons annihilate shortly after coming into contact, a process in which the resulting photons conserve the total momentum and energy of the original particles, makes that positrons are convenient to characterize these open volumes in materials.

A downside of positron annihilation experiments is that one has little control of where positrons end up in the material. An additional complication is that different situations can result in qualitatively similar outcomes for the experiment. In many cases, first-principles calculations can help significantly in the interpretation of experiments. Indeed, from these calculations, it is possible to predict where in the material positrons will annihilate as well as the resulting spectrum measured in the experiment.

The existing theoretical description of positron states in bulk materials is quite accurate. Using local or semi-local approximations to describe electron-positron correlations, it is possible to obtain electron-positron annihilation properties, such as the positron's annihilation rate, which closely match the experiment. In the case of surfaces, however, the situation is quite different. Indeed, the aforementioned approximations are unable to describe long-range correlation effects that are critical to obtain a correct description of positron states at the surface of a material.

A non-local approximation that captures long-range correlation effects was developed in this thesis. Additionally, we critically investigated a phenomenological model from literature. Both approaches were applied to provide theoretical support for three recent positron annihilation experiments on surfaces. In all cases, we managed to obtain satisfactory agreement with the experiment, demonstrating the usefulness of our approach.

Nederlandstalige Abstract

Positronen zijn de anti-deeltjes van elektronen, en hebben dezelfde massa maar een tegengestelde lading. Als gevolg van de sterke Coulomb afstoting met atoomkernen, zijn positronen zeer gevoelig voor open volumes in materialen, zoals vacatures, maar ook voor oppervlakken. Het feit dat elektronen en positronen, kort na met elkaar in contact te komen, annihileren, een proces waarin de resulterende fotonen de totale energie en impuls van de originele deeltjes behouden, maakt positronen nuttige deeltjes om open volumes in materialen te karakteriseren.

Een nadeel van positron annihilatie experimenten is dat men weinig controle heeft over waar de positronen naartoe gaan in het materiaal. Een bijkomende moeilijkheid is dat verschillende situaties een kwalitatief gelijkaardig resultaat van het experiment kunnen opleveren. In veel gevallen kunnen eerste principes berekeningen significant bijdragen aan de correcte interpretatie van de experimenten. Het is immers mogelijk om met deze berekeningen te voorspellen waar in het materiaal het positron zal annihileren, en hoe het annihilatie spectrum er zal uitzien.

De bestaande theorie voor de beschrijving van positron toestanden in de bulk van materialen is redelijke accuraat. Gebruik makend van lokale of semi-lokale benaderingen om elektron-positron correlaties te beschrijven, is het mogelijk om elektron-positron annihilatie eigenschappen, zoals de annihilatie snelheid van het positron, te berekenen die in goede overeenstemming zijn met experimenten. De situatie is echter heel verschillend voor oppervlakken van materialen. De zonet vernoemde benaderingen zijn immers niet in staat om lange dracht correlatie effecten te beschrijven, welke net kritisch zijn om een correcte beschrijving van positron toestanden te bekomen aan het oppervlak van materialen.

In deze thesis werd een niet-lokale benadering ontwikkeld die lange dracht correlaties wel correct beschrijft. Bovendien hebben we een bestaand fenomenologisch model uit de literatuur kritisch onderzocht. Beide aanpakken werden toegepast om theoretische ondersteuning te bieden aan drie recente positron annihilatie experimenten uitgevoerd op oppervlakken. In alle gevallen zijn we erin geslaagd om een goede overeenstemming met het experiment te bekomen, wat de bruikbaarheid van onze aanpak aantoont.

Contents

Frequently used Symbols and Abbreviations

Acronyms

2CDFT	Two Component Density Functional Theory
2D-ACAR	Two-dimensional Angular Correlation of the Annihilation Radiation
2RDM	Two-Body Reduced Density Matrix
ACAR	Angular Correlation of the Annihilation Radiation
AES	Auger Electron Spectroscopy
AMPS	Auger Mediated Positron Sticking
ARPES	Angular Resolved Photoemission Spectroscopy
BZ	(First) Brillouin Zone
CMM	Corrugated Mirror Model
DBAR	Doppler Broadening of the Annihilation Radiation
DFT	Density Functional Theory
DOS	Density Of States
GGA	Generalized Gradient Approximation
HF	Hartree-Fock
IPM	Independent Particle Model
KS	Kohn-Sham
LCW	Lock-Crisp-West
LDA	Local Density Approximation
MLG	Multi Layer Graphene
o-Ps	Ortho-Positronium
PAES	Positron Induced Auger Electron Spectroscopy
PAS	Positron Annihilation Spectroscopy
PAW	Projector Augmented Wave

PBE	Perdew-Burke-Ernzerhof
p-Ps	Para-Positronium
Ps	Positronium
QD	Quantum Dot
QED	Quantum Electrodynamics
QL	Quintuple Layer
REELS	Reflected Electron Energy Loss Spectroscopy
SLG	Single Layer Graphene
TI	Topological Insulator
TOF	Time Of Flight
VASP	The Vienna Ab-initio Simulation Package
VVV	Valence-Valence-Valence Auger Transition
WDA	Weighted Density Approximation
XPS	X-ray Photoemission Spectroscopy

Glossary

γ	(Density) enhancement factor
$\rho^{2\gamma}$	Electron-Positron momentum density
ρ^{ep}	Electron-Positron pair density
g^{ep}	Electron-Positron pair correlation function
λ_a	Positron annihilation rate
τ	Positron annihilation lifetime
ψ^e	Electron orbital
ψ^p	Positron orbital
ρ^e	Electron density
ρ^p	Positron density
ϱ^e	Weighted (electron) density
$\tilde{\varrho}^e$	Total weighted (electron) density
$\Delta\rho$	Screening cloud

Chapter 1

Introduction

In this chapter, I provide a general introduction to the work presented in this thesis. To this end, a brief description of different positron spectroscopy techniques and some of their applications are given. It is not my intention to give an exhaustive overview of all existing positron techniques as they are quite numerous. The focus lies on the experimental techniques which are relevant in the rest of the thesis. Afterwards, the status of the theory at the start of my PhD is discussed, and I pinpoint the shortcomings. This will clarify the main topic of the thesis. At the end of this chapter, I provide an overview of the work presented in this thesis.

1.1 Positron Spectroscopy

It is well-known that positrons annihilate with electrons when they come into contact. Less well-known is that the typical positron annihilation lifetime of a few 100 ps allows practical applications exploited in various spectroscopic techniques, denoted with the umbrella term Positron Annihilation Spectroscopy (PAS). What all these techniques have in common, is that they rely on electron-positron annihilation, either to measure the annihilation radiation, or as starting point for another process. Fig. 1.1 shows a schematic overview of several processes, which will be discussed in more detail in the coming sections.

Aside from more fundamental experiments, PAS finds its application in largely two domains. The first is mainly concerned with finite sized systems such as atoms, molecules and polymers. In this introduction and the rest of the thesis, we are concerned with the second application area, which focusses on solid state systems. The purpose of this section is to give the reader a basic background on the topic of PAS. More detailed discussions can be found in several reviews, e.g. Refs. [1, 2].

1.1.1 Sources and beams

An obvious question about PAS is where the positrons come from. We can determine two main categories of positron sources. The first are β^+ emitters, radioactive isotopes that decay with the emission of positrons. In particular, ^{22}Na is a widely used positron source in many positron labs. Much higher luminosity can be achieved with the second category, where positrons created in pair production from highly energetic γ-rays are extracted

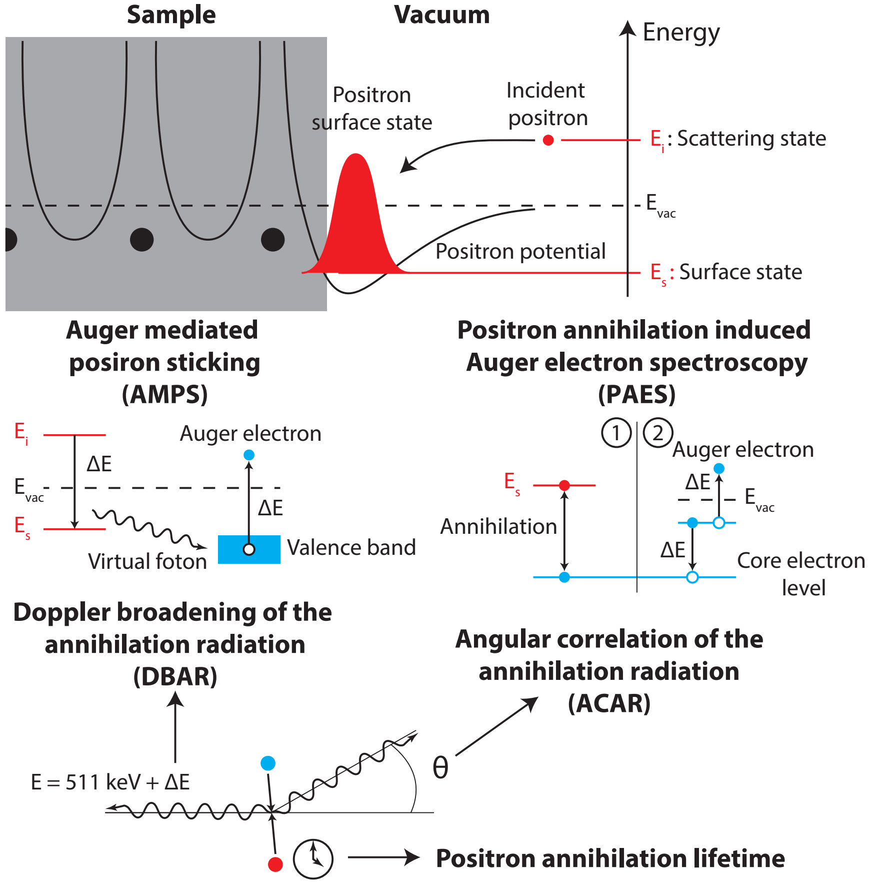

Figure 1.1: Schematic overview of some PAS techniques relevant to the work presented in this thesis. At the top of the figure, an incident positron with kinetic energy E_i is shown. If its energy is sufficiently low, it can get trapped in the image potential at the surface of the sample in a one-step process called AMPS, shown schematically in the middle left. The energy difference between the scattering state and the surface state $\Delta E = E_i - E_s$, is transferred to a valence electron in the material, which can escape as an Auger electron from the sample if it absorbs sufficient energy. After a positron gets trapped in a surface state, it has a small probability to annihilate with a core electron. This highly unstable empty core level is usually neutralized through an Auger process, as shown in the middle right of the figure. When an Auger process is triggered by electron-positron annihilation, it is called PAES. Most PAS studies on solid state systems are concerned with measuring the annihilation radiation, however. At the bottom of the figure, the most important quantities that can be extracted from the annihilation γ-rays are shown. The time that passes between the entrance of the positron in the sample and the annihilation event, is called the positron annihilation lifetime and is characteristic for the electron density at the annihilation site. Deviations in the angle and energy of the annihilation photons w.r.t. annihilation in the centre-of-mass system, give information about the electron momentum density. The former is called the ACAR and the latter DBAR.

from a nuclear reactor. Using such setups, up to $\sim 10^9$ slow positrons/s can be produced versus $\sim 10^6$ positrons/s achievable with radioactive sources [3].

Important in many modern positron setups is the moderation step in which energetic positrons are converted to a mono-energetic beam. Quite often, this step is realized by passing energetic positrons created by the source through a thin W-foil. A small fraction ($< 0.1\%$) thermalizes in the moderator and gets re-emitted as slow ($\sim 2-3$ eV) positrons. The spontaneous re-emission occurs due to the negative positron workfunction of the moderator ($\phi^+ \approx -3.0$ eV for W(001) [4]). Afterwards, the positrons can be accelerated again, typically to energies between $20 - 20000$ eV. Remoderated beams are usually called slow positron beams as incident energies are significantly lower than the ~ 0.5 MeV positrons emitted by a ^{22}Na source. The tunable energy of the beam allows researchers to vary the penetration depth of the positrons in the sample, which is, e.g., useful to characterize heterostructures or the depth-dependence of defects. Especially for positron surface studies, it is important that very low-energy positrons $E \leq 20$ eV are used to maximize the number of positrons that diffuse back to the surface. The highly energetic positrons emitted by a conventional source remain useful for bulk studies. Indeed, the penetration depth of $\sim 0.1 - 0.3$ mm lies significantly higher than the ~ 1 μm attainable with remoderated beams.

1.1.2 Thermalization and trapping

An important observation that underlies the usefulness of PAS techniques in the study of solid state systems, is that energetic positrons quickly thermalize ($1 - 3$ ps) after entering the sample [1]. Between the time that a positron reaches its groundstate and the moment it annihilates, it diffuses in the order of ~ 100 ps through the sample. During its diffusive motion, a positron can get trapped in (neutral or negatively charged) vacancy type defects, embedded nanoparticles, or in its image potential well at the surface of the sample. A different process with which positrons can end up at the surface is through AMPS. Here, incident positrons with very low kinetic energy ($E < 10$ eV) transition directly to their groundstate upon arrival at the sample by transferring their excess kinetic energy to a valence electron of the sample [5]. This process has been shown to be rather efficient to deposit positrons at the surface.

An important application of PAS stems from the sensitivity of positrons to open volumes, where they often get trapped during their thermal motion through the material. Indeed PAS techniques can pick up signals when vacancy concentrations are as low as $\sim 1/10^8$ units cells [1]. This sensitivity follows from the strong Coulomb repulsion positrons experience by the ions, which confines them in the interstitial region of the lattice. When a positron encounters open volume, it can further lower the Coulomb repulsion of the ions and reduce its confinement energy. Furthermore, electrons in these regions are generally more polarizable, such that electron-positron correlation effects further lower the total energy of the system. In this regard, it is not very surprising that positrons are sensitive to surfaces as well.

Several materials have a negative positron workfunction, such that they would get spontaneously emitted in the vacuum when they reach the surface. In many cases, however, the positron induced polarization of the sample can bind the particle in a surface state. This long range correlation effect is known from elementary electrostatics as the ‘image potential’ and decays as $\sim 1/z$, with z the distance from the surface. Positrons captured in a surface state typically overlap only with the topmost few atomic layers of the material. This gives PAS techniques a surface sensitivity capable of, e.g., monitoring sub-monolayer coverages of surfaces with adatoms [6].

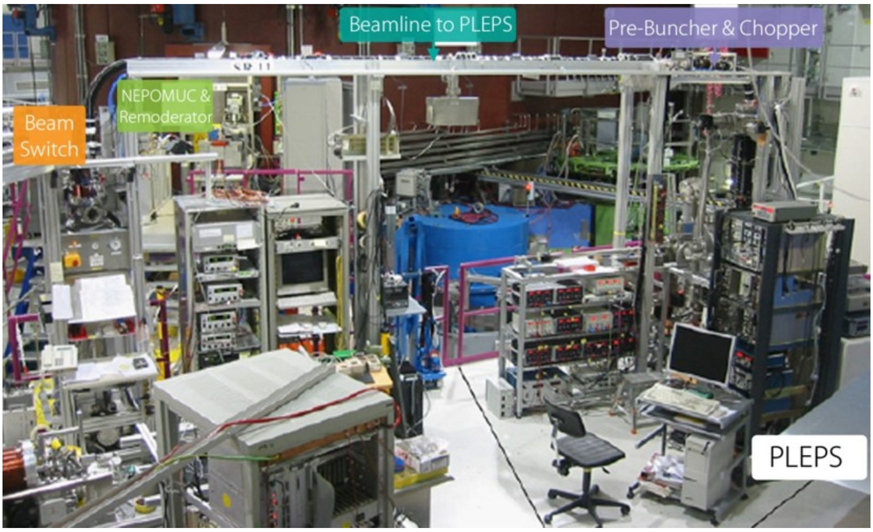

Figure 1.2: The pulsed low-energy positron system (PLEPS) at Garching; a positron annihilation lifetime setup coupled to a reactor beamline. NEPOMUC is the name of the beamline which is coupled to the reactor. The buncher and chopper are part of the system that transforms the continuous flow of positrons to short, time-separated pulses required to measure the annihilation lifetimes.

1.1.3 Positron annihilation lifetime

Since the annihilation rate is roughly proportional to the electron density, the positron annihilation lifetime in a sample is a useful quantity to identify and characterize open volumes. In positron lifetime experiments, one tries to accurately determine the time that passes between the entry of the positron in the sample and the moment it annihilates. The time of the annihilation event is easily obtained from measuring the annihilation rays. Figuring out when a positron enters the sample turns out to be more difficult, however.

The simplest lifetime measurements are performed by preparing a sandwich with the sample of interest and a radioactive source, typically ^{22}Na. The 1.27 MeV photon emitted (nearly) simultaneously with the positron during the β-decay in the source provides the start signal for the timer, and the 2γ annihilation radiation the stop signal.

Lifetime measurements are significantly more complicated with moderated positron beams. The primary issue lies with generating a useful start signal. Indeed, moderated beams have a roughly uniform temporal intensity but there is no accompanying signal that indicates when a positron arrives at the sample as with the ^{22}Na source. One approach is to bunch the positrons in a pulse train. Here, the repetition rate is limited by the lifetime of the positron in the sample. Indeed, the positrons of a previous pulse should have annihilated before the next one arrives. A second important factor is the temporal width of the pulse itself, which limits the accuracy of the positron lifetime that can be extracted from experiments. Fig. 1.2 shows the lifetime setup at the NEPOMUC beamline in Garching, Germany, which is operated with moderated positrons.

Fig. 1.3 shows a typical lifetime spectrum obtained in experiment. Lifetimes are obtained by fitting a set of exponentials to the data

$$I(t) = \sum_i A_i e^{-t/\tau_i}. \tag{1.1}$$

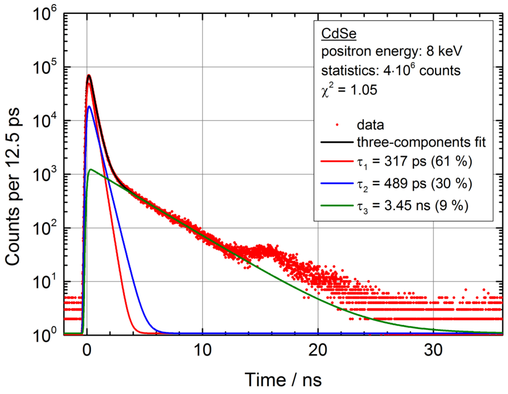

Figure 1.3: A positron annihilation lifetime spectrum measured for CdSe quantum dots. The red dots indicate measured data, the full black line the fit to the data which consist out of a sum of three exponentials, shown in red blue and green. The lifetimes and relative amplitudes are indicated in the legend. The bump in the spectrum around 16 ns was identified with positrons that are scattered from the surface and annihilate elsewhere in the sample chamber.

Typically between one and three components are required to accurately fit a spectrum. Different components in the fit indicate different initial states of the positron prior to annihilation. For instance, one might find two components of which one indicates annihilation in bulk and a second component with a larger lifetime that indicates annihilation of a positron trapped in a vacancy. It is not always possible, however, to discriminate between different components of a lifetime spectrum, e.g. when two similarly sized vacancies exist in a system. In such cases, a fit with a single component is likely to give a good fit, but the obtained lifetime will be a weighted average of the constituent lifetimes.

1.1.4 Angular correlation of the annihilation radiation

In ACAR experiments deviations from perfect anti-collinearity, expected for electron-positron pairs at rest, of the two annihilation photons are measured. The deviations are a result of the non-zero total momentum of the annihilating electron-positron pair.

In the ideal case, one would measure directly the momentum density of the electrons in the material. It turns out, however, that several effects cause a distortion. First, due to the Coulomb repulsion between the ions of the material with the positron, the measured momentum distribution will contain a much larger contribution from the valence electrons than from core electrons. Due to the large difference in the momentum distribution of valence electrons and different core shell electrons, one can still measure the contribution of the core electrons, though. It just takes more time to accumulate a sufficient signal from the core electrons.

Second, as we will show in a later section, the positron distorts the momentum distribution of the electrons in the material. Two effects come into play. First, we note that the observed momentum distribution depends on the positron's groundstate momentum distribution. This means that if the positron is, e.g., confined in a potential well, the observed momentum distribution will broaden. Second are enhancement effects; due to the conditional nature of the many-body wavefunction, the momentum distribution of an electron-positron pair residing at the same point in space (required for annihilation)

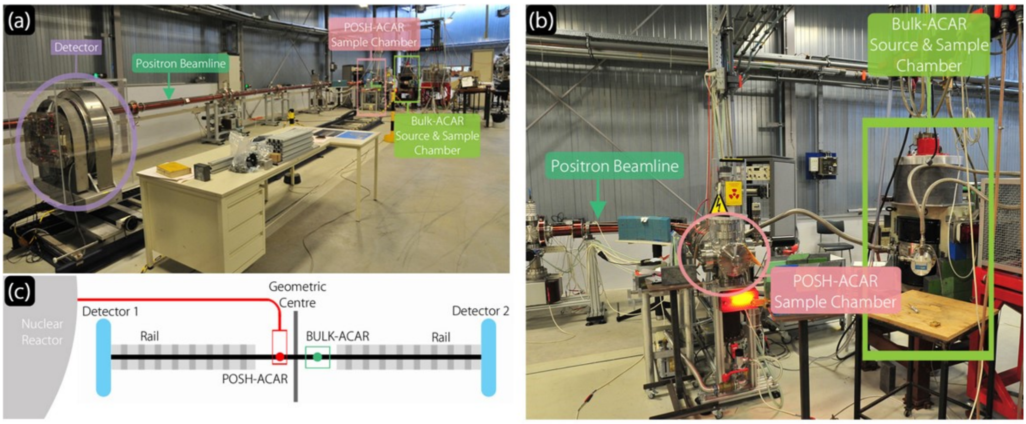

Figure 1.4: The 2D-ACAR setup at TU Delft. Panel (a) shows one of the two scintillation cameras (detector), which are used to measure the angle between the annihilation photons. The positron beamline in the background is coupled to the reactor and provides a high intensity positron flux that can be tuned in the energy range between $100eV - 13.5$ keV. A closer view of the sample chambers are shows in panel (b). The POSH-ACAR sample chamber is coupled to the reactor beam. The bulk-ACAR chamber is operated with a conventional radioactive source, due to the higher penetration depth of the highly energetic unmoderated positrons. Panel (c) shows a schematic of the setup.

is not the same as the individual electron and positron momentum distributions at that point. For instance, if one were to fix the positron at a given position in the sample, it is conceivable that the electrons will react to this and form a cloud around the positron (due to the attractive Coulomb interaction). This distortion of the electron density with respect to its ground state in real space is reflected in momentum space.

In practice, Two-dimensional Angular Correlation of the Annihilation Radiation (2D-ACAR) experiments employ two positron-sensitive detectors (such as scintillation detectors) that are positioned several metres from the sample. Fig. 1.4 shows the 2D-ACAR setup from TU Delft. Decreasing the distance to the sample increases the count rate but at the same time decreases the momentum resolution. The limiting factor in these type of experiments is typically the count rate, which is directly linked with the beam intensity. ACAR experiments were used to measure Fermi-surfaces before Angular Resolved Photoemission Spectroscopy (ARPES) became widespread. Despite the latter being superior in some ways, ACAR experiments still find their applications in areas where ARPES measurements have limited applicability due to stringent requirements on sample preparation. The study of colloidial quantum dots, presented in a later chapter, is one such example. Another difference between ARPES and ACAR is that the former is mainly a surface selective technique as the photoelectrons have to be close to the surface in order to escape without scattering. ACAR on the other hand, can be used for both bulk and surfaces, as the γ-rays only interact weakly with the sample.

Since a one dimensional projection of the momentum density is often sufficient for chemical characterization of the positron's annihilation site, DBAR experiments are more widespread in defect studies. Instead of measuring the net momentum of annihilating electron-positron pairs, DBAR experiments determine the Doppler shift from the broadening of the 511 keV annihilation line. Exactly the same information can be extracted from Doppler spectra as from ACAR experiments. Though, typically Doppler spectra have a lower resolution but obtain a higher count rate.

1.1.5 Auger electron spectroscopy

The Auger process typically occurs when a hole is present in a core level of an atom. In the actual Auger transition, an electron from a higher energy level will fill the empty level, and transfer the freed energy to a second electron. Often, the energy difference is sufficient to kick out the second electron, called an Auger electron, as a free particle.

Since the transferred energies in Auger processes are characteristic to different elements, Auger Electron Spectroscopy (AES) is a useful technique to chemically characterize surfaces[1]. To initiate Auger transitions, one first needs to create holes in the core levels. Both X-rays and energetic electron beams can be used for this purpose but their downside is that they create a large secondary electron background which is unrelated with the actual Auger electrons. Weiss et al. showed that the core holes can also be created through electron-positron annihilation [7]. Even though the probability of annihilation of positrons with core electrons is small, it is sufficient to create a strong Auger signal. The advantages of positrons over more traditional beams is twofold. First, the core electron and positron disappear from the sample as two γ-rays, which interact very little with the sample, and hence create practically no secondary electron background. Second, the positron beam can be low energetic, which reduces significantly impact induced electron emission. In fact, recent advances in slow positron beams have allowed measurements that are nearly completely free of a beam induced secondary electron background. Several discoveries related with Auger processes have been made using positrons. Amongst them are the realization that low energy positrons can initiate electron emission if they transition from their (incident) scattering state to the groundstate in the sample, which is often a surface state. The technique is relatively new and is coined AMPS [5]. Next is the direct observation of an Auger process initiated by a hole in the valence band, which is usually masked by the secondary electron background with conventional AES techniques, in contrast to the core shell levels [8]. Chapter 6 is devoted to modelling this last Auger process.

PAES experiment usually operate with a low energetic moderated positron beam to make sure as many positrons as possible annihilate close to the surface. Typical energies lie between $2 - 20$ eV, where beam energies of a couple eV allow direct deposition of positrons in a surface state through positron sticking. One limitation, especially with ^{22}Na sources is the limited beam intensity and correspondingly low Auger electron intensity. Thanks to its very low background, however, conventional source based beams are still sufficient for PAES experiments. The much higher intensities of reactor based beams allow experiments such as time-resolved PAES. For instance, one application of this technique tracked segregation of Cu in Pd over several hours [9]. The energy distribution of the Auger electrons can be inferred from their Time Of Flight (TOF), i.e. the time which passes between the detection of an annihilation photon and the detection of an electron through a specialized tube. The experimental setup of the TOF-PAES system of the positron lab of Weiss' group is shown in Fig. 1.5.

---

[1] Similar to ARPES, the technique is surface sensitive because excited electrons do not travel far in a sample before being scattered.

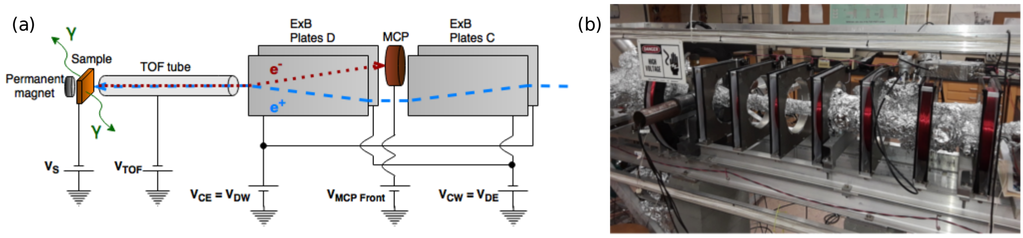

Figure 1.5: (a) Schematic of the TOF-PAES setup used in the positron group of A. Weiss at Arlington, Texas in the United States. Remoderated positrons are guided to the sample with help of the $\mathbf{E} \times \mathbf{B}$ plates, and can be accelerated in the TOF tube. The annihilation γ-rays are recorded with NaI and BaF_2 scintillators (not shown in the schematic), of which the latter provides the start signal for the TOF. (b) Photograph of the actual setup.

1.2 Motivation, Goals & Overview

Although positron surface studies have been quite scarce compared to bulk studies, the topic received a considerable amount of attention in the late 1970's and 1980's [10–18]. Afterwards, the interest has faded, but recent years have witnessed a renewed interest in positron surface experiments, see e.g. Refs. [5, 9, 19–21].

The purpose of this thesis is to provide theoretical support for several recent positron experiments performed on surfaces. In Chapter 5, we study whether a positron surface state exists near the Topological Insulator (TI) Bi_2Te_2Se, as PAES and AMPS studies seem to suggest [8]. In our theoretical survey, we also investigate whether future experiments can probe the topological states of this system. For this purpose, we extend the existing theory for the calculation of electron-positron momentum densities to deal with systems in which the electron spins are non-collinear. This result is presented in Chapter 2. Another system of interest is graphene deposited on a Cu(111) substrate, studied in Chapter 6. Here, PAES experiments have revealed the emission of Auger electrons initiated by holes created in the valence band of graphene, which requires the presence of a surface state. In our study, we investigate whether this interpretation can be reconciled with first-principles calculations of the positron state. Thereafter, we study in some detail the Auger spectrum for comparison with experiment. Finally, we try to resolve a long-standing debate on whether positrons annihilate from a surface state or from the interior of colloidal CdSe Quantum Dots in Chapter 7.

Before we present these applications, we explain the theoretical background relevant to this work in Chapter 2. There, we derive how one can calculate electron-positron annihilation characteristics from the groundstate of the system. The theoretical basis of the Two Component Density Functional Theory (2CDFT), which we apply to calculate electron and positron groundstate properties, is also be treated. Finally, we point out the approximations that are involved in the calculation of electron-positron annihilation spectra in the framework of the 2CDFT.

Simple electron-positron correlation functionals used in the 2CDFT, such as the Local Density Approximation (LDA) and Generalized Gradient Approximation (GGA), provide good results for most bulk studies. Unfortunately, they give an erroneous limit in the vacuum when performing calculations for surfaces. It turns out that this is a fundamental limitation of (semi-)local approximations, such that non-local functionals are required in order to make progress. Research in this direction has remained limited in the field, however, and modelling of positron surface states has hence lagged behind compared to their bulk counterparts.

During the 1980's, when positron surface experiments received considerable attention, a popular model, the Corrugated Mirror Model (CMM) [22, 23], emerged. In this model, the erroneous potential predicted by LDA and GGA potentials is empirically corrected to give the correct long-range limit. Despite its shortcomings and limited applicability outside the simplest surfaces, it is still the only widely applied model. After the 1980's interest in the theoretical description of surface states has faded, likely due to the limited amount of experiments in this direction. In Chapter 4 we present the details of the CMM and apply it to a set of simple surfaces to assess its accuracy. Some of its shortcomings are illustrated as well.

Application of non-local electron-positron functionals in literature is rather limited. The Weighted Density Approximation (WDA) by Jensen [24] and Rubaszek [25–31] are notable exceptions. We note that most of these references are studies of bulk systems, with the exception of Refs. [24–26] where surfaces are represented by jellium models. We see several factors for the limited application of non-local models in positron literature: (i) LDA and GGA functionals generally give satisfactory results for bulk systems, (ii) positron surface experiments have been relatively scarce compared to bulk studies, (iii) the application of the WDA (and non-local functionals in general) is hindered by the much higher computational resources required to evaluate them, and (iv) the implementation of the WDA is considerably more involved than the LDA or GGA, and publicly available implementations are not present.

A large part of this work went into the development of a WDA applicable for the study of positron surface states. Before such a functional can be confidently applied to surfaces, a required first step is to make sure that it gives acceptable results for annihilation properties in bulk. This is the topic of Chapter 3, where we investigate the positron annihilation lifetime for a set of elementary bulk material for which experimental data is available. The application of the developed WDA to surfaces is deferred to chapter 4. There, we compare the positron workfunctions and surface binding energies predicted by the WDA with the CMM predictions and experiment. Next, we analyse some qualitative features such as in how far the WDA reproduces the correct long range behaviour of the potential. Shortcoming of the WDA approach developed in Chapter 3 are pinpointed, and possible improvements are suggested.

Chapter 2

Theory of electron-positron annihilation in solids

The purpose of this chapter is to introduce the basic theory required to understand the rest of this thesis. To this end, I will first show how we can calculate PAS spectra. Afterwards, we discuss two approximate methods to obtain the groundstate of the system. The first is the Hartree-Fock (HF) approach, in which we directly approximate the many-body wave function. We will see, however, that in this approximation we obtain the so-called Independent Particle Model (IPM) for the calculation of PAS spectra, which does not provide sufficiently accurate results as it neglects correlation effects. The second method is the 2CDFT, which is a generalization of regular Density Functional Theory (DFT) to include positrons as well, where the fundamental quantities are the groundstate densities. Correlation effects can be treated in this framework, though only for the densities which is, strictly speaking, not enough to calculate PAS spectra. We will discuss, however, how we can get around this limitation.

2.1 Electron-Positron annihilation

2.1.1 Introduction

The purpose of the research presented in this thesis is to calculate PAS spectra from first-principles. An obvious first element to discuss is then how to obtain electron-positron annihilation characteristics from the system's properties.

We restrict our discussion to the production of two photons from an initial electron-positron pair. In the introduction, we already discussed that this two photon annihilation is the relevant one in momentum density studies. Decay with more gamma rays is also possible, but much less likely as they are higher order processes. One notable exception is the three gamma decay of Ortho-Positronium (o-Ps), which cannot decay through two photons due to conservation of angular momentum. The lifetime of isolated o-Ps is, however, well-known and these lifetime components are easily recognized in lifetime spectra. Deviations from the vacuum value are possible and occur due to pick-off annihilations, i.e. annihilation of the positron with electrons from e.g. a surface in the vicinity. We will, however, not be concerned with describing these effects in this work. In momentum density studies where the targets are operated in coincidence mode, the contribution to the spectrum from o-Ps is also expected to be small. Indeed, two of the

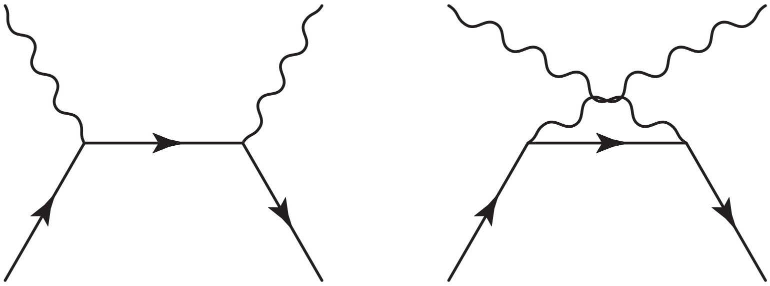

Figure 2.1: The two distinct lowest order QED-diagrams that describes the annihilation of an electron-positron pair in vacuum. The time axis is chosen to point upwards. The full lines indicate electron and positron propagators and the wavy lines photon propagators.

three photons would have to be emitted antiparallel to each other, which is generally not the case in the three-gamma decay.

2.1.2 Isolated electron-positron pair

The annihilation rate of an isolated electron-positron pair to a pair of photons is well-known from particle physics. Though, as is common in that field, these rates are expressed as a Lorentz invariant that is convenient in collision experiments: the cross section. According to Ref. [32] the cross section σ for a two particle collision is easily related to the transition rate Γ_{fi} as

$$\sigma = \frac{\Gamma_{fi}}{v_{\mathrm{rel}}}, \tag{2.1}$$

where v_{rel} is the relative speed of the particles involved.

The cross section for an isolated electron-positron pair is obtained by calculating the contribution from the lowest non-trivial Feynmann diagrams, shown in figure 2.1, and multiplying it with the phase space available for the final states. The result is given by [33, 34]

$$\sigma = \frac{\pi r_e^2}{2\tau^2(\tau-1)} \left\{ \left(\tau^2 + \tau - \frac{1}{2}\right) \log\left(\frac{\sqrt{\tau}+\sqrt{\tau-1}}{\sqrt{\tau}-\sqrt{\tau-1}}\right) - (\tau+1)\sqrt{\tau(\tau-1)} \right\} \tag{2.2}$$

with r_e the classical electron radius, and where

$$\tau = \frac{t}{4m^2}, \quad t = (p_e + p_p)^2 = (k_1 + k_2)^2, \tag{2.3}$$

with p_e, p_p, k_1 and k_2 the four momenta of the electron, positron, and photons, respectively. In the non-relativistic limit $\tau \approx 1$ this reduces to

$$\sigma = \frac{\pi r_e^2}{2\sqrt{\tau - 1}}. \tag{2.4}$$

In this limit we have up to first order for the energy

$$E_\alpha \approx m\left(1 + \frac{|\mathbf{p}_\alpha|^2}{2m^2}\right), \tag{2.5}$$

such that

$$\tau \approx 1 + \frac{1}{4m^2}(\mathbf{p}_e - \mathbf{p}_p)^2. \tag{2.6}$$

After restoring c[1], we thus obtain for the cross section

$$\sigma \approx \frac{\pi r_e^2 c}{v_{\mathrm{rel}}}, \tag{2.7}$$

from which we can easily extract the transition rate

$$\Gamma_{fi} = \pi r_e^2 c. \tag{2.8}$$

2.1.3 Spin considerations

Note that the result in Eq. (2.8) is the result averaged over the initial spins of the positron and electron. Let us examine how to obtain the non-averaged result, which will be used in the rest of the derivation. We follow the arguments given in Ref. [35], which treats the decay of Positronium (Ps) in the non-relativistic case.

First, we note that we can separate the centre of mass and relative motions of the isolated electron-positron pair. The centre of mass motion can be described by a plane wave, and that of the relative motion by (a linear combination of) rescaled solutions of the H atom. The spin angular momentum is either in a singlet state (Para-Positronium (p-Ps)) or a triplet state (o-Ps) with $S = 0$ and $S = 1$, respectively.

In the decay process, the parity of the system has to be conserved as it is a fundamental symmetry of QED, i.e. the state of the system is either symmetric or anti-symmetric under inversion of all vector quantities. For the relative motion we have $P\psi_{nlm}(\mathbf{r}) = \psi_{nlm}(-\mathbf{r}) = (-1)^l \psi_{nlm}(\mathbf{r})$ and for the spin part, the parity is determined by the product of the intrinsic parity of the particles. Since particles and anti-particles have opposite intrinsic parity, we get a minus by applying the parity operator. The total parity of the Ps system is thus $-(-1)^l$. Since in the non-relativistic case the annihilation takes place in a point in space only the $l = 0$ terms can contribute, such that the photon states resulting from the decay should have odd parity. It is always possible to construct an n photon state that has the correct Bose symmetry, and furthermore can be written as a linear combination of even and odd parity. Hence, the parity operator does not restrict the number of photons produced in the decay of the Ps state.

Next, Ps is an eigenstate of charge conjugation, which exchanges particles and anti-particles. We can calculate the eigenvalue easily in this case by noting that applying the parity operator and exchanging the spins of the particles is equivalent to charge conjugation. From the spin exchange, we obtain $-(-1)^S$, such that we get $(-1)^{l+S}$ under charge conjugation. For the photon states, the charge conjugation changes the sign of the associated electrical fields, and we get $(-1)^n$ for decay into a n photon state. As a result, p-Ps, with $l = 0$ and $S = 0$, can only decay in an even number of photons, and o-Ps, with $l = 0$ and $S = 1$, in states with an odd number of photons.

From this last argument, we note that only the singlet state contributes to the two-gamma annihilation, hence the non-averaged transition rate is

$$\Gamma_{fi} = 4\pi r_e^2 c. \tag{2.9}$$

If we use this expression for the transition rate, we should be careful to select only singlet states as initial states.

---

[1] The required modification is found by introducing a factor c such that the correct dimension of the cross section (an area) is obtained.

2.1.4 Many-body systems

So far we have obtained the transition rate for an isolated singlet electron-positron pair with momenta $\mathbf{p}^e$ and $\mathbf{p}^p$, respectively, to a two-photon state with the same total momentum $\mathbf{p}$. In condensed matter systems, however, the initial state contains N_e electrons and a single positron, and the final state $N_e - 1$ electrons and two photons. To obtain the total transition rate, we generalize the derivation for isolated pair annihilation in vacuum.

Applying Fermi's golden rule

According to Fermi's golden rule, the total transition rate for annihilation of electron-positron pairs in the sample to pairs of photons with total momentum $\mathbf{p}$ is given by

$$\rho^{2\gamma}(\mathbf{p}) = \frac{2\pi}{\hbar} \sum_{\text{Final States}} \left| \langle \Psi_f | \hat{H}_\mathrm{I}(\mathbf{p}) | \Psi_i \rangle \right|^2, \tag{2.10}$$

where $|\Psi_i\rangle$ is the N_e electron plus a single positron initial state, and $|\Psi_f\rangle$ a $N_e - 1$ electron $|\Phi_\nu\rangle$ plus two photon final state. The perturbation $\hat{H}_I$ that couples the initial state to the final state is the same as for annihilation in vacuum. We already know the result of the matrix element between an initial plane wave electron and positron pair to a two photon final state, which simplifies the calculation. Indeed, if we can count the number of initial electron-positron plane wave states with total momentum $\mathbf{p}$, then we can substitute the result of Eq. (2.9) for each of these pair. We can accomplish this by defining [36]

$$\hat{H}_I(\mathbf{p}) \to \hat{A}(\mathbf{p}) = \int dp^e dp^p \, \hat{a}^e_{p^e} \hat{a}^p_{p^p} \hat{S}_{\sigma^e,\sigma^p} \delta(\mathbf{p}^e + \mathbf{p}^p - \mathbf{p}). \tag{2.11}$$

The symbol $\hat{a}^\alpha_p$ is the annihilation operator for a particle of type α in a plane wave state with momentum and spin $p^\alpha = \{\mathbf{p}, \sigma\}$. To ensure we only count singlet states, we introduced the singlet projection operator [37]

$$\hat{S}_{\sigma^e,\sigma^p} |\sigma^e, \sigma^p\rangle = \left(\frac{1}{4} - \sigma^e \sigma^p \right) \left(|\sigma^e, \sigma^p\rangle - |-\sigma^e, -\sigma^p\rangle \right). \tag{2.12}$$

Counting indistinguishable final states

We make the reasonable assumption that we can factorize the final state as a $N_e - 1$ electron wave function $|\Phi_\nu\rangle$ multiplied by two plane wave photon states. This enables us to carry out the summation over indistinguishable photon and electron states separately. The result of Eq. (2.9) is ultimately derived from an application of Fermi's golden rule and includes the phase space considerations for the final photon states, such that we substitute $2\pi/\hbar \sum_{\text{photon states}} \to 4\pi r_e^2 c$. Next, in PAS experiments, we cannot distinguish between the different possible $N_e - 1$ electron states $|\Phi_\nu\rangle$. Therefore

$$\begin{aligned} \rho^{2\gamma}(\mathbf{p}) &= 4\pi r_e^2 c \sum_\nu \langle \Psi_i | \hat{A}^\dagger(\mathbf{p}) | \Phi_\nu \rangle \langle \Phi_\nu | \hat{A}(\mathbf{p}) | \Psi_i \rangle & (2.13) \\ &= 4\pi r_e^2 c \, \langle \Psi_i | \hat{A}^\dagger(\mathbf{p}) \hat{A}(\mathbf{p}) | \Psi_i \rangle, & (2.14) \end{aligned}$$

where we exploited the completeness relation $\sum_\nu |\Phi_\nu\rangle\langle\Phi_\nu| = 1$.

Note that the result of a PAS experiment is not influenced by the final electronic state of the system. This absence of 'matrix element effects' is an advantage over some other spectroscopic methods. Take for example ARPES, which uses light to excite electrons from their groundstate to an empty state above the Fermi level. The electrical field of the incident light is the perturbation that couples the initial and final states. It is possible that certain transitions are forbidden by fundamental conservation rules. For example, the initial and final states cannot have the same total angular momentum due to the unit angular momentum carried by the indicdent photon. Also the energy and polarization of the incident light can affect the results in non-trivial ways [38, 39].

Counting electron-positron pairs

We can write the many-body initial state in terms of field operators as [40]

$$|\Psi_i\rangle = \frac{1}{\sqrt{N_e!}} \int dr_1^e \dots dr_{N_e}^e dr^p \, \Psi(r_1^e, \cdots, r_{N_e}^e, r^p) \times \hat{\psi}^{e+}(r_1^e) \cdots \hat{\psi}^{e+}(r_{N_e}^e) \hat{\psi}^{p+}(r^p)|0\rangle \quad (2.15)$$

where $\hat{\psi}^{\alpha+}(r)$ creates a particle of species α at position and in spin state $r = \{\mathbf{r}, \sigma\}$. Expanding the field operators in terms of plane-wave creation operators

$$\hat{\psi}^{\alpha+}(r) = \int \frac{d\mathbf{k}}{(2\pi)^{3/2}} \, \hat{a}_k^{\alpha+} e^{-i\mathbf{k}\cdot\mathbf{r}}, \quad (2.16)$$

and substituting the Fourier transform of the many-body wave function

$$\Psi(k_1^e, \dots, k_{N_e}^e, k^p) = \int \frac{d\mathbf{r}_1^e}{(2\pi)^{3/2}} \cdots \frac{d\mathbf{r}_{N_e}^e}{(2\pi)^{3/2}} \frac{d\mathbf{r}^p}{(2\pi)^{3/2}} \times e^{-i\mathbf{k}_1^e\cdot\mathbf{r}_1^e} \cdots e^{-i\mathbf{k}_{N_e}^e\cdot\mathbf{r}_{N_e}^e} e^{-i\mathbf{k}_p^e\cdot\mathbf{r}^p} \, \Psi(r_1^e, \dots, r_{N_e}^e, r^p), \quad (2.17)$$

we can rewrite our many-body state as

$$|\Psi_i\rangle = \frac{1}{\sqrt{N_e!}} \int dk_1^e \dots dk_{N_e}^e dk^p \, \Psi(k_1^e, \cdots, k_{N_e}^e, k^p) \, \hat{a}_{k_1^e}^{e+} \cdots \hat{a}_{k_{N_e}^e}^{e+} \, \hat{a}_{k^p}^{p+}|0\rangle. \quad (2.18)$$

Using the standard anti-commutation rules between fermion operators, and commutation rules between electron and positron operators, we can show that the effect of the annihilation operator, Eq. (2.11), on the initial state gives

$$\hat{A}(\mathbf{p})|\Psi_i\rangle = \frac{1}{\sqrt{N_e!}} \int dp^e dp^p \, \delta(\mathbf{p}^e + \mathbf{p}^p - \mathbf{p}) \hat{S}_{\sigma^e,\sigma^p} \times \int dk_1^e \dots dk_{N_e}^e dk^p \, \Psi(k_1^e, \dots, k_{N_e}^e, k^p) \times \sum_{j=1}^{N_e} (-1)^{j+1} \delta(p^e - k_j^e) \delta(p^p - k^p) \prod_{\substack{i=1 \\ i\neq j}}^{N_e} \left[\hat{a}_{k_i^e}^{e+}\right] |0\rangle. \quad (2.19)$$

For convenience in the rest of the derivation, we will write $\Psi^s(\dots)$ for the wavefunctions to denote the effect of the singlet projection operator. This eliminates the sum over the spins of the annihilating pair $\int dp^e dp^p = \sum_{\sigma^e,\sigma^p} \int d\mathbf{p}^e d\mathbf{p}^p \to \int d\mathbf{p}^e d\mathbf{p}^p$. At the end of the derivation we just need to remember that we need to take the singlet combinations of the annihilating pairs. The matrix element of interest gives

$$\begin{aligned}
\langle\Psi_i|\hat{A}^\dagger(\mathbf{p})\hat{A}(\mathbf{p})|\Psi_i\rangle = \frac{1}{N_e!}\int d\mathbf{p}^{e\prime} d\mathbf{p}^{p\prime} d\mathbf{p}^{e} d\mathbf{p}^{p}\, \delta(\mathbf{p}^{e\prime}+\mathbf{p}^{p\prime}-\mathbf{p})\delta(\mathbf{p}^{e}+\mathbf{p}^{p}-\mathbf{p}) \\
\times \int \left(\prod_{i=1}^{N_e} dk_i^{e\prime} dk_i^{e}\right) dk^{p\prime} dk^{p}\, \Psi^{s*}(k_1^{e\prime},\ldots,k_{N_e}^{e\prime},k^{p\prime})\Psi^{s}(k_1^{e},\ldots,k_{N_e}^{e},k^{p}) \\
\times \sum_{\substack{j=1\\ j'=1}}^{N_e} (-1)^{j+j'}\delta(p^e-k_j^e)\delta(p^p-k^p)\delta(p^{e\prime}-k_{j'}^{e\prime})\delta(p^{p\prime}-k^{p\prime}) \\
\times \langle 0| \prod_{\substack{i'=1\\ i'\neq j'}}^{N_e}\left[\hat{a}^{e}_{k^{e\prime}_{i'}}\right] \prod_{\substack{i=1\\ i\neq j}}^{N_e}\left[\hat{a}^{e+}_{k^{e}_{i}}\right] |0\rangle. \qquad (2.20)
\end{aligned}$$

To work out this rather daunting expression, let us first focus on the matrix element between the creation and annihilation operators on the last line. The result can be obtained by noting that (i) every creation operator must have a matching annihilation operator with the same momentum and spin k in order to obtain non-zero results, (ii) if the previous point is satisfied, we can form $(N_e-1)!$ such pairs, and (iii) $\langle 0|\hat{a}^e_{k_1}\ldots\hat{a}^e_{k_{N_e}}\,\hat{a}^{e+}_{k_{N_e}}\ldots\hat{a}^{e+}_{k_1}|0\rangle = 1$ [40]. Next, note that we generally need to permute the annihilation operators to bring them in the order depicted in point (iii), which gives an extra minus sign if the number of permutations is odd. However, the same permutations can be applied to the coordinates of Ψ^{s*} and due to its anti-symmetry, the minus signs cancel and all $(N_e-1)!$ terms give the same result. Finally, using a similar argument, one can realize that also all $(N_e)^2$ terms contained in the sums over j and j' give identical results. Our result becomes, choosing the index of the annihilating electron equal to N_e,

$$\begin{aligned}
\langle\Psi_i|\hat{A}^\dagger(\mathbf{p})\hat{A}(\mathbf{p})|\Psi_i\rangle = N_e \int dk_1^e\cdots dk_{N_e-1}^e \\
\times \left|\int d\mathbf{k}^e d\mathbf{k}^p\, \Psi^s(k_1^e,\ldots,k_{N_e-1}^e,\mathbf{k}^e,\mathbf{k}^p)\delta(\mathbf{k}^e+\mathbf{k}^p-\mathbf{p})\right|^2 \qquad (2.21)
\end{aligned}$$

We get for the electron-positron momentum density

$$\begin{aligned}
\rho^{2\gamma}(\mathbf{p}) &= 4\pi r_e^2 c N_e \int dk_1^e\ldots dk_{N_e-1}^e \left|\int d\mathbf{k}^p\, \Psi^s(k_1^e,\ldots,k_{N_e-1}^e,\mathbf{p}-\mathbf{k}^p,\mathbf{k}^p)\right|^2 \qquad (2.22)\\
&= 4\pi r_e^2 c N_e \int d\tau \left|\int d\mathbf{r}\, e^{-i\mathbf{p}\cdot\mathbf{r}}\Psi^s(r_1^e,\ldots,r_{N_e-1}^e,\mathbf{r},\mathbf{r})\right|^2, \qquad (2.23)
\end{aligned}$$

where in the last step, we have performed the Fourier transformation to real space. Here, $d\tau = \prod_{i=1}^{N_e-1} dr_i^e$ denotes integration over all electron coordinates that do not belong to the annihilating electron-positron pair. Notice that the last expression tells us that the electron and positron have to reside at the same point in space in order to annihilate.

To obtain the total transition rate, or the positron annihilation lifetime, we still need to count the total number of accessible final photon states. This gives[2]

$$\lambda_a = \frac{1}{\tau} = \int \frac{d\mathbf{p}}{(2\pi)^3}\rho^{2\gamma}(\mathbf{p}) = 4\pi r_e^2 c N_e \int d\tau d\mathbf{r}\, |\Psi^s(r_1^e,\ldots,r_{N_e-1}^e,\mathbf{r},\mathbf{r})|^2. \qquad (2.24)$$

---

[2] The factor $1/(2\pi)^3$ gives the number of accessible states within in the infinitesimal volume $d\mathbf{p}$ [32].

We have succeeded in writing down the expressions for the electron-positron momentum density $\rho^{2\gamma}(\mathbf{p})$ and the total annihilation rate λ_a in terms of the many-body wave function of our system. For practical calculations, we still need to make a connection with a single particle picture as obtaining the many-body wave function is unfeasible. In the next section, we introduce what can be interpreted as electron-positron pair wave functions that will prove useful for this purpose.

2.1.5 Geminals

In the above equations, we can recognize the electron-positron Two-Body Reduced Density Matrix (2RDM), defined as

$$\Gamma^{ep}(r^e, r^p, r^{e\prime}, r^{p\prime}) = N_e \int d\tau\, \Psi^*(r^e_1, \dots, r^e_{N_e-1}, r^e, r^p) \times \Psi(r^e_1, \dots, r^e_{N_e-1}, r^{e\prime}, r^{p\prime}). \quad (2.25)$$

Though, instead of the 16 possible spin components of the above 2RDM, we should only consider the 4 combinations that have non-zero singlet components. It is convenient to introduce the so-called 'natural geminals' α_j which are the orthonormal eigenfunction of the electron-positron 2RDM [41] and can be interpreted as electron-positron pairing wave functions,

$$\Gamma^{ep}(r^e, r^p, r^{e\prime}, r^{p\prime}) = \sum_j g_j \alpha^*_j(r^e, r^p) \alpha_j(r^{e\prime}, r^{p\prime}). \quad (2.26)$$

The singlet components of the 2RDM are obtained by taking the singlet projected geminals, which will again be denoted with a superscript s. Substituting the above in Eq. (2.23) gives

$$\rho^{2\gamma}(\mathbf{p}) = 4\pi r_e^2 c \sum_j g_j \left| \int d\mathbf{r}\, e^{-i\mathbf{p}\cdot\mathbf{r}} \alpha^s_j(\mathbf{r}, \mathbf{r}) \right|^2. \quad (2.27)$$

For the annihilation rate, we obtain

$$\lambda_a = \frac{1}{\tau} = 4\pi r_e^2 c \sum_j g_j \int d\mathbf{r} |\alpha^s_j(\mathbf{r}, \mathbf{r})|^2 \quad (2.28)$$

2.1.6 Spin-polarized measurements

We continue our derivation by taking into account the polarization of the incoming positron beam[3], which determines the initial states. An approximation we will make is that the positron does not experience any interactions acting on its spin, such that it retains the polarization with which it enters the sample. As a consequence, the geminals are collinear in the positron spin. If we represent a general geminal by a four-component spinor, we get

$$\alpha_j(p^e, p^p) = \begin{pmatrix} \alpha_j(\mathbf{p}^e, \uparrow, \mathbf{p}^p, \uparrow) \\ \alpha_j(\mathbf{p}^e, \uparrow, \mathbf{p}^p, \downarrow) \\ \alpha_j(\mathbf{p}^e, \downarrow, \mathbf{p}^p, \uparrow) \\ \alpha_j(\mathbf{p}^e, \downarrow, \mathbf{p}^p, \downarrow) \end{pmatrix} = \begin{pmatrix} \alpha_j(\mathbf{p}^e, \uparrow, \mathbf{p}^p) \\ \alpha_j(\mathbf{p}^e, \downarrow, \mathbf{p}^p) \end{pmatrix} \otimes \chi^p, \quad (2.29)$$

---

[3] The derivation in this section is part of my work published in Ref. [42].

where $\otimes$ denotes the direct product and χ^p is the positron spinor. In most experiments, the incident positron beam is has a given polarization P along a chosen quantization axis. Analogous to the density matrix formalism, we sum over all distinct initial states of the systems and weight them by their statistical probability

$$\rho^{2\gamma}(\mathbf{p}) = 4\pi r_e^2 c \sum_{i=\{\chi_+^p,\chi_-^p\}} p_i \sum_j g_j \left| \int d\mathbf{r}\, e^{-i\mathbf{p}\cdot\mathbf{r}} \alpha^s_{j,i}(\mathbf{r},\mathbf{r}) \right|^2 , \tag{2.30}$$

where extra sum is taken over the polarization states for the positron, and the extra subscript on the geminal denotes the positron spinor that enters the expression of the geminals.

Let us have a closer look at the most common case, in which we have an unpolarized positron beam. If we take the quantization axis along the z-axis, we have for the spin-up and spin-down positron spinors

$$\chi^p_{z+} = \begin{pmatrix} 1 \\ 0 \end{pmatrix} \quad \text{and} \quad \chi^p_{z-} = \begin{pmatrix} 0 \\ 1 \end{pmatrix} , \tag{2.31}$$

respectively, which both have equal statistical weights $p_{\chi^p_{z+}} = p_{\chi^p_{z-}} = 1/2$. The singlet component of the geminals is in general

$$\alpha^s_j(\mathbf{r}^e, \mathbf{r}^p) = \frac{1}{\sqrt{2}} \left[\alpha_j(\mathbf{r}^e, \uparrow, \mathbf{r}^p, \downarrow) - \alpha_j(\mathbf{r}^e, \downarrow, \mathbf{r}^p, \uparrow) \right] , \tag{2.32}$$

such that the singlet components for the oppositely polarized positron states become

$$\alpha^s_{j,\chi^p_{z+}}(\mathbf{r}^e, \mathbf{r}^p) = -\alpha_j(\mathbf{r}^e, \downarrow, \mathbf{r}^p, \uparrow), \quad \alpha^s_{j,\chi^p_{z-}}(\mathbf{r}^e, \mathbf{r}^p) = \alpha_j(\mathbf{r}^e, \uparrow, \mathbf{r}^p, \downarrow). \tag{2.33}$$

Substituting these in the equation for the momentum density gives

$$\begin{aligned} \rho^{2\gamma}(\mathbf{p}) = \pi r_e^2 c \sum_j g_j \iint d\mathbf{r} d\mathbf{r}'\, e^{-i\mathbf{p}\cdot(\mathbf{r}-\mathbf{r}')} \{ & \alpha^*_j(\mathbf{r}', \uparrow, \mathbf{r}', \downarrow) \alpha_j(\mathbf{r}, \uparrow, \mathbf{r}, \downarrow) \\ & + \alpha^*_j(\mathbf{r}', \downarrow, \mathbf{r}', \uparrow) \alpha_j(\mathbf{r}, \downarrow, \mathbf{r}, \uparrow) \}. \end{aligned} \tag{2.34}$$

Using spin-polarized positron beams, it is possible to measure the spin dependence of the momentum density. This sounds plausible since the positron can only annihilate with electrons that have the opposite spin. In practice this requires two measurements; each one with the opposite direction for the positron spin. The magnetization is then obtained by taking the difference between the measured spectra [42–44]. If we take again the polarization along the z-axis, and call the polarization of the bundle P, then we have for the first measurement $p_{\chi^p_{z+}} = P$, $p_{\chi^p_{z-}} = (1-P)$, and vice-versa for the second measurement. The difference between the two measurements is then

$$\begin{aligned} \rho^{2\gamma}(\mathbf{p}) = 4\pi r_e^2 c \sum_j g_j \iint d\mathbf{r} d\mathbf{r}'\, e^{-i\mathbf{p}\cdot(\mathbf{r}-\mathbf{r}')} & \\ \times \left\{ \frac{2P-1}{2} \left[\alpha^*_j(\mathbf{r}', \uparrow, \mathbf{r}', \downarrow) \alpha_j(\mathbf{r}, \uparrow, \mathbf{r}, \downarrow) \right] + \frac{1-2P}{2} \left[\alpha^*_j(\mathbf{r}', \downarrow, \mathbf{r}', \uparrow) \alpha_j(\mathbf{r}, \downarrow, \mathbf{r}, \uparrow) \right] \right\} & \end{aligned} \tag{2.35}$$

Similar derivations can be made for the magnetization along the other axes, where the positron spinor then has to be replaced by

$$\chi^p_{x+} = \frac{1}{\sqrt{2}} \begin{pmatrix} 1 \\ 1 \end{pmatrix}, \quad \chi^p_{x-} = \frac{1}{\sqrt{2}} \begin{pmatrix} 1 \\ -1 \end{pmatrix}, \quad \chi^p_{y+} = \frac{1}{\sqrt{2}} \begin{pmatrix} 1 \\ i \end{pmatrix}, \quad \chi^p_{y-} = \frac{1}{\sqrt{2}} \begin{pmatrix} 1 \\ -i \end{pmatrix}. \tag{2.36}$$

In the ideal case of a perfectly polarized positron beam, we can bundle our results in a more concise form. For this, we first introduce the following notation for the Fourier transform of the contact term of the geminals

$$A_{j,\sigma^e\sigma^p}(\mathbf{p}) = \int d\mathbf{r}\, e^{-i\mathbf{p}\cdot\mathbf{r}} \alpha_j(\mathbf{r}, \sigma^e, \mathbf{r}, \sigma^p). \tag{2.37}$$

The four possible terms that can be obtained by taking the modulus squared of a general singlet geminal are then contained in the matrix

$$\Gamma_j(\mathbf{p}) = \begin{pmatrix} |A_{j,\uparrow\downarrow}(\mathbf{p})|^2 & A_{j,\uparrow\downarrow}(\mathbf{p})A^*_{j,\downarrow\uparrow}(\mathbf{p}) \\ A_{j,\downarrow\uparrow}(\mathbf{p})A^*_{j,\uparrow\downarrow}(\mathbf{p}) & |A_{j,\downarrow\uparrow}(\mathbf{p})|^2 \end{pmatrix}. \tag{2.38}$$

The magnetization of the momentum density extracted from experiment is then given by

$$\rho_i^{2\gamma}(\mathbf{p}) = 2\pi r_e^2 c \sum_j g_j \operatorname{Tr}[\sigma_i \Gamma_j(\mathbf{p})], \tag{2.39}$$

with $i = \{x, y, z\}$ and where σ_i are the Pauli matrices. Note that the unpolarized case is obtained by setting $\sigma_i = \mathbf{1}/2$, i.e. half the unit matrix.

Finally, we note that positron annihilation lifetime experiments are generally performed using unpolarized beams, for which the relevant expression then becomes

$$\lambda_a = \frac{1}{\tau} = \pi r_e^2 c \sum_j g_j \int d\mathbf{r}\, \left[|\alpha_j(\mathbf{r}, \uparrow, \mathbf{r}, \downarrow)|^2 + |\alpha_j(\mathbf{r}, \downarrow, \mathbf{r}, \uparrow)|^2\right] \tag{2.40}$$

2.2 The Many-Body Problem

In the previous section, we saw that we need the 2RDM in order to calculate the desired PAS characteristics. Since these are derived from the many-body wave function, we have to solve the following many-body Schrödinger equation

$$\left[\hat{H}_e + \hat{H}_p + \hat{H}_I + \hat{H}_{ee} + \hat{H}_{pp} + \hat{H}_{II} + \hat{H}_{ep} + \hat{H}_{eI} + \hat{H}_{pI}\right] \Psi = E\Psi \tag{2.41}$$

Here,

$$\hat{H}_\alpha = -\frac{1}{2} \sum_{i=1}^{N_\alpha} m_i \nabla_i^2 \tag{2.42}$$

is the usual kinetic energy operator, with m_i the mass of the particle, N_α is the number of particles of a particular species, and ∇_i^2 the Laplace operator. The subscript e is used to denote electrons, p for positrons and I for ions. Next we have

$$\hat{H}_{\alpha\beta} = c_{\mathrm{dc}} \sum_{i=1}^{N_\alpha} \sum_{j=1}^{N_\beta} \frac{q_i q_j}{|\mathbf{r}_i - \mathbf{r}_j|}, \tag{2.43}$$

the interaction between the particles. In this equation, q_i is the charge of particle i and $\mathbf{r}_i$ its position in space. The constant c_{dc} is equal to $1/2$ when $\alpha = \beta$ to avoid double counting.

It is well-known, however, that directly solving the many-body Schrödinger equation is unfeasible due to the dimensionality of the problem. Hence, approximations have to be made in order to obtain any results at all. The first simplification we will make is the Born-Oppenheimer approximation [45]. This basically means that we will ignore the quantum character of the ions. The approximation is justified because the masses of the ions are much larger than of the electrons (and positrons) in the material, which implies that they are much more localized in space and move slowly compared to the electrons and positrons. As a consequence we can treat them as classical particles, that create a static potential for the electrons and positrons, which adapt instantaneously to this potential. In the rest of this chapter, we will use Ψ to denote a wave function that depends on the electron and positron coordinates, and only parametrically on the ionic coordinates. We will also write the Hamiltonian as $\hat{H} = \hat{H}_e + \hat{H}_p + \hat{H}_{ee} + \hat{H}_{pp} + \hat{H}_{ep} + V_{ext}$, where the latter term indicates the 'external' potential. This includes, among external fields, the potential created by the presence of the ions.

Further simplifications can be achieved by writing the remaining electron-positron wave function as a product of one-particle wave functions (orbitals). In the simplest case, this leads to the HF equations. Alternatively, one can treat the electron and positron densities as the fundamental quantities, which are inherently three dimensional. This is the 2CDFT approach, and we will study some aspects of it in this chapter.

2.2.1 Many-Body quantities

Let us introduce some quantities that are important in the rest of the thesis. The first is the joint probability density between two particles α and β, $\rho^{\alpha\beta}$. This *pair density* is derived from the many-body probability density by integrating out all coordinates except those for the particles in question. For example, if we have a system of N_e electrons, we get the electron pair density[4]

$$\rho^{ee}(\mathbf{r}_1^e, \mathbf{r}_2^e) = N_e(N_e - 1) \int d\mathbf{r}_3^e \cdots \int d\mathbf{r}_{N_e}^e \left|\Psi(\mathbf{r}_1^e, \ldots, \mathbf{r}_{N_e}^e)\right|^2, \tag{2.44}$$

and similarly, for a system with N_e electrons and a single positron,

$$\rho^{ep}(\mathbf{r}^e, \mathbf{r}^p) = N_e \int d\mathbf{r}_2^e \cdots \int d\mathbf{r}_{N_e}^e \left|\Psi(\mathbf{r}_1^e, \ldots, \mathbf{r}_{N_e}^e, \mathbf{r}^p)\right|^2, \tag{2.45}$$

gives the electron-positron pair density. The *contact density* is obtained by evaluating the pair density at the same position for both particles, e.g. $\rho^{ee}(\mathbf{r}, \mathbf{r})$. This is not to be confused by the *particle density*, where an additional coordinate is integrated out; for the positron density

$$\rho^p(\mathbf{r}^p) = \int d\mathbf{r}^e \, \rho^{ep}(\mathbf{r}^e, \mathbf{r}^p). \tag{2.46}$$

As shown in the previous sections, the contact density is used to calculate the annihilation rate. Note from Eq. (2.24) that the annihilation rate is proportional to the contact density.

For the rest of this thesis, it is important to realize that the densities ρ^e and ρ^p give us, respectively, the probability of finding an electron or positron at some position in space, *independent of where the other particles are.* This means that, given that a positron is at $\mathbf{r}^p$, the probability of finding some electron at $\mathbf{r}^e$, is not given by multiplying the densities $\rho^{ep}(\mathbf{r}^e, \mathbf{r}^p) \neq \rho^e(\mathbf{r}^e)\rho^p(\mathbf{r}^p)$. Instead, we have $\rho^{ep}(\mathbf{r}^e, \mathbf{r}^p) = g^{ep}(\mathbf{r}^e, \mathbf{r}^p)\rho^e(\mathbf{r}^e)\rho^p(\mathbf{r}^p)$, where $g^{ep}(\mathbf{r}^e, \mathbf{r}^p)$ is the *electron-positron pair correlation function.* It is defined by the equation just shown, and thus describes the change in the probability, relative to the unconditional

---

[4] Due to the symmetry of the wave function it does not matter which electron coordinates we choose, i.e. the subscript numbers have no special meaning.

probability, of finding an electron at $\mathbf{r}^e$ given a positron density ρ^p at $\mathbf{r}^p$. The change in the electron density at $\mathbf{r}^e$ due to a positron at $\mathbf{r}^p$ is then given by[5]

$$\Delta\rho^e(\mathbf{r}^e|\mathbf{r}^p) = (g^{ep}(\mathbf{r}^e,\mathbf{r}^p) - 1)\rho^e(\mathbf{r}^e). \tag{2.47}$$

We will call this quantity the *screening cloud* and it has a central role in the rest of this thesis. Finally, the screening cloud at zero distance $\gamma(\mathbf{r}^p) = \Delta\rho^e(\mathbf{r}^p|\mathbf{r}^p)$ is important for the calculation of PAS spectra and is called the *enhancement factor*.

2.3 Hartree-Fock

We now proceed by presenting one of the most well-known methods to approximately solve the many-body Schrödinger equation, namely HF theory. In this approach, we are interested in minimizing the total energy of the system

$$E = \langle\Psi|\hat{H}|\Psi\rangle, \tag{2.48}$$

with some approximate wave function Ψ. Since electrons are fermions, the wave function has to be antisymmetric under exchange of two of these particles. If we would only be dealing with electrons, the simplest wave function build from one-particle wave functions with the correct permutation symmetry is a Slater determinant

$$\begin{aligned}\Psi(r_1^e,\dots,r_{N_e}^e) &= \frac{1}{\sqrt{N_e!}}\begin{vmatrix}\psi_1^e(r_1^e) & \dots & \psi_{N_e}^e(r_1^e)\\ \vdots & \ddots & \vdots\\ \psi_1^e(r_{N_e}^e) & \dots & \psi_{N_e}^e(r_{N_e}^e)\end{vmatrix}\\ &\equiv |\psi_1^e\dots\psi_{N_e}^e|.\end{aligned} \tag{2.49}$$

Here the ψ_i^e are the orbitals and $r_i^e = \{\mathbf{r}_i^e, \sigma_i^e\}$ denotes both the position $\mathbf{r}_i^e$ and spin σ_i^e of the particle. It is simple to extend this to include positrons as well. Since all positrons are also identical particles, we have the same anti-symmetry requirement for the wave function under permutation of a pair of positrons. Next, since electrons and positrons have opposite charge, the Hamiltonian is in general not invariant under permutation of an electron and positron coordinate. Hence, there is no symmetry under exchange of electrons and positrons. The trial wave function for our problem is thus given by the product of two Slater determinants $\Psi(r_1^e,\dots,r_{N_e}^e,r_1^p,\dots,r_{N_p}^p) = |\psi_1^e\dots\psi_{N_e}^e| \times |\psi_1^p\dots\psi_{N_p}^p|$, one for the electrons and one for the positrons.

One can find the set of electron and positron orbitals that minimize the total energy by applying the variational principle

$$\delta\left(E - \sum_{i,j}\lambda_{i,j}^e\left[\langle\psi_i^e|\psi_j^e\rangle - \delta_{i,j}\right] - \sum_{i,j}\lambda_{i,j}^p\left[\langle\psi_i^p|\psi_j^p\rangle - \delta_{i,j}\right]\right) = 0, \tag{2.50}$$

where we introduced the Lagrange multipliers $\lambda_{i,j}^\alpha$ to ensure that the orbitals of each species are orthonormal. The derivation then proceeds as usual [45] and the result is

---

[5] Assuming that there is a positron at $\mathbf{r}^p$ means $\rho^p(\mathbf{r}^p) = 1$.

given by

$$\begin{gathered}\left[\hat{H}_e+\sum_{i=1}^{N_e}\left(\hat{J}_i^e-\hat{K}_i^e\right)+\sum_{i=1}^{N_p}\hat{J}_i^p\right]\psi_k^e=\varepsilon_k^e\psi_k^e\\ \left[\hat{H}_p+\sum_{i=1}^{N_p}\left(\hat{J}_i^p-\hat{K}_i^p\right)+\sum_{i=1}^{N_e}\hat{J}_i^e\right]\psi_k^p=\varepsilon_k^p\psi_k^p.\end{gathered}\tag{2.51}$$

We thus end up with two sets of equations, one for the electrons and one for the positrons. In the above equations, we have the direct interaction

$$\hat{J}_i^\alpha\psi_k^\beta(r)=q_\alpha q_\beta\left(\int dr'\,\frac{|\psi^\alpha(r')|^2}{|\mathbf{r}-\mathbf{r}'|}\right)\psi_k^\beta(r),\tag{2.52}$$

where the prefactor $q_\alpha q_\beta$ ensures a positive result if the interaction is between particles of the same species, and negative if they are between electrons and positrons. The exchange interaction only exists between particles of the same species[6], and is given by

$$\hat{K}_i^\alpha\psi_k^\alpha(r)=\left(\int dr'\,\frac{\psi_i^{\alpha*}(r')\psi_k^\alpha(r')}{|\mathbf{r}-\mathbf{r}'|}\right)\psi_i^\alpha(r).\tag{2.53}$$

Just as with the regular HF equations, these equations have to be solved self-consistently. In this case, however, one would need three self-consistent loops instead of one. This because we have an equation for each of the species, and because they are coupled to each other. We will see momentarily, however, that in many cases this can be significantly simplified.

2.3.1 The zero-density limit

Let us now focus on the special case where we only have a single positron in the sample. This case is the relevant one in most PAS setups, as the beam intensity is low compared to the typical lifetime of a positron in a sample[7]. Since we have $N_p=1$, we see that the direct and exchange interaction for the positron cancel in Eq. (2.51). This makes sense as the positron should not interact with itself. As a consequence, the positron equation only depends on the electron orbitals, which removes one of the self-consistent loops.

A next simplification comes from the fact that in many cases the potential is periodic in at least one dimension. This is for instance the case when we study a perfect bulk crystal (or surface). The positron state is then delocalized, and, if we assume we have only a single positron in the system, the positron orbital approaches zero everywhere, $\psi_1^p(r)\approx 0,\ \forall\mathbf{r}$. As a consequence, the direct interaction with the positron state in the electron equation vanishes, $\hat{J}_1^p\psi_k^e(\mathbf{x})=0$. This removes the dependence of the electronic part of the equations on the positron orbital.

---

[6] The exchange interaction does not affect particles in orthogonal spin states either, which is implicit in equation (2.53). Note, though, that we are treating the orbitals as spinors in this section, and it is thus possible that the spin parts of different orbitals are not aligned. Hence, there is exchange interaction between the like components of the spinors.

[7] The brightest documented positron beam at the time of writing is NEPOMUC, which produces slightly more than 10^9 positrons/second [46]. The lifetime of positrons is typically a few 100 ps. This means that the likelihood of two positrons encountering each other in the sample is vanishingly small.

In the zero-density limit the equations (2.51) thus simplify to

$$\begin{aligned}\left[\hat{H}_e + \sum_{i=1}^{N_e}\left(\hat{J}_i^e - \hat{K}_i^e\right)\right]\psi_k^e &= \varepsilon_k^e \psi_k^e \\ \left[\hat{H}_p + \sum_{i=1}^{N_e}\hat{J}_i^e\right]\psi_k^p &= \varepsilon_k^p \psi_k^p.\end{aligned} \tag{2.54}$$

Compared to the original problem, this is an important simplification. Indeed, we see that we can solve the electronic problem separately, without any dependence on the positron part of the problem. This means that we can use existing electronic structure programs to solve the electron part of the problem and use its output to tackle the positron problem. Furthermore, the positron problem is reduced to a simple Schrödinger equation for a particle moving in an external potential, which unlike the HF equations, does not have to be solved self-consistently.

2.3.2 Limitations of the Hartree-Fock approach

Since the HF approach gives us an approximation for the many-body wave function, we can proceed with the evaluation of the annihilation formulas derived in an earlier section. Our many-body wave function is build from a Slater determinant for the electrons multiplied with a positron orbital. We then have for the 2RDM

$$\Gamma^{ep}(r^e, r^p, r^{e\prime}, r^{p\prime}) = \sum_{j=1}^{N_e}\left(\psi_j^e(r^e)\right)^* \psi_j^e(r^{e\prime})\left(\psi^p(r^p)\right)^* \psi^p(r^{p\prime}). \tag{2.55}$$

It is easy to identify from Eq. (2.26) that the natural geminals are simply the product of the one-particle wave functions in the HF approximation

$$\alpha_j(r^e, r^p) = \psi_j^e(r^e)\psi^p(r^p), \tag{2.56}$$

and the eigenvalues g_j are replaced by the occupation number of the electronic orbitals. The annihilation rate in the HF approximation becomes

$$\lambda_a = \pi r_e^2 c \int d\mathbf{r}\, \rho^e(\mathbf{r})\rho^p(\mathbf{r}), \tag{2.57}$$

where $\rho^e(\mathbf{r}) = \sum_i^{N_e}|\psi_i^e(\mathbf{r})|^2$, and $\rho^p(\mathbf{r}) = |\psi^p(\mathbf{r})|^2$.

In the above results, we have $\rho^{ep}(\mathbf{r},\mathbf{r}') = \rho^e(\mathbf{r})\rho^p(\mathbf{r})$, such that the pair correlation function $g(\mathbf{r},\mathbf{r}') = 1$. Hence, a positron does not attract a screening cloud in the HF approximation, $\Delta\rho^e(\mathbf{r}^e|\mathbf{r}^p) = 0$. The positron orbital is still determined by the electronic orbitals (and vice-versa if the zero-density limit is not taken), but there is no reaction of the electron density when one 'pins down' the positron at a specific position. This approximations is therefore often called the IPM model in PAS literature. Physically, we expect of course an enhancement of the electron density around the positron position. This is also confirmed by positron lifetime experiments, which measure much higher annihilation rates than predicted with the IPM model. Hence, in order to get useful results, we should include correlation effects that describe the electron enhancement around the positron. In the following section, we will see one such approach to this problem.

2.4 Two Component Density Functional Theory

In this section, we discuss the 2CDFT, which allows us to include correlation effects in the calculation of the electron and positron groundstate densities. This is already an improvement over HF, where these effects are not incorporated. We will see, though, that the framework only provides the electron and positron groundstate densities, but not the pair density. Hence, strictly speaking, we cannot evaluate annihilation properties in the framework. We could of course approximate the pair density with the product of the electron and positron groundstate densities, but that would yield the IPM we have encountered in the HF approach. A common workaround exists by introducing a density enhancement term, which models the reaction of the electron density upon pinning of the positron to point in space[8].

In this section, we start by generalizing DFT to include the positron component of the system, which gives the 2CDFT. Afterwards, we examine the simplifications that are obtained by taking the zero-density limit. At the end of the section, we discuss how annihilation properties are commonly calculated starting from the groundstate results obtained from 2CDFT calculations, and the approximations involved.

2.4.1 The energy functional

In regular DFT [47, 48], the Hohenberg-Kohn theorems tell us that there exists a universal functional of the density $F[\rho^e]$, which is independent of the external potential, such that the total energy functional defined by

$$E_{\text{tot}}[\rho^e] = F[\rho^e] + \int d\mathbf{r}\, \rho^e(\mathbf{r}) v_{\text{ext}}(\mathbf{r}) \tag{2.58}$$

is minimized by the exact groundstate density for the given external potential $v_{\text{ext}}(\mathbf{r})$. Furthermore, the minimum of the above energy functional is equal to the true groundstate energy of the system. The extension of the theory to include effects of the electron spins can be found in Refs. [49, 50]. We will neglect spin effects in the rest of this section, however.

One can easily generalize the proofs given in Ref. [47] to include densities for several kinds of particles. In our case, this means that total energy functional

$$E_{\text{tot}}[\rho^e, \rho^p] = F[\rho^e, \rho^p] + \int d\mathbf{r}\, \rho^e(\mathbf{r}) v^e_{\text{ext}}(\mathbf{r}) + \int d\mathbf{r}\, \rho^p(\mathbf{r}) v^p_{\text{ext}}(\mathbf{r}) \tag{2.59}$$

is minimized for the exact groundstate electron and positron densities ρ^e_0 and ρ^p_0. From now on we will use $E_{\text{ext}}[\rho^e, \rho^p]$ to denote the energy due to external potentials. The universal functional $F[\rho^e, \rho^p]$ should give the same energy as the groundstate energy calculated from the wave function, i.e.

$$F[\rho^e, \rho^p] = E_{\text{tot}}[\Psi] = \langle \Psi | \hat{H}_e + \hat{H}_p + \hat{H}_{ee} + \hat{H}_{pp} + \hat{H}_{ep} | \Psi \rangle, \tag{2.60}$$

but, like for regular DFT, no exact expression in terms of the electron and positron densities is known.

The Kohn-Sham (KS) approach [51], which has been extended to deal with electron-positron mixtures [52, 53], provides a way to get accurate approximations of the total

---

[8] Although practically always applied in conjunction with 2CDFT, the enhancement correction could also be applied to HF results.

energy functional. To this extent, we write the total energy functional as

$$E_{\text{tot}}[\rho^e, \rho^p] = F[\rho^e] + F[\rho^p] + E_H[\rho^e, \rho^p] + E_c[\rho^e, \rho^p] + E_{\text{ext}}[\rho^e, \rho^p], \tag{2.61}$$

The first two terms on the right-hand side are the universal functional for a single component gas, which is written as

$$F[\rho^\alpha] = T[\rho^\alpha] + E_H[\rho^\alpha] + E_{xc}[\rho^\alpha]. \tag{2.62}$$

The kinetic energy T is obtained by taking the kinetic energy of the (fictitious) non-interacting electron or positron gas at the same density as the interacting system. The second term is the Hartree energy

$$E_H[\rho^\alpha] = \iint d\mathbf{r}d\mathbf{r}' \frac{\rho^\alpha(\mathbf{r})\rho^\alpha(\mathbf{r}')}{|\mathbf{r} - \mathbf{r}'|}, \tag{2.63}$$

and the last term is everything of the single component gas we do not know exactly in terms of the density, i.e. the exchange and correlation energy. This includes both corrections to the kinetic and Coulomb energies of the single component system. Next, we have the Hartree energy between the electron and positron density in Eq. (2.61), which is very similar the Hartree energy between like particles, but instead lowers the energy

$$E_H[\rho^e, \rho^p] = -\iint d\mathbf{r}d\mathbf{r}' \frac{\rho^e(\mathbf{r})\rho^p(\mathbf{r}')}{|\mathbf{r} - \mathbf{r}'|}. \tag{2.64}$$

Like the exchange and correlation energy for the single component functionals, we gather the remaining energy which we do not know how to express in terms of the electron and positron densities in $E_c[\rho^e, \rho^p]$, and call it the electron-positron correlation energy. Note that since the many-body wave function is not anti-symmetric between electrons and positrons, as discussed in Sec. 2.3, it contains no contribution from exchange.

2.4.2 Minimization of the energy

In order to find the groundstate of the system, we need to minimize the total energy functional in Eq. (2.61). At the minimum, the energy has to be stationary under a variations of both the electron and positron densities around the groundstate values ρ_0^e, ρ_0^p. Denoting the variations as $\delta\rho^e, \delta\rho^p$, we need to determine

$$\delta E_{\text{tot}} = E_{\text{tot}}[\rho_0^e + \delta\rho^e, \rho_0^p + \delta\rho^p] - E_{\text{tot}}[\rho_0^e, \rho_0^p] = 0. \tag{2.65}$$

Interaction terms

Expanding up to first order, we find for the single component functionals

$$\delta F = \delta T + \int d\mathbf{r}\,(v_H^\alpha(\mathbf{r}) + v_{xc}^\alpha(\mathbf{r}))\,\delta\rho^\alpha(\mathbf{r}), \tag{2.66}$$

with $\alpha = \{e, p\}$ and where we defined the Hartree potential

$$v_H^\alpha(\mathbf{r}) = \int d\mathbf{r}' \frac{\rho_0^\alpha(\mathbf{r}')}{|\mathbf{r} - \mathbf{r}'|}, \tag{2.67}$$

and exchange and correlation potential

$$v_{xc}^\alpha(\mathbf{r}) = \left.\frac{\delta E_{xc}[\rho^\alpha]}{\delta\rho^\alpha(\mathbf{r})}\right|_{\rho^\alpha = \rho_0^\alpha}. \tag{2.68}$$

We will work out an expression for the variation of the kinetic energy in the next paragraph. The variation of the remaining terms in the energy functional gives

$$\int d\mathbf{r}\,[v^e_{ext}(\mathbf{r}) + v^p_H(\mathbf{r}) + v^e_c(\mathbf{r})]\,\delta\rho^e(\mathbf{r}) + [v^p_{ext}(\mathbf{r}) + v^e_H(\mathbf{r}) + v^p_c(\mathbf{r})]\,\delta\rho^p(\mathbf{r}), \tag{2.69}$$

with v^α_{ext} the external potential experienced by the particles, and the electron-positron correlation potentials[9]

$$v^\alpha_c(\mathbf{r}) = \left.\frac{\delta E_c[\rho^e, \rho^p]}{\delta\rho^\alpha(\mathbf{r})}\right|_{\rho^\alpha=\rho^\alpha_0}. \tag{2.70}$$

Kinetic energy; The Kohn-Sham system

What remains to be sought is the variation of the kinetic energy, for which I will follow the derivation given in Ref. [54]. This question brings us to the central assumption of the KS approach: We assume that there exists a local, orbital independent potential $v^\alpha_f(\mathbf{r})$ for each component of the system, such that the groundstate density of a non-interacting system moving through it, is the same as the groundstate density of the interacting many-body system. How this potential can be determined, will become apparent later in the derivation. Since each fictitious system is non-interacting, their groundstates can be represented exactly by a Slater determinant $\Psi^\alpha_f(\mathbf{r}^\alpha_1, \ldots \mathbf{r}^\alpha_{N_\alpha}) = |\psi^\alpha_1 \ldots \psi^\alpha_{N_\alpha}|$. The orbitals ψ^α_i that result in the lowest energy for the non-interacting system are obtained by solving

$$\left(-\frac{1}{2}\nabla^2 + v^\alpha_f(\mathbf{r})\right)\psi^\alpha_i(\mathbf{r}) = \varepsilon^\alpha_i\psi^\alpha_i(\mathbf{r}), \tag{2.71}$$

which are of course the KS equations. The density is obtained from the Slater determinant by summing the moduli squared of the occupied orbitals

$$\rho^\alpha(\mathbf{r}) = \sum_{i=1}^{N_\alpha}|\psi^\alpha_i(\mathbf{r})|^2. \tag{2.72}$$

The kinetic energy of the system is easy to evaluate

$$T[\rho^\alpha] = -\frac{1}{2}\sum_{i=1}^{N_\alpha}\langle\psi^\alpha_i|\nabla^2|\psi^\alpha_i\rangle. \tag{2.73}$$

Minimization of the kinetic energy

We can now determine the variation of the kinetic energy, which gives

$$\delta T = -\frac{1}{2}\sum_{i=1}^{N_\alpha}\int d\mathbf{r}\,\left[\delta(\psi^\alpha_i)^*(\mathbf{r})\nabla^2\psi^\alpha_i(\mathbf{r}) + (\psi^\alpha_i)^*(\mathbf{r})\nabla^2\delta\psi^\alpha_i(\mathbf{r})\right] \tag{2.74}$$

$$= -\frac{1}{2}\sum_{i=1}^{N_\alpha}\int d\mathbf{r}\,\left[\delta(\psi^\alpha_i)^*(\mathbf{r})\nabla^2\psi^\alpha_i(\mathbf{r}) + \delta\psi^\alpha(\mathbf{r})\nabla^2(\psi^\alpha_i)^*(\mathbf{r})\right], \tag{2.75}$$

---

[9] I realize that the notation is quite similar to the exchange and correlation potential between like species. Whenever the subscript does not contain x for exchange, I will denote the correlation between electrons and positrons. The focus of this thesis is on the electron-positron correlation potential, so the chance for confusion in the rest of the work should be small.

where last step follows from Green's second identity[10]. Since the orbitals satisfy the KS equations, we find

$$\delta T = \sum_{i=1}^{N_\alpha} \varepsilon_i^\alpha \int d\mathbf{r}\, \delta|\psi_i^\alpha(\mathbf{r})|^2 - \sum_{i=1}^{N_\alpha} \int d\mathbf{r}\, v_f^\alpha(\mathbf{r})\delta|\psi_i^\alpha(\mathbf{r})|^2. \tag{2.76}$$

Expanding the variation up to first order

$$\delta|\psi_i^\alpha|^2 \approx (\delta(\psi_i^\alpha)^*)\psi_i^\alpha + (\psi_i^\alpha)^*(\delta\psi_i^\alpha) = |\psi_i^\alpha + \delta\psi_i^\alpha|^2 - |\psi_i^\alpha|^2, \tag{2.77}$$

we note that the first term of Eq. (2.76) vanishes since both the first and second term in the last result have to be normalized. Next, since $\delta\rho^\alpha(x) = \delta(\sum_{i=1}^{N_\alpha}|\psi_i^\alpha|^2)$, we arrive at the result

$$\delta T = -\int d\mathbf{x}\, v_f^\alpha(\mathbf{x})\delta\rho^\alpha(\mathbf{x}). \tag{2.78}$$

Note that at this point, do not have a formal expression for the external potentials v_f^α.

Minimum of the total energy; Kohn-Sham equations

If we now collect the results (2.66), (2.69) and (2.78), we see that the variation of the total energy functional becomes

$$\begin{aligned}\delta F = &\int d\mathbf{x}\, \delta\rho^e(\mathbf{x}) \left\{-v_f^e(\mathbf{x}) + v_H^e(\mathbf{x}) + v_H^p(\mathbf{x}) + v_{xc}^e(\mathbf{x}) + v_c^e(\mathbf{x}) + v_{ext}^e(\mathbf{x})\right\} \\ &+ \int d\mathbf{x}\, \delta\rho^p(\mathbf{x}) \left\{-v_f^p(\mathbf{x}) + v_H^e(\mathbf{x}) + v_H^p(\mathbf{x}) + v_{xc}^p(\mathbf{x}) + v_c^p(\mathbf{x}) + v_{ext}^p(\mathbf{x})\right\}.\end{aligned} \tag{2.79}$$

The variation can only vanish for an arbitrary variation of the densities around their groundstate value if the terms in between the curly brackets vanish separately. This determines the external potentials for the non-interacting electron and positron systems.

$$v_f^\alpha(\mathbf{x}) = v_H^e(\mathbf{x}) + v_H^p(\mathbf{x}) + v_{xc}^\alpha(\mathbf{x}) + v_c^\alpha(\mathbf{x}) + v_{ext}^\alpha(\mathbf{x}). \tag{2.80}$$

Thus, solving the set of coupled equations

$$\left(-\frac{1}{2}\nabla^2 + v_H^e(\mathbf{x}) + v_H^p(\mathbf{x}) + v_{xc}^e(\mathbf{x}) + v_c^e(\mathbf{x}) + v_{ext}^e(\mathbf{x})\right)\psi_i^e(\mathbf{x}) = \varepsilon_i^e\psi_i^e(\mathbf{x}) \tag{2.81}$$

$$\left(-\frac{1}{2}\nabla^2 + v_H^e(\mathbf{x}) + v_H^p(\mathbf{x}) + v_{xc}^p(\mathbf{x}) + v_c^p(\mathbf{x}) + v_{ext}^p(\mathbf{x})\right)\psi_i^p(\mathbf{x}) = \varepsilon_i^p\psi_i^p(\mathbf{x}) \tag{2.82}$$

for the N_e and N_p lowest orbitals, gives us the groundstate densities through Eq. (2.72) that minimize the energy functional defined in Eq. (2.61).

2.4.3 Zero-density limit

In this thesis, we will be working in the zero positron density limit of the 2CDFT. As with the HF approach, this implies an important practical simplification. In this section,

---

[10] For finite systems, the wave function have to be square integrable such that the boundary terms vanish. For periodic systems, we also have $\int_c f\nabla^2 g = \int_c g\nabla^2 f$, where the integration is taken over the primitive cell, but for a different reason. See e.g. Ref. [55] Appendix I for a proof.

we investigate how the two component KS problem changes in the zero positron density limit.

Note that the Hartree potential is equivalent to the direct interaction defined for Hartree-Fock

$$v_H^\alpha(\mathbf{x})\psi_i^\alpha(\mathbf{x}) = \sum_{i=1}^{N_\alpha} \hat{J}_i^\alpha \psi_i^\alpha(\mathbf{x}), \tag{2.83}$$

such that we can apply the same reasoning as presented in Sec. 2.3.1. We thus have $v_H^p(\mathbf{x}) = 0$ in the electron KS equation. Next, since we only have a single positron, we do not have to approximate a many-body positron wave function with a product of single positron wave functions. As a consequence v_{xc}^p certainly does not contain correlation effects. Next, we argued in Sec. 2.3.1 that the exchange potential for a single particle systems cancels the self-interaction of the Hartree potential. We conclude that $v_H^p(\mathbf{x}) = -v_{xc}^p(\mathbf{x})$, such that both drop out of the positron KS equation.

Let us now have a more detailed look at the electron-positron correlation energy. In regular DFT, one can write the exchange-correlation energy as [51]

$$E_{xc}[\rho] = \int d\mathbf{x}\, \rho(\mathbf{x})\epsilon_{xc}[\rho(\mathbf{x})], \tag{2.84}$$

provided that the density varies sufficiently slowly. In the above equation, ϵ_{xc} is an energy *per particle*. This forms the basis of (semi-) local density functionals, where ϵ_{xc} is then taken as a function of the local density, and possibly gradients and higher order derivatives of the density.

In multi-component mixtures, the situation is generally more complicated, as the correlation energy cannot be written as a particle density multiplied with an energy per particle [53]. Fortunately, in the zero-density limit, it is possible to write a LDA in the form

$$E_c[\rho^e, \rho^p] = \int d\mathbf{x}\, \rho^p(\mathbf{x})\epsilon_c^{ep}(\rho^e(\mathbf{x})). \tag{2.85}$$

The local correlation energy $\epsilon_c^{ep}(\rho^e(\mathbf{x}))$ is defined as the energy difference of an electron gas at density $\rho^e(\mathbf{x})$ without and with a single immersed positron [56]. The correlation potentials obtained from this expression are

$$v_c^e(\mathbf{x}) = \frac{\delta E_c[\rho^e, \rho^p]}{\delta \rho^e(\mathbf{x})} = 0, \tag{2.86}$$

$$v_c^p(\mathbf{x}) = \frac{\delta E_c[\rho^e, \rho^p]}{\delta \rho^p(\mathbf{x})} = \epsilon_c^{ep}(\rho^e(\mathbf{x})). \tag{2.87}$$

If we gather the above results, we find that the 2CDFT equations reduce to

$$\left(-\frac{1}{2}\nabla^2 + v_H^e(\mathbf{x}) + v_{xc}^e(\mathbf{x}) + v_{ext}^e(\mathbf{x})\right)\psi_i^e(\mathbf{x}) = \varepsilon_i^e \psi_i^e(\mathbf{x}), \tag{2.88}$$

$$\left(-\frac{1}{2}\nabla^2 + v_H^e(\mathbf{x}) + v_c^p(\mathbf{x}) + v_{ext}^p(\mathbf{x})\right)\psi_i^p(\mathbf{x}) = \varepsilon_i^p \psi_i^p(\mathbf{x}). \tag{2.89}$$

There are two important simplifications with respect to the full 2CDFT problem. The first is that the electron part of the problem is decoupled from the positron problem, which means we can use existing electronic structure codes without modifications to obtain the groundstate electron density. The second is that, the positron equation only depends on the electron density, and thus does not have to be solved self-consistently.

2.4.4 Annihilation characteristics

One issue with the calculation of PAS spectra in the framework of 2CDFT is that strictly speaking, we only have access to the groundstate electron and positron densities. For the calculation of the positron annihilation lifetime and the electron-positron momentum density, we require, however, the geminals or the contact density.

From our discussion of the many-body wave function and its derived properties, we note that we can in principle obtain the contact density from the groundstate electron and positron densities as

$$\rho^{ep}(\mathbf{r},\mathbf{r}) = g^{ep}(\mathbf{r},\mathbf{r})\rho^{e}(\mathbf{r})\rho^{p}(\mathbf{r}). \tag{2.90}$$

The pair-correlation function is, however, a system dependent quantity which we cannot calculate in the framework of 2CDFT.

A common approximation is to replace the pair correlation function by the pair correlation function of a homogeneous electron gas. This pair correlation function only depends on the distance between the particles, and the local electron and positron densities $g^{ep}(\mathbf{r}^e,\mathbf{r}^p) \rightarrow g_h^{ep}(|\mathbf{r}^e-\mathbf{r}^p|,\rho^e(\mathbf{r}^e),\rho^p(\mathbf{r}^p))$. The pair correlation function at zero distance is commonly called the enhancement factor, $\gamma(\rho^e(\mathbf{r}),\rho^p(\mathbf{r})) = g_h^{ep}(0,\rho^e(\mathbf{r}),\rho^p(\mathbf{r}))$. Several parametrizations (fits to the results of accurate many-body calculations) of the enhancement factor exist in literature both for finite positron densities [53, 57], as the zero-density limit which only depends on the electron density [53, 56, 58]. The positron annihilation rate is then obtained by calculating

$$\lambda_a = \frac{1}{\tau} = \pi r_e^2 c \int d\mathbf{r}\, \rho^e(\mathbf{r})\rho^p(\mathbf{r})\gamma(\rho^e(\mathbf{r}),\rho^p(\mathbf{r})). \tag{2.91}$$

The LDA enhancement factor is well-known to slightly overestimate the annihilation rate, which in turn is attributed to the overestimation of the core electron enhancement. This overestimation can be cured to some extent by introducing a correction based on the gradient of the electron density [59–62]. Note that in the calculation of annihilation rates, the individual contributions of different electron shells to the total annihilation rate is generally less important. This makes that the overestimation of the core electron annihilation is not severe in many cases, since the overlap of the positron with these states is small due to the strong Coulomb repulsion of the ions.

In contrast to lifetime studies, the relative contribution of core electrons to the spectrum is important in many momentum density studies. Since core electrons of different species give characteristic contributions to the momentum density, the medium to high momentum part of Doppler spectra are often used to characterize vacancy type defects. As the lifetime is usually not simultaneously measured with Doppler spectra, these are typically normalized to unity. This operation puts the emphasis on the correct relative contributions to the spectrum, instead of the total annihilation rate.

Ref. [41] addresses the question whether it is feasible to obtain an accurate result for the electron-positron momentum density starting from a set of single particle functions. It turns out that a reasonable approximation of the geminals can be obtained by taking the product of the Kohn-Sham orbitals with the square root of the LDA density enhancement factor

$$\alpha_{j,\sigma^e\sigma^p}(\mathbf{r},\mathbf{r}) = \psi^e_{j\sigma_e}(\mathbf{r})\psi^p_{\sigma_p}(\mathbf{r})\sqrt{\gamma(\mathbf{r})}, \tag{2.92}$$

and setting the geminal eigenvalues equal to the occupation numbers of the electron orbitals.

In defect identification, one often uses ratio plots to investigate the relative increase and decrease of the momentum density spectrum relative to a defect-free bulk sample, i.e. $\rho^{2\gamma}(\mathbf{p})/\rho^{2\gamma}_{\text{ref}}(\mathbf{p})$. The above approximation provides overall a reasonable approximation for the momentum density, but oscillates around the exact result. A state-dependent enhancement factor

$$\alpha_{j,\sigma^e\sigma^p}(\mathbf{r},\mathbf{r}) = \psi^e_{j\sigma_e}(\mathbf{r})\psi^p_{\sigma_p}(\mathbf{r})\sqrt{\gamma_{j,\sigma^e}} \tag{2.93}$$

on the other hand gives worse overall agreement in the least-squares sense, but due to its rather monotonic discrepancy with the exact results, provides better results in ratio plots. In the above equation, the state-dependent enhancement factor is often defined by the enhancement of the state-dependent annihilation rate in the LDA over its IPM annihilation rate [61, 63], i.e.

$$\gamma_{j,\sigma^e} = \frac{\lambda^{\text{LDA}}_{j,\sigma^e}}{\lambda^{\text{IPM}}_{j,\sigma^e}}, \tag{2.94}$$

where the state-dependent annihilation rates are defined as

$$\lambda^{\text{LDA}}_{j,\sigma^e} = \pi r_e^2 c \int d\mathbf{r}\, |\psi^e_{j\sigma^e}(\mathbf{r})|^2 \rho^p(\mathbf{r})\sqrt{\gamma(\mathbf{r})}, \tag{2.95}$$

and similarly $\lambda^{\text{IPM}}_{j,\sigma^e}$ but with $\gamma(\mathbf{r}) = 1$.

Chapter 3

The Weighted Density Approximation

3.1 Introduction

In this chapter, we introduce the framework of the WDA. We start by presenting the adiabatic connection formula, which is an exact expression for the electron-positron correlation energy. Central in the adiabatic connection formula is the electron-positron pair-correlation function. The WDA is obtained by choosing an approximate form for this pair-correlation function, and constraining it by means of a sum rule. Due to its importance in the WDA, we will spend some time discussing exact constraints that can be placed on the pair correlation function. Next, we will introduce the practical WDA scheme from Ref. [25].

We investigate the WDA mainly to describe positron states at surfaces. Indeed, due to its non-local nature, it is capable to reproduce long ranged correlation effects required to obtain the correct image potential at surfaces, as opposed to semi-local functionals such as the LDA and GGA. Extensive experimental data, of typical properties such as lifetimes and surface binding energies, are unfortunately not available in literature. As a consequence, it is hard to test the accuracy of the WDA directly on surfaces. Instead, we will use the WDA to calculate a set of bulk lifetimes of simple elemental materials for which experimental data are available.

We will see that the initial formulation of the WDA yields lifetimes in poor agreement with experiment. The rest of the chapter is devoted to proposing modifications to the WDA scheme in order to obtain more accurate results. One of the modifications is a gradient correction, which has been investigated as a correction to local functionals, but has not been considered in literature as a correction to the non-local WDA. The other modification we propose is a shell partitioning scheme in which core and valence electrons are treated on a different footing. This idea has been investigated before, e.g. in Ref. [28], but the details will differ in our implementation for reasons we will explain in the respective section. At the end of the chapter, we propose to use a sum rule parameter to fit the experimental bulk lifetimes. This approach is in the same spirit as hybrid functionals in electronic structure calculations, where the ammount of the exact exchange is used to fit the experimental badgap. The results presented in this chapter are published in Ref. [64].

3.2 Theory

An exact expression for the electron-positron correlation energy can be written in terms of a coupling constant (or adiabatic) integration [1, 24]

$$E_c[\rho^e, \rho^p] \quad = \quad -\int_0^1 d\lambda \iint d\mathbf{r}^e d\mathbf{r}^p \, \frac{\rho^e(\mathbf{r}^e)\rho^p(\mathbf{r}^p)\left\{g(\mathbf{r}^e, \mathbf{r}^p; [\rho^e, \rho^p]; \lambda) - 1\right\}}{|\mathbf{r}^e - \mathbf{r}^p|}, \tag{3.1}$$

where ρ^e and ρ^p are the electron and positron densities, respectively. The pair-correlation function $g(\mathbf{r}^e, \mathbf{r}^p; [\rho^e, \rho^p]; \lambda)$ describes the relative increase of the electron density ρ^e at $\mathbf{r}^e$ given a positron density ρ^p at $\mathbf{r}^p$. The pair correlation function is itself a functional of the electron and positron densities, and thus, unknown *a priori.* The coupling constant λ takes the electron-positron interaction from the non-interacting, $\lambda = 0$, to the fully interacting limit, $\lambda = 1$.

The electron-positron correlation potentials are obtained by taking the functional derivatives w.r.t. the densities. The positron correlation potential then becomes

$$\frac{\delta E_c}{\delta\rho^p(\mathbf{r})} = -\int_0^1 d\lambda \int d\mathbf{r}^e \frac{\rho^e(\mathbf{r}^e)}{|\mathbf{r}^e - \mathbf{r}|} \left\{ \{g(\mathbf{r}^e, \mathbf{r}, [\rho^e, \rho^p]; \lambda) - 1\} + \rho^p(\mathbf{r}) \frac{\delta g}{\delta\rho^p(\mathbf{r})} \right\}. \tag{3.2}$$

The result for the electron correlation potential is obtained by swapping the appropriate indices. In the zero-density limit, which will be the focus of the rest of this chapter, we have $\rho^p(\mathbf{r}) \approx 0$, such that the electron correlation potential vanishes everywhere. This is in accordance with our discussion of the zero-density limit of the previous chapter. Also the expression for the positron simplifies since the term with the functional derivative of the pair correlation function gives no contribution to the potential. This allows us to identify what we will call the 'screening cloud'

$$\Delta\rho(\mathbf{r}^e|\mathbf{r}^p; \lambda) = \rho^e(\mathbf{r}^e)\{g(\mathbf{r}^e, \mathbf{r}^p; [\rho^e, \rho^p]; \lambda) - 1\}, \tag{3.3}$$

and we can interpret the correlation potential as the coupling constant averaged Coulomb interaction of the positron with its screening cloud

$$v_c^p(\mathbf{r}^p) = -\int_0^1 d\lambda \int d\mathbf{r}^e \frac{\Delta\rho(\mathbf{r}^e|\mathbf{r}^p; \lambda)}{|\mathbf{r}^e - \mathbf{r}^p|}. \tag{3.4}$$

The expressions (3.3) and (3.4) are formally exact but do not provide a scheme for practical calculations. The pair-correlation function g is an unknown, system-dependent function, and in order to proceed the true pair-correlation function must necessarily be approximated. In fact, the LDA is obtained by replacing both the pair-correlation function and the electron-density prefactor in eq. (3.3) by the corresponding quantities from the homogeneous electron gas at the local density $\rho^e(\mathbf{r}^p)$,

$$\Delta\rho^{\mathrm{LDA}}(\mathbf{r}^e|\mathbf{r}^p; \lambda) = \rho^e(\mathbf{r}^p)\{g^h(|\mathbf{r}^e - \mathbf{r}^p|; \rho^e(\mathbf{r}^p); \lambda) - 1\}, \tag{3.5}$$

where the pair-correlation function for the homogeneous electron gas g^h depends only on the electron-positron distance. Note that in the zero-density limit, the pair-correlation function does not depend on the local positron density. Since the resulting potential then only depends on the local electron density at $\mathbf{r}^p$, one can immediately parametrize the correlation energy as a function of the local electron density. In the WDA, the idea is to keep the pair correlation function of the homogeneous electron gas, but restore the proper electron density prefactor in the equation for the screening cloud. In order to retain some of the favourable properties of the LDA, one additionally imposes conditions on the screening cloud in the form of a sum rule, e.g. on the net induced screening charge.

3.2.1 Sum rule

An important reason why the LDA for electron-electron correlations works well for a large variety of systems is that it is in principle the *exact* functional for the homogeneous electron gas. It thus also satisfies all exact conditions that can be imposed on the functional in the homogeneous case. In order to construct reliable functionals that go beyond the LDA, it is important in this spirit to satisfy known exact constrains and limits as far as possible[1]. In this connection, Gunnarsson *et al.* realized that the sum rule on the electron-electron exchange-correlation hole, which states that the hole corresponds to the removal of one electron worth of charge, is a key reason for the success of the LDA [67].

Note, though, that the preceding sum rule arises because the interaction involves indistinguishable particles, so that the exchange-correlation energy should cancel the self-interaction of the Hartree term. Since electrons and positrons are different particles, there is no formal reason for the same sum rule to hold for the electron-positron correlation cloud. In fact, the Coulomb correlation can now only cause a redistribution of the electron charge, suggesting that the positron's correlation cloud should integrate to zero[2]. This observation is in conflict with the 'charge neutrality' condition, which is imposed in several works on the electron-positron WDA [25, 27, 30]. This sum rule states that the positron always has a screening cloud which is exactly opposite to its own charge.

Despite these remarks, some statements can be made about the short-range part of the correlation cloud. In a very dilute homogeneous electron gas, one expects the formation of Ps$^-$ [56], indicating that a charge equal to twice the electron charge is accumulated in the screening cloud. With this motivation, we assume that the screening cloud can be written as $\Delta\rho = \Delta\rho_{\text{sr}} + \Delta\rho_{\text{lr}}$, where the first term is to capture the short-range part and the second for the long range part of the screening cloud. From electron-positron pair-correlation data, we expect that the short range part can be described roughly by an exponentially decaying function, while the long range part resembles Friedel oscillations [56, 68, 69]. Fig. 3.1(a) shows in the full lines the recent quantum Monte Carlo data for a single positron immersed in a homogeneous electron gas of Ref. [56], and largely confirms our assumption. Indeed, the dashed and dotted lines in Fig. 3.1(a) show exponentially decaying functions (defined later in this chapter) that fit the data well for high densities and the short-range part at lower densities. Subtracting the exponential part shows the Friedel oscillations that develop at lower densities, as shown in Fig. 3.1(b). If we now make the assumption that the charge in the short range part is compensated by the long range part[3], i.e. $\int d\mathbf{r}^e\, \Delta\rho_{\text{sr}}(\mathbf{r}^e|\mathbf{r}^p;\lambda) = -\int d\mathbf{r}^e\, \Delta\rho_{\text{lr}}(\mathbf{r}^e|\mathbf{r}^e;\lambda)$, we can write

$$\int d\mathbf{r}^e\, \Delta\rho_{\text{sr}}(\mathbf{r}^e|\mathbf{r}^p;\lambda) = \mathcal{Q}(\mathbf{r}^p;\rho^e;\lambda). \tag{3.6}$$

It is important to recognize that, in general, the screening charge $\mathcal{Q}$ depends on the screening properties of a specific system and thus does not provide a sum rule that holds for all systems. Indeed, going back to the case of Ps$^-$ formation, we have $\lim_{\rho^e\to 0}\mathcal{Q}(\mathbf{r}^p;\rho^e;1) = 2$ for the homogeneous electron gas. On the other hand, for metallic systems, we generally expect $\mathcal{Q}(\mathbf{r}^p;\rho^e;1) \approx 1$, whereas for good insulators, it seems reasonable to assume $\mathcal{Q}(\mathbf{r}^p;\rho^e;1) \ll 1$.

---

[1] Some of the most widely applied electron-electron exchange-correlation functional are designed this way [65, 66].

[2] Formally, this statement is correct only for finite systems. In an infinite system, the integral over the correlation hole could strictly take a finite value [68].

[3] Note that inclusion of the volume element upon integration of the screening cloud significantly alters the data shown in Fig. 3.1(a). A plot of $(g(r)-1)r^2$ shows that it is plausible that the long range part compensates the short range part.

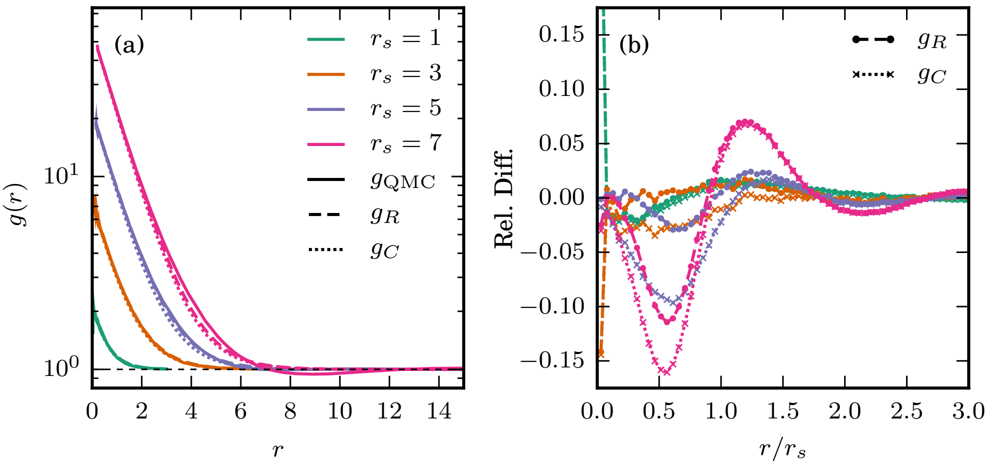

Figure 3.1: (a) Plot of electron-positron pair correlation data from the quantum Monte Carlo calculations (g_{QMC}) of Ref. [56] for several values of the electron density parameter r_s (full lines). Dashed and dotted lines show the pair correlation functions used in Rubaszek's WDA (g_R), Eq. (3.14), and the constrained pair correlation function (g_C) of Eq. (3.13). The enhancement factor used in these results is the one paramaterized by Drummond *et al.* [56], derived from the same quantum Monte Carlo data. (b) Relative difference of the pair correlation functions with the Monte Carlo data. Unlike panel (a), the results are plotted as function of the dimensionless parameter r/r_s to show relevant regions on the same plot. Note that excellent agreement is obtained at high densities (low r_s) but that the defined pair correlation functions do not capture the Friedel oscillations that develop at lower densities (high r_s). Remarkably, g_C, which satisfies the cusp condition, shows somewhat worse agreement with the Monte Carlo results than the more phenomenological g_R. Large deviations near the origin are due to numerical noise in the Monte Carlo results.

We would already like to emphasize that there is a large difference between the 'true' screening charge $\mathcal{Q}$, i.e. the one we would obtain from the true pair correlation function and ground state densities, and the screening charge Q, which is used in the sum rule of the WDA. We will show below, for example, that even though for insulators $\mathcal{Q}$ is expected to be small, a large Q has to be imposed in order to obtain reasonable results within the WDA. The reason for the counterintuitive behaviour will become apparent later in this chapter.

In order to construct a WDA functional for the electron-positron problem, Jensen and Walker [24] imposed the charge-neutrality condition, which states that the screening and positron charge should be exactly equal. Formulated differently, they assumed that the positron charge is always perfectly screened by the electrons. Their charge-neutrality condition takes the form

$$\int_0^1 d\lambda \int d\mathbf{r}^e \, \Delta\rho(\mathbf{r}^e|\mathbf{r}^p;\lambda) = 1. \tag{3.7}$$

Rubaszek [25, 27], on the other hand, interpreted the coupling constant λ as the scaled charge of the positron, and hence concluded that the charge neutrality condition should hold for any λ. This slightly different interpretation yields the sum rule

$$\int d\mathbf{r}^e \, \Delta\rho(\mathbf{r}^e|\mathbf{r}^p;\lambda) = \lambda, \quad \forall\, \lambda \in [0,1]. \tag{3.8}$$

From our discussion above, it is clear that these sum rules should not be interpreted as exact conditions on the electron-positron screening cloud but merely represent an *ad hoc* assumption on the screening properties of the system. In fact, *a priori* there is no guarantee that imposing either of these conditions will yield improved results.

3.2.2 Electron-positron pair correlation function

If the electron-positron pair correlation function were known exactly for a given system, we could obtain the exact KS potential for the positron through equation (3.4). As mentioned before, however, the exact pair correlation function is in general not known and an essential step in the WDA is the replacement of the true pair correlation function by the one for the homogeneous electron gas (in the zero-density limit)

$$g(\mathbf{r}^e,\mathbf{r}^p;[\rho^e,\rho^p];\lambda) \to g^h(r;\rho^e(\mathbf{r}^e);\lambda), \tag{3.9}$$

where $r = |\mathbf{r}^e - \mathbf{r}^p|$. Also, the pair correlation g^h is not known in closed form, and additional assumptions have to be made to obtain a useful expression. In the remainder of this section, we first discuss the known part of the pair correlation function, then introduce a reasonable general form based on the exact limit at low electron densities, and finally, we impose additional exact conditions which will be seen to almost completely determine g^h.

An important constraint we can place on the pair correlation function is that it should reproduce the enhancement factor γ of the LDA in the fully interacting case, i.e. $\gamma(\rho^e(\mathbf{r})) = g^h(0;\rho^e(\mathbf{r});1)$. The $g^h(0;\rho^e;1)$ dependence of the pair correlation function alone is not sufficient, though, to obtain a useful form of the pair correlation function. One can make progress by assuming that the short-range part of the screening cloud resembles the Ps atom. Since the Ps problem is equivalent to the Hydrogen problem with rescaled length and energy scales, we can take the functional form of the radial part of the 1s orbital

$$g^h(r;\rho^e(\mathbf{r}^e);\lambda) = 1 + \alpha(\rho^e(\mathbf{r}^e);\lambda)e^{-\beta(\rho^e(\mathbf{r}^e);\lambda)r}, \tag{3.10}$$

where several choices for α and β can be made. Interestingly, a number of parametrizations of the LDA correlation energy and the enhancement factor γ assume that $g(r;\rho^e;1) = 1 + e^{-r}/(8\pi\rho^e)$ is an exact limit for $\rho^e \to 0$ as it yield the Ps contact density [53, 58]. As mentioned earlier, and as shown in Fig. 3.1, recent quantum Monte Carlo data confirm that this is a reasonable assumption for the short range part of the screening cloud over a wide range of electron densities [56].

We now discuss additional constraints on the pair correlation function. Two obvious conditions are $\lim_{r\to\infty} g^h(r;\rho^e(\mathbf{r}^e);\lambda) = 1$ and $g^h(r;\rho^e(\mathbf{r}^e);0) = 1$. The first condition tells us that the electron density remains unperturbed far away from the positron and it is satisfied by the Ps form for any reasonable choice of α and β. The second condition simply states that electrons remain unperturbed by the presence of the positron, if there is no interaction between them, so that $\alpha(\rho^e(\mathbf{r}^e);0) = 0$. Next, we should recover the LDA enhancement term in the fully interacting case, which poses the condition $\alpha(\rho^e(\mathbf{r}^e);1) = \{\gamma(\rho^e(\mathbf{r}^e)) - 1\}$. A final condition comes from the Coulomb interaction between the particles, namely the Kimball cusp condition [68, 70]

$$\left(\frac{\partial g^h}{\partial r}\right)_{r=0} = -g^h(0), \tag{3.11}$$

from which one can easily derive that

$$\beta(\rho^e(\mathbf{r}^e);\lambda) = \frac{1 + \alpha(\rho^e(\mathbf{r}^e);\lambda)}{\alpha(\rho^e(\mathbf{r}^e);\lambda)}. \tag{3.12}$$

Note that, with the exception of the scaling of α with λ, the Ps form of the pair correlation function is thus completely determined by the enhancement term $\gamma(\rho^e(\mathbf{r}^e))$. If we assume linear scaling for α, the pair correlation function becomes

$$g^h(r;\rho^e(\mathbf{r}^e);\lambda) = 1 + \lambda\{\gamma(\rho^e(\mathbf{r}^e)) - 1\} \exp\left[-\frac{\gamma(\rho^e(\mathbf{r}^e))r}{\gamma(\rho^e(\mathbf{r}^e)) - 1}\right], \tag{3.13}$$

which is plotted in Fig. 3.1 in the dotted lines.

3.2.3 The weighted density approximation

We now present the WDA approximation developed by Rubaszek [25]. In this approach, the starting point is the sum rule (3.8), which is imposed to hold for all $\mathbf{r}^p$. The pair correlation function is assumed to take the form

$$g^h(r;\rho^e(\mathbf{r}^p);\lambda) = 1 + \lambda\left\{\gamma(\rho^e(\mathbf{r}^p)) - 1\right\} e^{-a(\rho^e(\mathbf{r}^p))r}, \tag{3.14}$$

where the decay length a is derived from the sum rule (3.8) for the homogeneous electron gas

$$a^3(\rho^e(\mathbf{r}^p)) = 8\pi\rho^e(\mathbf{r}^p)\left\{\gamma(\rho^e(\mathbf{r}^p)) - 1\right\}. \tag{3.15}$$

For inhomogeneous systems, the sum rule is, using the pair correlation function for the homogeneous electron gas, generally not satisfied. In order to restore it, one introduces an effective (weighted) electron density $\varrho^e(\mathbf{r}^p)$ at each point, i.e. one determines $\varrho^e(\mathbf{r}^p)$ such that

$$\{\gamma(\varrho^e(\mathbf{r}^p)) - 1\} \int d\mathbf{r}^e \rho^e(\mathbf{r}^e) e^{-a(\varrho^e(\mathbf{r}^p))|\mathbf{r}^e - \mathbf{r}^p|} = 1, \tag{3.16}$$

where the coupling constant dependence drops out due to the linear scaling of g^h with λ, and as a result the adiabatic integration in the expression for the correlation potential (3.4) can be performed analytically to obtain

$$v_c^p(\mathbf{r}^p) = -\frac{1}{2}\left\{\gamma(\varrho^e(\mathbf{r}^e)) - 1\right\}\int d\mathbf{r}^e\,\frac{\rho^e(\mathbf{r}^e)e^{-a(\varrho^e(\mathbf{r}^p))|\mathbf{r}^e-\mathbf{r}^p|}}{|\mathbf{r}^e-\mathbf{r}^p|}. \tag{3.17}$$

For the calculation of positron lifetimes, the local density ρ^e in the enhancement factor has to be replaced by the effective density ϱ^e,

$$\lambda_a = \frac{1}{\tau} = \pi r_e^2 c\int d\mathbf{r}\,\rho^e(\mathbf{r})\rho^p(\mathbf{r})\gamma(\varrho^e(\mathbf{r})). \tag{3.18}$$

We note that the pair correlation function in this approach does not satisfy the Kimball cusp condition (3.11), and as discussed earlier, there is no formal reason why the sum rule should hold. Fig. 3.1 shows, however, that for $\lambda = 1$ better overall agreement with the quantum Monte Carlo data is obtained with this form of the pair correlation function, than the constrained form of Eq. (3.13). We will return to investigate the effect of modifying the sum rule in a later section.

Aside from these remarks, the pair correlation function defined by Eqs. (3.14) and (3.15) has some favourable properties. The first is that the correlation potential for the homogeneous electron gas obtained within this approach

$$v_c^p = -\frac{3\left\{\gamma(\rho^e) - 1\right\}^{1/3}}{2\times 6^{2/3}\times r_s}, \tag{3.19}$$

results in the correct Ps limit $v_c^p = -1/4$ Ha for the dilute electron gas, if the enhancement factor has the correct coresponding limiting $\gamma \sim r_s^3/6$ behaviour. In the limit $r_s \to 0$, on the other hand, the potential goes as $\sim r_s^{-2/3}$ and does not reduce to the RPA limit $\sim r_s^{-1/2}$ [71]. A second advantage is that the adiabatic integration can be performed analytically, which reduces the required computational resources.

Fig. 3.2 shows a comparison between the LDA parametrizations of Refs. [53, 56] and the WDA potential for the homogeneous electron gas. Note that the WDA predicts a correlation potential which is generally more negative than the LDA. Only at very high densities ($r_s < 0.9$), the Drummond LDA is more negative than the WDA. The agreement between the LDA and WDA is reasonable for the Boronski-Nieminen parametrization [53], whereas the WDA is substantially more negative for the Drummond parametrization [56]. It is important to point out that in the study of bulk positron annihilation lifetimes of the present chapter, only the relative values of the positron correlation potential in different parts of the unit cell can influence the results, i.e. our results do not depend on the absolute value of the potential.

3.3 Bulk tests

Here we consider a set of elemental bulk materials for which experimental positron-annihilation lifetimes are available [62]. Details of the electronic structure calculations and the implementation details of the WDA are presented in the Appendices of this chapter. Table 3.1 gives the experimental and LDA lifetimes, obtained with the Brandt-Reinheimer expression [25, 72, 73], the Boronski-Nieminen parametrization [53] and the Drummond parametrization [56] of the LDA. In principle, the Drummond parametrization is the most

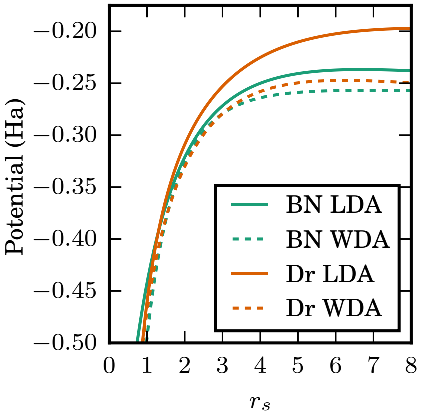

Figure 3.2: Comparison of the LDA potentials as parametrized by Boronski and Nieminen [53] (BN), and Drummond *et al.* [56] (Dr) with the corresponding WDA potentials of Eq. (3.19) for the homogeneous electron gas. For the enhancement factors, we took the parametrizations from the same references.

accurate one currently available but the Boronski-Nieminen parametrization is still in wide use. The Brandt-Reinheimer expression is not a very accurate parametrization of the enhancement term, including the fact that it does not satisfy the RPA limit, but we consider it nonetheless because it was used in early WDA work [24, 25, 74]. The potential for the Brandt-Reinheimer expression is not given explicitly in literature, but can be derived by solving the WDA potential equation (3.17) for the homogeneous electron gas. The result is given by $v_c^p(r_s) = -0.25(1 + 10/r_s^3)^{1/3}$.

3.3.1 Rubaszek WDA

We now apply the WDA of Rubaszek as explained in Sec. 3.2.3 for different parametrizations of the enhancement factor to a set of elemental bulk materials. Figure 3.3(a) shows the results of our calculations. Our WDA based on the Boronski-Nieminen and Drummond enhancements is seen to result in a systematic overestimation of the lifetime. The Brandt-Reinheimer expression for the enhancement term gives somewhat better results, although it does not satisfy the RPA limit, and that the Boronski-Nieminen and Drummond parametrizations are more accurate. We expect the Brandt-Reinheimer-based WDA to benefit from a fortunate cancellation of errors.

Insight into the failure of the present WDA approach is obtained by considering the expression of the annihilation rate, Eq. (3.18), which shows that the decrease of the annihilation rate (increase of the lifetime) with respect to the LDA could result from two different factors: (1) a decrease of the electron-positron overlap, or (2) a decrease of the enhancement factor. The first factor is driven by the change in the correlation potential between the LDA and WDA. This effect can be quantified by comparing the lifetimes obtained within the IPM (setting $\gamma(\mathbf{r}) = 1$) from the LDA and WDA positron densities. More specifically, we examine the relative increase of the electron-positron overlap for the WDA, i.e. $(\lambda_{\mathrm{IPM}}^{\mathrm{WDA}} - \lambda_{\mathrm{IPM}}^{\mathrm{LDA}})/\lambda_{\mathrm{IPM}}^{\mathrm{LDA}}$. The results are displayed in Fig. 3.3(b). The WDA is seen to systematically predict a larger electron-positron overlap compared to the LDA. This implies that, relative to the LDA, the WDA correlation potential is more attractive

System	Structure	BR	BN	Dr	Expt.
Li	bcc	296	300	304	291
C	diamond	81	93	95	98
Na	bcc	316	328	343	338
Al	fcc	158	165	161	160
Si	diamond	204	211	208	216
Fe	bcc	86	100	101	105
Cu	fcc	88	105	106	110
Nb	bcc	112	121	121	120
W	bcc	89	100	100	105
Pt	fcc	84	96	97	99

Table 3.1: Overview of the elemental materials considered. The third to fifth columns give positron-annihilation lifetimes (in ps) using an LDA derived from the Brandt-Reinheimer (BR) expression, the Boronski-Niemenen (BN) LDA and the Drummond (Dr) LDA. The last column gives experimental lifetimes taken from Ref. [62] and references therein.

near the cores compared to the interstitial region. Since an increase of the overlap will lead to an increased annihilation rate, our lifetime results can only be explained through a decrease of the enhancement factor.

In this connection, it is interesting to examine the behaviour of the effective density ϱ^e in the vicinity of a local minimum and maximum[4]. For the minimum case, consider the model density

$$\rho^e(\mathbf{r}^e) = \frac{1}{2}(1 + \sin^2(r)), \tag{3.20}$$

where $r = |\mathbf{r}^e|$, and we take $\mathbf{r}^p = 0$. In the LDA, the screening charge is given by

$$\Delta\rho(r) = \rho^e(0)\{\gamma(\rho^e(0)) - 1\}e^{-a(\rho^e(0))r}, \tag{3.21}$$

which, by the choice of a (Eq. (3.15)), satisfies the sum rule. The dependence is plotted (green line) in Fig. 3.4(b). In the WDA, we take into account the inhomogeneity of the electron density around $\mathbf{r}^p$

$$\Delta\rho(r) = \rho^e(r)\{\gamma(\varrho^e) - 1\}e^{-a(\varrho^e)r}, \tag{3.22}$$

where ϱ^e has to be determined such that $\Delta\rho(r)$ integrates to one. If one takes $\varrho^e = \rho^e(0)$ around a local minimum, the screening charge will be overestimated, see the orange curves in Figs. 3.4(b) and (c). For this simple model, one can easily solve (3.16) to find $\varrho^e \approx 1.59\,\rho^e(0)$, where we used the enhancement factor parametrized by Boronski and Nieminen [53], see the blue curves in Figs. 3.4(b)-(c). The final result is that the local contribution to the annihilation rate decreases due to a decrease in the enhancement term $g(0, \varrho^e) \approx 0.94\, g(0, \rho^e(0))$. Around a local maximum, the opposite conclusion holds. Indeed, consider

$$\rho^e(\mathbf{r}^e) = \frac{1}{2}(1 + \cos^2(r)), \tag{3.23}$$

for which the effective density is found to be $\varrho^e \approx 0.70\,\rho^e(0)$, which yields a relative increase of the enhancement term $g(0, \varrho^e) \approx 1.05\, g(0, \rho^e(0))$. The corresponding curves are given in Figs. 3.4(d)-(f).

---

[4] Here, we assume that the electron density varies smoothly on the length scale of the decay length $1/a$.

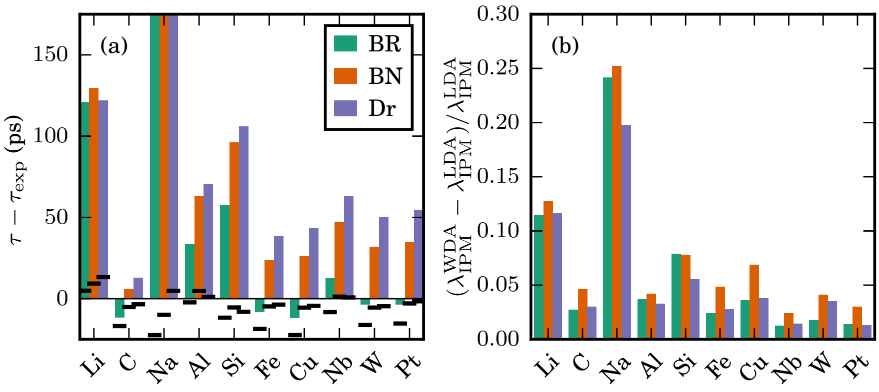

Figure 3.3: Results of (a) positron annihilation lifetime calculations and (b) the relative change in the electron positron overlap w.r.t. the LDA for various elemental materials using Rubaszek's [25] approach. Horizontal black lines denote the LDA lifetimes for each system. Different colors are used to distinguish the results for various choices of the enhancement factor γ: BR (Brandt-Reinheimer); BN (Boronski-Nieminen); and, Dr (Drummond).

These results explain why the average enhancement factor decreases. The reason is that even though there is a shift of the positron density towards the core regions in the WDA, the positron is still mostly localized in the interstitial region due to the large Coulomb repulsion from the ions. In the interstitial region, the effective density will generally decrease due to the large contributions of the cores to the screening charge, leading to a decrease in the enhancement factor and, hence, the annihilation rate.

We note that, physically, the charge of the positron will mostly be screened by the valence electrons, so that core electrons should not contribute significantly to the screening charge. If we can reduce the contribution of the cores to the screening charge, we expect an increase in the annihilation rate. In the next sections, we will explore two such approaches, which are motivated by these observations.

3.3.2 Gradient correction

One obvious way to reduce the screening effect of core electrons is to introduce a correction based on the gradient of the electron density. Since the density varies rapidly near the ions but more smoothly in the interstitial region, the density gradient provides a convenient quantity to selectively reduce the core contribution to the screening cloud. In fact, the GGA correction to the LDA positron correlation potential is derived from a gradient correction to the induced contact charge density [59]

$$\Delta\rho^{\mathrm{GGA}}(\mathbf{r}^p|\mathbf{r}^p) = \Delta\rho^{\mathrm{LDA}}(\mathbf{r}^p|\mathbf{r}^p)e^{-\alpha\epsilon(\mathbf{r}^p)}, \tag{3.24}$$

with $\epsilon = |\nabla\rho^e|^2/q_{\mathrm{TF}}^2$, where $1/q_{\mathrm{TF}}$ is the Thomas-Fermi screening length, and $q_{\mathrm{TF}}^2 = 4(3\rho^e/\pi)^{1/3}$. The parameter α can be chosen phenomenologically [59, 75], though recently a connection with the LDA potential was found [62].

In the non-local case we want to apply this gradient correction to the electron density surrounding the positron position. Indeed, if we would use the gradient of the electron

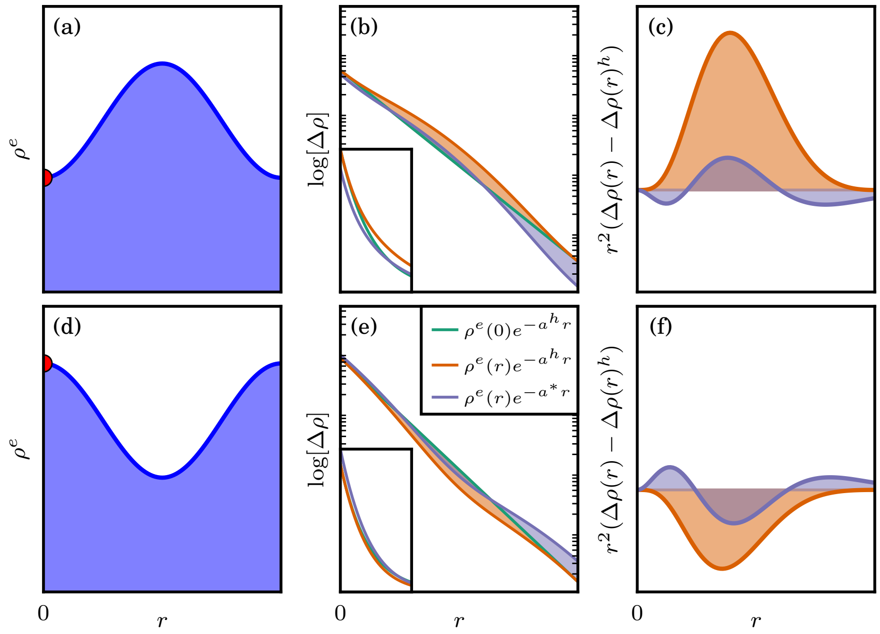

Figure 3.4: Results of a simple model to illustrate the behaviour of WDA screening in the vicinity of a local minimum (top row of panels) and maximum (bottom row of panels) of the electron density. The position of the positron, $\mathbf{r}^p$, is taken at $r = 0$ (red dots in leftmost figures). The second column plots the radial dependence of the screening cloud for the LDA (green), the WDA using the local electron density (orange), and the WDA using an effective density that satisfies the sum rule (blue). The insets show the same quantities on a linear scale. Figures in the last column show the spherically integrated differences between the WDA and LDA screening clouds; in order to satisfy the sum rule, this quantity should integrate to zero.

density at the positron's position, the screening of the core electrons would, e.g., not be reduced in the interstitial region. We thus suggest the modified pair correlation function

$$g(\mathbf{r}^e, \mathbf{r}^p; \rho^e(\mathbf{r}^p); \lambda) = 1 + \lambda \left\{\gamma(\rho^e(\mathbf{r}^p)) - 1\right\} e^{-a(\rho^e(\mathbf{r}^p))r} e^{-\alpha\epsilon(\mathbf{r}^e)}. \tag{3.25}$$

The screening cloud then becomes

$$\Delta\rho(\mathbf{r}^e|\mathbf{r}^p) = \rho^e(\mathbf{r}^e) e^{-\alpha\epsilon(\mathbf{r}^e)} \lambda \left\{\gamma(\rho^e(\mathbf{r}^p)) - 1\right\} e^{-a(\rho^e(\mathbf{r}^p))r}, \tag{3.26}$$

from which we can see that we replace the electron density with a modified version that takes into account its local ability to screen external charges $\rho^e(\mathbf{r}^e) \rightarrow \rho^e(\mathbf{r}^e)e^{-\alpha\epsilon(\mathbf{r}^e)}$. The enhancement factor is obtained as usual by setting $\mathbf{r}^e = \mathbf{r}^p$ in the pair correlation function, such that the lifetime formula becomes

$$\lambda_a = \frac{1}{\tau} = \int d\mathbf{r}\, \rho^e(\mathbf{r})\rho^p(\mathbf{r}) \left[1 + \left\{\gamma(\varrho^e(\mathbf{r})) - 1\right\} e^{-\alpha\epsilon(\mathbf{r})}\right], \tag{3.27}$$

which, with exception of the effective density ϱ^e in the enhancement term, has the same form as the GGA correction to the lifetime formula [59].

An important difference between the gradient correction proposed here and the GGA correction to the LDA should be emphasized. In the LDA, the potential is too attractive and the enhancement factor is overestimated in the core region due to an overestimation of the *local* screening of the core electrons. As a result, positron lifetimes are generally slightly underestimated. By introducing a local gradient correction [59] both these effects are corrected, leading to an *increase* in the lifetime because the gradient corrections dominate in the core regions. In our proposed gradient correction to the WDA, we attempt to correct for the overestimation of the *non-local* screening of the core densities, i.e. the contribution of the core charges to the screening cloud of the positron at a (possibly) different position. Since the density participating in the screening is decreased with respect to the true electron density, the screening length must be increased with respect to the unmodified WDA in order to accumulate the same total amount of screening charge. An increase of the screening length is obtained via a decrease of the effective density and, as a consequence, the enhancement term is increased everywhere. A second consequence of the increase of the screening length is that the accumulated screening cloud is on average located further away from the positron, which lowers the Coulomb interaction. This, and because the correction will dominate in the core regions, leads us to expect a shift of the positron density away from the ions. If the gradient correction to the annihilation rate is neglected, these effects will always lead to a *decrease* of the lifetime. In reality, however, the results depend on the balance between the decreased effective density and the gradient correction to the enhancement term.

The results for this approach with the Drummond enhancement are shown in Fig. 3.5 as a function of the parameter α, which controls the strength of the gradient correction. We start our evaluation of the gradient correction by discussing the change in the electron-positron overlap, shown in Fig. 3.5(b), which results from the change in the correlation potential. In most cases, we see a slight, nearly linear decrease in the overlap with increasing α. For diamond and Si, the change in the overlap quickly saturates and the gradient correction has a relatively small effect. On the other hand, this correction is much more pronounced for the alkali metals Li and Na. Note that the gradient correction decreases the electron density participating in the screening cloud mainly in the core regions. As a result, it yields a correlation potential that is less attractive in the core regions relative to the interstitial region when compared to the uncorrected WDA, hence explaining the observed decrease in the overlap.

Next, we discuss the decrease in annihilation rate caused by the gradient correction to the enhancement factor. For this purpose, we replace the effective electron density ϱ^e in the enhancement factor γ in Eq. (3.27) by the true electron density ρ^e. The results are shown in Fig. 3.5(c). Note that the gradient correction has the largest effect on the lifetime in those regions where the positron density is large. This explains why the gradient correction has a more pronounced effect in systems such as Si and diamond, where there are larger inhomogeneities in the valence electron density due to covalent bonding, than in metals like Al and W.

The final lifetime results are shown in Fig. 3.5(a). The gradient correction to the WDA is seen to decrease the lifetime with increasing α for all metals considered. This implies that the effect of the decrease of the effective density ϱ^e in the interstitial regions dominates over that of the decrease in the electron-positron overlap and the gradient correction to the enhancement factor. On the other hand, for diamond, the opposite scenario holds, leading to a slight increase of the lifetime. The results show, though, that we cannot expect accurate lifetimes from the gradient correction to the WDA proposed in this section. Despite a slight improvement for the metallic systems, we do not obtain

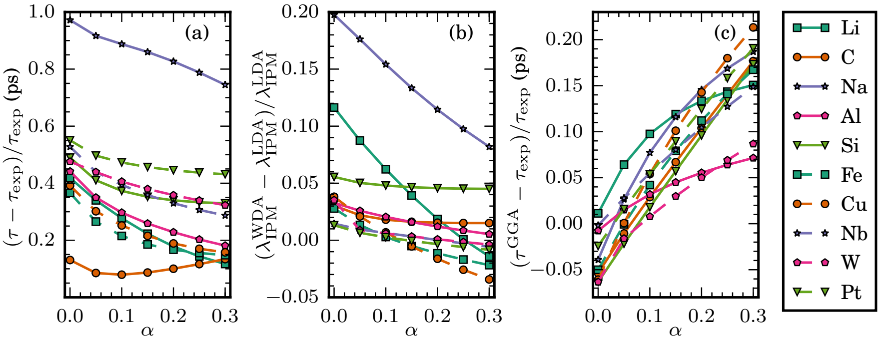

Figure 3.5: Scaling of (a) the relative error of the lifetime and (b) the relative change in the electron-positron overlap w.r.t. the LDA with the gradient correction parameter α applied to the WDA. (c) Lifetimes obtained via Eq. (3.27) where the local density is inserted in the enhancement factor instead of the effective density (unlike the results in panel (a)). Only results obtained with the Drummond enhancement term are shown. Markers indicate calculated results and lines serve as guides to the eye.

acceptable lifetimes with reasonable values of the parameter α, which for the Boronski-Nieminen LDA is set to $\alpha = 0.22$ [59] and for the Drummond LDA to $\alpha = 0.05$ [75]. It is clear that another approach is needed for reducing the screening of the core electrons.

3.3.3 Shell-partitioning

The idea of shell-partitioning is as old as the WDA itself and in connection with electron-electron exchange, it provides a scheme to correct the (erroneous) large exchange interaction involved in the WDA between spatially well separated electron shells [67]. Rubaszek *et al.* [27, 28] proposed such a scheme for electron-positron correlation in which the electron density is separated into core and valence parts. The latter is again split into its s-, p-, d- and f-components in a sphere around each ion, and the part in the remainder of the unit cell. The idea is that each of these electrons will in general contribute differently to the screening cloud around the positron [30, 60, 76–80]. One can then introduce a specific enhancement factor γ_t for each type of electron density ρ^e_t. For instance, for the core electrons we expect $\gamma_c \approx 1$ whereas for the valence electrons in the interstitial region the LDA enhancement factor is likely a reasonable approximation. Next, for each contribution, a sum rule is imposed, which in the work of Rubasek *et al.* is assumed to take the form

$$\begin{aligned}\int d\mathbf{r}^e\, \rho^e_t(\mathbf{r}^e) \left\{g^h_t(|\mathbf{r}^e - \mathbf{r}^p|, \tilde{\varrho}_t(\mathbf{r}^p), \lambda) - 1\right\} \\ = \lambda \frac{\left\{g^h_t(0, \rho^e(\mathbf{r}^p), \lambda) - 1\right\} \rho^e_t(\mathbf{r}^p)}{\sum_{t'} \left\{g^h_{t'}(0, \rho^e(\mathbf{r}^p), \lambda) - 1\right\} \rho^e_{t'}(\mathbf{r}^p)},\end{aligned} \tag{3.28}$$

where

$$\tilde{\varrho}_t(\mathbf{r}^e) = \rho^e(\mathbf{r}^e) + (\varrho^e_t(\mathbf{r}^e) - \rho^e_t(\mathbf{r}^e)), \tag{3.29}$$

is the effective density for a given type of electron t. The preceding sum rule states that various electrons contribute to the screening charge depending on the ratios of their local densities to the total electron density. Though, note that each electron type is weighted by its local enhancement term $g_t^h - 1$, and not the bare density. As a result, valence electrons, for example, can contribute a larger fraction to the screening cloud than d-electrons, even though their local density can be smaller. As required, this form reproduces the LDA in the homogeneous electron gas [27].

Although excellent results for positron lifetimes have been obtained within this shell-partitioning approach, a first point of critique is that no clear motivation for the above form of the sum rule is given in Ref. [27]. For instance, it is not obvious why a separate sum rule should be imposed for each partition of the electron density. Instead, we could impose a single sum rule and simply use a different pair correlation function for the individual densities as follows

$$\int d\mathbf{r}^e \sum_t \left[\rho_t^e(\mathbf{r}^e)\{g_t^h(|\mathbf{r}^e - \mathbf{r}^p|, \varrho^e(\mathbf{r}^p), \lambda) - 1\}\right] = \lambda. \tag{3.30}$$

This seems a more natural extension of the WDA, since it simply states that not all electrons contribute equally to the screening charge and substitutes a suitable pair correlation function to describe the effect. It avoids placing the additional restrictions that each electron type should contribute a fixed amount of charge depending on a strictly local quantity. Furthermore, the simplified version suggested above avoids solving multiple sum rules, and hence makes it more computationally tractable. On the other hand, imposing fixed fractions for the screening of each electron type depending on the local (enhanced) density certainly avoids overestimating the core electron screening in the interstitial region. Hence, it is guaranteed to solve the issue we are dealing with.

A second point of critique is that a number of technical issues arise. One is that there is no unique way to split the electron density into an interstitial part and its angular momentum components around each ion. It is also not clear what form for the enhancement factor should be used for each l channel. Rubaszek *et al.* [27] used a Kahana-type enhancement factor $\epsilon(E_l/E_F, \rho^e(\mathbf{r}^p))$, where E_l are the l-dependent linearization energies used in the linear muffin tin orbital method and E_F is the Fermi energy. Even though the results obtained are excellent, this choice is arbitrary and depends on method-specific computational parameters, which do not carry over easily to our present approach, where the electron density is presented on a grid and no linearization energies are used.

In order to address these difficulties, we investigate a simpler shell partitioning scheme in this study in which we distinguish only between the valence and core electrons. The latter are treated within the LDA and the former within the WDA. We expect that the essence of the problems in the previous sections will be solved by removing the core electrons from the non-local screening. The introduction of l-dependent enhancement factors can be expected to provide a further improvement of the results, but are likely only of secondary importance.

We now turn to present the details of our shell-partitioning approach, which is based on Refs. [81, 82]. We start by writing the (total) effective electron density as

$$\tilde{\varrho}^e(\mathbf{r}) = \varrho_v^e(\mathbf{r}) + \rho_c^e(\mathbf{r}), \tag{3.31}$$

where ρ_c^e is the core electron density and ϱ_v^e is an effective valence electron density, which is determined by solving the modified sum rule

$$\int d\mathbf{r}^e\, \Delta\rho(\mathbf{r}^e|\mathbf{r}^p) = \{\gamma(\tilde{\varrho}^e(\mathbf{r}^p)) - 1\} \int d\mathbf{r}^e\, \rho_v^e(\mathbf{r}^e) e^{-a(\tilde{\varrho}^e(\mathbf{r}^p))|\mathbf{r}^e - \mathbf{r}^p|} = \frac{\rho_v^e(\mathbf{r}^p)}{\rho^e(\mathbf{r}^p)}. \tag{3.32}$$

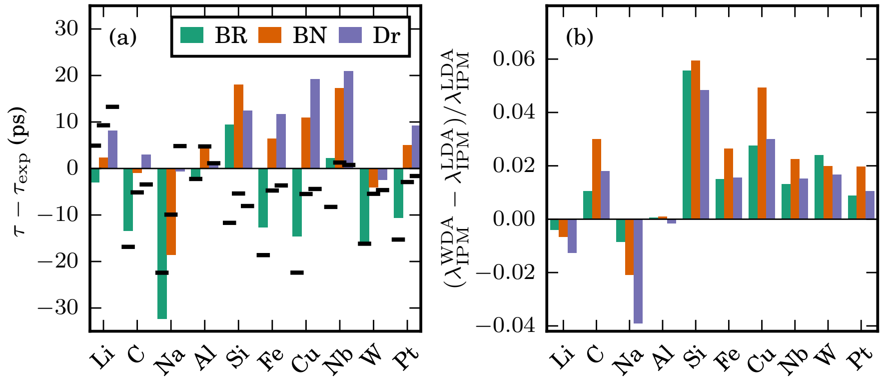

Figure 3.6: Results of (a) positron annihilation lifetime calculations and (b) the relative change in the electron positron overlap w.r.t. the LDA for various elemental materials using the WDA with shell partitioning. Horizontal black lines denote the LDA lifetimes for each system. Different colors are used to distinguish the results for various choices of the enhancement factor γ: BR (Brandt-Reinheimer); BN (Boronski-Nieminen); and, Dr (Drummond).

The correlation potential is given by

$$v_c^p(\mathbf{r}^p) = \frac{\rho_c^e(\mathbf{r}^p)}{\rho^e(\mathbf{r}^p)}\epsilon_c(\rho^e(\mathbf{r}^e)) + \frac{1}{2}\int d\mathbf{r}^e \frac{\Delta\rho(\mathbf{r}^e|\mathbf{r}^p)}{|\mathbf{r}^e - \mathbf{r}^p|}, \tag{3.33}$$

where ϵ_c is the LDA correlation potential. Lifetimes are obtain from

$$\lambda_a = \frac{1}{\tau} = \pi r_e^2 c \int d\mathbf{r}\, \rho^e(\mathbf{r})\rho^p(\mathbf{r})\gamma(\tilde{\varrho}^e(\mathbf{r})). \tag{3.34}$$

The electrons taken as valence electrons are listed in table 3.3.

This approach, even though somewhat arbitrary as it depends on the chosen partitioning between core and valence electrons, leads to substantially improved lifetime results, see Fig. 3.6. In particular, Li and Na now give better lifetimes than the LDA, whereas WDA results without shell-partitioning were poor. We attribute this striking improvement to the fact that valence electrons of alkali metals are quite free electron-like. These electrons are very efficient in screening the positron charge, so that the core electrons contribute little to screening. For the five materials in our test set that do not have d-electron valence orbitals and W, we obtain results comparable to the LDA using the Drummond parametrization of the LDA potentials and enhancement factors. The results for transition metals (expect W) are notably poorer due to an overestimation of the effect of d-electrons in the screening process. Overall, our analysis indicates that the WDA with shell-partitioning yields reasonable results. An l-dependent shell-partitioning should provide further improvement.

Our tests of shell partitioning indicate that the LDA is generally more reliable than the WDA, although the WDA appears to work well when all valence electrons are sufficiently free-electron-like. This is a consequence of the local nature of the LDA, which prevents localized non free electron like core electrons from strongly influencing the overall potential and enhancement factor.

3.3.4 Effect of the sum rule

In section 3.2.1, we pointed out that in the treatment of electron-electron correlation, the sum rule expresses that electrons should not experience self-interaction. We also commented that such a self-interaction is not involved in treating electron-positron correlation effects, and we argued that there is no real reason why the short ranged part of the screening cloud should have a value of one.

To illustrate this, let us take the gradient correction of Eq. (3.25), but instead apply it at the positron position, we obtain

$$\Delta\rho'(\mathbf{r}^e|\mathbf{r}^p) = \{\gamma(\varrho^e(\mathbf{r}^p)) - 1\}\,\rho^e(\mathbf{r}^e)e^{-\alpha\epsilon(\mathbf{r}^p)}e^{-a(\varrho^e(\mathbf{r}^p))|\mathbf{r}^e-\mathbf{r}^p|}. \tag{3.35}$$

Since the term gradient correction term does not depend on the positron position, we can rewrite the sum rule equation based on the above screening cloud in terms of the original screening cloud but with a modified screening charge

$$\int d\mathbf{r}^e \Delta\rho(\mathbf{r}^e|\mathbf{r}^p) = e^{\alpha\epsilon(\mathbf{r}^e)}. \tag{3.36}$$

Thus, such a gradient correction would correspond with imposing a position dependent sum rule. It also shows that the screening charge determines an average screening length of the system. Next, note that, even though the gradient correction decreases the screening, it is equivalent with imposing an *increased* screening charge. This may seem counter intuitive, but on setting aside physical intuition and thinking about the mechanics of the WDA reveals the underlying reason: The gradient term uniformly decreases the charge contained in the screening cloud, hence in order to satisfy the sum rule $Q = 1$ the screening length has to be increased (through tuning of the effective density) to accumulate sufficient charge. Taking a different point of view, we can impose a larger screening charge instead of reducing uniformly the charge of the screening cloud. This exactly what we did in Eq. (3.36).

In the remainder of this section we discuss, within the framework of the shell-partitioning scheme of the preceding section, effects of the imposed screening charge on the positron lifetime, i.e. we now determine the effective electron density by solving the modified sum rule

$$\int d\mathbf{r}^e\, \Delta\rho(\mathbf{r}^e|\mathbf{r}^p) = \{\gamma(\tilde{\varrho}^e(\mathbf{r}^p)) - 1\} \int d\mathbf{r}^e\, \rho^e_v(\mathbf{r}^e)e^{-a(\tilde{\varrho}^e(\mathbf{r}^p))|\mathbf{r}^e-\mathbf{r}^p|} = Q\frac{\rho^e_v(\mathbf{r}^p)}{\rho^e(\mathbf{r}^p)}. \tag{3.37}$$

In particular, we determine which value of the screening charge Q reproduces the experimental lifetime. In order to accumulate more charge in the screening cloud, the effective density $\tilde{\varrho}^e$ must decrease, and thus we expect the lifetime to decrease monotonically with increasing Q. The scaling of the lifetime w.r.t. the imposed value of the sum rule is displayed in Fig. 3.7 and the related values which reproduce experimental lifetimes are given in table 3.2.

Table 3.2 reveals interesting trends. The experimental lifetimes in free-electron-like materials (Li, Na and Al) are all reproduced with $Q \approx 1$. The d-electron materials with exception of W, on the other hand, require significantly larger values of Q, especially Cu and Nb. We attribute this to the presence of the 3d-shell in Cu and the 4p-shell in Nb, both of which are physically expected to contribute little to the screening of the positron. For Si and diamond, which have strong covalent bonds, we also find an optimal value of Q slightly larger than one. This again is in line with the expectation that screening in these materials is less effective than in metals, a point to which we return in the next

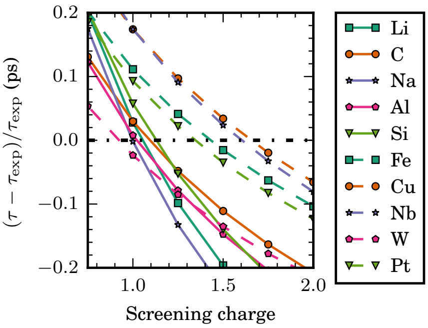

Figure 3.7: Scaling of the calculated positron annihilation lifetimes with an imposed screening charge in the sum rule. The results have been obtained with shell-partitioning and the Drummond enhancement factor.

paragraph. The sensitivity of the lifetime w.r.t. changes in Q, see Fig. 3.7, is related to the density ρ^e which enters in the sum rule, where lower densities yield greater sensitivity to the choice of Q.

Values of $Q > 1$ discussed above seem counterintuitive and deserve further explanation. Physically, we expect the true screening cloud to have $\mathcal{Q} < 1$ in a good insulator. Even so, we need to impose $Q > 1$ in the WDA because, like the core electrons, the electron density in the sum rule involves electrons which do not participate efficiently in the screening process, at least not as efficiently as free electrons, which is implicit through the use of the pair correlation function of the homogeneous electron gas. In order to understand how this plays out technically, assume that the positron is located at a point where the local electron density screens the positron like free electrons, even though there may be some electrons in the neighborhood that are very ineffective in screening, such as the those forming strong covalent bonds. The enhancement effect in this case is described correctly by the LDA evaluated at the local electron density. In the WDA, however, the effective density will generally be higher than the local electron density since the regions where electrons do not participate significantly in screening are often characterized by large local electron densities. Thus, the (approximately) free electrons in the material are located close to local minima, and the conclusions from our simple model of section 3.3.1 hold. These considerations also lead to an underestimation of the local enhancement factor. There are two ways to address this problem. The first approach is to replace the true electron density in the sum rule with a modified value (generally reduced) that takes into account its screening capacity. We investigated this approach within the gradient correction and shell-partitioning schemes in the previous sections. The second approach is to allow the screening cloud to accumulate more than one electron to approximately account for the fact that too many electrons are contained in the electron density that enters in the sum rule equation.

With all this in mind, it is natural to wonder if the results could be improved by applying the gradient correction of section 3.3.2 in combination with the shell partioning. We have investigated this possibility but did not find any improvement. The reason is that the decrease in the effective density turns out to be too small to compensate for the gradient correction to the enhancement term in the lifetime formula, Eq. (3.27).

The screening charge Q can, in principle, be used as a phenomenological parameter in

Li	C	Na	Al	Si	Fe	Cu	Nb	W	Pt
1.06	1.10	1.00	1.02	1.13	1.43	1.66	1.60	0.92	1.35

Table 3.2: Screening charge values that reproduce experimental lifetimes using the WDA scheme with the Drummond enhancement term and shell-partitioning.

WDA calculations[5]. In this vein, we could fit the Q value to reproduce the experimental lifetime in a specific material. This value of Q can then be employed to investigate PAS properties at defects and surfaces/interfaces more generally. This approach will be in the spirit of the hybrid functionals in electronic structure calculations, where a part of the exact exchange is used to correct the bandgap. It is not guaranteed that this approach will give a reliable description of the positron properties. Tests will have to point out whether it is a useful scheme. In the Chapter 4, we investigate whether the approach yields accurate positron surface binding energies.

3.4 Summary

In this chapter, we have carried out an in-depth study of the WDA approach for describing electron-positron correlations as a basis for constructing a functional, which is suitable for modeling PAS properties of strongly inhomogeneous systems such as surfaces. We critically examined the general theory behind the WDA and the approximations and assumptions underlying earlier related work in the literature [24, 25, 27].

Positron annihilation lifetimes obtained from the WDA of Ref. [25] were shown to yield poor results due to the (unphysical) involvement of core electrons in the screening of the positron charge. This leads us to consider a gradient correction for removing the large core-electron contribution to the screening cloud, but this approach fails to obtain accurate lifetimes. A shell-partitioning scheme, on the other hand, was shown to yield excellent results for positron lifetimes in free-electron-like materials. The results are somewhat worse for insulators and most d-electron systems, though, where not all valence electrons participate in the screening of the positron as free electrons. We have attempted to account for this by combining the gradient correction with the shell partitioning but, unfortunately, found no further improvement of the results. It is expected that more sophisticated versions of the shell partitioning, such as the one from Ref. [27] can further improve the results. Finally, we considered a semi-empirical scheme in which the screening charge is described in terms of a single material-specific parameter, which is fitted to reproduce experimental lifetimes; the scheme will then allow effective treatment of positron properties in strongly inhomogeneous regions such as surfaces and large voids. Tests will have to point out, though, if a realistic description of positron properties in strongly inhomogeneous environments can be obtained in this way.

Notably, we do not expect the WDA and its modifications discussed in this chapter to provide more accurate functionals (compared to the standard LDA or GGA schemes) for treating relatively homogenous bulk systems and small defects. Instead, their usefulness lies in the treatment of strongly inhomogeneous systems where the semi-local approximations are known to fail.

Recent work has shown that incorporation of exact constraints on electron-electron correlation functionals can yield improved results in a wide variety of diversely bonded systems [66, 83, 84]. It will be interesting to explore the extent to which improvements in

---

[5] As we have already pointed out, Q defines a material-dependent screening length.

Li	C	Na	Al	Si
$2s$	$2s^2\,2p^2$	$3s$	$3s^2\,3p$	$3s^2\,3p^2$

Fe	Cu	Nb	W	Pt
$3d^6\,4s^2$	$3d^{10}\,4s$	$4p^6\,4d^4\,5s$	$5d^4\,6s^2$	$5d^9\,6s$

Table 3.3: Electrons treated as valence electrons in the ground state calculations and in the shell-partitioning of Sec. 3.3.3.

WDA-based electron-positron correlation functionals could be obtained along similar lines. A specific example will be the imposition of the Kimball cusp condition [68, 70] on the WDA-based electron-positron functional. A different approach to achieve better results would be to move away from results for the homogeneous gas, and instead calculate a pair correlation function directly from the electronic structure of the material.

3.A Details of the electronic structure calculations

The electronic densities used in this chapter were obtained with the Projector Augmented Wave (PAW) method [85] as implemented in The Vienna Ab-initio Simulation Package (VASP) [86–88]. The plane wave cutoff and k-mesh in the calculation were checked until the positron lifetimes were converged to within 1 ps. Due to the sensitivity of the positron lifetimes to the lattice constant of the material, we used experimental lattice parameters [89] for all systems. In Sec. 3.3.3, we distinguish between the core and valence electrons in each system for which we take the same partitioning as in the electronic groundstate calculation. The electrons taken as valence electrons are summarized in table 3.3.

We compared the lifetimes obtained with the ground state LDA [90, 91] and Perdew-Burke-Ernzerhof (PBE) [65] electron densities (using experimental lattice parameters) but in none of the considered cases, we found a difference in the lifetime larger than 1 ps. Therefore, the uncertainty in positron lifetimes due to electronic and structural properties depends mainly on the accuracy with which the electron correlation functional used can predict lattice constants. Accordingly, only the results obtained with the LDA are reported.

3.B Details of the positron calculations

3.B.1 Positron groundstate calculations

Positron groundstate and lifetime calculations were performed with the MIKA/doppler package [92]. Calculations are performed in an all-electron way in the sense that the Hartree and correlation potentials are calculated using the total electron density. The total electron density is constructed by taking the sum of the self-consistent groundstate electron density from VASP, and a superposition of free atomic core densities. All densities and potentials in the positron calculations are represented on real-space three-dimensional grids unless mentioned otherwise. The spacing of the grid is determined by the plane-wave cutoff in the electronic structure calculations. The positron groundstate is sought using a conjugate gradient algorithm.

This rest of this appendix provides some details about the WDA implementation used in this work. The primary goal in the WDA to determine the effective electron density $\varrho^e(\mathbf{r})$, by solving the sum rule, and subsequently the correlation potential $v_c(\mathbf{r})$ on a regular 3-dimensional real space grid.

3.B.2 Solving the sum rule

The value of the effective density $\varrho^e(\mathbf{r}^p)$ is determined at all grid points by searching for the roots of the sum rule equation. To search for the roots of this equation, we first bracket the root, i.e. determine two values ϱ^e such that each yields a different sign for the sum rule equation. Then we update our guess for ϱ^e according to Newton's method, with a bisection method fallback if the updated guess lies outside the bracket interval. Despite the necessity to evaluate the derivative of the sum rule equation in each step, our tests have shown that this approach is roughly twice as fast as Brent's method. The latter method avoids analytic evaluation of the derivative and instead uses either the secant method or inverse quadratic interpolation on the guess history.

3.B.3 Calculation of the screening charge and potential

Because it is not feasible to accurately integrate the contribution of core and valence charges on the same grid, we separate the total charge density as, $\rho^e(\mathbf{r}) = \rho^e_v(\mathbf{r}) + \rho^e_c(\mathbf{r})$, where ρ^e_v and ρ^e_c are the valence and core charge distributions, respectively. The valence electron density is represented on a regular 3-dimensional real-space grid, while the core charges are stored on logarithmic radial grids, which are centered around ionic positions. The screening charge is thus calculated as

$$Q = \{\gamma(\varrho^e) - 1\} \left(Q^v + \sum_\alpha Q^\alpha \right), \tag{3.38}$$

where Q^v and Q^α are valence and core contributions, respectively. An analogue partitioning scheme is used for the calculation of the potential as well.

Core integration

Core contributions are taken into account for all ions for which $d^\alpha = |\mathbf{R}^\alpha - \mathbf{r}^p| < R^{\max} + R^{c,\alpha}$, where $\mathbf{R}^\alpha$ denotes the position of the ion and $R^{c,\alpha}$ is its core radius. In spherical coordinates, chosing the z-axis along $\mathbf{R}^\alpha - \mathbf{r}^p$, the contribution of an ion labeled α is

$$Q^\alpha = \int_0^{R^{\max}} dr\, r^2 \rho^e_c(r) \int_0^\pi d\theta \sin(\theta) \int_0^{2\pi} d\phi\, e^{-a\sqrt{(d^\alpha)^2 + r^2 + 2d^\alpha r\cos(\theta)}}, \tag{3.39}$$

where r is the radial distance from the ion. The angular integrals can be performed analytically, and the remaining radial integral is performed numerically. We have

$$Q^\alpha = 4\pi \sum_i w^i r^i (\rho^e_c)^{\alpha,i} f^i \tag{3.40}$$

where, for $d \neq 0$,

$$f^i = \frac{1}{2ad^\alpha} \left[\left(\frac{1}{a} + |d^\alpha - r^i| \right) e^{-a|d^\alpha - r^i|} - \left(\frac{1}{a} + |d^\alpha + r^i| \right) e^{-a|d^\alpha + r^i|} \right], \tag{3.41}$$

and, for $d = 0$,

$$f^i = r^i e^{-ar^i}. \tag{3.42}$$

For the correlation potential, the relevant formulas are

$$v_c^\alpha = 4\pi \sum_i w^i r^i (\rho_c^e)^{\alpha,i} f^i, \tag{3.43}$$

where

$$f^i = \frac{1}{2ad^\alpha} \left(e^{-a|d^\alpha - r^i|} - e^{-a|d^\alpha + r^i|} \right) \tag{3.44}$$

for $d \neq 0$ and

$$f^i = e^{-ar^i} \tag{3.45}$$

for $d^\alpha = 0$.

Valence integration

The most straightforward way to integrate the valence contribution to the screening charge is to use a weighted sum over all grid points within a selected cutoff radius $R^{\max}$

$$Q^v = \sum_{r^i \leq R^{\max}} w^i (\rho_v^e)^i e^{-ar^i}, \tag{3.46}$$

with $(\rho_v^e)^i = \rho_v^e(\mathbf{r}^{e,i})$, $r^i = |\mathbf{r}^{e,i} - \mathbf{r}^p|$ and the w^i are integration weights. In practice, though, we simply set all w^i equal to the volume element since in general we are working with non-orthogonal grids[6]. The integral for the potential is

$$v_c^v = \sum_{r^i \leq R^{\max}} w^i (\rho_v^e)^i \frac{e^{-ar^i}}{r^i}. \tag{3.47}$$

A different integration scheme is obtained by substituting the Fourier transform of the density in the sum rule equation

$$Q^v = \int d\mathbf{r}^e \left(\sum_{\mathbf{G}} c_{\mathbf{G}} e^{i\mathbf{G}\cdot\mathbf{r}^e} \right) e^{-a|\mathbf{r}^e - \mathbf{r}^p|}. \tag{3.48}$$

The integral can be carried out analytically, and the result is given by

$$Q^v = \sum_{\mathbf{G}} \frac{8\pi a}{(a^2 + G^2)^2} c_{\mathbf{G}} e^{i\mathbf{G}\cdot\mathbf{r}^p}, \tag{3.49}$$

where $G = |\mathbf{G}|$. Similarly, we find that the integral in the potential equation can be replaced by

$$\sum_{\mathbf{G}} \frac{4\pi}{(a^2 + G^2)} c_{\mathbf{G}} e^{i\mathbf{G}\cdot\mathbf{r}^p}, \tag{3.50}$$

Note that since the electron density a real quantity, we have $c_{-\mathbf{G}} = c_{\mathbf{G}}^*$ and

$$\sum_{\mathbf{G}\neq 0} c_{\mathbf{G}} e^{i\mathbf{G}\cdot\mathbf{r}^p} = \sum_{\mathbf{G}^+} 2\Re(c_{\mathbf{G}}) \cos(\mathbf{G}\cdot\mathbf{r}^p) - 2\Im(c_{\mathbf{C}}) \sin(\mathbf{G}\cdot\mathbf{r}^p). \tag{3.51}$$

---

[6] For orthogonal grids we could easily use, e.g., Simpson's rule on the successive one dimensional integrals.

The sum on the right hand side runs over the positive half-space of the reciprocal space.

A first major advantage of the reciprocal space integration is that it is in principle exact, in contrast to the real space integration scheme. The only approximation comes from the **G** vector cutoff of the electron density. Usually, though, the valence electron density can be very accurate represented with a reasonable amount of plane waves. Next is that the reciprocal space integration is generally significantly faster to evaluate when solving the sum rule. The reason is that the exponential factors, which are very slow to evaluate, do not depend on the inverse screening length a, and thus do not have to be reevaluated in every step of the root finding algorithm. For very large systems, it is expected, however, that the real space integration becomes faster than the reciprocal one. Indeed, in real space the number of elements in the screening charge integral is determined by $R^{\max}$ which is independent of the system size, such that the algorithm scales linearly. In reciprocal space the overall scaling is quadratic because the number of plane waves increases linearly with the system size.

Chapter 4

Comparison of Positron Surface Models

4.1 Introduction

The LDA for electron-positron correlations is fundamentally limited for the description of positron surface states. To understand this, we first examine the correct limit of the electron-positron correlation energy in a three dimensional homogeneous electron gas. The most stable isolated electron-positron system is Ps^-, with a binding energy of 7.130 eV [93] which is slightly larger than the binding energy of 6.803 eV for Ps. In the low-density limit of the homogeneous electron gas with a single immersed positron, Ps^- is thus expected to form. When we study surfaces, the electron density in the vacuum region typically decays exponentially, and hence the LDA will predict a correlation energy in the vacuum region equal to the Ps^- binding energy. In reality, however, electrons at a surface are confined to the material, and cannot follow the positron outside the surface to form Ps^-.

In the case of the GGAs from Refs. [59, 62, 75] a simple derivation shows that the potential decays faster than exponentially at a surface. This is a consequence of the functional form of the GGA

$$v^p_{c,\mathrm{GGA}} = v^p_{c,\mathrm{LDA}} e^{-\alpha\epsilon/3}, \tag{4.1}$$

where $\epsilon = (|\nabla\rho^e|/q_{\mathrm{TF}})^2$. The Thomas-Fermi wave vector is given by $q^2_{\mathrm{TF}} = 4(3\pi^2\rho^e)^{1/3}/\pi$. The parameter α is either a phenomenological constant, or an expression that depends on the LDA potential. Both give the same super-exponential decay though.

Fig. 4.1 shows the results of positron calculations with the LDA and GGA at a CdSe $(10\bar{1}0)$ surface. When left uncorrected, positron surface calculations with the LDA will generally predict a positron state in the vacuum region. This is because the correlation energy there is significant and the confinement of the wavefunction in the vacuum is low[1]. The outcome of a GGA calculation is harder to predict in general. Despite the fast asymptotic decay, a wide potential well at the surface is possible. For the CdSe $(10\bar{1}0)$, for instance, the groundstate as predicted by the GGA turns out the be a surface state.

Neither the LDA or the GGA capture the correct $\sim 1/z$ dependence of the correlation potential outside the surface, known from elementary electrostatics as the image potential

---

[1] There is some finite confinement energy in the calculations due to the periodic images of the slab model.

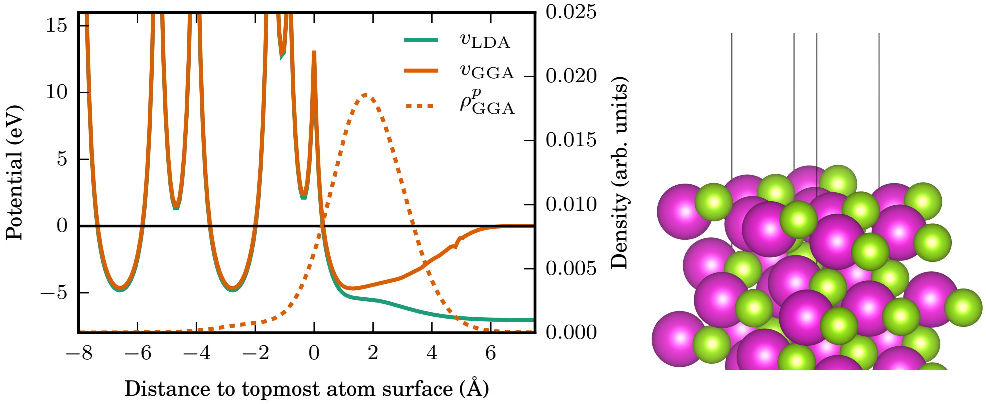

Figure 4.1: Planar averages of the positron Kohn-Sham potential (full lines), i.e. the sum of the Hartree and correlation potentials, and of the positron densities (dashed lines) at a CdSe $(10\bar{1}0)$ surface. The green and orange curves represent the LDA and GGA results, respectively. The sharp feature in the GGA potential around ~ 5 Å is a due to numerical noise in in the calculated gradients. Note that the LDA positron density is not shown because the calculation predicts a positron state in the middle of the vacuum. Hence any density we show would be a consequence of the finite width of the vacuum in our simulation cell. The figure on the right shows the CdSe $(10\bar{1}0)$ surface with Cd atoms in purple and Se atoms in green.

for a point charge outside a metallic surface. This long-range correlation effect arises because the screening cloud, which is centered around the positron inside materials, detaches from the positron and spreads out over the surface when the positron is outside the material. To obtain this long-range correlation effect, one has to turn to non-local functionals. Such functionals are, however, notorious for the large increase in the required computational resources necessary to evaluate them. Furthermore, as we have seen in Chapter 3, accurate non-local functionals are hard to construct. It is thus not unsurprising that the first solution to the problem in the literature was an empirical one, namely the CMM [22], which is in fact the only widely applied approach for theoretical work on positron surface states at the time of writing [42, 94–98]. In the WDA on the other hand, the image potential can be anticipated to arise naturally because the correlation potential is obtained directly from the Coulomb interaction with its screening cloud. This was in fact already shown to be true for jellium surfaces in the early work of Rubaszek on the WDA [25].

The purpose of this chapter is to assess the accuracy of the CMM and WDA for the calculation of positron surface properties, by comparing calculated positron workfunctions and surface binding energies with experiment. Additionally, we look into qualitative features of the models, such as the asymptotic decay of the potential far from the surface. Before presenting results of the calculations, we give a brief background on how positron workfunctions and surface binding energies can be obtained experimentally.

The rest of the chapter is organized as follows. In Sec. 4.2 we briefly discuss experimental techniques to determine positron workfunctions and surface binding energies, and we present reference results from literature. Sec. 4.3 provides the details of the CMM. Afterwards, in Sec. 4.4, we compare CMM and WDA results for positron workfunctions

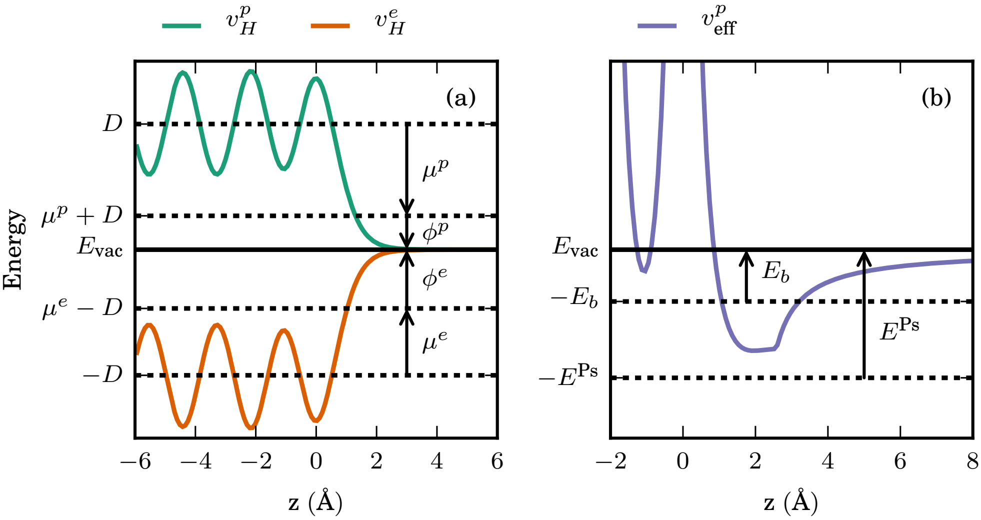

Figure 4.2: Schematic overview of some electron and positron energy levels. Panel (a) shows the electrostatic (Hartree) potentials for the positron v_H^p and electron v_H^e in green and orange lines, respectively. The surface dipole D is the same in magnitude for both particles, but has the opposite sign. It is defined as the energy difference between average Hartree potential in the bulk of the material and the vacuum level E_{vac}. The electron and positron chemical potentials are given by the highest occupied level, and the lowest available state in the bulk crystal, respectively. In panel (b), we show the positron potential at the surface, which generally hosts a positron surface state with binding energy E_b. For completeness, we also indicated the Ps binding energy E^{Ps}. In both figures, the origin of the z-axis is taken at the position of the last atom at the surface.

and surface binding energies to experiments. Qualitative aspects, such as the continuation of the positron potential across the vacuum interface, are presented in Sec. 4.5. A summary of our most important findings and an outlook are provided in Sec. 4.6.

4.2 Experimental reference values

For many materials, it turns out that positron workfunctions are negative, as indicated in Fig. 4.2. Hence, when positrons diffuse back to the surface after thermalization in the bulk of the material, they are spontaneously ejected from the material if they do not get trapped in a surface state. Positron workfunctions can thus be determined straightforwardly from the kinetic energy of re-emitted positrons.

Modern positron beams have advanced to the point where deposition of positrons directly into a surface state without thermalization in bulk, through AMPS, becomes possible [21]. Fig. 1.1 shows the process schematically. The maximal kinetic energy of an Auger electron is determined by the relation $E_{\mathrm{max}} = E_{\mathrm{beam}} + E_b - \phi^e$, with E_{beam} the kinetic energy of the incident positrons, E_b the binding energy of the positron to the surface and ϕ^e the electron workfunction. By tuning the incident beam energy, one can determine the threshold value of the incident beam energy for which the Auger peak disappears: $0 = E_{\mathrm{beam}}^{\mathrm{Thr}} + E_b - \phi^e$. Hence, from such experiments the binding energy of the positron can be extracted if the sample's electron workfunction ϕ^e is known. This technique is however, relatively recent and only binding energies for Cu, Ag and Bi_2Te_2Se obtained this way have been reported in literature [21, 42].

Older experiments relied on thermally activated Ps emission from surfaces, after positrons diffuse back to the surface and become trapped in a surface state [11, 15]. It turns out that for many surfaces the Ps workfunction, in contrast to the positron workfunction ϕ^p, is positive. Hence, to form Ps in the vacuum, extra energy has to be added to the system. The activation energy E_a for the process is determined by

$$\phi^e + E_b = E^{\mathrm{Ps}} + E_a, \tag{4.2}$$

where $E^{\mathrm{Ps}} = 6.8$ eV is the Ps binding energy. Once the activation energy is determined, the positron binding energy E_b can be extracted if the electron workfunction is known. In experiment, E_a is extracted from the temperature dependence of the Ps fraction observed in the annihilation data. Note that it is reasonable to assume that thermally desorbed Ps originates from a positron surface state. Indeed, electron workfunctions are typically between $4-5$ eV, whereas positron workfunctions are generally negative (or close to zero), such that Ps desorption with a positron originating from a bulk state should happen spontaneously.

We note that both methods above require a value for the electron workfunction. As these values are generally taken from other experiments, this adds some extra uncertainty to the cited values. Indeed, it is known that the electron workfunction is sensitive to the precise surface conditions of the sample as contaminants alter the surface dipole. For this reason, we also cite the electron workfunctions in Table 4.1 used to determine the positron binding energies. We note that by combining AMPS and thermal Ps desorption experiments, one can determine the binding energy without knowledge of the electron workfunction. This is the approach we use in Chapter 5 to find E_b at the Bi_2Te_2Se surface.

Table 4.1 summarizes the experimental values for low index surfaces of Al, Cu, W and diamond. Note that all positron binding energies are remarkable close, which could be a consequence of the metallic nature of the considered systems. Indeed, for Si (100) and Si (111), binding energies of $E_b = 2.06$ and $E_b = 2.69$ were observed [11]. This is likely explained by the fact that for semi-conductors and insulators, the image potential strength should be rescaled by $(\epsilon_0 - 1)/(\epsilon_0 + 1)$ [95][2].

Instead of the Si (001) surface, we study the diamond (001) surface, mainly because of its simpler surface reconstruction [104]. Unfortunately, we were unable to find experimental binding energies for this surface. The main reason we consider it, however, is to investigate the applicability of the CMM model to somewhat more complex surfaces. In particular, we will study the (001) diamond surface in its pristine form, when dangling bonds are passivated with H, and the (2 x 1) dimer reconstructed surface. Fig. 4.3 shows these structures. The details of our electronic structure calculations for the systems in the Table 4.1 can be found in appendix 4.A.

---

[2] We will not take into account this factor in the rest of this chapter since we are mainly studying metallic systems for which the correction is negligible. Whereas for the only non-metallic system in our tests, diamond, we did not find any reference value for the positron binding energy.

System	E_a (eV)	ϕ^e (eV)	E_b (eV)	ϕ^p (eV)
Al (001)	0.64 ± 0.02^a, 0.41 ± 0.01^b	4.41^a	3.03 ± 0.05^a	-0.30 ± 0.03^c
Al (011)	0.40 ± 0.01^a	4.28^a	2.92 ± 0.04^a	
Al (111)	0.34 ± 0.03^a, 0.33 ± 0.01^b	4.24^a	2.90 ± 0.06^a	-0.08 ± 0.03^c
Cu (001)	0.56 ± 0.02^a	4.59^a, 4.65^e	2.77 ± 0.05^a, 2.79^e	-0.24^d
Cu (011)	0.64 ± 0.02^a	4.48^a	2.97 ± 0.05^a	-0.13 ± 0.08^f
Cu (111)	0.85 ± 0.02^a	4.85^a	2.80 ± 0.05^a	-0.40 ± 0.09^f
W (001)				-3.00 ± 0.15^g, -3.0 ± 0.3^h
W (011)				-2.96 ± 0.20^i
W (111)	0.48 ± 0.10^j	4.47^j	2.81 ± 0.10^j	-2.59 ± 0.10^j
C (001)				-4.13 ± 0.10^k
C (001) + H				-3.83 ± 0.10^k
C (001) (2 x 1)				-4.20 ± 0.10^k

Table 4.1: Experimental values for the positron workfunction ϕ^p and binding energies E_b. The latter are derived from the equation $E_a = \phi^e + E_b - E^{\mathrm{Ps}}$, where ϕ^e is the electron workfunction and $E^{\mathrm{Ps}} = 6.8$ eV is the Ps binding energy. Hence, the cited values for the positron binding energy depend on the value of the electron workfunction, which are experimental values taken from literature for all references cited here. [a]: Ref. [11], [b]: Ref. [14], [c]: Ref. [99], [d]: Ref. [100], [e]: Ref. [5], [f]: Ref. [13], [g]: Ref. [4], [h]: Ref. [101], [i]: Ref. [102], [j]: Ref. [15], [k]: Ref. [103].

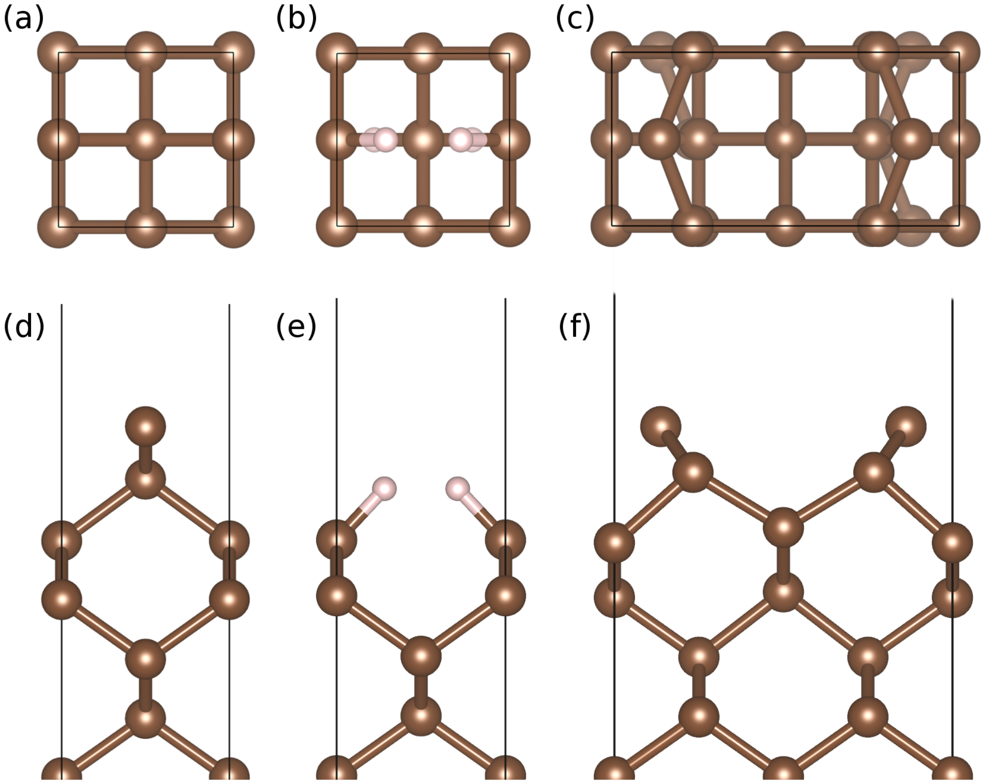

Figure 4.3: Unit cells of the considered diamond surfaces: Top (a) and side (d) view of the diamond (001) surface. The H passivated surface is shown in panels (b) and (e), and the (2×1) dimer reconstructed surface in panels (c) and (f). Results for the reconstructed surface agree well with the results of Ref. [104].

4.3 Corrugated Mirror Model

4.3.1 Theory

In the CMM, the image potential is enforced in the vacuum area, in such a way that (i) continuity of the potential is ensured, and (ii) the potential and the electron density show the same corrugations, i.e. equal values of the electron density correspond with equal values of the image potential [22]. The positron correlation potential in the CMM can be written as

$$v_c^p(\rho^e(\mathbf{r}^p)) = \begin{cases} v_{c,\mathrm{LDA}}^p(\rho^e(\mathbf{r}^p)) & z \leq z_0 \\ \max\{v_{c,\mathrm{LDA}}^p(\rho^e(\mathbf{r}^p)), v_{c,\mathrm{im}}^p(\rho^e(\mathbf{r}^p))\} & z > z_0 \end{cases}, \tag{4.3}$$

where z_0 is the image potential reference plane, $v_{c,\mathrm{LDA}}^p$ is the LDA potential, and [94]

$$v_{c,\mathrm{im}}^p(\rho^e(\mathbf{r}^p)) = -\frac{1}{4(z_{\mathrm{eff}}(\rho^e(\mathbf{r}^p)) - z_0)}. \tag{4.4}$$

The effective distance to the surface is determined as

$$z_{\mathrm{eff}}(\rho^e(\mathbf{r}^p)) = \int_{z_0}^{\infty} dz'\, z'\delta(\rho^e(\mathbf{r}^p) - \langle\rho^e\rangle(z')). \tag{4.5}$$

In the last equation $\langle\rho^e\rangle$ denotes the electron density averaged over the planes parallel to the surface. Hence, $z_{\mathrm{eff}}(\rho^e(\mathbf{r}^p))$ gives the distance from the surface where the electron density is on average equal to $\rho^e(\mathbf{r}^p)$. This definition ensures that points with the same electron density will map to the same value of the image potential, such that condition (ii) is fulfilled. By taking the maximal value (i.e. the least negative) of the LDA and image potential in Eq. (4.3) for $z > z_0$, we replace the problematic behaviour of the LDA in a continuous way by the image potential. Note that if the GGA would be used instead, one should be more careful in the construction of the potential; Unlike in the LDA, the correlation potential decays to zero. Hence, taking the maximum in Eq. 4.3 will not yield the desired result. One possibility would be to track the behaviour of the potential from the bulk into the vacuum region along each line perpendicular to the surface and impose the image potential for $z \geq z_1$, where z_1 is the first point for which the image potential is less negative than the GGA potential.

The image potential arises because the positron's screening cloud is spread over the sample's surface when the particle resides in the vacuum. Even though the CMM implicitly assumes this, it provides no direct modification for the enhancement factor. Remember that the LDA enhancement factor depends only on the local electron density, and assumes that the screening cloud is centered around the positron and resembles the Ps atom. If the LDA enhancement factor is applied in the calculation of the positron annihilation rate, we can expect lifetimes are underestimated. This is indeed what experiments on Al point out [17]. One workaround from literature suggests to assume that the positron will not annihilate where the image potential is imposed [23]. This would, however, imply that the pair density far in the vacuum is lower than the unperturbed electron density. A conceptually more acceptable modification is to set the enhancement factor to unity everywhere the image potential is imposed, i.e. use the IPM model[3]. Explicitly

$$\gamma(\rho^e(\mathbf{r}^p)) = \begin{cases} \gamma_{\mathrm{LDA}}(\rho^e(\mathbf{r}^p)) & z \leq z_0 \\ \gamma_{\mathrm{LDA}}(\rho^e(\mathbf{r}^p))\Theta\left(v_c^p(\rho^e(\mathbf{r}^p)) = v_{c,\mathrm{LDA}}^p(\rho^e(\mathbf{r}^p))\right) & \\ \quad +\Theta\left(v_c^p(\rho^e(\mathbf{r}^p)) = v_{c,\mathrm{im}}^p(\rho^e(\mathbf{r}^p))\right) & z > z_0 \end{cases}, \tag{4.6}$$

---

[3] This means assuming that the pair density and unperturbed electron density are the same.

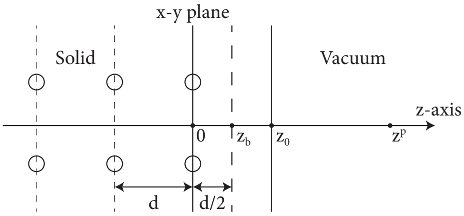

Figure 4.4: Illustration of the different parameters that enter in the Lang-Kohn method to determine the image potential reference plane z_0. The position of the positron along the z-axis, i.e. the normal to the surface, is given by z^p. Subsequent atomic layers are separated by a distance d. The background edge z_b is located half this spacing $d/2$ outside the surface, measured from the topmost atom at $z = 0$. Offsets between the background edge and the location of the image potential reference plane z_0, are taken from results for the jellium model.

with Θ the Heaviside function. We note that, unlike the potential, the electron-positron contact density obtained this way is not continuous.

In linear response theory the image potential reference plane z_0 corresponds with the centre of mass of the induced charge density by an external point charge, as shown by Lang and Kohn [105]. Non-linear effects, however, shift the position of the induced charge density while the image potential reference plane remains fixed [106]. To apply the CMM, we thus have to determine the center of mass of the positron screening cloud when the particle resides far in the vacuum. Unfortunately, we do not have a clear recipe to calculate the screening cloud from first-principles. Hence, in literature, authors use different methods to determine an approximation of the image potential reference plane. For instance some authors have treated z_0 as a fitting parameter for the experimental positron binding energy [107], or equated z_0 with the Wigner-Seitz radius of the material [94].

A common approximation, applied in Refs. [22, 95, 97][4], is the 'Lang-Kohn' method. In this approach one takes $(z_0 - z_b) = (z_0 - z_b)_{\text{jellium}}$, where the right hand side is the location of the center of mass of the induced charge density z_0 for a jellium slab model measured from the edge of its positive background z_b. These results are obtained by applying a small homogeneous electrical field perpendicular to the surface, and are tabulated for a few electron density values in Refs. [105, 108]. The background edge z_b for the material is set to $z_b = d/2$, where the topmost atomic position is taken as the origin of the z-axis and d is the spacing between subsequent atomic layers. A sketch of the different quantities is given in Fig. 4.4.

In our work on Bi_2Te_2Se, discussed in more detail in Chapter 5, we have set z_0 to the background edge z_b calculated from the self-consistent electron density. The procedure is presented in more detail in Appendix 4.C, and turned out to yield a positron binding energy in close agreement with experiment [42]. Even though we possibly obtained a more accurate value for z_b by calculating it from the electron density rather than taking $d/2$, we have as such neglected the (possible) shift of the induced charge density with respect to the materials 'edge'. We attempt to evaluate the accuracy of the approaches described in this and the previous paragraph in some detail in the following sections.

---

[4] Unfortunately, Refs. [95, 97] only refer vaguely to 'the method of Lang and Kohn' with a citation to Ref. [105], without providing any further details. Hence, I am not 100% sure that they actually applied the procedure described in the text, but it seems plausible.

			$z_0 = z_b$			$z_0 = z_b + (z_0 - z_b)_{\text{jellium}}$			$z_0 = d/2 + (z_0 - z_b)_{\text{jellium}}$		
System	ϕ^p (eV)	$d/2$ (Å)	z_b (Å)	τ (ps)	E_b (eV)	z_0 (Å)	τ (ps)	E_b (eV)	z_0 (Å)	τ (ps)	E_b (eV)
Al (001)	-0.18	1.01	$1.66^{+0.21}_{-0.26}$	541^{+20}_{-11}	$2.82^{+0.21}_{-0.31}$	$2.48^{+0.21}_{-0.26}$	512^{+8}_{-6}	$3.55^{+0.16}_{-0.21}$	1.83	532	3.00
Al (011)	-0.02	0.72	$1.26^{+0.05}_{-0.09}$	547^{+9}_{-4}	$2.56^{+0.06}_{-0.11}$	$2.08^{+0.05}_{-0.09}$	512^{+2}_{-1}	$3.39^{+0.04}_{-0.07}$	1.53	529	2.88
Al (111)	0.04	1.17	$1.36^{+0.06}_{-0.10}$	589^{+16}_{-10}	$2.34^{+0.08}_{-0.15}$	$2.17^{+0.06}_{-0.10}$	526^{+6}_{-0}	$3.24^{+0.05}_{-0.09}$	1.99	536	3.07
Cu (001)	-0.27	0.90	$0.84^{+0.10}_{-0.05}$	495^{+12}_{-17}	$1.86^{+0.16}_{-0.09}$	$1.61^{+0.08}_{-0.05}$	452^{+1}_{-0}	$2.90^{+0.08}_{-0.05}$	1.66	452	2.96
Cu (011)	-0.09	0.64	$1.29^{+0.02}_{-0.01}$	429^{+1}_{-0}	$2.81^{+0.03}_{-0.02}$	$2.05^{+0.02}_{-0.01}$	443^{+1}_{-1}	$3.50^{+0.02}_{-0.01}$	1.40	430	2.93
Cu (111)	-0.57	1.04	$1.01^{+0.04}_{-0.03}$	535^{+7}_{-8}	$1.94^{+0.06}_{-0.05}$	$1.77^{+0.04}_{-0.03}$	473^{+8}_{-0}	$2.94^{+0.04}_{-0.03}$	1.80	478	2.97
W (001)	-2.17	0.79	$0.99^{+0.04}_{-0.05}$	589^{+19}_{-14}	$1.79^{+0.07}_{-0.08}$	$1.78^{+0.04}_{-0.05}$	492^{+1}_{-2}	$2.88^{+0.04}_{-0.05}$	1.58	497	2.66
W (011)	-2.88	1.12	$1.64^{+0.07}_{-0.11}$	570^{+20}_{-11}	$2.41^{+0.09}_{-0.15}$	$2.43^{+0.07}_{-0.11}$	516^{+2}_{-6}	$3.26^{+0.06}_{-0.10}$	1.91	546	2.75
W (111)	-2.06	0.46	$0.90^{+0.02}_{-0.01}$	516^{+3}_{-5}	$2.19^{+0.03}_{-0.02}$	$1.69^{+0.02}_{-0.01}$	459^{+1}_{-1}	$3.19^{+0.02}_{-0.01}$	1.25	471	2.71
C (001)	-5.35	0.45	$0.52^{+0.02}_{-0.03}$	890^{+46}_{-31}	$1.44^{+0.04}_{-0.05}$	$1.38^{+0.02}_{-0.03}$	498^{+2}_{-2}	$2.82^{+0.02}_{-0.03}$	1.31	504	2.73
C (001) + H	0.22	0.45	$0.52^{+0.02}_{-0.03}$	297^{+1}_{-1}	$2.79^{+0.03}_{-0.03}$	$1.36^{+0.02}_{-0.03}$	336^{+1}_{-2}	$3.58^{+0.02}_{-0.02}$	1.31	334	3.54
C (001) dimer	-3.55	0.45	$1.83^{+0.04}_{-0.04}$	490^{+2}_{-2}	$3.22^{+0.04}_{-0.04}$	$2.69^{+0.04}_{-0.04}$	466^{+2}_{-2}	$3.95^{+0.03}_{-0.03}$	1.31	517	2.65

Table 4.2: Results of positron calculations with the CMM for the surfaces considered in this chapter. The second last and last line are the results for the H passivated and the (2×1) dimer reconstructed diamond (001) surfaces, respectively. The second and third column give the positron workfunction ϕ^p and half the spacing between subsequent atomic layers $d/2$. The rest of the columns are the value of the image potential reference plane used in the calculations z_0, the calculated positron annihilation lifetimes τ and the energy of the positron binding energy to the surface E_b. The first set of results is obtained by setting the background edge z_b, calculated from the self-consistent electron density, equal to the image potential reference plane. In the second set of results, the jellium shift of the reference plane position $(z_0 - z_b)_{\text{jellium}}$ is added to the calculated z_b. In the final results, $d/2$ is substituted for z_b. For the positron workfunction ϕ^p, we take the lowest positron state from a bulk calculation. Hence note that the differences between facets of the same material only reflect the change in the surface dipole. As explained in Appendix 4.C, there is an uncertainty involved in determining the background edge values z_b, which are indicated by the sub- and superscripts. This in turn gives an uncertainty on the lifetimes and binding energies.

4.3.2 Parameters in the model

In this section, we discuss in some detail different approaches to approximate the image potential reference plane z_0. We start by comparing calculated background edges z_b with half the distance between subsequent atomic layers along the normal of the surface $d/2$. Technical details concerning the calculation of the background edge from the electron density can be found in Appendix 4.C. Afterwards, we discuss how to obtain the approximations for z_0. The results are gathered in Table 4.2. The discussion of the positron binding energies E_b and positron workfunctions ϕ^p is deferred to a later section where we compare the CMM and WDA results with experiment. Positron annihilation lifetimes are given for completeness, as we are only aware of experimental results for the Al (011) surface [17].

The background edge

We start our discussion of the results by comparing the calculated z_b values, which is the position where the exponential decay of the electron density sets in, with the simple approximation of Lang and Kohn [105]. In their work, Lang and Kohn replace the ionic lattice with a uniform positive background (i.e. jellium) which terminates at $z_b = z_{\text{last}} + d/2$, where z_{last} is the coordinate of the last atomic layer along the normal of the surface and d the distance between subsequent atomic layers. The results are given in the second and third column of Table 4.2. We mention that for the H passivated surface, we could not accurately fit the decay of the electron density with a single exponential function. As a consequence, our method to calculated z_b does not yield a sensible value. Therefor we choose to take the same value for the image potential reference plane as for the non-passivated surface[5].

With the exception of Cu (001) and Cu (111), the calculated background edges are located further in the vacuum than half the interlayer distance. Aside from that, it is difficult, however, to observe general trends in the results. For the Cu (001), Cu (111) and C (001) surface the values determined with both methods are in close agreement, with differences ≤ 0.1 Å. On the other hand, for Al (001), Al (011), Cu (011), W (011) and W (111) the results differ > 0.5 Å. Also the dimer reconstructed diamond surface shows a large difference between the two methods, which is however expected due to the reconstruction at the surface. This example also illustrates that setting $z_b = d/2$ is largely limited to simple elemental surfaces. On the other hand, as mention previously, we did not manage to determine an accurate value for z_b from the self-consistent electron density for the H passivated diamond surface either. Hence we conclude that z_b introduces an important uncertainty in the results of the CMM method.

Image potential reference plane

In the Lang-Kohn method, z_0 is determined by applying the offset for jellium of the image potential reference plane with respect to z_b. These values can be found in Table I of their work [105], though we will instead use the slightly more accurate results reported in Table I of Ref. [108]. The values give the centroids of the induced charge density as calculated for the jellium model in the presence of a small electrical field perpendicular to the surface. To use this scheme, we first determine an effective uniform density by dividing the valence charge in the unit cell by its volume. Afterwards, we determine

---

[5] Note that distances are measured with respect to the last atom at the surface, i.e. from the H atom for the passivated surface.

System	z_{val}	r_s (a.u.)	$z_0 - z_b$ (a.u.)	$z_0 - z_b$ (Å)
Al	3	2.07	1.55	0.82
Cu	1	2.67	1.43	0.76
W	2	2.34	1.50	0.79
C	4	1.66	1.62	0.86

Table 4.3: Effective electron density parameters and image potential reference planes offsets following Lang and Kohn [105]. The effective densities are equal to the average valence electron density in the unit cells. Following Ref. [109], only s and p electrons in the outer shells are counted here. The offset of the image potential reference plane with respect the jellium edge is found by linearly interpolating the results given in Table I of Ref. [108].

the offset by linearly interpolating the results from Ref. [108]. Table 4.3 summarizes the results. Note that these shifts are comparable with $d/2$ and the calculated z_b values, such that they are not a small correction in determining the image potential reference plane.

In the next sections, we will discuss results of three methods used to determine the value of the image potential reference plane. In the first, we follow the approach taken in Ref. [42] and set $z_0 = z_b$. With this method we obtained excellent agreement with measured positron binding energies for Bi_2Te_2Se. In the second method, we add to the background egde the shift of the reference plane obtained for jellium $(z_0 - z_b)_{\text{jellium}}$ [105, 108]. Finally, we apply the Lang-Kohn method, which is obtained by replacing the calculated background edge with half of the interplanar distance along the normal to the surface $d/2$: $z_0 = d/2 + (z_0 - z_b)_{\text{jellium}}$.

Considering that the three methods described above give large differences in the value for z_0, one can wonder if it is not possible to calculate the value of z_0 directly. In principle this is possible, as the induced charge density in the linear response regime can be obtained by applying a small electrical field perpendicular to the surface [105, 106]. One important assumption that is made in the derivation of the image potential is, though, that a point charge outside the surface attracts an equal but opposite charge to the surface region. In practice, this turns out to be problematic for many modern first-principles electronic structure codes which use periodic boundary conditions. In such packages surfaces are modelled by a slab, with a vacuum added to the simulation cell to avoid interactions with its periodic images. We found that the response under an applied electrical field in such calculations is quadratic instead of linear. The reason is that the net induced charge has to be zero, since the number of electrons in a calculation is fixed. On the other hand, if we add additional electrons to the system to allow a screening charge to build up at the surface, we face the problem that the energy diverges due to the long range Coulomb interaction of the slab with its periodic images. Hence, no sensible results can be obtained this way. Lang and Kohn [105, 110, 111] modelled instead a semi-infinite jellium model where appropriate boundary conditions can be applied and enable the calculation of the induced charge density.

4.4 Comparison with experiment

In this section we compare results obtained with the CMM and the WDA with experimental values where available. The results of the latter are gathered in Table 4.4. Details of the

	$Q = 1.00$			$Q = Q_{\text{opt}}$		
System	ϕ^p (eV)	τ (ps)	E_b (eV)	ϕ^p (eV)	τ (ps)	E_b (eV)
Al (001)	0.74	664	3.10	0.85	642	3.19
Al (011)	0.90	673	3.16	1.02	651	3.26
Al (111)	0.96	674	3.02	1.07	652	3.11
Cu (001)	−0.61	963	2.22	4.02	288	5.02
Cu (011)	−0.43	902	2.30	4.21	285	5.16
Cu (111)	−0.91	1082	2.15	3.72	315	4.84
W (001)	−1.69	883	2.72	−2.20	1056	2.42
W (011)	−2.39	970	2.56	−2.91	1152	2.28
W (111)	−1.57	747	2.82	−2.09	868	2.50
C (001)	−5.06	821	2.45	−4.23	682	2.85
C (001) + H	0.51	336	3.05	1.33	280	3.58
C (001) dimer	−3.26	876	2.35	−2.44	718	2.74

Table 4.4: Results of positron calculations in the WDA with the screening parameter set to $Q = 1$ (columns 2-4), and with the screening parameter that reproduces the experimental bulk lifetime $Q = Q_{\text{opt}}$ from Table 3.2 (columns 5-7). The last two lines give the results for the H passivated and the (2×1) dimer reconstructed diamond (001) surfaces, respectively. ϕ^p: Positron workfunction. τ : Positron surface state annihilation lifetime. E_b: Binding energy of the positron state. The workfunction is determined by the surface dipole and the lowest available positron level in the bulk of the material. The first depends on the material's facet whereas the latter is purely a bulk quantity.

positron calculations are given in Appendix 4.B. For the WDA we use the shell partitioning from Sec. 3.3.3. We investigate the WDA results both with the screening parameter $Q = 1$ and the optimized parameter $Q = Q_{\text{opt}}$ which reproduces the experimental bulk positron annihilation lifetimes, as explained in Sec. 3.3.4 and given in Table 3.2.

4.4.1 Positron workfunctions

We first discuss the results for positron workfunctions, which do not depend on the details of the positron potential at the surface. Indeed, the positron workfunction is obtained as $\phi^p = -(\mu^p + D)$, with D the surface dipole barrier, which is purely electrostatic in nature[6], and μ^p the positron chemical potential. The latter is obtained from a bulk calculation and hence is not influenced by the image potential, but does depend on the electron-positron correlation functional. By comparing the workfunction values, we hope to gain some insight on the accuracy of the correlation potential in the bulk of the material.

The comparison with experiment is displayed in Fig. 4.5, with LDA and WDA results in green and orange, respectively. We find that for Al and Cu, the obtained LDA results are in very good agreement with experiment. For W, we only obtain reasonable results for the (011) facet, whereas the other facets show discrepancies of > 0.5 eV. The WDA results with both considered Q parameters are worse than the LDA for most surfaces.

---

[6] Since we are working in the zero positron density limit, the presence of the positron does not alter the electron density or ionic positions and hence has no effect on the dipole barrier. We note, though, that the dipole barrier is influenced by electron-electron exchange and correlation effects.

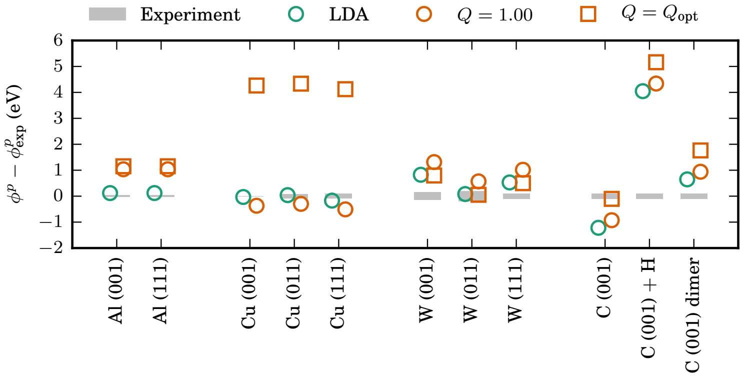

Figure 4.5: Energy differences between calculated and experimental values for positron workfunctions ϕ^p. Results are taken from Tables 4.1, 4.2 and 4.4. The gray area indicates the uncertainty on the experimental values, LDA results are indicated by green symbols and WDA results with orange symbols. For the WDA, circles indicate workfunction obtained by setting $Q = 1.00$; for the squares the Q parameters from Table 3.2 were used.

The exceptions are the workfunctions calculated with $Q = Q_{\text{opt}}$ for W, which differ only -0.03 eV with the LDA, and C (001). Notably, the WDA wrongly predicts positive workfunctions for all Al surfaces with both Q values, and for the Cu surface with $Q = Q_{\text{opt}}$, as can be seen from Table 4.4. The only WDA results that agree with experiment to within ~ 0.5 eV are the Cu surfaces with $Q = 1.00$, and the W (011), W (111) and C (001) with $Q = Q_{\text{opt}}$.

Both the LDA and WDA show large deviations for the workfunctions calculated for the diamond surfaces, with expection of the WDA results for the C (001) surface with $Q = 1.10$. Especially our result for the H passivated surface gives a very different result than measured in experiment. Indeed, from Table 4.2 and Table 4.4, we see that all functionals predict a positive workfunction for this surface, in contrast to the strongly negative value for the pristine diamond surface. The reason is that the dipole at the surface is largely reversed by the presence of the positively polarized side of the H at the vacuum interface. It is highly unlikely that the observed differences with experiment can be attributed solely to correlation energy. Instead, it seems plausible that our model surface does not quite correspond with the sample in the experiments reported in Ref. [103]. Although this reference claims that the difference in the workfunction they observe upon heating the sample is due to desorption of H from the surface, it could be that their surface was only partially passivated for instance. For the reconstructed surface, our calculations predict an increase of the workfunction by $\Delta\phi^p = 1.80$ eV. This again contradicts the experiment, where a small decrease of the workfunction was observed $\Delta\phi^p = -0.07$ eV. Hence, considering these discrepancies which cannot be attributed to the positron correlation functional, it is difficult to extract any meaningful conclusions from the diamond results about the accuracy of the LDA compared to the WDA.

It is interesting to observe that with $Q = 1$ the chemical potential obtained with the WDA is generally lower than with the LDA, as reflected by the higher value of the workfuntion[7]. With larger Q values, this trend becomes more obvious as is apparent by comparing the results for Cu with $Q = 1.00$ and $Q = 1.66$. This follows from the fact

---

[7] We keep in mind, though, that our benchmark here is too limited to draw general conclusions.

that Q determines the charge in the screening cloud, and hence directly influences the correlation energy. This exposes a shortcoming of the sumrule tuning scheme we proposed in Sec. 3.3.4. Indeed, we raised the parameter Q to account for the fact that d electrons do not screen the positron charge very efficiently. On the other hand, this operation simultaneously increases the correlation energy. However, for materials in which screening is less efficient we instead expect lower correlation energies. Only for Cu, the results with $Q = 1.00$ seems to underestimate the correlation energy as they are the only ones (disregarding diamond) that gives lower workfunctions as measured in experiment. As a consequence the 'ideal' Q that reproduces the correct chemical potential is likely obtained with screening parameters $Q < 1$, even for free-electron like materials. Comparing the WDA and LDA correlation energies for the free electron gas in Fig. 3.2, we indeed see that the WDA potential is more negative for the homogeneous electron gas.

From this section, we can conclude that the LDA predictions for workfunctions, and thus also positron chemical potentials, are quite accurate. In most cases, the WDA predictions are worse due to an overestimation of the correlation energy. This worsens when the screening parameter is raised $Q > 1$. Hence, our scheme proposed in Sec. 3.3.4 is unlikely to give both accurate positron annihilation lifetimes *and* correlation energies at the same time.

4.4.2 Positron binding energies

We now examine calculated positron binding energies, of which differences with experimental values are shown in Fig. 4.6. Before starting our discussion, we first point out that for all considered surfaces, the positron groundstate is strongly localized at the surface with vanishing overlap with the material beyond the first few atomic layers below the surface. Next, it is important to realize that our findings of the correlation energy in bulk materials derived from the workfunctions in the previous section, do not directly carry over to surface states. Indeed, since the positron is mainly localized in the vacuum region, the correlation energy is mostly determined by the behaviour of the correlation potential in this region. From the introduction, we already know that this is very different from the bulk situation.

Let us first investigate which of the three methods to determine the background edge position z_0 gives the best results with the CMM. From Fig. 4.6, we can see that this is consistently Lang and Kohn's simple approach which sets $z_0 = d/2 + (z_0 - z_b)_{\text{jellium}}$. The largest discrepancies with experiment following this method are observed for Al (111), Cu (001) and Cu (111), for which $E_b - E_{b,\text{exp}} \approx 0.18$ eV. For all other surfaces differences with experiment are ≤ 0.10 eV. Clearly, taking the calculated background edge z_b as an approximation for z_0 sets the reference plane too close to the surface, at least for the results displayed in Fig. 4.6. As a consequence, binding energies are significantly underestimated in most cases. On the other hand, adding the jellium offset of the image potential reference plane to the calculated background edge, i.e. $z_0 = z_b + (z_0 - z_b)_{\text{jellium}}$, places z_0 too far out in the vacuum. This can be derived from the consistent overestimation of the binding energy. Notable exception here are Cu (001) and Cu (111) for which $d/2 \approx z_b$.

Considering the simplicity of the Lang-Kohn method, the results above are maybe somewhat surprising. Mainly the observation that a, presumably, more sophisticated approach to determine the material's 'edge' does not bring any improvement is puzzling. This indicates that the effect of the ionic lattice on z_0 is small. Ref. [108] investigated the effect of the lattice[8] on the position of z_0. For Al (111) the author finds $z_0 = 1.76$ Å,

---

[8] We note that lattice effects are only accounted for approximately in this work.

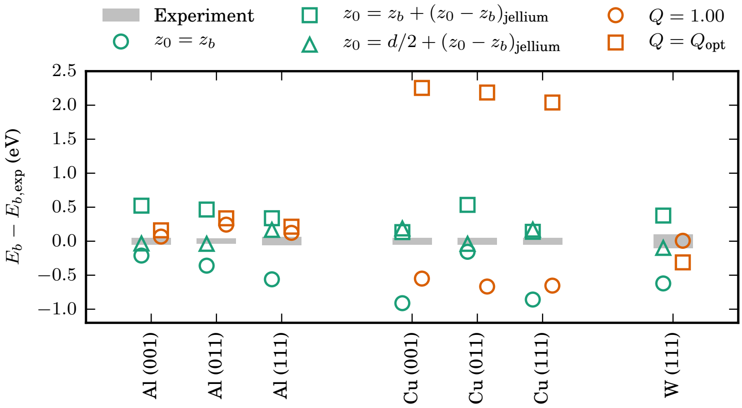

Figure 4.6: Energy differences between experimental and calculated positron binding energies. The figure shows the CMM results from Table 4.2, obtained by using three different methods to determine the image potential reference plane z_0, in green symbols. WDA results from Table 4.4 are shown in orange symbols. The gray area denotes the experimental uncertainty. We have left out the error bars due to the uncertainty on z_b on the calculated CMM results to avoid cluttering the plot. For most studied surfaces, these uncertainties are significantly smaller than the discrepancy with the experimental value. One notable exception is the CMM result for Al (001) obtained with $z_0 = z_b$ for which the experimental and calculated uncertainties overlap.

i.e. 0.17 Å closer to the surface than obtained by applying the Lang-Kohn method. For some Alkali metals, much larger deviations are observed, however. Hence, despite good agreement for the three considered metals, it seems unlikely that the Lang-Kohn method will work as well for other systems. Aside from the apparent limited effect of the lattice on the image potential reference plane, the results show that our method to calculate the background edge is not very accurate in general. Hence, a robust method to directly determine the location of the image potential reference plane z_0, that is also applicable when periodic boundary conditions are used, is desirable and requires further research.

The WDA gives very decent results with $Q = 1.00$ for the Al and W surfaces, on par with the CMM where z_0 is set using the Lang-Kohn method. We note that changing the screening parameter to $Q = Q_{\text{opt}}$ consistently worsens the results. Our observation from the previous section that correlation energies and lifetimes cannot be simultaneously improved by tuning Q is thus confirmed here. On the other hand, the binding energies calculated with the WDA are, overall, in better agreement with experiment than the positron workfunctions, certainly with $Q = 1.00$. This indicates that the WDA gives a more accurate description of the correlation potential in the surface region than in bulk. Hence the WDA with $Q = 1.00$ may still provide a somewhat reliable approach to describe positron surface states when the CMM is not applicable, e.g. for surface with complex geometries.

4.5 Qualitative aspects

Previous section showed that for simple metallic surfaces, the WDA does not give a quantitative improvement for positron binding energies over the CMM. In this section we focus on some qualitative aspects of both approaches, namely the transition from the bulk potential to the long-range image potential, as well as the continuation of the enhancement factor in the vacuum.

4.5.1 Potentials

Let us first discuss the transition of the potential from the bulk region into the vacuum region. Panel (a) of Fig. 4.7 shows the potential averaged over planes parallel to the surface. For certain values of z_0, the transition of the LDA to the imposed image potential part, appears to happen quite smoothly. This is for instance the case with $z_0 = d/2 + (z_0 - z_b)_{\text{jellium}}$, for which the potential is shown by the green curve. On the other hand, if the image potential reference plane is further out in the vacuum, a plateau develops as is illustrated by the orange curve. When we look at cuts through the potential (Fig. 4.7(b)) we notice that generally, the transition is quite abrupt, and that the potential's derivative shows a significant discontinuity. Note that in the WDA, the transition happens smoothly, which is at least a qualitative improvement over the CMM.

We now examine in more detail the long-range behaviour of the potential. For the CMM, we find that the averaged potential closely follows the $\sim 1/c(z - z_0)$ behaviour, with $c = 4$. A fit to the averaged potential in the region defined by $z \in [3, 6]$ Å results in $c = -3.98, z_0 = 1.22$ Å and $c = -3.99, z_0 = 1.68$ Å for the CMM results with $z_0 = d/2 + (z_0 - z_b)_{\text{jellium}}$ and $z_0 = z_b + (z_0 - z_b)_{\text{jellium}}$. That the z_0 values do not exactly match the parameters from Table 4.2 is a consequence of the fact that the image potential is first parametrized as a function of the averaged electron density, see Eq. (4.4) and Eq. (4.5).

We have also attempted to fit the image potential form to the WDA potential. Our first observation is that the WDA only closely follows the image potential decay in the intermediate region from the surface, for the W (111) surface roughly for $z \in [2, 4]$ Å. Further away, the decay of the potential becomes slower. In fact, in the middle of the vacuum (not shown in the figures), there is generally a potential well present. This is a consequence of numerical limitations that cause the electron density far in the vacuum region to approach a constant, low value. The WDA will thus start sampling a nearly homogeneous low density electron gas, and the potential accordingly approaches the Ps binding energy. Second, fitting the image potential to the WDA potential for W (111) in the region $z \in [2, 4]$ Å yields $c = -1.43, z_0 = -0.42$ Å and $c = -1.57, z_0 = -0.38$ Å, with $Q = 1.00$ and $Q = Q_{\text{opt}}$, respectively. Hence, as is also clear from the blue and pink curves in Fig. 4.7, the decay of the WDA potential is significantly slower than the exact limit for a perfect metal. Additionally, the reference plane is placed behind the first row of atoms[9]. Physically, we expect, however, that the screening charge is concentrated in front of the first row of atoms.

The wrong c coefficient has been found in studies of the WDA in the context of electron-electron exchange and correlation as well. According to Refs. [112, 113], this can be attributed to the fact that the pair correlation function used in the WDA is spherically symmetric. This assumption is justified for a particle in the bulk of a material. However, when the particle resides in the vacuum region, the screening cloud strongly deforms, which cannot be described appropriately by the spherically symmetric pair correlation function. These arguments are quite general and likely apply to the electron-positron WDA as well. Ref. [112] found that by allowing anisotropic scaling of the screening cloud,

---

[9] The location of the reference plane can be estimate from Fig. 4.7 by extrapolating the $1/z$ dependence of the potential in the direction of the surface and looking for the location where it diverges.

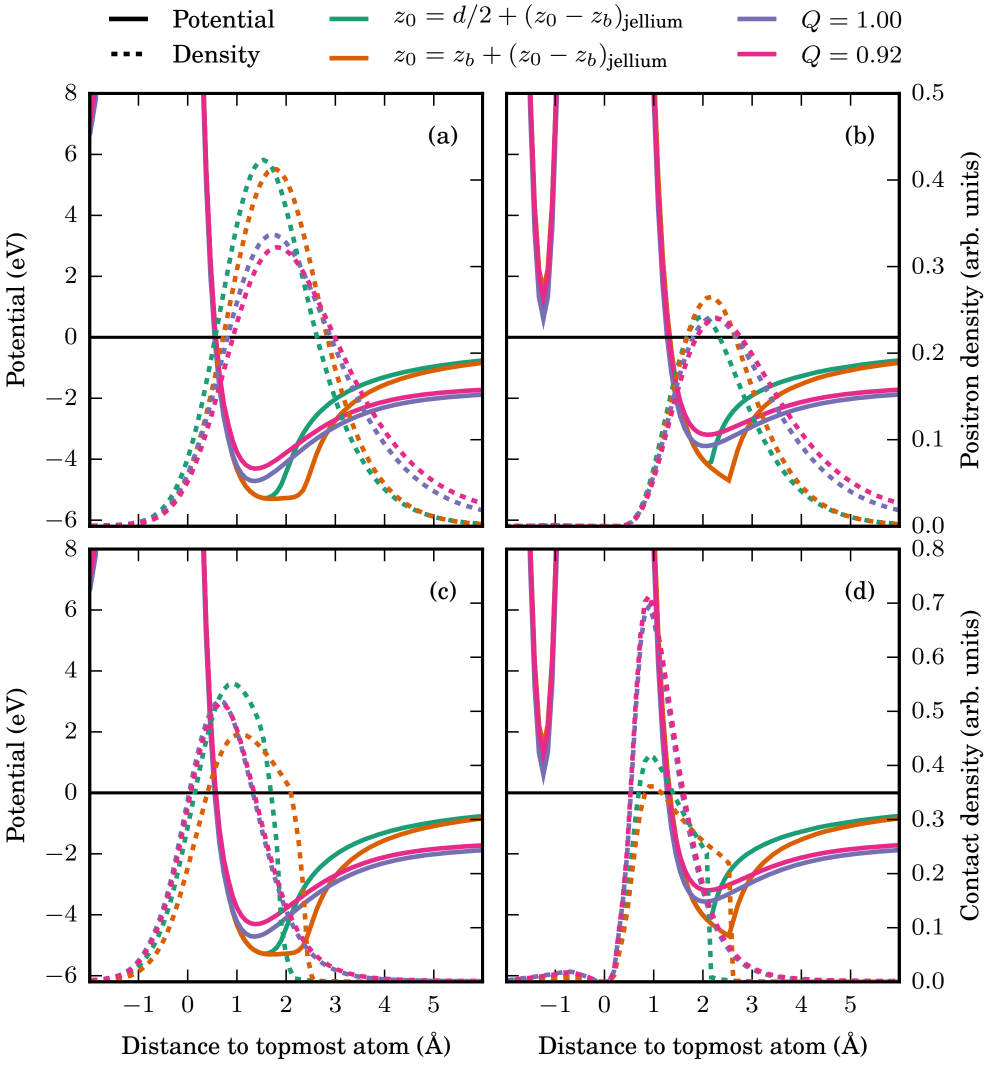

Figure 4.7: Positron total potentials, densities and electron-positron contact densities for the W (111) surface. Panel (a) shows laterally averaged potentials (full lines) and positron groundstate densities (dashed lines). In panel (c) the density is replaced by the laterally averaged contact density, obtained by multiplying the groundstate electron and positron densities including the enhancement factor. Panels (b) and (d) show the same as panels (a) and (c), respectively, but now for a cut through the quantities instead of the average. The cut is taken at the position of the topmost W ion in the plane of the surface. Green and orange lines show CMM results, with z_0 as indicated in the legend, and blue and pink lines WDA results with specific values for the screening parameter Q, also displayed in the legend.

the correct constant $c = 4$ can be obtained in the WDA.

4.5.2 Densities

We now examine the positron densities obtained with the CMM and the WDA, displayed in the dashed lines in Fig. 4.7(a) and (b). From panel (b), we note that positron densities in the CMM (green and orange lines) are peaked close to the transition point between the LDA and image potential. Hence, it is expected that the potential in the vicinity of this point, which is presumably the least accurate region, has a non-negligible influence on the calculated binding energies. The slow decay of the WDA potential in the vacuum region makes that the calculated positron states are less confined in the well close to the surface compared to the CMM results. From Fig. 4.7(a) we see that $> 50\%$ of the density is located in the region where the potential decays as $\sim 1/z$. Hence, this part of the potential has an important effect on the predicted binding energy. From the previous section, we know, however, that the decay of the potential in the WDA is incorrect. We can thus not attribute the good agreement of the WDA binding energy with experiment to a proper description of the potential. Instead, they likely follow from a cancellation of errors, and the results for Cu in Fig. 4.6 show that the cancellation is certainly not a general trend.

One qualitative shortcoming of the CMM is solved by the WDA, though. Panels (c) and (d) show the contact densities obtained in both models. The dashed green and orange lines in panel (d) illustrate the discontinuity in the contact density when the LDA enhancement is replaced by the IPM for $z > z_0$. On the other hand, from the slow decay of the LDA contact density right before z_0, we can appreciate that the decay is really too slow in the LDA and roughly follows the decay of the positron density itself, i.e. disregarding the rapid decay of the electron density in the vacuum. This is because the positron always attracts an electron density close to the Ps density in the LDA. The WDA contact densities (pink and blue dashed lines) on the other hand decay smoothly and significantly faster than the LDA. Qualitatively at least, this seems to better represent the detachment of the screening cloud when the positron resides in the vacuum[10].

Quantitative comparison of the contact densities with experiment is difficult as we are only aware of one experimental result, namely $\tau = 580 \pm 10$ ps for the Al (011) surface [17]. Our calculated results are compared with experiment in Table 4.5, which shows that the best result is obtained in the CMM with $z_0 = z_b$. The WDA gives worse lifetimes, though we note that the relative differences in the contact densities are actually comparable to the CMM results with $z_0 = z_b + (z_0 - z_b)_{\text{jellium}}$ and $z_0 = d/2 + (z_0 - z_b)_{\text{jellium}}$. Overall, we see that the CMM results underestimate the lifetime, even though the enhancement factor is abruptly set to unity when the image potential is imposed. This indicates that the LDA enhancement is already overestimated for $z < z_0$. The WDA thus qualitatively improves on this point, as it yields a contact density which is more localized to the surface[11]. On the other hand, the WDA significantly underestimates the total contact density. One reason might be the (too) slow decay of the positron state in the vacuum, which lowers the electron-positron overlap. Of course this one experimental result does not permit us to draw general conclusions.

---

[10] Note that all densities shown in Fig. 4.7 have been normalized to unity. The actual contact densities in the WDA are smaller than in the CMM, as reflected by the calculated lifetimes in Table 4.4 and Table 4.2

[11] We do not show the positron state for Al (011) here, though the same conclusions can be drawn as for the W (111) surface. In fact, all surface states studied in this chapter look very similar.

	CMM			WDA	
	$z_0 = 1.26$ Å	$z_0 = 2.08$ Å	$z_0 = 1.53$ Å	$Q = 1.00$	$Q = 1.02$
$(\Delta\tau)_{\rm abs}$	-33 ps	-68 ps	-51 ps	93 ps	71 ps
$(\Delta\lambda_a)_{\rm rel}$	0.06	0.13	0.10	-0.14	-0.11

Table 4.5: Comparison of calculated lifetimes and annihilation rates for Al (011) with the experimental results $\tau = 580 \pm 10$ ps from Ref. [17]. Lifetimes differences are calculated as $(\Delta\tau)_{\rm abs} = \tau - \tau_{\rm exp}$, differences in the corresponding annihilation rates are given as relative differences $(\Delta\lambda_a)_{\rm rel} = (\lambda_a - \lambda_{a,\rm exp})/\lambda_{a,\rm exp}$. The CMM results use the image potential references planes set by $z_0 = z_b$, $z_0 = z_b + (z_0 - z_b)_{\rm jellium}$ and $z_0 = d/2 + (z_0 - z_b)_{\rm jellium}$ in that order.

4.6 Conclusions and Outlook

In this chapter, we presented the theory of the CMM. An important parameter in this model is the image potential reference plane z_0, which is difficult to calculate directly using modern first-principles electronic structure packages. Hence, we used three approximations to determine the location of the reference plane (taking $z = 0$ at the topmost atomic position): (i) $z_0 = z_b$, with z_b the point where the self-consistent electron density starts decaying exponentially, (ii) $z_0 = z_b + (z_0 - z_b)_{\rm jellium}$ where $(z_0 - z_b)_{\rm jellium}$ is the offset of the reference plane calculated for a jellium model, measured with respect to the jellium edge [105, 108], and (iii) $z_0 = d/2 + (z_0 - z_b)_{\rm jellium}$ where the $d/2$ is half the spacing between subsequent atomic planes along the normal to the surface.

To assess the accuracy of the correlation energy in bulk materials, we compared calculated positron workfunctions, using the LDA and WDA, with experiments. Our results showed that the LDA results are generally in very good agreement with experiment. In the WDA, most of the results are worse. Notably, we found that in the Q tuning scheme from Sec. 3.3.4, raising Q increases the correlation energy as it directly controls the total amount of charge the positron interacts with. For Cu, for instance, this leads to a severe overestimation of the correlation energy in bulk.

For surface binding energies, we found that, of the investigated approximations for the image potential reference plane, setting $z_0 = d/2 + (z_0 - z_b)_{\rm jellium}$ consistently compares best with experiment. In fact, for all surfaces considered in this chapter, this method yields binding energies with errors < 0.2 eV. The WDA results are somewhat worse, but still acceptable for Al and W. Notably, using $Q = 1.00$ we obtained better results than $Q = Q_{\rm opt}$ from Table 3.2. For Cu, we found that $Q = 1.00$ significantly underestimates binding to the surface, and $Q_{\rm opt}$ serverely overestimates the binding energy. This illustrates that fitting Q to reproduce experimental bulk lifetimes in general does not improve correlation energies. In fact, our results show that $Q = 1.00$ might in general give better results for binding energies at the surface.

Next, we evaluated some qualitative features of both the CMM and the WDA. The most import shortcomings in the CMM are (i) the transition region of the bulk LDA potential to the image potential, and (ii) the enhancement factor in the near-surface and vacuum region. For point (i), we saw that the potential's derivative shows a significant discontinuity, and as a consequence we can expect that this region is not very accurately described. At the same time, the positron density is peaked near the transition point between the LDA and image potential. This likely has some effect on the accuracy of calculated binding energies. For the enhancement factor, we discussed that the LDA overestimates the contact density, and thus the annihilation rate, by incorrectly imposing Ps formation in the vacuum. Setting the enhancement to unity wherever the image potential is imposed improves the situation somewhat, but leads to discontinuity in the contact density. Furthermore, our result for Al (011) seems to suggest that even then the enhancement is still overestimated. In the WDA, we showed that both the potential and enhancement factor are continuous across the vacuum interface, which is a qualitative improvement over the CMM. On the other hand, we showed that, even though the potential decays as $\sim 1/z$, the expected image potential is not accurately reproduced. Notably, the potential decays too slowly, which results in positron states that extend too far in the vacuum. This has an important effect on calculated binding energies, and good agreement with experiment for some materials has to be attributed to cancellation effects rather than an accurate description of the overall potential. Next, the image potential reference plane for W (111) was found to lie behind the first row of atoms inside the material. This observation does not correspond with the assumed physical picture that the screening cloud is concentrated at the surface. As for the electron-positron contact density, we found that at least qualitatively there is an improvement. Indeed, the WDA predicts a contact density located closer to the surface than in the CMM. On the other hand, the lifetime for Al (011) is overestimated, which we attributed to the slow decay of the positron state in the vacuum.

From the results presented in this chapter, it is clear that further work is required to arrive at a widely applicable, reliable model to describe positron surface states. For elemental materials with simple surface geometries, the CMM model has proven to yield the best surface binding energies when setting $z_0 = d/2 + (z_0 - z_b)_{\text{jellium}}$. It is difficult to say, however, if this simple approach is as effective for more complex materials. Hence, a method to directly calculate the value of z_0, that is applicable with periodic boundary conditions, is desirable. We note, though, that even if we can obtain an exact value for z_0, the problem with the enhancement factor in the vacuum region remains. Complex surface geometries also lie outside the capabilities of the model.

The WDA shows potential to improve on these points, but further work is required to ensure that (i) both lifetimes and correlation energies are accurately described simultaneously, and (ii) the correct constant in the image potential is reproduced. Both are ultimately a consequence of the crude approximation of the pair correlation function used in the WDA. Point (i) is caused by neglecting the screening properties of individual electron states and instead treating all of them as free electrons. Point (ii) is, according to Ref. [112], caused by the imposed spherical symmetry of the electron enhancement, and anisotropic scaling of the screening cloud is required to reproduce the correct constant [112, 113]. We expect that many of these issues can be solved by replacing the approximate pair correlation function for the homogeneous electron gas by one that is directly calculated from the electronic structure of the material. Indeed, such a pair correlation function is expected to include the screening properties of the electron states, and does not impose a shape approximation for the screening cloud.

4.A Details of the electronic structure calculations

Electronic groundstate calculations are performed using the PAW [85] method as implemented in VASP [86–88]. Electron exchange and correlation effect are described with the PBE functional [65]. Parameters in the calculations were checked for convergence of the positron annihilation lifetimes within 1 ps. A vacuum width of 15 Å was found to be sufficient for all quantities of interest in this chapter. Experimental lattice parameters [89] were used for all considered surfaces. In the relaxation the middlemost atoms were fixed to their bulk locations, and atoms close to the surface were allowed to relax until forces on the atoms were converged to within 0.01 eV/Å. Valence electrons taken as valence for the different considered elements can be found in table 3.3.

4.B Details of the positron calculations

Positron lifetime calculations were performed with the MIKA/doppler package [92], and follow the details given in Sec. 3.B.1. The Drummond LDA [56] was used in the bulk of the unit cell in conjunction with the CMM discussed in Sec. 4.3. Calculations with the WDA use the shell partitioning discussed in Sec. 3.3.3. Details of the Q-value tuning can be found in Sec. 3.3.4.

4.C Determination of the background edge

The background edge in the CMM calculations, is determined by the point where the exponential decay of the electron density sets in. To determine this value, we fit a line to the logarithm of the laterally averaged electron density, and look for the point where the relative difference between the fit and the density becomes larger than a threshold value. For the calculations reported in this chapter, we selected a threshold value of 0.1.

In practice, the electron density saturates far in the vacuum region to a small value due to numerical limitations. Thus, the decay of the density is only exponential in the intermediate range from the surface and we select a window outside the surface for the fit. The choice of this window influences the obtained result for z_b. To obtain an estimate of the involved uncertainty, we first select a window for the fit in the vacuum where the decay of the electron density is close to exponential, and subsequently repeat the fitting procedure in which we shrink the window symmetrically. The reported values for z_b in this chapter are the average value for z_b obtained by the fits, and the lower and upper bounds are, respectively, the smallest and largest value for z_b obtained from the different fits.

Chapter 5

Positron surface state and spin-texture of Bi_2Te_2Se

In this chapter we show that PAS can be used to investigate the spin-texture associated with the surface states of TIs. After a short motivation for this work, we describe the experiments on the prototypical 3D TI Bi_2Te_2Se, performed at the University of Texas at Arlington by the group of A. Weiss, which showed compelling evidence for the existence of positron surface states. We provide theoretical support for these observations by obtaining close agreement with experiment. Afterwards we show that the positron state has sufficient overlap with the edge states of the TI to expect a significant signal in the annihilation radiation originating from them. Finally, we show they indeed leave a clear fingerprint in the electron-positron momentum density, and that it should be possible to measure the spin-texture associated with them using spin-polarized positron experiments. The results in this chapter have been published in Ref. [42].

5.1 Introduction

5.1.1 Topological insulators

We first provide a short description of TIs and what properties we want to investigate. Our discussion of TIs here is very limited, and we refer the interested reader to review papers for a thorough discussion of the matter [114, 115].

Concisely, a TI is a material that behaves as an ordinary insulator in the interior of the material, but hosts conductive states at its surface (or edge) that are topologically protected. In the rest of this chapter, we will refer to these conductive states also as edge, Dirac or topological states. The interest in TIs stems from the special properties of the edge states.

A first remarkable property is that the existence of such edge states is unaffected by imperfections in the lattice such as (non-magnetic) impurities. Indeed, the origin of the states lies in what is called a 'band inversion' in the bulk of the material, in which the normal ordering of the (atomic) energy levels in vacuum gets inverted due to a combination of chemical bonding, the crystal potential, and spin-orbit coupling. The normal ordering has to be restored when transitioning from the bulk of the material to the vacuum, and can only occur when a band passes through the bulk band gap [114, 116]. In this chapter, we study the prototypical TI Bi_2Te_2Se, which consists of a stacking

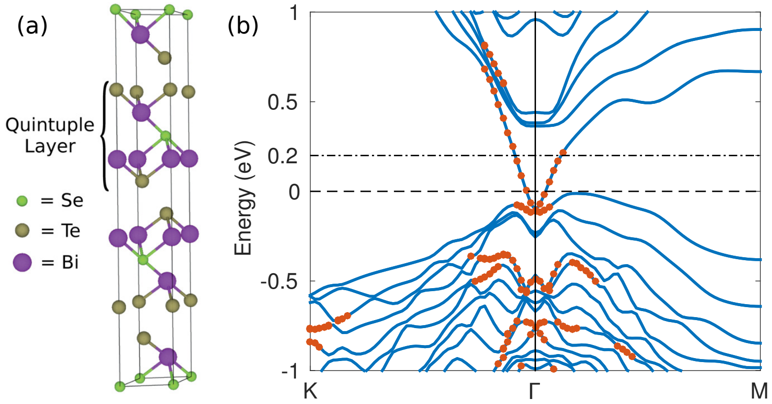

Figure 5.1: (a) Hexagonal bulk unit cell of Bi_2Te_2Se, which consists of a stacking of QL, as indicated in the figure. Inside each QL, the atoms form strong covalent bonds, whereas separate QLs are held together by weak Van der Waals forces. (b) Bandstructure calculated for a Bi_2Te_2Se slab consisting of four stacked QLs. The Fermi level is set at 0 eV. Red dots indicate states located close to the surface. More precisely, they have a density that is at least 40% located in the outermost QLs at the top and bottom of the slab.

of covalently bonded Te-Bi-Se-Bi-Te Quintuple Layers (QLs) held together by weak Van der Waals forces. In this material, the topological states show up in the surface band structure as a cone with an approximately linear dispersion, i.e. a Dirac cone, centered around the Γ-point in the (First) Brillouin Zone (BZ). This is shown in Fig. 5.1(b), where surface states are identified by the red dots.

A second special property relevant to our study is the spin-momentum locking of the edge states, due to the spin-orbit coupling: The spin of the states located on the Dirac cone around the Γ point are oriented perpendicular to their crystal momentum **k**. A consequence thereof is the suppression of backscattering of the edge states [117]. Indeed, in absence of magnetic impurities, clockwise or anti-clockwise rotation of the electron's spin in the scattering process is equally likely, and due to the fermionic nature of the particles, these two states interfere destructively.

5.1.2 Motivation

In this chapter, we demonstrate that positrons provide a highly surface-sensitive probe for the topological Dirac states. Since PAS techniques, with measurements of the 2D-ACAR in particular, are well suited to measure both the low- and the high-momentum components of the annihilating electronic states without complication of matrix element effects, they can provide useful information on the Dirac state orbitals. Additionally, our calculations will show that spin-polarized positron beams can resolve the spin textures associated with the topological states, owing to the predominant annihilation between electron-positron pairs with opposite spins [43].

The matrix element effects mentioned in the previous paragraph are important in, e.g., photoemission experiments, where it is required that the initial and final electron state have a net angular momentum difference of 1, due to the angular momentum carried by the absorbed photon. In some cases, this can render certain states 'invisible' to the experiment, as certain transitions are forbidden by fundamental conservation rules.

Furthermore, spin-orbit effects have been shown to significantly distort the observed photoelectron's properties compared to the quasi-particle excitations of the material [39, 118, 119]. Similar limitations apply to many other frequently used spectroscopy methods. PAS does not suffer from such final state effects since the final photon states form a continuum, and can safely be summed over. This is in fact always assumed in the calculation of electron-positron annihilation properties[1].

5.1.3 Overview

In Sec. 5.2, we present the experimental evidence for the existence of a bound positron state at the surface of the TI Bi_2Te_2Se. The experiments furthermore provide the energy of the state [120]. In Sec. 5.3, we show that the theory confirms the experimental interpretation with a binding energy of the positron state close to the experimental result. The calculations predict a significant overlap between the positron and the topological states. We also demonstrate that spin-polarized positron measurements can reveal the spin structure at the surface. Technical details concerning the calculations can be found in the appendices at the end of the chapter.

5.2 Experiments

Three distinct experiments have been performed on Bi_2Te_2Se, which point convincingly in the direction of a bound state at the surface of the sample. The PAES and AMPS experiments both point directly to the presence of a positron state. The last experiment provides less direct evidence as it deals with Ps rather than (bare) positron states. Nevertheless, the results of the experiment are useful to estimate the positron binding energy, and therefore will be discussed as well. Modelling Ps states will not be undertaken here as it lies outside the scope of this thesis, but has been discussed at length elsewhere [42, 121]. Details related to the sample preparation and experimental setup are left out in the present discussion, but can be found in Refs. [42, 120].

5.2.1 Positron annihilation induced Auger emission

Positrons annihilate predominantly with the valence electrons but the small fraction that annihilates with core electrons produces highly unstable core holes, which are filled via an Auger process. Therefore, if positrons annihilate in a surface state, PAES provides a method to determine the composition of the surface, free from a secondary electron background [7]. A schematic of the process is drawn in Fig. 5.2(a).

Results of PAES experiments from the TI Bi_2Te_2Se surface are shown in Fig. 5.2(b) where signals from Bi, Te, Se, C, and O can be identified; the latter two are caused by the presence of a small concentration of contaminants adsorbed on the surface [120]. These results reveal the presence of a bound positron surface state. Were this not the case, positrons would either get trapped between the slabs of QLs of the material or would be reemitted before they annihilate. Since the thickness of one QL is about $10,\text{Å}$, which corresponds roughly to the mean free path of a $60,\text{eV}$ electron, any Auger signal coming from below the first QL is too weak to be detected. Thus, the fact that the annihilation

---

[1] The summation over the final states is already contained in the pair-annihilation rate for an isolated electron-positron pair, Eq. (2.9). Since this expression lies at the basis of expressions for electron-positron annihilation properties, the final state summation is contained in the standard expressions for the electron-positron momentum density and positron annihilation lifetime.

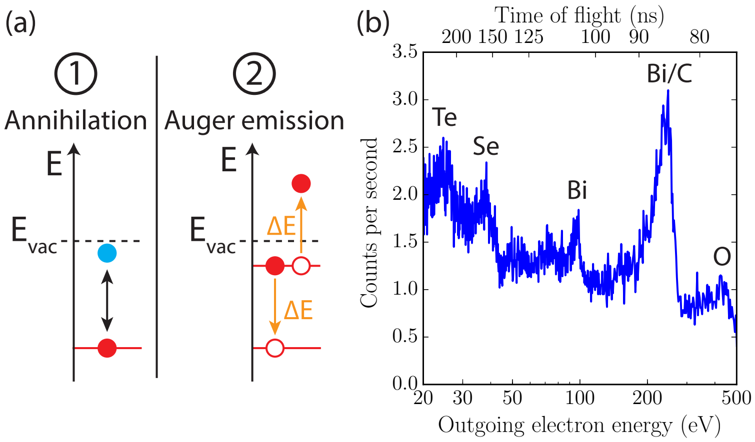

Figure 5.2: (a) Schematic of the PAES mechanism. In the first step, a positron (blue) annihilates with an electron (red) occupying a core level and creates a highly unstable hole. In the second step, an electron from a higher level fills this hole and transfers the energy difference between the two levels to a second electron. If the energy difference is sufficiently large and the second electron is close enough to the surface, it can traverse the surface dipole and escape from the sample. The measured outgoing electron energy corresponds to the transferred energy in the Auger process minus the energy difference between the second electron's state and the vacuum level. (b) Results of the PAES measurements on the Bi_2Te_2Se sample in which Auger signals from the different elements are indicated.

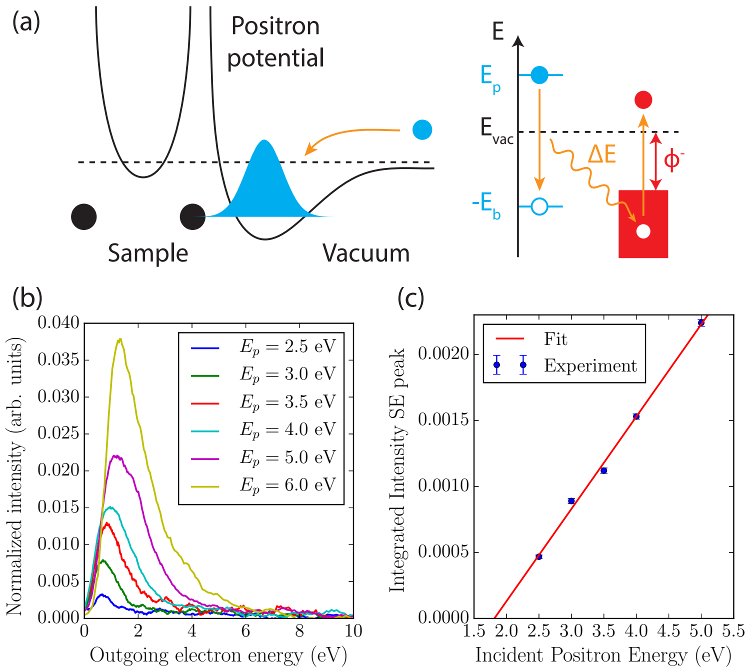

Figure 5.3: (a) Schematic of the AMPS mechanism. The left part of the diagram shows the incident positron (blue) that drops in the image potential well. In this process, the positron transfers an energy ΔE, determined by the incident kinetic energy E_p and the binding energy of the surface state E_b, to an electron of the system through a virtual photon as indicated in the right part of the figure. If the energy difference is larger than the electronic work function ϕ^-, the electron can escape to the vacuum. (b) The measured low-energy Auger signals for the Bi_2Te_2Se sample. The outgoing electron energy is determined by the transferred energy ΔE minus the required energy to escape from the sample. The different lines show the result for varying energies of the incident positron. (c) The integrated peak amplitudes of the low-energy Auger signal associated with the AMPS mechanism as a function of the incident positron energy.

induced Auger peak intensities are observable provides strong evidence that the positron is in a state localized at the surface at the time it annihilates.

5.2.2 Auger mediated positron sticking

AMPS experiments provide an independent proof for the existence of the positron surface state and allow us to determine its binding energy [5]. In the AMPS mechanism, the excess energy from a positron dropping into the image potential well is transferred to a valence electron. This can result in the emission of an Auger electron if the energy difference between the positron's final and initial state, determined by the incident positron's kinetic energy, is larger than the electron work function [5]. The maximum kinetic energy of the Auger electrons is then given by $E_{\max} = E_p + E_b - \phi^-$, where E_p is the energy of the incident positron, E_b is the binding energy of the positron surface state, and ϕ^- is the electron workfunction. Figure 5.3(a) illustrates the AMPS mechanism schematically.

The observed increase in amplitude of the Auger signal at low energies as the energy of the incident positrons is increased is shown in Fig. 5.3(b), and it confirms the presence of the surface state. Knowing the electron workfunction, the binding energy of the surface state can be determined from the positron energy threshold value for Auger electron emission: $E_{\text{Th}} = E_p$ for which $E_{\max} = 0$, i.e.

$$E_b = \phi^e - E_{\text{Th}} \tag{5.1}$$

The linear fit shown in Fig. 5.3(c) yields $E_{\text{Th}} = 1.8$ eV. Our calculations give a workfunction of $\phi^e = 4.9$ eV, which then results in a binding energy for the positron surface state of $E_b = \phi^e - E_{\text{Th}} = 3.1$ eV.

We note that the value of the electron workfunction can be influenced significantly by the presence of adatoms on the surface. In fact, from the PAES experiment, we know there is a significant amount of O and C present at the sample's surface. Hence, our estimate for the positron binding energy in this section is somewhat uncertain. In the next section we will show that, by combining the results of the AMPS and Ps desorption experiments, we can obtain an estimate for the positron binding energy that does not depend on the value of the electron workfunction.

5.2.3 Positronium desorption

In the third experiment, Ps desorption from the surface was monitored by heating the sample. The idea behind such experiments is that spontaneous emission, i.e. at $T = 0$ K, of Ps is generally forbidden. Indeed, energy should be conserved when a positron and an electron are brought from the sample to the vacuum in a bound Ps state: $E_b + E_e = E_{b,\text{Ps}} + E_{k,\text{Ps}}$. Here, $E_{b,\text{Ps}} = 6.80$ eV is the Ps binding energy, and $E_{k,\text{Ps}} > 0$ its kinetic energy. At absolute zero, the minimal binding energy of an electron E_e is equal to the electron workfunction, and generally $E_b + \phi^e < 6.80$ eV. By heating the sample, however, we can populate excited electrons states and enhance Ps emission. The minimal required excitation energy for the electrons for Ps desorption to be possible ($E_{k,\text{Ps}} = 0$) is called the activation energy E_a, and is determined by the relation

$$E_b + (\phi^e - E_a) = 6.80 \text{ eV}. \tag{5.2}$$

Combining the above with Eq. (5.1) to eliminate the electronic workfunction gives the binding energy in terms of the measured values

$$E_b = \frac{1}{2}\left(E_a - E_{\text{Th}} + 6.80 \text{ eV}\right). \tag{5.3}$$

Using the activation energy $E_a = 0.4$ eV determined from the Ps-desorption experiment [120] along with the threshold value from the AMPS experiment, an estimated binding energy of $E_b = 2.7 \pm 0.2$ eV for the positron surface state is obtained. Working backwards, we find that this corresponds with an electronic workfunction of $\phi^e = 4.5$ eV. Since the workfunction of materials can change significantly due to the presence of contaminants at the surface, this derived value seems quite reasonable. In the rest of this chapter, we will also take $E_b = 2.7 \pm 0.2$ eV as the experimental value for the positron binding energy, as it does not rely on any theoretical input.

5.3 Results of the calculations

The experiments discussed in the previous section provide convincing evidence for the existence of a positron state at the Bi_2Te_2Se surface, with a binding energy of $E_b =$

2.7 ± 0.2 eV. In this section we discuss the results of our first-principles calculations. As a first step, we show that the calculated positron groundstate is indeed located at the surface of the material and that its binding energy is close to experiment. Next, we demonstrate that there is sufficient overlap between the positron state and the topological states to expect that PAS experiments can pick up a significant signal from the Dirac states. Finally, we calculate the electron-positron momentum density and find that 2D-ACAR experiments should be able to distinguish the topological states in this system, and furthermore resolve the spin-texture associated with them.

5.3.1 Positron state

We start our discussion with the positron state to establish that they support the interpretation put forward by the experiment. Fig. 5.4(a) shows the averaged positron density at the Bi_2Te_2Se surface as the blue curve, calculated using the CMM model of which the details are presented in Appendix 5.A.2. Our first observation is that the positron in its ground state indeed resides at the surface, due to the image potential well, rather than the gaps in between the QLs, which also act as strong positron traps. This observation is by itself sufficient to support the PAES experiment.

Next, we obtain the binding energy of the positron by taking the difference between the vacuum level and the positron's chemical potential. The vacuum level is determined in the usual way by the taking the value of the Hartree potential in the middle of the vacuum region. We find that the positron surface state has a binding energy of $E_b = 2.69$ eV, in excellent agreement with the measured value[2].

5.3.2 Overlap with Topological states

Now that the calculations confirmed the existence of the bound positron surface state, we turn to the question of the extent to which this surface state overlaps with the Dirac cone electrons. This overlap is of central importance because it determines the annihilation rate of the positron with the electrons occupying the topological states and thus the sensitivity with which PAS can probe the Dirac states.

The computed densities of the positron surface state, ρ^p, and the topological Dirac states ρ^e_{Dirac} are shown in Fig. 5.4. The density of the topological states is obtained by summing the one-particle densities for all states on the cone between the Dirac point, i.e. the apex of the Dirac cone, and the specified value for the electron chemical potential μ^e indicated in the legend of the figure. Note from Fig. 5.4 that even though the Dirac states are commonly referred to as protected surface states, they are not confined to a thin layer at the surface but instead over the first few QLs below the surface. Although the positron is seen to probe only the topmost atomic layers of the material, it still penetrates the material sufficiently to have a significant overlap with the Dirac states[3]. Moreover, the left panel of Fig. 5.4 shows that the overlap with the Dirac states changes sensitively depending on the population of the Dirac states near the Fermi level. Our calculations of the momentum density, discussed below, demonstrate that this underlying overlap

---

[2] This value is obtained with the CMM with the image potential reference plane set to the background edge $z_0 = z_b$. The results of the CMM where z_0 is determined with the Lang-Kohn method yields $E_b = 3.91$ eV, and the WDA, with $Q = 1.0$ yields $E_b = 3.13$ eV. More details are provided in Appendix 5.A.2. The results in the rest of the chapter are obtained using the positron state for which we reported the binding energy in the text.

[3] Note that the one-dimensional averages shown in Fig. 5.4(a) exagerate the overlap. Indeed, Fig. 5.4(b) shows that the density related to the topological states (red isosurfaces) mostly located around the ions, whereas the positron density (blue isosurfaces) resides mostly in the interstitial regions.

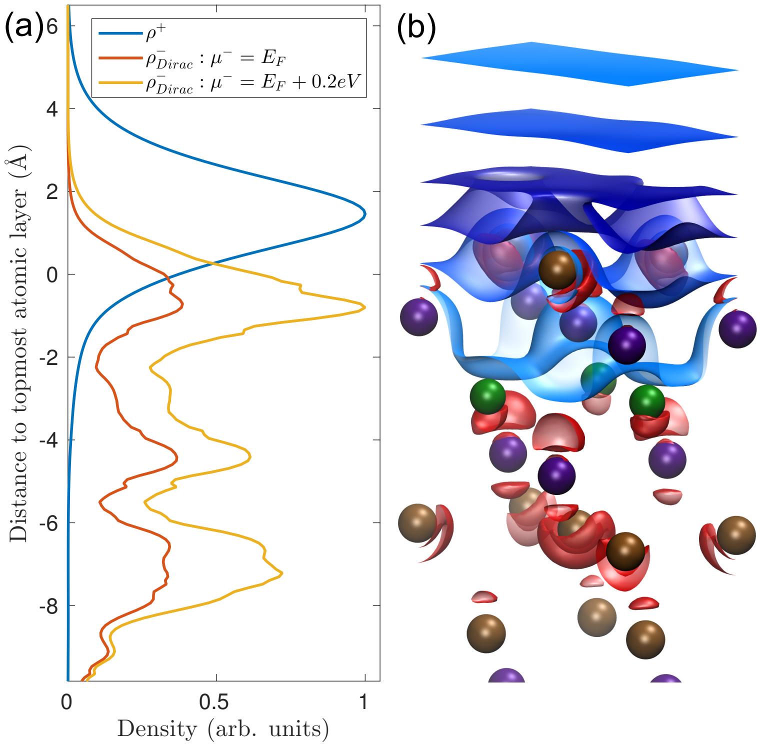

Figure 5.4: Overlap of the positron surface state with the Dirac states. (a) Planar average of the positron (blue) and electron (red/yellow) densities associated with the Dirac states below the Fermi energy for two different values of the chemical potential μ^-. (b) Density of the topological surface state and the positron in the same spatial region as panel (a). The progressively lighter blue isosurfaces show the positron density at 80%, 20%, and 2% of the maximum value, respectively, and the red isosurfaces show the electronic charge density associated with the electron states on the Dirac cone below the Fermi-level at 10% of the maximum value. The Bi, Te, and Se atoms are shown in purple, brown, and green colors, respectively.

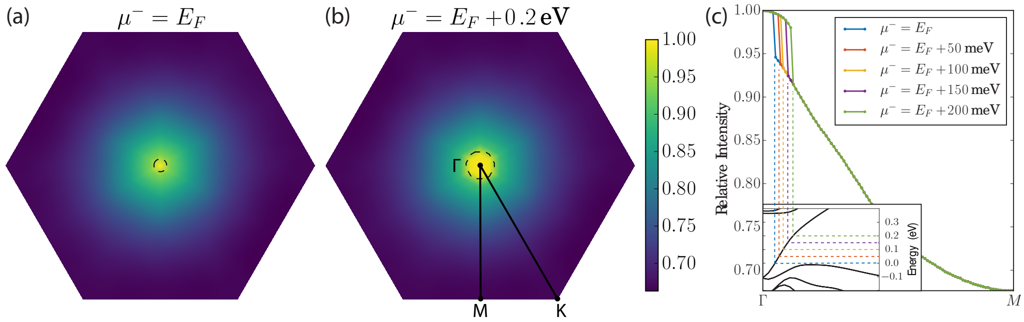

Figure 5.5: Calculated momentum densities. (a) LCW-map with the chemical potential located at the Fermi level. (b) LCW-map with the chemical potential raised by 0.2 eV. The dashed lines denote the location of the Fermi-surface as derived from the electronic band structure. (c) High resolution cuts through the LCW-map along the $\Gamma - M$ direction for different values of the chemical potential. The inset shows the band structure near the Fermi level ($E_F = 0.0$ eV).

translates into a clear signal coming from the annihilation of the positron with the Dirac fermions.

5.3.3 Electron-positron momentum density

We now investigate the fingerprint the topological states leave in 2D-ACAR spectra, and importantly whether the signal is strong enough to distinguish it from annihilation with other electrons from the sample.

A partially filled energy band when it crosses the Fermi energy gives rise to a break in the electron momentum density, which is the basis of the measurement of Fermi surfaces in materials via 2D-ACAR experiments. The Lock-Crisp-West (LCW)-map enhances this signal by folding all the higher momentum contributions into the first Brillouin zone [122], as detailed in the Appendix of this chapter. Figure 5.5 shows the calculated LCW-map together with a cut along $\Gamma - M$ over a range of values of the electron chemical potential, which simulates different doping levels of the Dirac cone. The evolution of the plateau around the Γ-point clearly indicates the sensitivity of the positron to the Dirac cone states. The relative drop in intensity between $5\% - 7\%$ at the Fermi momentum compares favourably with, for example, the 1% drop found for the $Nd_{2-x}Ce_xCuO_{4-\delta}$ high-T_c superconductor in which 2D-ACAR experiments have been shown previously to be viable in detecting Fermi surface sheets due to Cu-O planes [123, 124].

A topic which has drawn considerable interest in the case of topological insulators is the spin-momentum locking of the topological states. Measurements using spin-polarized positron beams exploit the fact that a two-photon decay is only possible between electrons and positrons with opposite spins [43]. This fact was exploited in pioneering 2D-ACAR experiments to provide direct evidence for the half-metallic character of the band structure of NiMnSb [125]. In recent work, spin-effects in the electronic structure of simple ferromagnets were observed using differences between the DBAR measured with positrons aligned parallel and antiparallel to a polarizing magnetic field. [126]. In a similar 2D-ACAR experiment, Weber *et al.* [44] successfully resolved the spin-dependent Fermi surface of the ferromagnetic Heusler compound Cu_2MnAl. This motivates us to investigate whether spin-polarized positrons can be used to detect the spin structure of the topological states at the surface.

The signal from the Dirac cone can be extracted from the LCW map by taking the difference between the signal obtained at different electron doping levels[4] In Fig. 5.6, we show the results obtained by taking the difference between the LCW-maps obtained with $\mu^e = E_F + 0.2\,\text{eV}$ and $\mu^e = E_F$ in the vicinity of the Γ-point. As expected, we see the plateau due to the extra occupation of the cone in the total amplitude. Our results for the magnetization along the x- and y-directions, agree well with the results obtained in several studies of various tetradymite TIs [127–130], which all predict a clockwise rotation of the spin. We see that the z-component of the magnetization increases gradually away from the Γ-point. This out-of-plane component develops due to the hexagonal warping of the Dirac cone as pointed out in Ref. [131]. We note that the difference in amplitude for the magnetic components is quite pronounced with regard to the Fermi-surface signal. Indeed, we find that the signal from the magnetization is about half that of the Fermi-surface signal obtainable with an unpolarized beam. This means that the magnetization signal still constitutes a promising $2\% - 4\%$ of the total signal. We note, though, that in real experiments, positron beams are not perfectly polarized as we have assumed in our calculations. Thus, in experiment, a proper weighting has to be performed which will lead to a smaller signal.

5.4 Conclusion and Outlook

Our study establishes the existence of a positron surface state near the topological insulator Bi_2Te_2Se. The results of our calculations show that this surface state can be exploited as a spectroscopic characterization tool for probing surfaces of topological materials. Since a significant fraction of positrons annihilate with electrons occupying Dirac cone states, 2D-ACAR experiments should be able to measure their momentum distribution with high precision [132], and thus obtain information concerning the nature of the Dirac states which is complementary to that accessed through angle-resolved photoemission, scanning tunneling and other surface-sensitive spectroscopies without the complications of related matrix element effects [38, 133, 134]. PAES and coincidence doppler broadening measurements can, in turn, be used to characterize the chemical composition of surfaces. In combination with 2D-ACAR experiments, these positron spectroscopies could be exploited to determine effects of various surface impurities on the topological states in addition to the role of bulk defects [135]. Now that our study identified a positron surface state, positron spectroscopies can prove valuable for the characterization of nanostructured topological insulators. Indeed, positrons have been shown to act as effective self-seeking probes for nanocrystal surfaces without requiring the preparation of single-crystal specimens [136], whereas the applicability of conventional spectroscopic techniques is limited. Finally, our calculations show that the spin textures of the Dirac states should be accessible through 2D-ACAR measurements using a spin-polarized positron beam since positrons predominantly annihilate with electrons of the opposite spin [43, 44, 126].

---

[4] In the ideal case one would do one measurement in which a large part of the Dirac cone is occupied, and a second measurement the chemical potential is as low as possible but such that all bulk bands remain occupied.

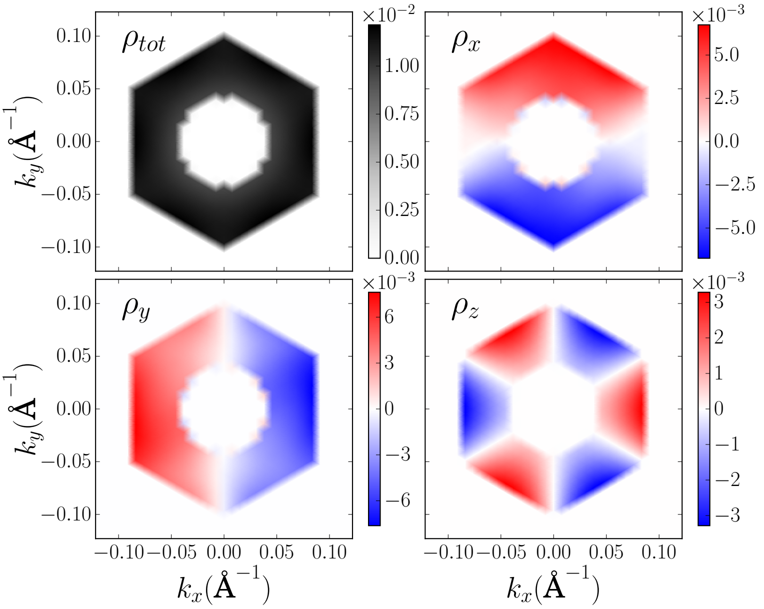

Figure 5.6: Difference between the LCW-maps obtained with different doping levels of the Dirac cone: $\mu^e = E_F + 0.2\,\text{eV}$ and $\mu^e = E_F$. The top left pane of the figure shows the total amplitude of the LCW-map. The top right, bottom left, and bottom right figures show the magnetization components along the x, y and z axes, respectively. We only show the result zoomed in around the Γ point as the difference between the LCW-maps is exactly zero in the rest of the Brillouin zone. The inner and othermost edges of the nonzero part in the plots correspond with the dashed lines shown in Figs. 5.5(a) and 5.5(b), respectively. The length of the reciprocal axes is $|\mathbf{b}| = 1.688\ \text{Å}^{-1}$ and the amplitudes are given in $\text{ps}^{-1}\text{Å}^2$. (It is readily seen that the units of the LCW-map are in $\text{ps}^{-1}\text{Å}^2$ by realizing that the integral over the LCW-map yields the positron's annihilation rate, or, in the case of the magnetic LCW-maps, the difference in annihilation rate between two measurements with opposite spin polarizations for the positron.)

5.A Computational details

The first-principles calculations carried out for this chapter are in line with the rest of the work: Since we consider a perfect surface, the positron will reside in a delocalized state, and the zero-positron-density limit of the 2CDFT applies [52, 53]. Hence, we can first calculate the electronic properties of the material, and once we obtain those, we proceed with the calculation the positron groundstate and related electron-positron annihilation properties. The rest of this appendix deals with the technical details of the calculations.

5.A.1 Electronic structure

The electronic ground state is obtained using the PAW method [85] as implemented in VASP [86–88]. Electron exchange-correlation effects are treated using the PBE functional [65], and spin-orbit coupling is included in the computations [137]. The kinetic energy cutoff for the plane-wave expansion of the wavefunctions is set at 275 eV. For the bulk calculations, we use the rhombohedral unit cell with a Γ-centered $11 \times 11 \times 11$ **k**-grid in combination with a Gaussian smearing of width 0.1 eV. In the surface calculations, we use a slab geometry with a vacuum of 15 Å to avoid spurious interactions between periodic images. Here, the calculations are performed with a Γ-centered **k**-grid with $11 \times 11 \times 1$ points in the hexagonal unit cell in combination with a Gaussian smearing of 0.1 eV.

We used the experimental lattice parameters in all our calculations. This because the distance between the QL blocks is severely overestimated when using the PBE functional. As positrons are strongly repelled by the ions, the separation between the QLs strongly influences the value of the positron workfunction and in order to obtain reliable results, we deem it appropriate to work with the experimental lattice parameters instead. The lattice parameters only slightly affect the electronic structure as the results of our bandstructure calculations agree very well with the previously reported first-principles results [129, 130, 138, 139] and those of ARPES measurements [140, 141].

5.A.2 Positron state

Positron calculations for this chapter are calculated in the zero-density limit of the 2CDFT. In the bulk part of the unit cell, the correlation potential is determined using the LDA parametrized by Drummond *et al.* [56]. The erroneous potential in the vacuum of the unit cell is corrected using the CMM [22]. Our recipe for this correction can be found in section 4.3.1. The image potential refence plane is approximated by background edge positions $z_0 = z_b$, for which we found $z_b = 1.25$ Å.

For completeness, we also mention here the results obtained following the Lang-Kohn method which sets $z_0 = d/2 + (z_0 - z_b)_{\text{jellium}}$. For the interplanar spacing d we considered the spacing between the QLs, and with $z_{\text{val, Bi}} = 5$, $z_{\text{val, Te}} = 6$ and $z_{\text{val, Se}} = 6$ to determine the effective electron density, we found $z_0 = 2.63$ Å. The resulting binding energy is $E_b = 3.91$ eV. The WDA with $Q = 1.00$ results in $E_b = 3.13$ eV. Note, though, that we only show results obtained from the CMM with $z_0 = 1.25$ Å in this chapter, which yields a binding energy of $E_b = 2.69$ eV.

5.A.3 Electron-positron momentum density

The electron-positron momentum density is calculated from Eq. (2.39), where the geminals are approximated by the product of the electron and positron orbitals with inclusion of the state-dependent enhancement factor (Eq. (2.93)). In the calculation of the state-dependent enhancement factors of Eq. (2.94), we do not set $\gamma(\mathbf{r}) = 1$ in the vacuum region where the image potential is imposed as suggested in Ref. [23]. This correction is mainly important in the calculation of positron annihilation lifetimes, and we expect it to be less important for momentum density calculations.

The high-momentum components of the wave functions are important to accurately calculate the electron-positron momentum density. It is thus necessary to use the all-electron wavefunctions in the above formulas instead of the soft pseudo wavefunctions, i.e., we explicitly perform the PAW transformation [85],

$$|\psi_j^e\rangle = |\tilde{\psi}_j^e\rangle + \sum_i \left(|\phi_i^e\rangle - |\tilde{\phi}_i^e\rangle\right) \langle\tilde{p}_i|\tilde{\psi}_j^e\rangle. \tag{5.4}$$

Here, $|\tilde{\psi}_j^e\rangle$ are the soft pseudowave functions, $\langle\tilde{p}_i|$ are the projectors and $|\phi_i^e\rangle$ and $|\tilde{\phi}_i^e\rangle$ are the localized all-electron and soft pseudo partial waves of the ions respectively. Details on how to performed this transformation can be found in Refs. [92, 142].

Since the Fermi-surface of Bi_2Te_2Se surface is made up of its topological states, the Fermi-surface is of special interest in this chapter. Note that the intensity of the electron-positron momentum density at a given momentum vector $\mathbf{k}+\mathbf{G}$, with $\mathbf{k}$ inside the BZ and $\mathbf{G}$ a reciprocal lattice vector, is determined by the number of occupied electrons states at $\mathbf{k}$. Hence, denoting $\mathbf{k}_F$ a vector on the Fermi-surface in the BZ, the momentum density will display a sharp intensity difference at all $\mathbf{k}_F + \mathbf{G}$. The so-called LCW-map [122] is specially useful to identify the Fermi-surface signature in the momentum density, as it enhances the intensity drop by folding all higher momentum contributions into the BZ:

$$\rho^{2\gamma}_{LCW}(\mathbf{k}) = \sum_{\mathbf{G}} \rho^{2\gamma}(\mathbf{k}+\mathbf{G}). \tag{5.5}$$

Chapter 6

Positron induced Auger spectroscopy of graphene

In this chapter we use the framework of the WDA to provide theoretical support for an experiment performed by the positron group of A. Weiss at the University of Texas at Arlington, USA. First, we explain the performed experiment and its results. Then we discuss the physical process that is expected to take place. Afterwards we present a theoretical model of said process, and discuss which ingredients we need to extract from first-principles calculations. The rest of the chapter is devoted to the analysis of the model and comparison with experiment. Part of the work presented in this chapter is published in Ref. [8].

6.1 Introduction

An Auger process denotes a process in which a core electron vacancy is filled by an electron of a higher shell, and the energy difference between the two levels is transferred to another electron. If the energy difference is sufficiently large, this second electron can escape from the sample as a free electron. Auger electron spectroscopy exploits the fact that core electron energy levels are characteristic for different species of atoms to analyse the chemical composition of surfaces.

Traditionally, Auger electron spectroscopy experiments use energetic beams of X-rays or electrons to create the core holes that trigger the Auger effect. The downside of these methods is that the beam creates a large background of secondary electrons in the low energy regime, e.g. scattered beam electrons or core electrons. On the other hand, positrons provide a particularly clean method to create core holes. Indeed, after annihilation of the positron with a core hole, only the gamma rays remain which typically escape the sample without scattering. This technique has been around for some time and has been termed PAES [7]. The only source of secondary electrons is caused by the impact of the positrons with the sample, i.e. if the kinetic energy of the positron is sufficiently large, it can knock valence electrons out of the sample. Another possible source of secondary electrons is that the energetic Auger electron causes a cascade effect, i.e. that it scatters off valence electrons which gain sufficient energy in the process to also leave the sample.

Recent advances in low energy positron beams allow the deposition of very low energy positrons on a sample's surface [5, 21]. Since these beams carry positrons with an energy of only a few eV, impact induced secondary electrons are not expected when the kinetic energy of the positron is smaller than the electron workfunction. Despite this fact, a beam-energy dependent peak at low energies has still been observed for several samples [21]. The effect that takes place in this case is called AMPS. In this Auger-like effect, the positron transfers the energy difference between its incident scattering state and surface or bulk final state to a valence electron, which can then escape from the sample if it has sufficient energy. The kinetic energy of the electron is then

$$\epsilon_k^e = (\epsilon_k^p - \epsilon_f^p) - \phi^e, \tag{6.1}$$

where ϵ_k^α denotes the kinetic energy of the particles, ϵ_f^p the energy of the final state of the positron and ϕ^e the electron workfunction. Hence, this process has a threshold value for the beam energy, below which no Auger electron can be observed, namely $\epsilon_{k,\mathrm{thr}}^p < \phi^e + \epsilon_f^p$.

In Auger experiments performed on Cu (111) and Single Layer Graphene (SLG) on top of Cu (111), the group of Weiss observed the spectrum shown in Fig. 6.1. This figure shows the number of Auger electrons on the y-axis versus the time of flight on the x-axis, of which the corresponding kinetic energy is shown on the top. Characteristic Auger peaks for different identified elements have been indicated. The PAES measurements confirm the presence of C in the graphene sample, but also O contamination, which is assumed to be absorbed on top of the graphene layer. The signal of the Cu substrate is also still clearly observable. Aside from the C and O signals, the most important difference between the two measurements is the prominent low energy electron peak for SLG on Cu which persists at beam energies even below the AMPS threshold. Indeed, the beam energy was set to 1.25 eV in the experiments, and electronic workfunction in graphene and Cu are ~ 4.5 eV and $\sim 4.5 - 5.1$ eV, respectively. Hence the positron states should have a binding energy of at least 3.25 eV in order to observe impact induced secondary electrons. This value is however significantly larger than typical values observed for the positron workfunction or surface state binding energies, hence this possibility is unlikely.

One possibility could be that the observed electrons at low energies originate from inelastic loss of the higher energy Auger electrons, created by core level holes. In the Cu spectrum, we can separate this inelastic tail by comparing the integrated amplitudes of the spectrum above and below ~ 30 eV. This choice of the energy separates the $\mathrm{M}_{2,3}\mathrm{VV}$ peak in the spectrum from the low-energy part. We then find that the intensity of low energy part is ~ 1.7 times the intensity of the Auger peaks above 30 eV. A similar intensity can be expected for the graphene sample. The same analysis points out, however, that the intensity at low energies (< 30 eV is an order of magnitude higher than the integrated intensity of the Auger peaks at higher energy (> 30 eV). We conclude it is hard to explain the observed low-energy peak with inelastic loss alone.

The only plausible explanation left, after ruling out impact induced electron emission and inelastic loss from Auger peaks at higher energies, is that the annihilation of the positron with valence electrons in the material causes an Auger transition including only valence electrons. This in contrast with the usual core hole that forms the starting point. The kinetic energy of the observed Auger electrons $\epsilon_{\mathrm{esc}} + \epsilon_{\mathrm{vac}}$ is determined by

$$\epsilon_{\mathrm{esc}} + \epsilon_{\mathrm{vac}} = \epsilon_2 + \phi^e + (\epsilon_1 - \epsilon_h) \tag{6.2}$$

where we dropped the superscripts on the energies as no positron energies will enter for the rest of the chapter, ϵ_h is the energy of the hole that is the starting point of the Auger transition, ϵ_1 and ϵ_2 are the initial energies of the two electrons, and ϕ^e is the electron workfunction of the sample. The vacuum energy ϵ_{vac} enters explicitly if we chose the Fermi level ϵ_F as the reference level. Fig. 6.2 clarifies the situation. A rough estimate

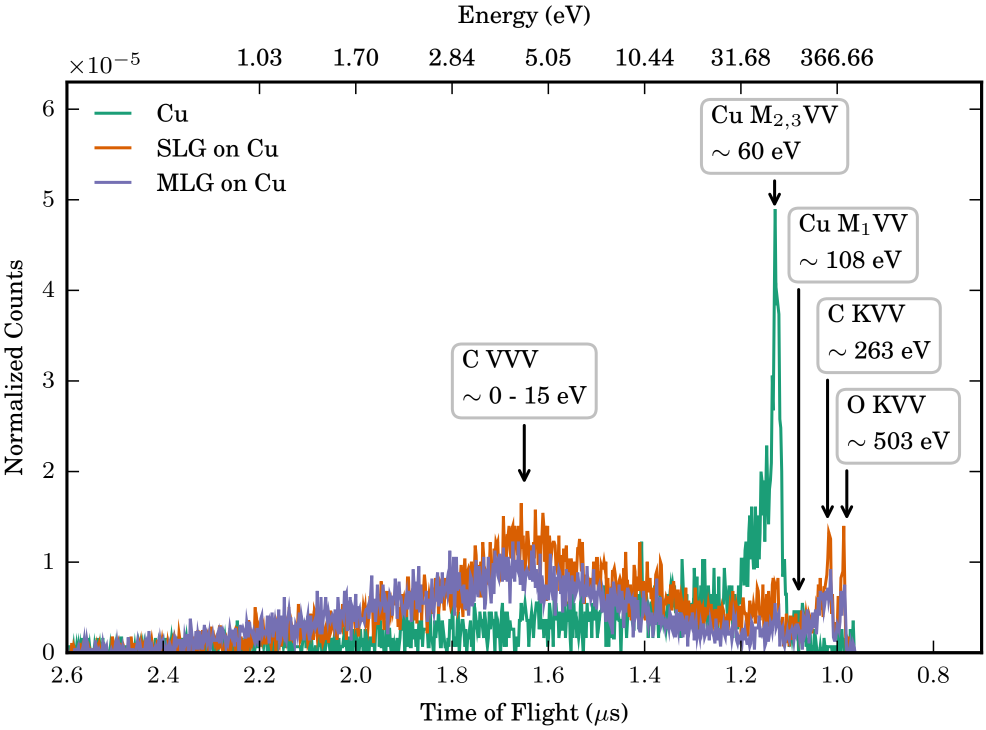

Figure 6.1: Results of the PAES experiment for Cu (111) (green curve), SLG on a Cu (111) substrate (orange curve) and MLG on a Cu (111) substrate (blue curve). Auger peaks that can be identified with specific elements have been indicated. Note the shorter time of flight corresponds with higher energies, as indicated with the axis at the top of the figure.

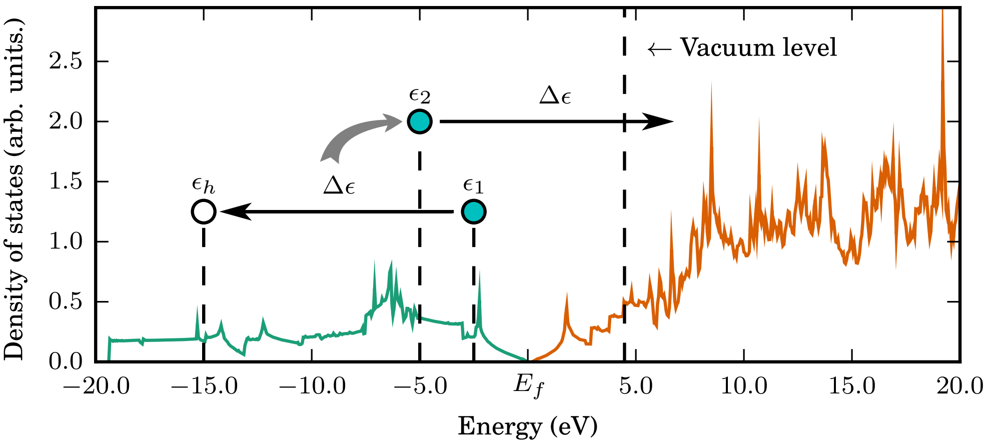

Figure 6.2: Schematic representation of the VVV process. An electron occupying an energy level ϵ_1 drops into a hole in the valence band at energy ϵ_h and releases an energy $\Delta\epsilon$. This energy is absorbed by a second electron from the valence band which occupies an initial energy level ϵ_2. If the resulting energy of this electron is sufficiently large, i.e. situated above the vacuum level, it can escape from the sample. The observed kinetic energy of the particle is equal to its initial energy plus the absorbed energy but minus the energy required to pass through the surface dipole barrier (the workfunction).

vouches for this process. Indeed, the width of the valence band of graphene is roughly ~ 20 eV, hence, using $\phi^e \approx 4.5$ eV, the spectrum should contain Auger electrons with kinetic energies up to ~ 15 eV, in agreement with the experiment. For Cu, the width of the valence band with an appreciable density of states is only 4 eV, which implies that the transition is not observable, again in agreement with what was measured. The process just described is, according to the Auger nomenclature, termed as a Valence-Valence-Valence Auger Transition (VVV). The first letter indicates the energy level of the initial hole, the second letter the energy level that transitions to the hole, and the final letter the one of the electron that absorbs the energy. Hence, the VVV Auger indicates that all states are located in the valence band.

The goal of the rest of this chapter is clear. We search a model to describe the VVV process and try to calculate it using input from first-principles calculations. If the calculated spectrum is in reasonable agreement with the experiment, we can confidently claim that the VVV process has been observed in graphene.

6.2 Theory

The transition rate of the Auger process for a given initial hole state can be calculated from Fermi's golden rule

$$A(\epsilon_{\text{Auger}}) = \frac{2\pi}{\hbar}|H_{fi}|^2\rho. \tag{6.3}$$

Let us first identify what we should take as the initial state and the final states in the matrix elements. We start with a system that contains N_e electrons. Afterwards, the positron enters the sample and annihilates with one of the electrons. We will assume that the resulting hole does not relax towards its groundstate (the top of the valence band) before the Auger process takes place. Hence, the initial state we should use in Fermi's golden rule is one with $N_e - 1$ electrons and a hole that occupies the state of the electron that annihilated with the positron. The final state after the Auger process is a state with $N_e - 1$ electrons, of which one in an excited state, and two holes. The perturbation that couples the two states is the Coulomb interaction. Assuming that the wavefunction can be written as a product of one-particle orbitals, we are interested in the matrix elements

$$H_{fi} = \iint d\mathbf{x}_1 d\mathbf{x}_2 \, \psi^*_{\text{hole}}(\mathbf{x}_1)\psi^*_{\text{ex}}(\mathbf{x}_2)\frac{1}{|\mathbf{r}_1 - \mathbf{r}_2|}\psi_1(\mathbf{x}_1)\psi_2(\mathbf{x}_2), \tag{6.4}$$

where ψ_1, ψ_2 are the orbitals of the initial electrons involved in the process, ψ_{hole} is the state occupied by the initial hole, and ψ_{ex} is the excited (Auger) electron. Note that the above formula ignores correlation effects. For instance, the states interact through a bare Coulomb interaction instead of a possibly more appropriate screened interaction. Since we currently consider only a fixed initial hole state, the density of (indistinguishable) final states is solely determined by the density of states of the excited state electron in the material at the relevant energy. We should take into account some geometrical factors, though, as we will only observe those electrons which have a momentum lying in the solid angle $d\Omega$ spanned by the detector. Hence, only that fraction of the density of states should be taken into account. Furthermore, if the excited state is created in the material, it has to traverse the surface dipole on its way to the detector. Finally, in order to obtain the total transition rate for the Auger process with a fixed initial hole state, we should additionally sum over all possible initial electron pairs that result in a final state with the same momentum and energy.

The calculation of the Auger matrix elements and the inclusion of the geometrical factors from first-principles is rather involved. Instead, we will use an approximate model described by Hagstrum [143, 144], in which matrix element effects are neglected and the escape of electrons to the vacuum is treated classically. This model was developed to describe Auger neutralization, a process in which an ion close to a surface is neutralized through an Auger transition. The main difference with our current problem is that the initial hole state is the one of the missing electron of the ion, instead of a missing electron in the material. We will see, though, that only the energy of the initial hole state enters in the model, such that it is suited to describe the VVV process as well.

The Hagstrum model does not give an absolute transition rate, but instead predicts the relative intensity of electrons escaping with a kinetic energy ϵ_k from the sample, which is given by

$$D_c(\epsilon_{\text{esc}} + \epsilon_{\text{vac}})P_e(\epsilon_{\text{esc}})T[\epsilon_h, \epsilon_{\text{esc}} + \epsilon_{\text{vac}}]. \tag{6.5}$$

Let us first discuss how this can be related with our general discussion of the transition rate in terms of Fermi's golden rule. First, in the above expression, we denote the measured kinetic energy of the Auger electron by ϵ_{esc}, and the reference energy is the Fermi level ϵ_F. The density of final states is here given by the density of states of the material D_c. The escape function $P_e(\epsilon_{\text{esc}})$ takes into account the probability that the excited electron has sufficient kinetic energy along the normal of the surface to climb the surface dipole barrier. Finally, T is the so-called Auger transform [145], and represents the sum over all initial state electron pairs that give a final state in which the excited state electron has energy $\epsilon_{\text{esc}} + \epsilon_{\text{vac}}$. It is given by a convolution of the valence density of states with itself,

$$T[\epsilon_h, \epsilon_{\text{esc}} + \epsilon_{\text{vac}}] = \int_{-\infty}^{\infty} d\epsilon_1 \int_{-\infty}^{\infty} d\epsilon_2 \, D_v(\epsilon_1) D_v(\epsilon_2) \\ \times \delta((\epsilon_1 - \epsilon_h) + (\epsilon_2 - \epsilon_{\text{vac}} - \epsilon_{\text{esc}}))\Theta(\epsilon_1 > \epsilon_h). \quad (6.6)$$

The valence density of states used above is simply the density of states below the valence band maximum $D_v(\epsilon) = D(\epsilon)\Theta(\epsilon < \epsilon_v)$. Energy conservation is taken into account through the delta function, and the Heaviside function ensures the hole in the valence band gets occupied by an electron from a state higher in energy. Note that the energy conservation we impose is only approximate. For example, it is possible that the excited electron does not carry away all energy released in the electron-hole transition as the two holes in the final state interact. We will not be concerned with these relaxation effects in the rest of this chapter.

Taking into account that we do not have a single hole at energy ϵ_h, but rather a distribution of holes $\lambda(\epsilon_h)$ which is determined by the annihilation probability of the positron with electrons at ϵ_h, we obtain

$$A(\epsilon_{\text{esc}}) = \int_{-\infty}^{\infty} d\epsilon_h \, \lambda(\epsilon_h) \frac{D_c(\epsilon_{\text{vac}} + \epsilon_{\text{esc}}) P_e(\epsilon_{\text{esc}}) T[\epsilon_h, \epsilon_{\text{vac}} + \epsilon_{\text{esc}}]}{N(\epsilon_h)} \Theta(\epsilon_h < \epsilon_g). \quad (6.7)$$

The Heaviside function indicates that Auger transitions can only happen when holes are created sufficiently deep in the valence band, such that the excited electrons can cross the band gap ϵ_g. We also introduced a normalization factor $N(\epsilon_h)$ which ensures that every hole created results in a single Auger transition, i.e.

$$N(\epsilon_h) = \int_{-\infty}^{\infty} d\epsilon_f \, D_c(\epsilon_f) T[\epsilon_h, \epsilon_f], \quad (6.8)$$

which simply gives all possible Auger transitions given the initial hole energy ϵ_h. The hole distribution can be extracted from the state-dependent electron-positron annihilation rates by integrating over the BZ

$$\lambda(\epsilon_h) = \frac{1}{\Omega} \sum_i \int_{\Omega} d\mathbf{k} \, \lambda_i(\mathbf{k}) f(\epsilon_i(\mathbf{k})) \delta(\epsilon_h - \epsilon_i(\mathbf{k})), \quad (6.9)$$

where the sum runs over all electronic energy levels i, which have an occupation $f(\epsilon_i(\mathbf{k}))$, and Ω denotes the volume of the BZ. The state dependent annihilation rates are calculated as

$$\lambda_i(\mathbf{k}) = \pi r_e^2 c \int d\mathbf{r} \, |\psi^e_{i,\mathbf{k}}(\mathbf{r})|^2 |\psi^p(\mathbf{r})|^2 \gamma(\mathbf{r}). \quad (6.10)$$

For the calculation of the BZ integral, we have used the tetrahedron method for which formulas are given in Ref. [146].

Hence, we have a recipe to calculate all quantities in Eq. (6.7) from first-principles with exception of the escape function, for which we now derive an expression. Hagstrum treats the excited electron as a classical particle that gets diffracted at the surface of the material. The kinetic energy of the particle in the material is assumed to be given by the energy of the electron above some reference energy ϵ_{ref}. In Hagstrum's work, this reference energy is the bottom of the conduction band for metals [143], or the bottom of the highest valence band for semi-conductors [144]. We take instead the average potential in the bulk of the sample. Our choice is merely conceptual, and has little effect on the actual results. Since we measure the final electron's energies with respect to the vacuum level, the kinetic energy in the material is given by $\epsilon_{\text{vac}} + \epsilon_{\text{esc}} - \epsilon_{\text{ref}}$. Passing through the surface dipole barrier, the particle loses kinetic energy equal to the energy difference between the reference energy and the vacuum level. The critical angle of incidence, measured from surface's normal, for which the particle retains a positive kinetic energy in the vacuum is

$$\theta_c = \arccos\left(\sqrt{\frac{\epsilon_{\text{vac}} - \epsilon_{\text{ref}}}{\epsilon_{\text{vac}} + \epsilon_{\text{esc}} - \epsilon_{\text{ref}}}}\right). \tag{6.11}$$

The escape function is then determined from

$$P_e(\epsilon_{\text{esc}}) = \int_0^{2\pi} d\phi \int_0^{\theta_c} d\theta \, P_\Omega(\theta, \phi, \epsilon_{\text{vac}} + \epsilon_{\text{esc}}), \tag{6.12}$$

where $P_\Omega(\theta, \phi, \epsilon_{\text{vac}} + \epsilon_{\text{esc}})$ is the probability that the wavevector of an excited state electron with energy $\epsilon_{\text{vac}} + \epsilon_{\text{esc}}$ is in the direction (θ, ϕ). Here, we take the z-axis along the direction of the surface normal. This probability is determined by the matrix elements, and for simplicity, we will assume that the distribution is isotropic, $P_\Omega(\theta, \phi, \epsilon_{\text{vac}} + \epsilon_{\text{esc}}) = 1/4\pi$. The resulting integral is easy to perform and gives

$$P_e(\epsilon_{\text{esc}}) = \frac{1}{2}\left[1 - \left(\frac{\epsilon_{\text{vac}} - \epsilon_{\text{ref}}}{\epsilon_{\text{vac}} + \epsilon_{\text{esc}} - \epsilon_{\text{ref}}}\right)^{\beta}\right]^{\alpha}, \tag{6.13}$$

with $\beta = 1/2$ and $\alpha = 1$. The parameters α and β were introduced by Hagstrum [144] to model the non-isotropy of the matrix elements. We will investigate their effect on our results in a later section.

6.3 Results

Now that we presented our recipe for the calculation of the Auger spectrum, we will gather the required ingredients from the first-principles calculations. We need the Density Of States (DOS) of the material, the energy dependent electron-positron annihilation rates, the vacuum level, and the average potential in the bulk of the material. Once we obtain these quantities, we will examine the result of the model and compare it with the experimental results. As we will see, the agreement is reasonable, but nonetheless we spend some extra time on refining the recipe to see if we can obtain better agreement. Finally, we make an attempt to estimate the relative contribution of the VVV Auger process to the decay of excited holes in the valence band[1], i.e. its branching ratio, by comparing calculated and measured values.

6.3.1 First-principles calculations

Technical details

To calculate the electronic properties of the samples, we used the PAW method, as implemented in VASP [86–88, 146]. The kinetic energy cutoff for the plane-wave expansion

---

[1] Other decay channels include excitation of phonons, creation of electron-hole pairs, etc.

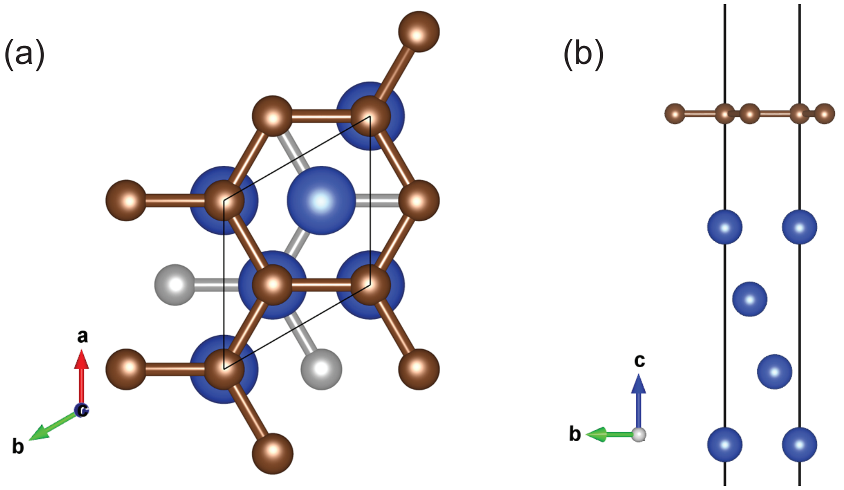

Figure 6.3: (a) Top view and (b) side view of the unit cell to model graphene on a Cu (111) substrate. Cu atoms are indicated in blue and C atoms in brown and gray, where, for clarity, C atoms at different Cu surfaces have different colors.

of the wave functions was set at 520 eV in all calculations containing C atoms, and 384 eV when only Cu was included. For the relaxation and ground state calculation of SLG, a Γ-centered k-mesh of 15 × 15 × 1 was used, and was refined to 45 × 45 × 1 to calculate the DOS accurately. In the case of the ground state calculation and relaxation of Cu (111) both with and without graphene layer(s), a Γ-centered k-mesh of 21 × 21 × 1 was selected. In all calculations, the structures were relaxed until the forces on the atoms were smaller than 5 meV/Å. A vacuum of 15 Å was present in all slab models to avoid interaction between periodic images. Electron-electron exchange and correlation effects were described using the optB88-vdW functional [147], appropriate for layered materials, which includes long-range Van der Waals effects and yields accurate lattice constants for both Cu [148] and Graphite [149]. We find that this functional yields a SLG - Cu interface spacing of 3.287 Å, which is in agreement with the value of 3.34 ± 0.06 Å obtained from total-reflection high-energy positron diffraction experiments [150]. Fig. 6.3 shows the unit cell used in the Cu (111) + SLG calculations. Our slab model for the Cu (111) substrate contains 9 atomic layers. For MLG, we found that electronic properties of interest, i.e. the DOS and electron workfunction, for a slab consisting of 6 layers approaches the bulk graphite limit sufficiently for our purposes.

The positron state was calculated with the MIKA/doppler program [92], the general details of which are explained in more detail in Sec. 3.B.1. We used the WDA with shell partitioning described in Sec. 3.3.3, where we take the C(2s), C(2p), Cu(3d) and Cu(4s) as the valence electrons. For the LDA part, and the enhancement factor, we take the parametrization by Drummond [56]. Since we have no experimental lifetime to compare with, we leave the screening charge at $Q = 1$ in the sum rule equation.

Positron states

Fig. 6.4 shows the localization of the positron state in our slab models. From these plots, we see that the positron forms surface states for SLG on Cu (111), Cu (111), SLG, and

MLG, which are shown in panels (a)-(d), respectively. In the case SLG on Cu (111) (Fig. 6.4(a)), the positron is mostly located at the vacuum side of the graphene sheet, though the overlap with the Cu substrate is not negligible. For the graphite surface, we note that the positron density decays slower in the bulk of the material compared to the other systems, which we can attribute mainly to the large open space between successive graphene layers. We also find a positron surface state for MLG on Cu (not shown), which is very similar to the result shown for graphite; the positron state is dominantly located at the vacuum side of the sample and has non-negligible overlap with the first few graphene layers. Note that this implies a negligible overlap with the Cu substrate.

Aside from the positron state, Fig. 6.4 also show the contact density (pink lines), which in essence shows the spatial distribution of the initial hole states. It is clear that, for SLG on Cu, most of the initial hole states are created in the graphene layer and only a small fraction in the Cu substrate.

Electronic structure

The calculated valence DOS, conduction DOS and the hole distributions for SLG on Cu (111), Cu (111), SLG, and MLG are shown in Fig. 6.5(a)-(d), respectively.

We start our discussion by noting the similarity in the valence DOS and hole distributions between SLG (Fig. 6.5(c)), MLG (Fig. 6.5(d)) and graphite (not shown). It is well-known, though, that graphene is a zero-gap semiconductor with a linear band dispersion around the Fermi-level, in contrast to MLG and graphite which are semi-metals [151]. The difference in the electronic structure is, however, located close to the Fermi-level and might have a very limited quantitative effect on our results, but qualitatively, we do not expect a notable difference originating from the occupied DOS and the hole distributions. The same applies for the calculated workfunction values of 4.47 eV, 4.45 eV and 4.45 eV for SLG, MLG and bulk graphite, respectively.

The results for Cu (111), shown in Fig. 6.5(b) support our earlier claim that we do not expect to observe a significant VVV signal from it. Indeed, from the energy resolved annihilation rates, we have calculated that barely 5% of the holes are created sufficiently deep in the valence band to allow any Auger electrons to escape from the sample. This corresponds with the portion of the blue curve not situated in the shaded area. Also, the DOS is relatively small up to $\sim 1.5\,\mathrm{eV}$ from the Fermi-level, from which we can already expect, without explicitly calculating the Auger transform, that most of the Auger electrons will end up below the vacuum level.

For SLG on Cu (111), we see in Fig. 6.5(a) that the DOS is dominated by the Cu contribution. This is to be expected since in our calculations 86% of the electrons belong to the Cu substrate. However, the hole distribution still closely resembles the SLG DOS, with exception of the region around $\sim 2\,\mathrm{eV}$ below the Fermi-level. This is line with our expectations from the results of the positron state and contact densities shown in Fig 6.4(a). Indeed, using the atomic densities, we calculated that 96% of the annihilation occurs with C states[2]. The difference in the hole distribution can safely be attributed to the annihilation with the Cu states, as the deviation compared to SLG is situated around the position where the Cu hole distribution, shown in Fig. 6.5(a), is peaked.

We note that there is a small contribution to the conduction DOS due to free electron-like states in the vacuum of the simulation cell, confined between periodic images of the slab [152]. This adds the well-known step like contribution of a confined 2D electron

---

[2] This is the LDA result. In the IPM we find 95%.

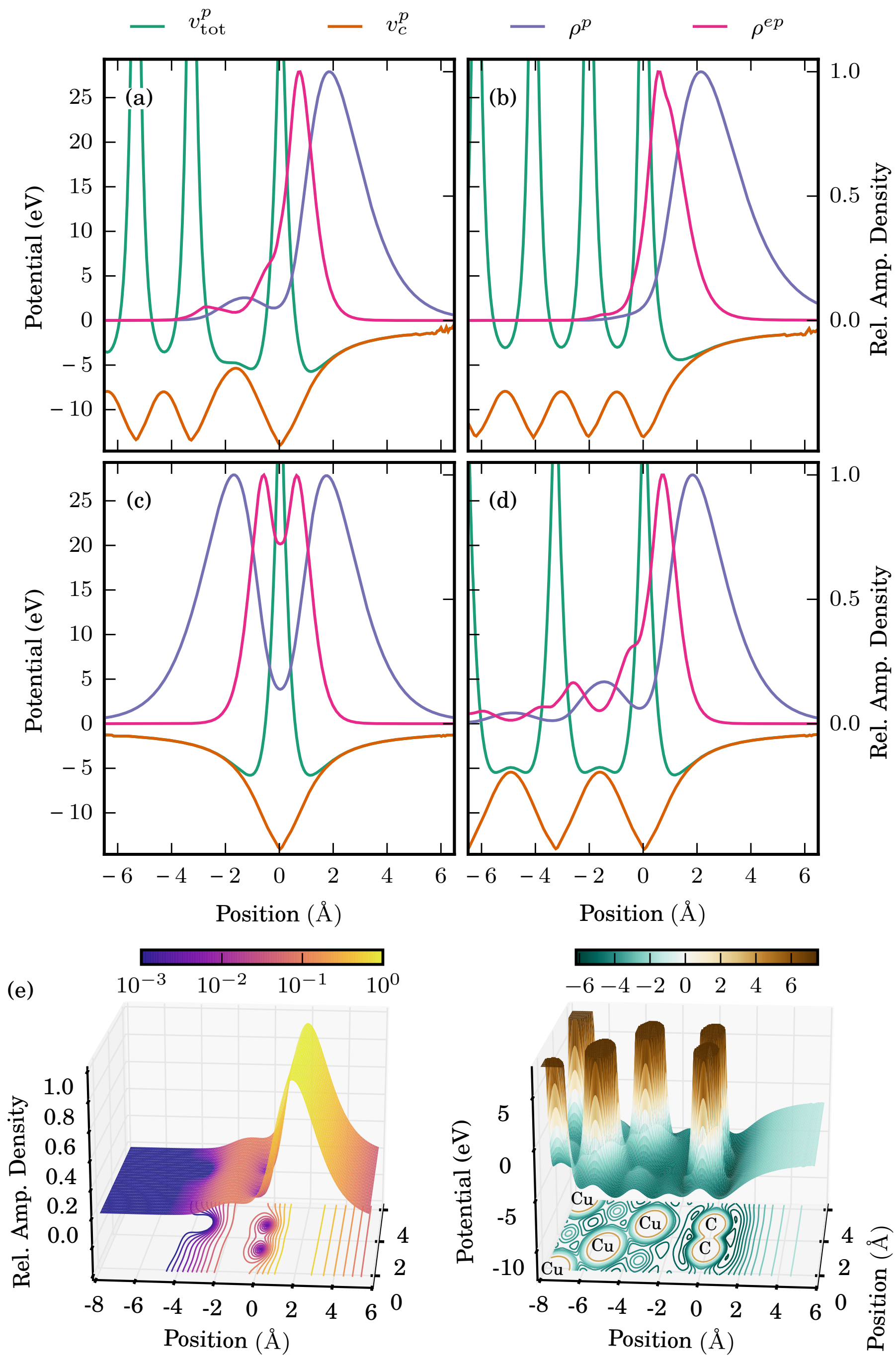

Figure 6.4: Results of the positron groundstate calculation for (a) SLG on Cu (111), (b) Cu (111), (c) SLG and (d) graphite. The curves show averages over the planes parallel to the surface. The densities are shows on a relative scale for ease of comparison. v^p_{tot}: Total positron potential, v^p_c: Positron correlation potential, ρ^p: Positron density, ρ^{ep}: Contact density. Panel (e) shows a cut through the positron density and potential for SLG on Cu (111) along the C-C bond. This result shows that the positron state is relatively uniform, except in the region close to the ions where it decays quickly, as can be expected from the potential.

gas to the conduction DOS above the vacuum level[3]. The spacing between these states increases as $\sim n^2/L$, with n indicating the level and L the width of the potential well created by the periodic images of the slab. As a consequence, the relative contribution to the conduction DOS due to these states is small, and in practice has little effect on our calculated spectra.

6.3.2 VVV spectrum

Preliminaries

Before presenting the VVV spectra calculated by applying Eq. (6.7), we study the integrand of this equation. This gives additional insight in how the different quantities from our first-principles calculations contribute to the VVV spectrum. The DOS and hole distribution of MLG, shown in Fig. 6.5(d), have a peak structure that makes it easy to interpret[4], and will be discussed here as an example.

Fig. 6.6(a) shows the Auger transform of Eq. (6.6) and quantifies the number of transitions possible for a given initial hole energy ϵ_h and excitation energy of the Auger electron $\epsilon_{\text{esc}} + \epsilon_{\text{vac}}$. We see that even for a material with a wide valence band such as MLG, the majority of the final state electrons end up below the vacuum energy, as indicated by the hatched region on the left side of the plot. Note also the small amplitude of the Auger transform for holes with an energy above the threshold value for Auger emission, i.e. $\epsilon_F - \epsilon_h < \phi^e$ which is delineated by the hatched region at the top of the plot. The reason for this is twofold: (i) The possible combinations of initial and final states become small because most of the DOS does not contribute to the Auger transform at that point, and (ii) the amplitude of the DOS vanishes towards the Fermi level. For point (i), consider for instance $\epsilon_h = \epsilon_F - \phi^e$, then only the shaded region in Fig. 6.5 is contained in the Auger transform.

The Auger transform weighted by the hole distribution and the conduction DOS, i.e. the product $\lambda(\epsilon_h) D_c(\epsilon_{\text{vac}} + \epsilon_{\text{esc}}) T[\epsilon_h, \epsilon_{\text{vac}} + \epsilon_{\text{esc}}]$ in Eq. (6.7), is shown in Fig. 6.6(b). The hole distribution can be recognized along the vertical lines of fixed final energy in the plots, in particular the peaks and the dip in the DOS a bit above $-15\,\text{eV}$. Analogously, the conduction DOS can be recognized by taking a cut through the plot at a fixed hole energy, with most notable feature the peak just below $10\,\text{eV}$.

The VVV spectrum is obtained from the results shown in Fig. 6.6(b) by additionally multiplying with the escape function $P_e(\epsilon_{\text{esc}})$, which will quench the amplitude to zero at the vacuum level, dividing by the normalization factor $\lambda(\epsilon_h)$ and integrating over the hole energies. Hence note that the fine structure of our calculated VVV spectra will clearly reflect the conduction DOS whereas the valence DOS and hole distribution only contribute to the overall amplitude.

Results VVV calculations

Now we illustrated how the different material properties contribute to the VVV spectra, we show the final results in Fig. 6.7. The result for Cu (111) confirms our earlier anticipation, showing that the VVV process has a vanishingly small amplitude. Likewise, the spectra for SLG and MLG are very similar. The differences between the two results are well explained by comparing the conduction DOS of the two systems. For SLG on the Cu (111)

---

[3] One such step can be identified in Fig. 6.5(c) at the vacuum level, indicated by the dashed vertical line. Mind that the two preceding steps in the conduction DOS correspond with conduction states of graphene. Hence, not all steps can straightforwardly be attributed to vacuum states.

[4] The results of SLG have several additional small peaks that clutter the plots.

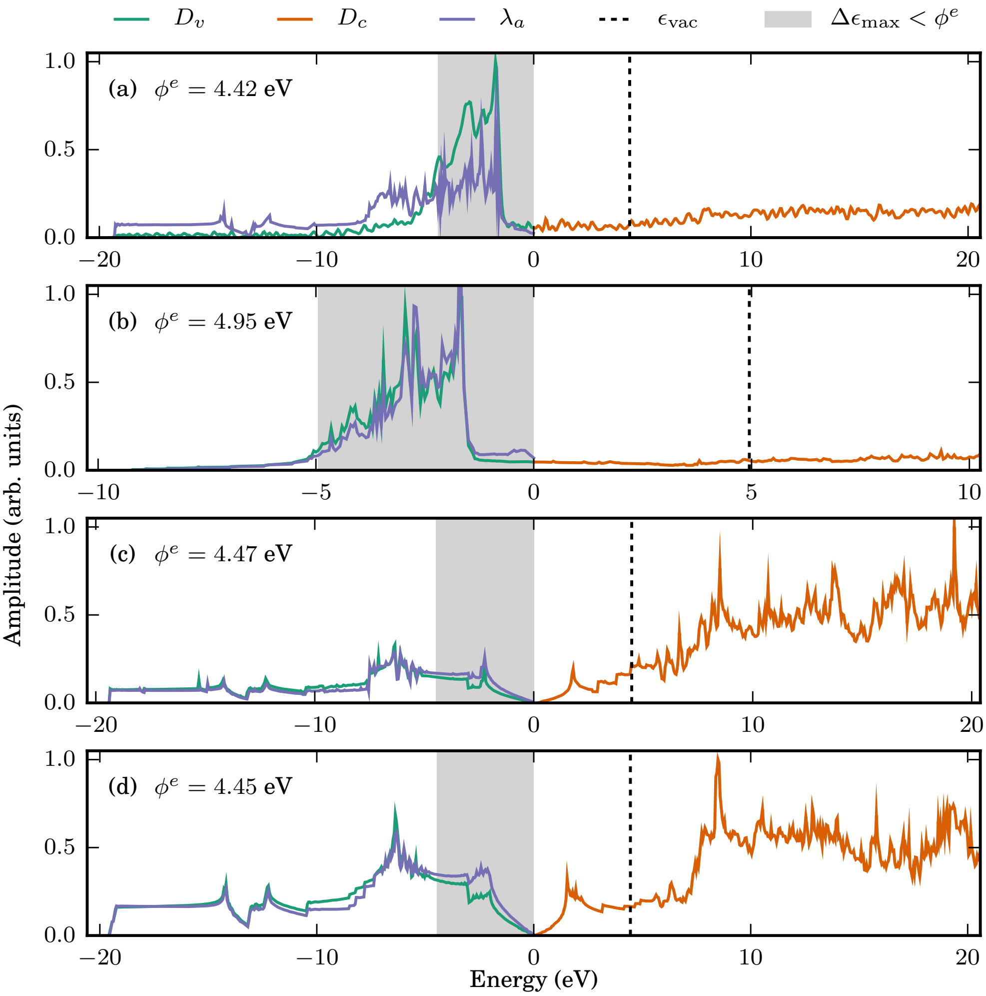

Figure 6.5: DOS and hole distribution for (a) SLG on Cu (111), (b) Cu (111), (c) SLG, and (d) MLG. All quantities are shown on a relative scale. Energies are measured with respect to the Fermi level, and the vacuum level ϵ_{vac} is indicated with the dashed line. The valence DOS D_v is shown in green, the conduction DOS D_c in orange, and the hole distribution λ_a, i.e. the energy resolved annihilation rate, in blue. The shaded region indicates the portion of the hole distribution that is too close to the Fermi energy to allow Auger transitions with an excited electron above the vacuum level, i.e. the maximal transferred energy is smaller than the electron workfunction $\Delta\epsilon_{\max} < \phi^e$. The values of the work functions are quoted in the plots for each sample.

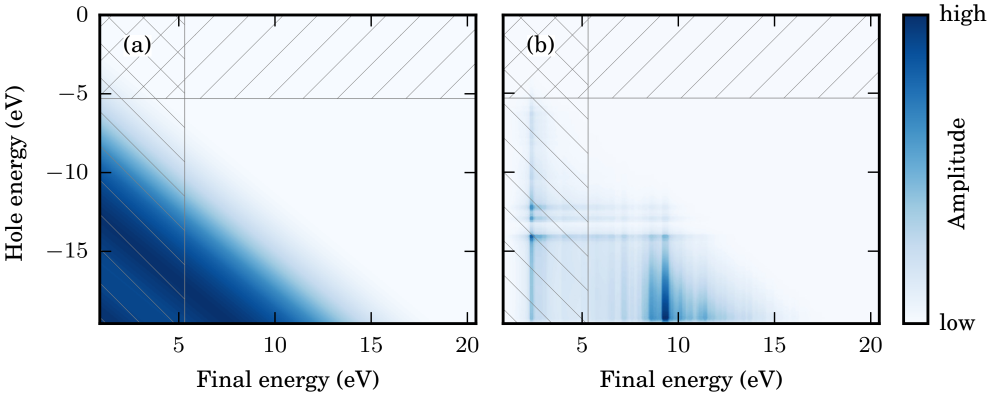

Figure 6.6: (a) The Auger transform (Eq. (6.6)) for MLG as a function of the initial hole energy (vertical axis) and the energy of the excited electron with respect to the Fermi energy (horizontal axis). (b) The Auger transform multiplied with the hole distribution λ_a and the conduction DOS D_c as in the integrand of Eq. (6.7). The hatched regions at the left of the plots indicates final energies that are below the vacuum level, and the hatched regions at the top initial hole energies that are too close to the Fermi level in order to create an Auger process with an excited electron above the vacuum level.

substrate, we find a rather different result without any pronounced peaks but instead a wide slowly varying amplitude over the range $0-12\,\text{eV}$. This is caused by the relatively flat, steadily increasing conduction DOS of the system.

The calculated result of SLG without inclusion of the Cu substrate (blue line) is in reasonable agreement with the experimental results of SLG (dotted green line). We find a peak position around $4\,\text{eV}$ in the calculated results, which is fairly close to the maximum at $\sim 3.5\,\text{eV}$ seen in experiment. Also the decay of the amplitude between $5-10\,\text{eV}$ compares well against the measured result. The major difference is the higher amplitude at low energies observed in the experiment. Somewhat surprisingly, our calculations of SLG with inclusion of the Cu substrate (orange line) shows notably worse agreement with experiment. The agreement between experiment (dotted yellow line) and theory (pink line) for MLG is somewhat worse than for SLG, mainly due to the shift in the amplitude towards lower energies in the experiment.

Let us search for an explanation why the SLG on Cu (111) calculation differs so strongly from the (better) SLG result. We already know that the conduction DOS is the most important factor that determines the shape of the spectrum. Earlier, we also noted that the calculated DOS of the Cu + SLG is dominated by the Cu states. Hence, in our result for this system, we mainly see transitions where the initial hole is situated in the graphene layer (due to the hole distribution) and the excited electrons occupy excited states of the Cu substrate. This is certainly not what we physically expect to happen. Indeed, since the graphene layer is only weakly coupled to the Cu substrate, there is little hybridization/overlap between the graphene and Cu states [153]. Hence, from the Auger matrix elements, Eq. (6.4), we expect that the electron that transitions to the hole state will also be a graphene state. This observation suggests that it is more appropriate to use the graphene valence DOS in the calculation of the Auger transform even though there is

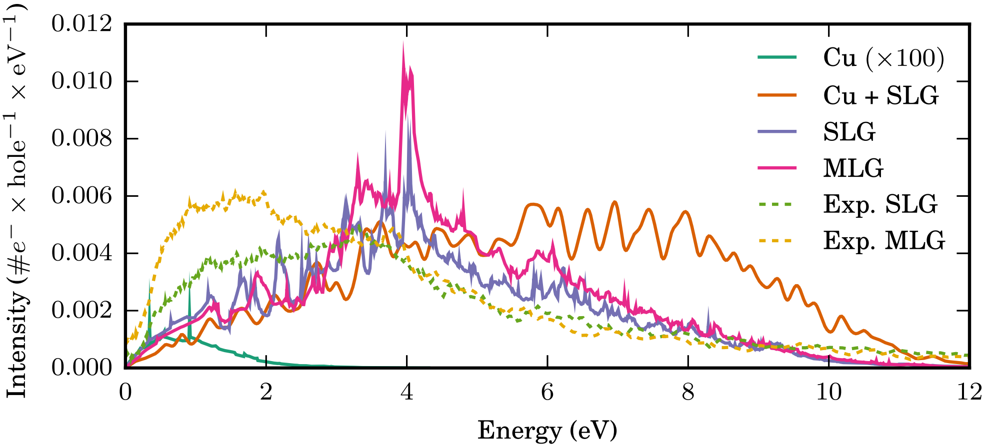

Figure 6.7: Results of the Auger calculation for the considered systems. The normalization is chosen such that, before applying the escape function and taking into account the fraction of electrons that end up below the vacuum level, there is a single Auger transition per created hole in the valence band (i.e. the normalization of Eq. (6.8)). Note that the amplitude for Cu (111) has been multiplied by a factor 100 in order to make it visible on the plot. Measured spectra are shown by the dotted lines, and have been normalized to the same total amplitude as the calculated results (without Cu substrate).

a Cu substrate present in the experiment[5]. Next, we expect that also the observed Auger electrons occupied initially graphene states. We have two reasons to make this claim. The first is that it is reasonable to expect that the Coulomb interaction between the graphene layer and the Cu substrate will be screened to some extent [154]. This decreases the amplitude of the Auger matrix elements between Cu and graphene states. The second is that if the excited electron is created in the Cu substrate, it is less likely to make it out of the sample without being scattered. However, if we use the DOS calculated for the Cu + SLG system in our model, we essentially assume that the final electrons in the Auger process are dominated by the Cu states. Hence, just as was the case for the valence DOS, it is again more appropriate to use the conduction DOS of SLG.

The above discussion shows that an important limitation of neglecting the matrix elements is the resultant lack of spatial selectivity. As we suggested, using the graphene DOS cures the problem to some extent, as confirmed by the reasonable agreement between the measured and calculated SLG spectra.

In the following sections, we explore three effects not directly related to matrix element effects (which we will not investigate in this work) that can ameliorate the agreement between experiment and theory in the low energy part of the spectrum. Cascade effects, in which a single electron-positron annihilation induced hole leads to a series of Auger transitions, will be explored first. Since the additional Auger electrons will generally have reduced energy, this should increase the amplitude of the calculated spectrum at lower energies. Second, we will attempt to model effects of inelastic scattering, which should shift the amplitude of the results presented in this section towards lower energies. Finally,

---

[5] Even better would be to sum the Auger transforms of the isolated SLG and Cu (111) systems. We know from the latter, though, that it gives a vanishingly small contribution, hence we will ignore it.

we will examine the effect of the parameters of the escape function on the VVV spectrum.

6.3.3 Cascade effects

One possibility to explain the higher intensity at low energies observed in the experiment is that multiple Auger processes happen in succession. Indeed, after the first Auger process, the system is actually left with two holes in the valence band. These two holes can serve as the starting point of an equal amount of additional Auger processes. Each of these successive transitions, will create holes higher up in energy, such that the additional Auger electrons are mainly expected in the low energy part of the spectrum. The amount of sufficiently energetic Auger electrons in the cascade effect is thus also limited.

Theory

We will now calculate the upper bound of this effect by assuming, as before, that the Auger process is the only decay channel, i.e. the holes do not loose energy through other processes. Hence, we start with the initial annihilation induced hole distribution, and obtain a new hole distribution in the second iteration which is determined by the initial energies of the two electrons of the first iteration. To derive a formula for the hole distribution after each iteration, we need to count the number of times that each initial electron state is involved in an Auger transition. Our expression for the VVV spectrum, Eq. (6.7), counts the number of possible transitions from all initial energy levels to a given final energy state, and weights them by the escape probability. The latter, we ignore for our current purpose, as we need to count all transitions, not just the ones that result in an escaping electron. Now, if we fix the initial energy of one of the electrons which appears in the Auger transform of Eq. (6.6), and integrate over all possible final energy levels, we obtain what we are looking for. Summing the contributions for both initial electrons, given us

$$
\begin{aligned}
\lambda_i(\epsilon_h) = \iint d\epsilon_h'\, d\epsilon_f\, \frac{\lambda_{i-1}(\epsilon_h')D_c(\epsilon_f)}{N(\epsilon_h')} \\
\times \Bigg\{ \int d\epsilon_1\, D_v(\epsilon_1)D_v(\epsilon_h)\delta((\epsilon_1 - \epsilon_h') - (\epsilon_h - \epsilon_f))\Theta(\epsilon_1 > \epsilon_h') \\
+ \int d\epsilon_2\, D_v(\epsilon_h)D_v(\epsilon_2)\delta((\epsilon_h - \epsilon_h') - (\epsilon_2 - \epsilon_f))\Theta(\epsilon_h > \epsilon_h') \Bigg\}, \quad (6.14)
\end{aligned}
$$

where we replaced $\epsilon_{\text{vac}} + \epsilon_{\text{esc}}$ by ϵ_f to indicate that we should integrate over all possible final energies, not just the ones above the vacuum level. The subscript i denotes the order of the hole distribution, with $\lambda_0 = \lambda_a$ the one created by the annihilation process.

Results

Fig. 6.8(a) shows the effect on the spectrum for graphene. We see that the cascade effect has a very limited impact on the spectrum. We get limited extra contribution at low energies, which quickly decreases towards higher energies. It is maybe slightly surprising that the effect is so small, but it turns out that the additional holes created in the valence band quickly end up above the threshold energy for Auger emission. This is indicated in panel (b) of the same figure. Still, according to the numbers given in Table 6.1, the first iterative contribution has about half as much holes with the potential to contribute to the spectrum, which is not at all reflected by the curve A_1 of Fig. 6.8(a). Indeed,

Iteration	$I(\lambda_i)$	$I(\lambda_i(\epsilon_h < \epsilon_f - \phi^e))$	$I(A_i)$
0	1	7.28e-01	1.44e-02
1	2	3.26e-01	1.94e-04
2	4	2.27e-02	9.08e-07
3	8	3.76e-04	1.80e-09

Table 6.1: Relative amounts per annihilation of $I(\lambda_i)$: holes in the valence band, $I(\lambda_i(\epsilon_h < \epsilon_f - \phi^e))$: holes sufficiently deep in the valence band to trigger an Auger transition with an electron above the vacuum level , and $I(A_i)$: Auger electrons that escape from the sample. $I(\lambda_i(\epsilon_h < \epsilon_f - \phi^e))$ corresponds with the integral over the hole distributions in Fig. 6.8 not contained in the gray region.

from our Table 6.1 we can read off that this contribution is only 1.3% of the that of the annihilation induced effect. There are two reasons for this rapid quenching of the iterative contributions. First, most of the transitions originating from the potentially contributing hole states, end up below the vacuum level. The actual amount of transitions with an electron above the vacuum level for iteration i is reflected by the hole distribution of iteration $i+1$. It can be seen from Fig. 6.8(b) as well as the third column of Table 6.1 that this decreases rapidly after the first order. Second, the escape function significantly damps the actual amount of escaping electrons in the low energy region. Indeed, this is illustrated by the numbers shown in the third and last column of our table. Whereas about 4% of the holes with $\epsilon_h < \epsilon_F - \phi^e$ result in an emitted electron for the annihilation induced step, this drops to barely 0.3% in the first cascade.

We can conclude from the results presented in this section that cascade effects cannot be responsible for the discrepancy in the amplitude between the calculated and measured VVV spectra. Indeed, our results here are an absolute upper bound and have no qualitative influence on the spectrum compared to the result without inclusion of higher order Auger effects.

6.3.4 Inelastic scattering

Inelastic scattering of Auger electrons as they make their way out of the material is the second effect we investigate to obtain better agreement with experiment. The Auger experiment for Cu contains, in fact, a significant low energy tail due to inelastic scattering [5, 8, 21], indicating that inelastic scattering could indeed be important. Modelling this effect accurately is, however, far from straightforward. Hence, we concentrate on a simple model to estimate if inelastic effects can be held responsible for the increased amplitude at low energies. We neglect the cascade effects from the previous section, and start from the results presented in Sec. 6.3.2.

In the following, we motivate the approach we take to model inelastic scattering. As we will see, we can obtain the spectrum of scattered electrons by convolving the original spectrum with an energy dependent cross section, and we will consider three different such cross sections found in literature. After discussing the cross sections, we present the required modifications to the equations for the VVV spectrum to incorporate the inelastic scattering. The results and discussion are presented in the subsequent section.

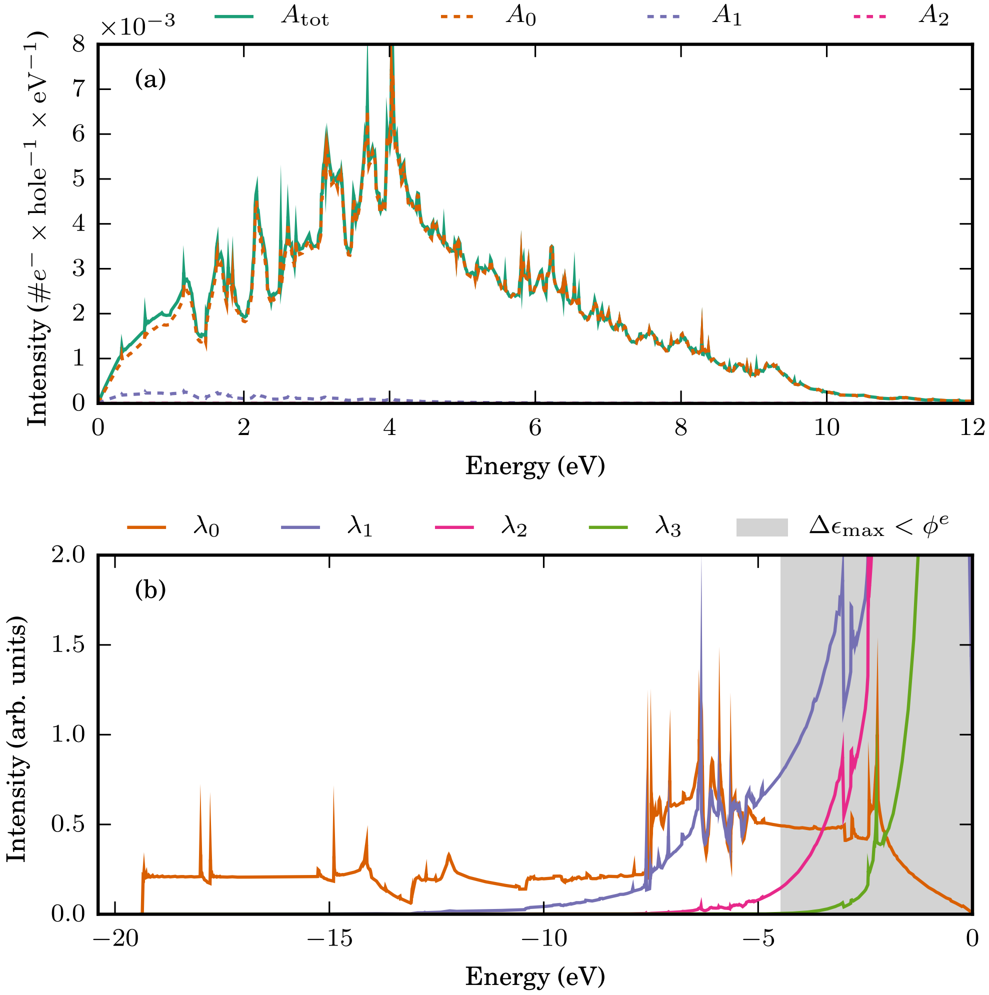

Figure 6.8: (a) The VVV Auger spectrum with inclusion of cascades effects. The full line indicates the total amplitude obtained by summing all the iterative contributions. The dashed lines show the contributions of the individual orders A_i. (b) Hole distributions λ_i at each step of the cascade, with $\lambda_0 = \lambda_a$ the hole distribution created by the positron annihilation. The shaded area indicates holes that cannot trigger Auger transitions that result in escaping electrons.

Theory

Introduction: The probability for an electron with kinetic energy E to lose an energy $\hbar\omega$ to an excitation in the solid, per unit length, is given by [155, 156]

$$K(E,\hbar\omega) = \frac{1}{\pi E a_0}\int_{k^-}^{k^+} dk\, \frac{1}{k}\Im\left[-\frac{1}{\epsilon(k,\omega)}\right], \tag{6.15}$$

where a_0 is the Bohr radius, $k^{\pm} = \sqrt{2m/\hbar^2}(\sqrt{E}\pm\sqrt{E-\hbar\omega})$, and $\epsilon(k,\omega)$ is the dielectric function, which is assumed to be a scalar rather than a tensor for simplicity. To obtain the energy distribution of scattered electrons, this quantity has to be multiplied with the inelastic mean free path $l(E)$ for electrons with kinetic energy E. Albeit computationally intensive, it is possible to calculate the full dielectric function from first-principles. We will not attempt to do so here, however, as our purpose is mainly to get a rough estimate of the inelastic scattering. What we will use later on, is the $k \to 0$ optical limit of the dielectric function which is much faster to calculate. This limit will prove useful in conjunction with the expansion [155–157]

$$\Im\left[-\frac{1}{\epsilon(k,\omega)}\right] = \sum_i A_i \frac{\Gamma_i\hbar\omega}{\left[\left(\hbar\omega_{0i}+\frac{\hbar^2k^2}{2m}\right)^2-(\hbar\omega)^2\right]^2+(\Gamma_i\hbar\omega)^2}. \tag{6.16}$$

The above expansion gives an approximation of the dependence of the loss function on the wave vector which satisfies some sum rules, and can be fitted to optical spectra [155–157]. For $k = 0$, Γ_i give the full width at half maximum of a peak i in the spectrum, ω_{0i} its center, and A_i the amplitude.

Tougaard noticed that the product $l(E)K(E,\hbar\omega)$ is weakly dependent on both the initial kinetic energy of the electrons and the material for several metals [155]. Motivated by this observation, he proposed a 'universal cross section' $\sigma(\hbar\omega)$ that roughly describes the energy loss of electrons over a wide energy range, and is applicable to a wide range of materials as well. The validity of the cross section has been confirmed by comparison with loss functions measured with Reflected Electron Energy Loss Spectroscopy (REELS) [156, 158, 159]. Later, it was noticed that when the loss spectra of certain materials display a clear plasmon peak, the cross section is better described with a slightly different form [156]. We will denote this form of the cross section as the 'plasmon' cross section in the rest of this section.

Usually, the cross sections mentioned above are used to subtract the background of inelastically scattered electrons from AES or X-ray Photoemission Spectroscopy (XPS) experiments. Aside from Tougaard's cross sections, the method proposed by Shirley [160] is also widely used to perform this background subtraction. It turns out that, although not initially formulated as such, this methods also coincides with assuming a cross section $\sigma(\hbar\omega)$, though with a somewhat different form as the one by Tougaard [161].

Cross sections: The functional forms of the cross sections discussed above are given by

$$\sigma_S(\epsilon) = \frac{B}{C+\epsilon^2}, \qquad \sigma_T(\epsilon) = \frac{B\epsilon}{(C+\epsilon^2)^2}, \quad \sigma_p(\epsilon) = \frac{\Gamma\epsilon}{(\omega_0^2-\epsilon^2)^2+(\Gamma\epsilon)^2}, \tag{6.17}$$

where we the subscripts denote the Shirley, Tougaard, and plasmon cross sections, respectively. We have written the plasmon cross section in a suggestive form that allows for easy identification with the energy loss expansion of Eq. (6.16). Notice that,

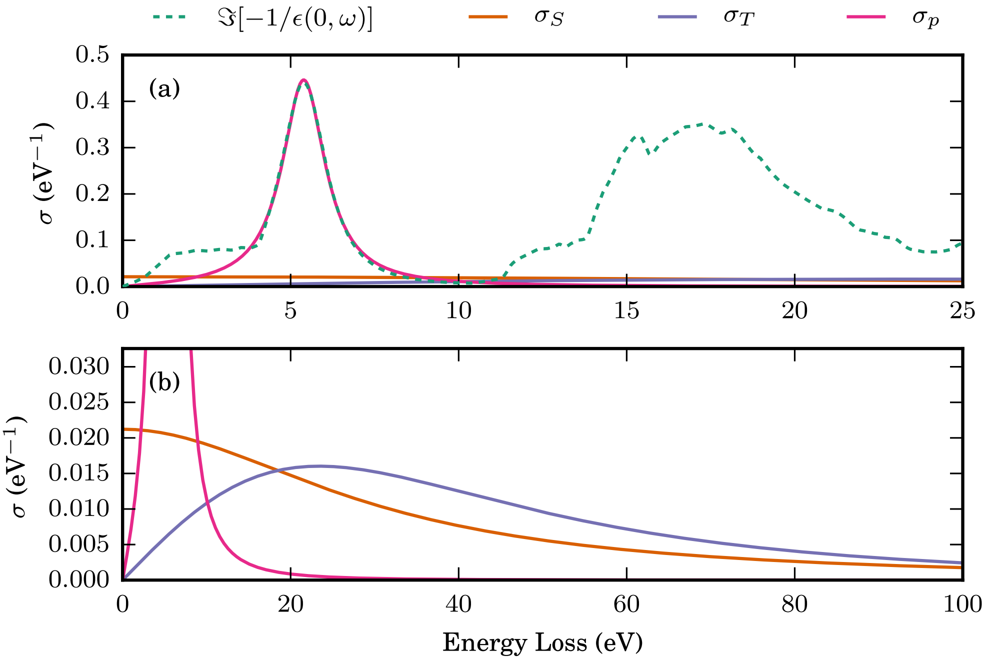

Figure 6.9: Plots of the Shirley σ_S, Tougaard σ_T and plasmon σ_p cross sections, normalized to unity. Panel (a) shows the optical spectrum as calculated from first principles. We have fitted the plasmon cross section to the prominent low-energy plasmon peak around ~ 5.5 eV, and obtained $\Gamma = 1.56$ eV^2 and $\omega_0 = 5.46$ eV. This single term fit reproduces the peak very well, but does not quite capture the plateau between $2-5$ eV, and obviously neglects the peak at higher energies. Panel (b) shows the dependences of the cross sections over a wider energy range. Note the difference in scale between the two plots.

aside from the amplitude parameter it corresponds with a single term fit to an optical spectrum. The usual parameters for the Tougaard cross section are given by $B = 2866$ eV^2, $C = 1643$ eV^2 [155]. A reasonable choice for the parameters in the Shirley cross section is $B = 36$ eV, $C = 900$ eV^2 [161].

The parameters mentioned above, have been chosen to describe the energy loss of electrons with kinetic energies of several 100 eV. A point of critique is then obviously that they may not quite describe the energy loss for the low energy electrons we are dealing with. To counter this critique, we have fitted the plasmon cross section to the low-energy plasmon peak in the graphene loss spectrum. The calculated energy loss spectrum $\Im[-1/\epsilon(0,\omega)]$ (dashed line), with the fitted cross section (full pink line) are shown in Fig. 6.9, along with the other two cross sections for comparison. Our result for optical loss spectrum agrees well with results from literature [162, 163]. Note that we have normalized the integral over the cross sections to unity for a fair comparison. The parameters of our fit are $\Gamma = 1.56$ eV^2 and $\omega_0 = 5.46$ eV. It will become apparent, though, that the exact choice of the parameters and the cross section do not crucially influence the results.

Modifications to the VVV model: The amplitude of inelastically scattered electrons can be obtained by convolving a spectrum A' with the energy dependent cross-sections $\sigma(\epsilon_1 - \epsilon_2)$, which describe the probability that an electron with energy ϵ_1 will scatter to a (lower) energy level ϵ_2 [161]

$$A'_n(\epsilon_2) = \int_{\epsilon_2}^{\infty} d\epsilon_1 \, \sigma(\epsilon_1 - \epsilon_2) A'_{n-1}(\epsilon_1). \tag{6.18}$$

Here, we introduce the subscript n since electrons can get scattered multiple times before they get detected. The limits on the integral indicate that, obviously, we only expect electrons to lose energy in the scattering process. We could substitute the calculated VVV spectrum for A'_0 in Eq. (6.18), but we already applied the escape function in calculating that result and do not expect electrons to scatter inelastically in the vacuum region[6]. Hence, we modify our expression for the VVV spectrum, Eq. (6.7), as follows

$$A(\epsilon_{\text{esc}}) = P_e(\epsilon_{\text{esc}}) \sum_{n=0}^{\infty} c_n A'_n(\epsilon_{\text{esc}}), \tag{6.19}$$

$$A'_0(\epsilon_{\text{esc}}) = \int d\epsilon_h \, \lambda(\epsilon_h) \frac{D_c(\epsilon_{\text{vac}} + \epsilon_{\text{esc}}) T[\epsilon_h, \epsilon_{\text{vac}} + \epsilon_{\text{esc}}]}{N(\epsilon_h)} \tag{6.20}$$

where the various symbols retain the same meaning, and A'_n is calculated from Eq. (6.18). In the above, we thus first calculate the transition amplitude A'_0 which is simply the VVV formula from before but without the escape function. Afterwards, we obtain the spectra A'_n of electrons that have undergone n scattering events through Eq. (6.18). Finally, we sum all these contributions and apply the escape function[7]. The constants c_n give the relative amplitudes of electrons that have been scattered n times. These coefficients are determined such that in each iteration a fixed relative amount D_{inel} are scattered inelastically[8]. Note that only the dependence of the cross section on the energy loss is relevant in our calculations, not its absolute amplitude.

Results

We tried several values for the amount of inelastic scattering, and found close agreement with the experimental spectrum (teal line) for $D_{\text{inel}} = 0.85$ with the fitted plasmon cross section (blue line), as depicted in Fig. 6.10(a). Note that the inelastic amplitude D_{inel} is the most important parameter is these calculations. Indeed, Fig. 6.10(b) demonstrates that the difference in the shape of the spectra obtained with the various cross sections is only minor, and corresponds with what can be anticipated from the plots of the individual cross sections. For the Shirley cross section, shown in pink, we find slightly higher amplitude at low energies for the same D_{inel} since it has a finite amplitude at zero energy loss, in contrast to the two other cross sections. The difference between the results obtained with the Tougaard (green line) and the plasmon (blue line) cross section is small, which is somewhat remarkable considering the difference of the actual loss functions, but

---

[6] A possible exception could be that electrons end up in the vacuum through the scattering process.

[7] In practice we select a maximum number of iterations n_{max} such that the result is sufficiently converged.

[8] More precisely, we set $c_n = I(A'_{n-1}) D_{\text{inel}}(1 - D_{\text{inel}})$, where $I(A'_{n-1})$ denotes the integrated intensity of the spectrum in the previous step. For the annihilation induced step we have $c_0 = I(A'_0)(1 - D_{\text{inel}})$, and for the final interaction $c_{n_{\text{max}}} = I(A'_{n_{\text{max}}-1}) D_{\text{inel}}$. Note that this choice takes into account that the number of excited electrons does not change due to the inelastic scattering. However, this does not imply that the final spectrum A has the same amplitude as the one calculated without inclusion of inelastic scattering. Indeed, there will be a shift of electrons towards lower energies, which implies that more electrons will be located below the vacuum level. Additionally, the escape function has a stronger damping effect for electrons closer to the vacuum level.

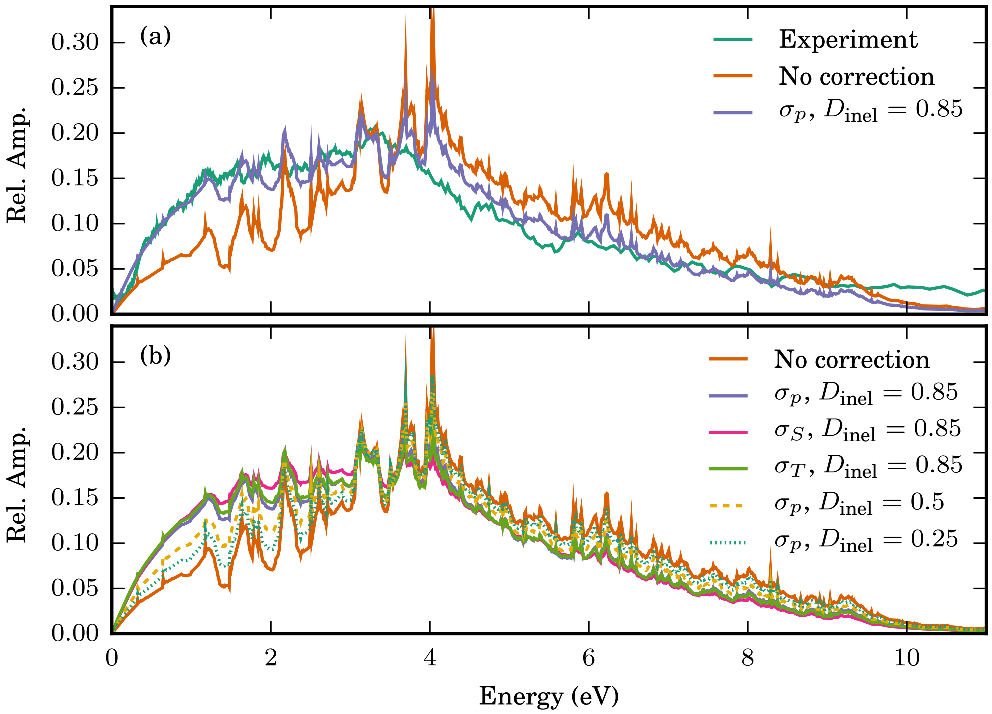

Figure 6.10: Influence of inelastic scattering on the shape of the VVV spectra. The total amplitudes of the results shown here have been normalized to unity over the shown range. Panel (a) compares the experimental spectrum with the result without inelastic scattering and the result with inclusion of inelastic scattering with the fitted plasmon cross section σ_p. The relative amount of inelastically scattered electrons D_{inel} is indicated in the legends of the plots. Panel (b) shows the effect of the different cross sections, as well as the influence of D_{inel} for the plasmon cross section.

demonstrates that the precise form and the parameters of the cross section are not that crucial. Table 6.2 gives the effect on the amplitudes of the VVV spectra for completeness.

In conclusion, a simple model for the inclusion of an inelastic scattering yields a remarkable improvement of the calculated spectrum's shape compared to the experimental spectrum. The amount of inelastic scattering ($D_{\text{inel}} = 0.85$) we have to impose is high, but seems reasonable compared to the values inelastic loss found in the experiment. Indeed, for the clean Cu substrate, the low energy tail ($< 30\,\text{eV}$) was found to have an intensity of ~ 1.7 times the amplitude at higher energies ($> 30\,\text{eV}$) [8]. If we assume that the scattered Auger electrons generate no secondary electrons, this amounts to a relative contribution of 63% of inelastically scattered electrons to the spectrum. From Table 6.2, we can calculate that the inelastic electrons make up 61%, 44% and 40% of the spectrum for the Shirley, Tougaard and plasmon cross sections, respectively, if we set $D_{\text{inel}} = 0.85$. Hence, we conclude that inelastic scattering forms a plausible explanation for the discrepancy between experiment and the theoretical result. We note, however, that there are too many other possible sources of error to make a definite conclusion.

D_{inel}	Shirley	Tougaard	plasmon
0.25	0.94	0.88	0.87
0.50	0.82	0.69	0.67
0.75	0.57	0.42	0.39
0.85	0.41	0.27	0.25

Table 6.2: Comparison of the total VVV amplitudes with inclusion of inelastic scattering relative to the result without. The columns give the results for each cross section for several values of the relative amount of inelastic scattering D_{inel}. Note that the relative contribution of electrons that have been scattered inelastically at least once can easily be calculated from this table as $(I - (1 - D_{\text{inel}}))/I$, with I the relative VVV amplitudes given in the table.

6.3.5 Effect of the escape function

We now investigate an alternative modification to our model that can ameliorate the agreement between theory and experiment. Specifically, we now are interested in the effect of the α and β parameters of the escape function in Eq. (6.13). Hagstrum namely noted in his work that the simple geometric factor, which assumes that the momentum distribution of final state electrons with energy ϵ_k is isotropic, yields insufficient amplitude of the spectrum at low energies in ion neutralization experiments [144]. He explained that the observed enhanced amplitude indicates that the momentum distribution of excited electrons is not isotropic. Hence, he introduced the parameters α and β in the escape function to fit the spectrum. In our problem, it seems unlikely that the momentum distribution of the final electrons is isotropic as well, considering the states involved in the transitions are part of a 2D system.

We start again from the unmodified VVV spectrum discussed in Sec. 6.3.2, ignoring cascade effects and inelastic scattering . In Fig. 6.11(a), we show the dependence of the escape function on both parameters. It is clear from the curves shown, that we can significantly modify the amplitude at low energies by tuning α and β.

Fig. 6.11(b) compares the shape of two modified VVV spectra with the measured and unmodified VVV spectra, shown in teal and orange, respectively. The green curve shows the result published in our work (Ref. [8]), obtained with the choices $\alpha = 1/4$ and $\beta = 1/2$, and gives better agreement of the amplitude between in the range $1 - 4\,\text{eV}$. The agreement is further enhanced when experimental broadening is accounted, as shown in Fig. 6.12. It is noteworthy that this value of α is also used in Hagstrum's work [144] and more recent applications of his model [164, 165], although in conjunction with $\beta = 1$. Comparing the dashed yellow and teal curves with the orange curve in Fig. 6.11(a), we see, though, that β mainly influences the overall amplitude of the spectrum and not so much its shape.

Better overall agreement with experiment is obtained by a more drastic change of the parameters to $\alpha = 3/2$ and $\beta = 10$. It is obvious we can likely fit whatever shape we want with unrestricted tuning of the escape function parameters. Whether the result with these parameters is realistic thus depends on if the escape probability shown in Fig. 6.11(a) accurately models the effect of the Auger matrix elements, and electron escape mechanisms.

In light of our last remark, we conclude this section by making some critical remarks about the appropriateness of the escape function in this study. First, we recall that the escape function is derived from a semi-classical picture in which the particle approaches

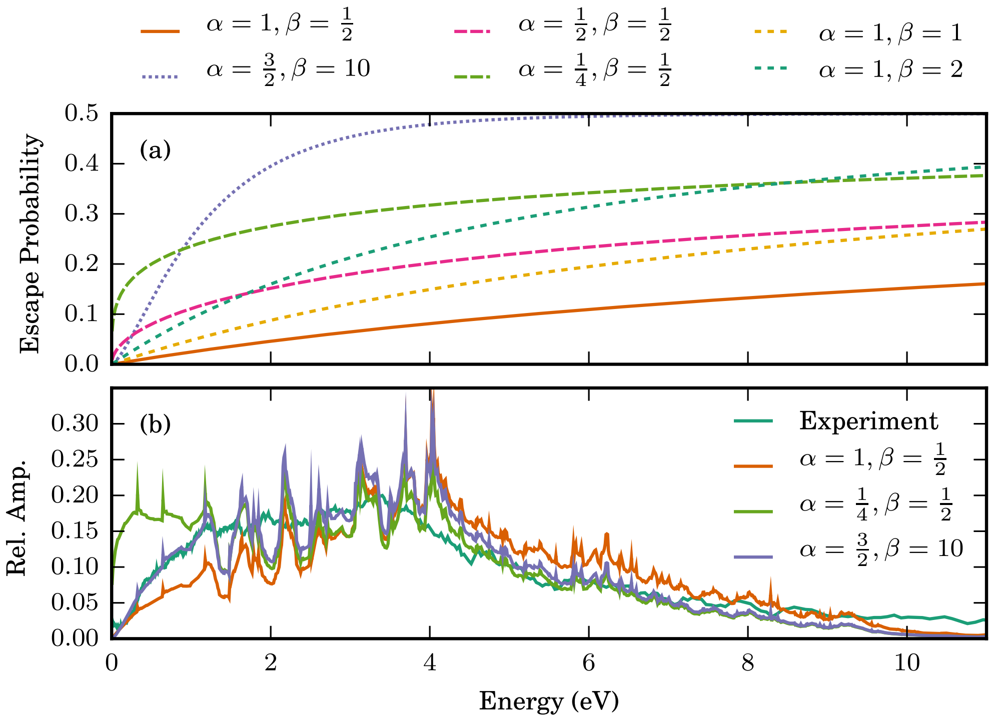

Figure 6.11: Panel (a) shows the dependence of the escape function from Eq. (6.13) on the parameters α and β. Increasing β and decreasing α both increase the escape probability. Panel (b) shows the effect on the shape of the VVV spectrum for two choices of parameters that give a good fit to the experiment. The unmodified result with $\alpha = 1, \beta = 1/2$ is also shown for comparison.

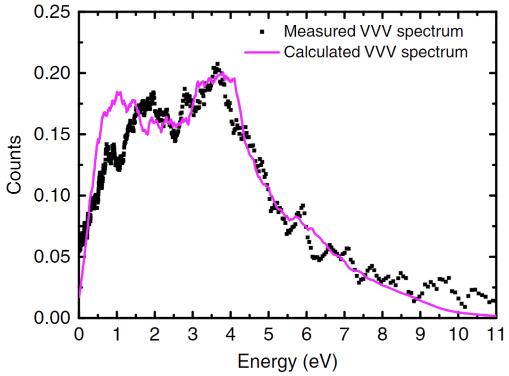

Figure 6.12: Comparison of the experimental spectrum (dots) and the calculated spectrum (line) for SLG on a Cu (111) substrate. The calculated spectrum is obtained with the parameters $\alpha = 1/4$ and $\beta = 1/2$ in the escape function from Eq. (6.13), and is broadened by an experimental response function, the details of which are given in Ref. [8]. Figure taken from Ref. [8].

an energy barrier from within the sample. We immediately run into issues when we go along with this line of reasoning. Indeed, if the excited states are created in the graphene sample, and if they are truly excited states of graphene, they need to have a momentum vector that lies in the plane of the graphene layer (otherwise they would escape). According to the classical picture, none of these electrons get to the vacuum because they have no (net) momentum component perpendicular to the sample. Hence, a collision process of some sort would be required for electron emission. An accurate model for the escape probability of electrons might thus require inclusion of phonon assisted electron emission. Another problem with the classical picture is that it does not consider the possibility that the Auger process couples immediately to a vacuum state, without the intermediate excited bulk state. It does seem likely that there is some overlap of vacuum states with the graphene orbitals, considering it is only a single atom thick. Such processes can be expected to increase the net 'escape probability' of the electrons at low energies. It is hard to judge how pronounced this effect is, however, and a definite answer likely has to come from an actual calculation of the Auger matrix elements.

6.3.6 Branching ratio

Introduction: Now that we have analysed in detail the VVV spectrum and searched for explanations for the differences seen between experiment and theory, we attempt to estimate the branching ratio of the Auger process for holes in the valence band. With branching ratio, we mean the number of excited holes that decay to the top of the valence band through Auger processes, compared to all possible decay channels, which include e.g. excitation of phonons or electron-hole pairs close to the Fermi-level.

In experiment, the measured intensity of the VVV peak was 21 ± 4 times the intensity of the KVV peak associated with a primary hole in the C($1s$) level [8]. What we will do in the following is determine this ratio from our calculated data, assuming that all holes decay through Auger processes. According to Ref. [166], the transition rate for the Auger process with a hole in the C($1s$) level is about 285 times larger than for radiative decays. Hence, for the KVV peak, our approximation is likely quite accurate. For the VVV transition rate, we expect an overestimation, since transition rates for alternative decay channels are expected to become more important for holes closer to the Fermi level. The ratio derived from experiment over the ratio obtained from theory then gives an estimation of the branching ratio for the Auger process for holes in the valence band. In what follows, we will attempt to get a conservative estimate of the branching ratio, which we can obtain by making sure we do not under- and overestimate the valence and core contributions to the spectrum, respectively.

The theoretical ratio of the VVV and KVV transition rates is given by

$$R = \frac{\lambda_v}{\lambda_{1s}} \frac{I(A_{VVV})}{I(A_{KVV})}, \tag{6.21}$$

where λ_v and λ_{1s} are the annihilation rate of positrons with valence electrons, and C($1s$) electrons, respectively. The integrated intensities of the VVV and KVV spectra are denoted $I(A_{VVV})$ and $I(A_{KVV})$[9].

Annihilation rates: The annihilation rates for the systems are summarized in Table 6.3. To make a fair comparison with experiment, we will take the annihilation rates obtained

---

[9] Remember that the intensities of the spectra are normalized such that every hole decays through an Auger process, i.e. Eq. (6.8)

	Graphene			Graphene + Cu (111)	
	λ_{1s}	λ_{2s+2p}	λ_v	λ_{1s}	λ_{2s+2p}
WDA/LDA	2.356e-05	1.890e-03	1.630e-03	1.937e-05	1.650e-03
IPM	1.394e-05	5.950e-04	5.335e-04	1.158e-05	5.145e-04

Table 6.3: Annihilation rates calculated for free standing graphene and graphene on a Cu (111) substrate. Subscripts indicate the partial annihilation rates with valence electrons, C(1s) electrons, or C(2s) and C(2p) electrons. The first row gives the annihilation rates obtained with inclusion of the enhancement factor, the second those without. The IPM is more appropriate for core electrons, the result with enhancement gives more accurate results for the valence electrons. Stated values are in ps^{-1}.

for the system with inclusion of the Cu (111) substrate, though, the difference in the ratio of the annihilation rates is not that different from the result without substrate. From the values in Table 6.3 for SLG, we find that the annihilation with valence electrons is somewhat exaggerated using free atomic orbitals (λ_{2s+2p}) as compared to the self-consistent electron density (λ_v). The influence on the fraction of the annihilation rates is, however, rather modest. Keeping in mind we are after a conservative estimate of the branching ratio, we will continue to work with the orbital annihilation rates. In this light, we should also select the IPM annihilation rates for the core orbitals, as the LDA enhancement factor is known to overestimate the core annihilation [59].

Intensity fraction: To determine the KVV intensity, we assume that the C(1s) level has a sharp energy level at 263 eV below the vacuum level, such that its amplitude is simply obtained by the escape probability evaluated with said escape energy. We do not want to underestimate the VVV transition rate, hence we neglect the inelastic scattering investigated earlier. It is more difficult to make a decision for the parameters of the escape function, as the choices considered earlier increase the VVV over the KVV intensities, but is unclear how realistically the results describes the Auger matrix element effects and escape probabilities. Hence, we summarize the results for various choices of the α and β parameters in table 6.4.

Discussion: From table 6.4, we see that only our most conservative estimate, which is not expected to be very accurate, gives a branching ratio $B = 0.459$ in which a slight minority of the holes in the valence band relax through Auger transitions. The Auger process is clearly the dominant decay channel, for all other cases. In fact, for many choices of parameters we find results which indicate that the VVV process would be more than 100% efficient, which is impossible unless a single hole in the valence bands results in the emission of multiple Auger electrons. We showed that cascade effects cannot account for a significant increase of the amplitude, and inclusion of inelastic scattering in our calculations would only increase the branching ratio. We could thus pose that the predicted branching ratios support the claim that the escape function does not provide a reasonable description of the escape probability for many parameters.

A quantitative estimate of the branching ratio is clearly not possible from our current results. We can, however, conclude quite confidently that the Auger process is the dominant decay channel for holes deep in the valence band. Ignoring the results with $\alpha = 0, \beta = 0$, we find a branching ratio of at least $> 65\%$ and more likely $> 80\%$, obtained by taking $R_{\text{exp}} = 21$ instead of the lower bound.

	$\alpha = 1, \beta = \frac{1}{2}$	$\alpha = \frac{1}{4}, \beta = \frac{1}{2}$	$\alpha = \frac{3}{2}, \beta = 10$	$\alpha = 0, \beta = 0$
$\frac{I(A_{VVV})}{I(A_{KVV})}$	0.036	0.149	0.183	0.260
R_{LDA}	3.103	12.700	15.561	22.161
R_{IPM}	5.189	21.236	26.020	37.056
B_{LDA}	5.478	1.339	1.092	0.767
B_{IPM}	3.276	0.801	0.653	0.459

Table 6.4: Overview of several theoretical ratios relevant to estimate the branching ratio of the VVV Auger process, for various choices of the escape function parameters. The first three columns correspond with the curves shown in Fig. 6.11, and the last with an escape probability of 1/2 for all electrons above the vacuum level. Peak intensities of the VVV over the KVV Auger transitions are given in the first row. Predicted ratios R, as defined in Eq. (6.21), are obtained from this result after weighting by the annihilation rates of the positron with the different orbitals, and are shown in the second and third row. The bottom two rows give the estimate for the branching ratio B, obtained by dividing the experimental peak ratio, for which we took the lower bound of $R_{\mathrm{exp}} = 17$, over the calculate one. The subscripts denotes whether the LDA or IPM annihilation rate for the C($1s$) orbital was taken.

6.4 Conclusions

6.4.1 Summary

PAES experiments performed on graphene deposited on a Cu (111) substrate showed compelling evidence for Auger emission initiated by holes in the valence band of graphene, denoted a VVV Auger process. In this chapter, we presented a thorough theoretical investigation of this process, based on first-principles calculations and a simple model for the Auger process.

As a first step, we performed first-principles calculations which showed that for graphene on the Cu (111) substrate, the positron groundstate is a surface state. Furthermore, we found that 96% of the annihilation occurs with electrons from the graphene layer. These results are important, as they confirm that VVV process should indeed be observable in experiment.

Next, we considered a model for the VVV spectrum which is an extension of a similar model for Auger neutralization formulated by Hagstrum [143], where the hole has a fixed energy, to a distribution of holes determined by the electron-positron annihilation. The main approximations of the model are the neglect of the Auger matrix elements and the introduction of a semi-classical energy dependent escape function that describes the transition of excited electron in the material to the vacuum. All other quantities that enter in the model, were obtained from our first-principles calculations.

One issue encountered early on in our study, was the lack of spatial selectivity that resulted from the neglect of the matrix elements. However, we argued that mostly the graphene states should be involved in the VVV process, and by using the electronic structure of a free standing graphene layer, we obtained satisfactory agreement with experiment. The measured VVV spectrum shows somewhat higher intensity at low energies, and a slightly longer tail at higher energies, however.

To explain the low-energy discrepancy we considered (i) cascade effects (ii) inelastic scattering of Auger electrons and (iii) the possible effects of the Auger matrix elements through tuning of the escape function parameters. It was found that cascade effects, even with the upper bound that we considered, only have a very small effect on the amplitude. The simple model we considered for inelastic scattering does give an important improvement compared to experiment. Furthermore, the amount of inelastic scattering assumed to obtain the agreement is close to the inelastic scattering found in PAES experiments for Cu. Alternative to inelastic scattering, we managed to obtain better agreement with experiment also with a modified escape function, although it is unclear how realistic these results are.

Finally, by comparing the KVV and VVV peak intensities with experimental results, we found that the VVV is the dominant decay channel for holes deep in the valence band. Indeed, our results show that the branching ratio lies somewhere between 65% and 100%.

6.4.2 Outlook

It would be interesting in future work to explicitly take into account the matrix element effects, as it remains the main source of uncertainty in our results. Indeed, inclusion of the matrix elements should solve the issue of the spatial selectivity described previously. Next, the escape function and its related uncertainties can be reduced, and could allow one to make a more definite conclusion about the importance of inelastic scattering. Additionally, it would allow us to get a tighter estimate of the branching ratio of the VVV Auger process. Finally, the effect of the substrate, which we had to neglect to isolate the graphene electronic structure, could be assessed. A second possible refinement of the model could include some correlation effects we have neglected in this study. For example, we did not investigate the effect of the final state hole-hole interaction energy, which could shift the peak in the calculated spectrum to lower energies.

Chapter 7

The positron state in CdSe quantum dots

In this chapter we attempt to resolve a long standing debate on the question whether positrons annihilate from the interior of colloidal CdSe Quantum Dots (QDs) or primarily from a surface state. The results presented here are published in Ref. [167].

7.1 Introduction

Positron spectroscopy proves useful in the study of embedded [168–172] and colloidal QDs [136, 173–176]. In both cases, positrons act as self-seeking[1] probes for the nanoparticles if the positron can occupy a lower energy state inside or at the surface of the dot compared to its surroundings[2]. Especially the self-seeking property of the positrons makes PAS a powerful tool for characterizing the electronic properties of QDs.

In the present study, we focus on colloidal CdSe QDs. CdSe, CdS, PbSe and PbS nanoparticles are promising candidates for, among other applications, use in solar cells because of their size-tunable optical properties. Due to confinement of frequencies in the electrons and holes, the absorption/fluorescence frequency of nanoparticles can be tuned over a wide range of the visible spectrum with particles sizes between $\sim 2-8$ nm. Hence, by selecting a size distribution of particles, an absorber layer with a wide absorption band can be manifactured. Recently, some of these QD solar cells have exceeded 10% power conversion efficiency [178]. One limiting factor arises from dangling bonds at the surface, which can form electron or hole trap states in the bandgap of the material, that promote carrier recombination. Hence, dangling bonds are detrimental for the power conversion efficiency of the QDs, and it is desirable to passivate them.

---

[1] Self-seeking in the sense that in experiment, one can rely on trapping of positrons inside or at the surface of the nanoparticles during their diffusive motion through the host matrix or through the colloid, without having to deposit the positrons precisely in the region of interest.

[2] For interfaces, the positron affinity $A^+ = \mu^- + \mu^+$, with μ^- and μ^+ the electron and positron chemical potentials, is a useful quantity to estimate if trapping in embedded QDs is probable. Indeed, it turns out that the difference in the positron affinities of two materials α and β is equal to the energy difference of the positron levels after the electron chemical potentials aligned, $A^+_\alpha - A^+_\beta = E^+_\alpha - E^+_\beta$ [177]. Hence, for trapping of positrons in an embedded QD of material β in a host matrix of material α, one needs to have $A^+_\alpha > A^+_\beta$. Note that this ignores confinement effects in the dot as well as other possible interface effects.

During solution based synthesis, QDs are typically capped with ligands [179]. A first reason for this is that attachment of ligands to the surface prevent clustering of particles during growth. Importantly, ligands also passivate dangling bonds at the surface, though the efficiency of the passivation depends on the type of ligand used [178]. A second reason is that the size of the ligands determines the distances between neighbouring QDs, which is important to tune the electronic coupling between the nanoparticles required for the transport of charge carriers. Hence the ligands should preferably be short[3] [180]. Finally, ligands are also found to influence the charge carriers' lifetime [180]. Not all ligands are suitable for synthesising the QDs, however. Thus, ligands are often replaced in a post-processing step called ligand exchange. Unfortunately, this process often creates extra dangling bonds at the surface [178]. Much research is conducted to determine the ideal ligands, which may differ depending on the envisioned application, as well as the process to attach them to the surface.

From the above, it is clear that precise information on the surface conditions of colloidal QDs is important to gain insight into the effect of different ligands on the surface conditions of the particles. The unique property of PAS, where positrons are believed to be attracted to the surface of the QDs, provides a potentially powerful tool in the study of these type of systems. Especially because with other technique the surface conditions of these nanocrystals are difficult to assess without a large background from the rest of the sample. For colloidal CdSe QDs, there is, however, discussion on the annihilation site of the positron. Hence, the annihilation of the positron from a surface state should first be established before trends in the annihilation spectra can confidently be attributed to changes in the surface conditions. We give an overview of the discussion in the literature on the topic in the next section.

7.2 Overview experimental results

The study of colloidal QDs with PAS was initiated by Weber *et al.* [173], who measured Doppler broadening spectra of CdSe QDs between 1.8 − 6.0 nm in diameter. They observed an increasing broadening of the electron-positron momentum density in particles with decreasing size, which is consistent with widening of the electronic band gap [181]. The same work reports a positron annihilation lifetime of 251 ps for the 6 nm QDs, which is significantly lower than the bulk CdSe lifetime of 275 ps reported in the same paper. Along with the very small Ps component ($< 1.3\%$), they concluded that positron get efficiently trapped inside the QDs and annihilate from the bulk (i.e. interior) of the dots.

Later, work conducted by Eijt *et al.* [136] largely reproduced the trends in the electron-positron momentum density found by Weber. Additional ACAR data and comparison with first-principles calculations for bulk CdSe showed, however, that the results were difficult to reconcile with the model of a positron annihilating in the bulk of the QD. In particular, the high momentum part of the momentum density revealed a strong but constant decrease as function of the particle's size in the contribution of Cd ($4d$) electrons when compared to the bulk sample. The observed effect is much larger than predicted by first-principles calculations for Cd vacancies [79]. Additionally, the authors argued that unrealistic concentrations of these vacancies should be present to explain the effect. Instead, they proposed a model in which the positron is strongly confined at the surface of the dot. The decreased annihilation with the Cd ($4d$) electrons is attributed to the

---

[3] Obviously, though, one wants to avoid clustering of the particles to retain the increased bandgap compared to bulk CdSe

outward relaxation of the Se atoms at the surface. With the exception of the positron annihilation lifetime, this model does not contradict the measurements of Weber.

Sharma *et al.* [182] also performed measurements on CdSe QDs, but of larger sizes ($7 - 17$ nm). Their results indicate an increased annihilation of positrons with Cd ($4d$) electrons with increasing QD sizes. The authors attribute this trend to an increase of Cd vacancies as the size of the QDs shrinks.

New positron annihilation lifetime measurements for CdSe QDs with a mean diameter of 6.5 nm capped with various ligands were recently reported by Shi *et al* [167]. In contrast with the initial work of Weber, this new work reports positron annihilation lifetimes well above the bulk CdSe value (275 ps), and rules out annihilation from bulk. With only weak dependence on the capping ligands, a lifetime component not attributable to Ps in the narrow range of $358 - 371$ ps was measured. The contribution of the component to the total annihilation was found to lie between $77 - 86\%$. Hence, the contribution of Ps is also significantly larger than reported in Weber's work. The observed increase in the lifetime ($+83 - 96$ ps) is much larger than calculated for Cd and Se monovacancies ($+12 - 19$ ps) [79, 183]. The Cd-Se divacancy is predicted to show an increase of 78 ps in the annihilation lifetime [183]. Although closer to the observed shift, the increase is still too small, and would anyways require unlikely high defect concentrations to explain the data. Hence, these results seem to point convincingly in the direction of a positron state at the surface of the CdSe QDs. In the rest of the chapter we investigate if this interpretation is supported by first-principles calculations.

7.3 Positron calculations

We now investigate from first-principles the nature of the positron state in CdSe QDs. As we have discussed in the preceding section, experimental data points convincingly in the direction of a positron surface state. In our calculations we will check if the positron groundstate is indeed located at the surface, and analyse the Se and Cd contributions to the annihilation rate.

Modeling entire QDs is computationally difficult, as a 6 nm diameter dot contains several thousand atoms. Only for the smallest particles (< 2 nm) it is feasible to simulate the complete particle. Instead, we will perform simulations for low index non-polar CdSe surfaces, which serve as a model for individual facets of a real QD. Computational details are given in Appendix 7.A.

7.3.1 Bulk properties

We begin our study with calculating the annihilation properties of the wurtzite CdSe bulk crystal, using relaxed lattice parameters. Using the Drummond LDA [56], we find a lifetime of 246 ps which is significantly shorter than the value measured by Weber *et al.* [173], but in good agreement with other calculations which find $253 - 254$ ps [79, 183]. The parameter-free GGA [62] on the other hand compares, with 267 ps, fairly good with experiment[4].

It is noteworthy that the bulk lifetime for CdSe reported by Weber [173] is close to the lifetime calculated for a Cd monovacancy in Refs. [79, 183]. At the same time, our calculated bulk lifetime in the defect-free crystal is close to the value reported by Weber for the CdSe QDs. It is tempting to reinterpret $\tau = 251$ ps as the bulk lifetime and

---

[4] With experimental lattice parameters [89], the LDA gives $\tau = 236$ ps and the parameter free GGA $\tau = 257$ ps

	Cd (4d)	Cd (5s)	Se (4s)	Se (4p)
LDA	0.165	0.319	0.089	0.384
WDA	0.200	0.225	0.122	0.373

Table 7.1: Relative contribution of the valence electron shells to the total annihilation rate as calculated with the LDA and the WDA with $Q = 1.35$.

$\tau = 275$ ps as the Cd mono vacancy lifetime. Unfortunately, no other sources report experimental lifetimes for CdSe, making it difficult to confidently draw conclusions. Hence, in the rest of the chapter we follow the interpretation of Weber *et al.*, and take the values of $\tau = 275$ ps for the defect free bulk lifetime.

We now apply the screening parameter tuning scheme proposed in Sec. 3.3.4. With $Q = 1.00$, the WDA overestimates the lifetime significantly: $\tau = 327$ ps. According to our discussion in Chapter 3, this can be attributed to the presence of the Cd (4d) electrons. By raising the screening parameter to $Q = 1.35$, we can reproduce the experimental value.

Part of the arguments given in the papers of Eijt and Sharma, rely on the contribution of the Cd (4d) electrons to annihilation spectra. For this reason, we calculate the relative contributions of the valence electron shells to the total annihilation rate[5]. The results are summarized in Table 7.1. We will use these results at a later stage when we compare the annihilation properties for the surface and bulk state. Note the large differences between the WDA and LDA. We expect that the WDA overestimates the relative contribution of the Cd (4d) and Se (4s) electrons. However, because we will only compare the contributions to the different shells in the surface calculations relative to the bulk obtained with the same functional, the overestimation should not be an issue.

7.3.2 Surface states

Standard approach

We now look at the surface states as predicted by the CMM and the WDA following the approaches we developed in earlier chapters, i.e. we use the background edge of the material as the image potential reference plane in the CMM and the screening parameter that reproduces the bulk lifetime in the WDA. The background edge positions are $z_0 = 1.84$ bohr (0.93 Å) and $z_0 = 1.91$ bohr (1.01 Å) for the CdSe $(10\bar{1}0)$ and CdSe $(11\bar{2}0)$ surfaces, respectively[6]. The positron annihilation lifetimes obtained with these values are, respectively, $\tau = 259$ ps and $\tau = 274$ ps. Both of these values are very close to the bulk lifetimes, and thus indicate that the positron groundstate is not located at the surface. In the WDA, setting $Q = 1.35$ as determined in the previous section, we find $\tau = 327$ ps and $\tau = 333$ ps for the CdSe $(10\bar{1}0)$ and CdSe $(11\bar{2}0)$ surfaces, respectively. Although these values are clearly lower than the experimental values, they are significantly closer than the CMM prediction. The large increase in the lifetime compared to the bulk lifetime signals that the positron does not annihilate (purely) from the bulk.

The positron states corresponding with the lifetimes, are shown as full lines in Fig. 7.1(a)

---

[5] Note that we used the free atomic densities instead of the self-consistent valence electron density to obtain these results

[6] The distance between the background edge and the centre of the induced charge density, calculated in accordance with the approach detailed in Table 4.3, yields $(z_b - z_0)_{\text{jellium}} = 1.51$ bohr. Including this shift leads to lifetimes between $\sim 340 - 350$ ps for the two CdSe surfaces. Hence this approach overestimates the experimental lifetimes but results in surface states. We discuss the results of the CMM with other values of z_0 later in the chapter.

and Fig. 7.1(b) for the CMM and WDA, respectively. We see that, as anticipated from the positron lifetime, the CMM model yields a positron state that is mainly localized in the bulk of our slab model. On the other hand, the WDA predicts a state that has a clear peak at the surface and decays slowly in the bulk of the material. Since the state has a non-negligible overlap with atoms up to > 20 a.u. below the surface, a significant bulk-like contribution to the annihilation signal can be expected.

Parameter analysis

So far, we have followed the approach that we developed in the previous chapters. It is interesting at this stage, however, to vary the parameters in both models, i.e. the image potential reference plane in the CMM and the screening parameter Q in the WDA, and fit the measured surface lifetimes. This way, we can evaluate what kind of positron states corresponds with the experimental lifetime in both models.

We plot the calculated positron annihilation lifetimes as a function of z_0 and Q in Fig. 7.2(a) and Fig. 7.2(b), respectively. The shaded area indicates the range of the lifetimes determined from experiment.

First, we discuss the evolution of the lifetimes in the CMM result. We note that between $z_0 \sim 1.8$ bohr and $z_0 \sim 3.0$ bohr, the positron annihilation lifetime increases steeply. This signals the transition of the positron groundstate from one that is located dominantly in the bulk of the material, to one that is located at the surface. This is also illustrated in Fig. 7.1(a). For $z_0 > 3.0$ bohr the lifetime saturates because the positron is already dominantly localized at the surface and the change in the electron-positron overlap becomes much smaller. The experimental lifetime is reproduced with $z_0 = 2.3$ bohr, which gives a lifetime of $\tau = 371$ ps for the CdSe $(10\bar{1}0)$ surface and $\tau = 369$ ps for the CdSe $(11\bar{2}0)$ surface. Fig. 7.1(a) shows this state in the dashed blue line for the former. Hence, in the CMM, the state that is consistent with the experimental lifetime, is one that is strongly localized at the surface with minimal overlap beyond the second layer below the surface.

We now turn to discuss the influence of the screening parameter on the WDA prediction for the lifetime. Fig. 7.2(b) shows a strong increase of the lifetime as we lower the screening parameter to $Q = 1.00$. Two effects are into play here. First, Fig. 7.1(b) shows that the positron becomes more localized at the surface if Q is decreased. This decreases the electron-positron overlap and thus the annihilation rate. The second effect comes from the fact that Q controls the charge in accumulated in the screening cloud, and hence determines the enhancement factor[7]. The lifetimes that corresponds with the experimental results are obtained with $Q = 1.30$ which gives $\tau = 357$ ps and $\tau = 359$ ps for the CdSe $(10\bar{1}0)$ and CdSe $(11\bar{2}0)$ surfaces, respectively. The corresponding state for the former surface (dashed blue line in Fig. 7.1(b)) is qualitatively very similar to the result with $Q = 1.35$. The peak at the surface is slightly more pronounced and the state decays somewhat faster in the bulk. In the WDA the measured lifetime thus also corresponds with a surface state. In contrast to the CMM, however, a significant annihilation signal from the bulk is expected. The slow decay of the positron state in the bulk of the QDs could additionally explain the increased annihilation with Cd $(4d)$ observed for larger QDs in Ref. [182], as the surface to volume ratio decreases.

---

[7] A decrease in Q leads to a decreased annihilation rate, or increased lifetime. Note that we increased Q in the first place to obtain a shorter lifetime in the bulk calculation.

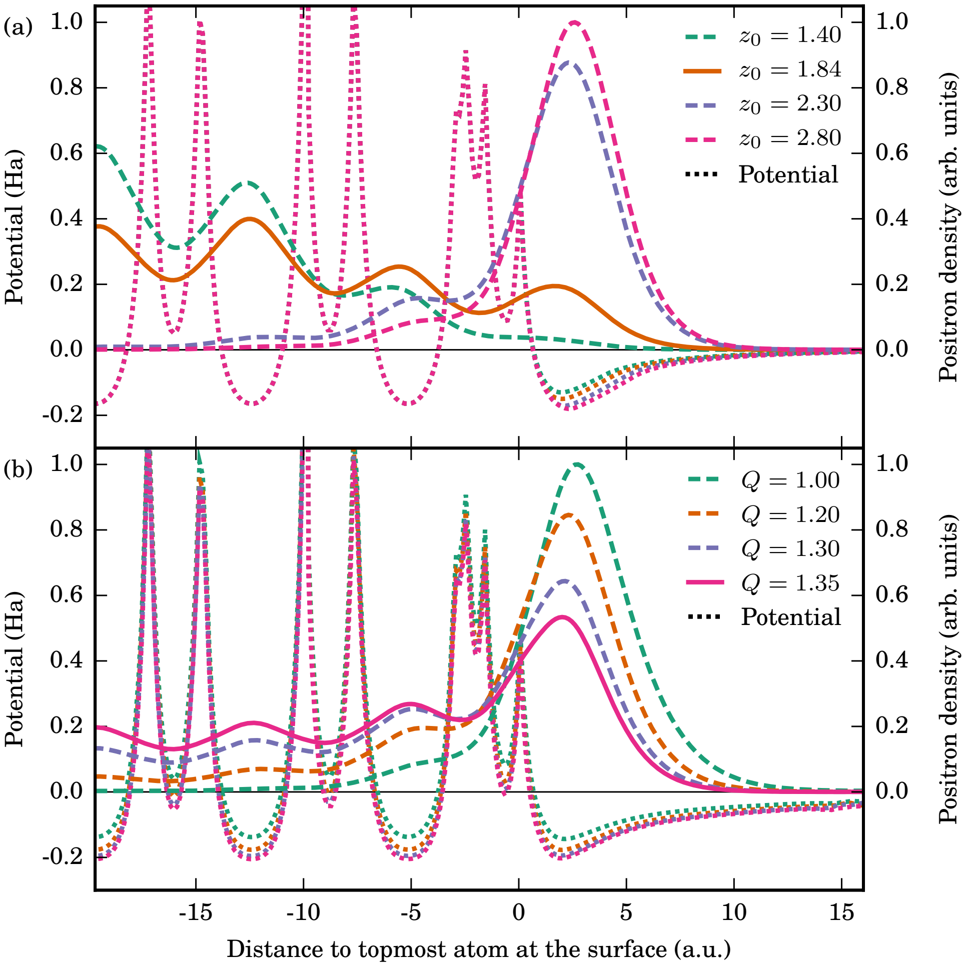

Figure 7.1: Positron potential (dotted lines) and density (full and dashed lines) at the CdSe $(10\bar{1}0)$ surface as calculated with (a) the CMM and (b) the WDA. Quantities are averaged over planes parallel to the surface. The full lines show the positron density obtained using the standard approach for (a) the background edge position $z_0 = 1.84$ bohr as the image potential reference plane and (b) the screening parameter $Q = 1.35$ that reproduces the experimental CdSe bulk lifetime. Dashed lines give the positron densities obtained by varying these parameters. The corresponding potentials are shown in the same color as the positron density.

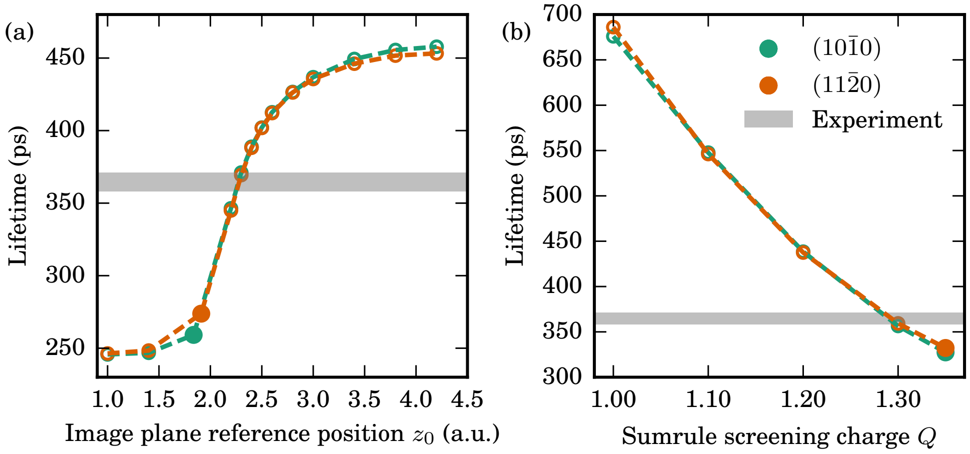

Figure 7.2: Lifetimes as computed with (a) the CMM as a function of the image potential reference plane z_0, and (b) the WDA as a function of the screening parameter Q. Markers indicate the calculated values; lines serve as a guide to the eye. The results with $z_0 = 1.8$ bohr and $Q = 1.35$ are shown in filled markers to emphasise that they are obtained by following the standard approach. The grey area in both panels indicates the range of lifetimes measured in the experiments [167].

7.3.3 Overlap with Cd and Se

We now discuss the change in the annihilation rate with the different orbitals at the surface compared to bulk. Eijt *et al.* found, from their analysis of the momentum density, that the annihilation with the Cd (4*d*) electrons is reduced by 50% at the surface [136]. They attribute this to the outwards relaxation of the Se atoms.

Our calculated results are summarized in Table 7.2. We have used the parameters $z_0 = 2.3$ bohr and $Q = 1.30$ that reproduced the experimental lifetimes at the surface. The values are given relative to the contributions found in the bulk calculations[8], given in Table 7.1.

Although the precise numeric values vary, the results obtained with both the CMM and WDA follow the same trend for both surfaces. There is a decrease in annihilation with the Cd orbitals of $10 - 20\%$ and a likewise increase in annihilation with the Se atoms. Notably, our results do not reproduce the strong 50% decreased annihilation with the Cd (4*d*) electrons reported in Eijt's work [136]. One possible explanation follows from the observation that the TOPO ligands used in their study bind preferably with the Cd atoms at the surface [136, 184, 185]. The presence of the ligands reduces the free volume available in the vicinity the Cd sites and as such further promotes annihilation with outward relaxed Se atoms.

Ref. [136] also notes that their measured ACAR profiles do not contain a clear fingerprint of the TOPO molecules. Furthermore, the same study obtained similar ACAR

---

[8] The bulk values with the WDA are obtained with $Q = 1.35$, hence we are comparing orbital annihilation rates obtained with different Q parameters. The fractions obtained with either $Q = 1.30$ or $Q = 1.35$ in both the bulk and the surface calculation, has little effect in the fractions reported here, however.

	Cd ($4d$)	Cd ($5s$)	Se ($4s$)	Se ($4p$)
$(10\bar{1}0)$ CMM	0.829	0.875	1.113	1.159
$(10\bar{1}0)$ WDA	0.862	0.873	1.118	1.116
$(11\bar{2}0)$ CMM	0.852	0.898	1.095	1.133
$(11\bar{2}0)$ WDA	0.900	0.908	1.081	1.086

Table 7.2: Relative contribution of the orbital annihilation rates to the total annihilation compared to the bulk situation. Hence, a value of 0.5 means that the positron only annihilates half as often with a certain orbital compared to annihilation in bulk. The values cited here are obtained with the optimized parameters $z_0 = 2.3$ bohr and $Q = 1.30$ that reproduce the measured surface lifetimes.

results when pyridine capping ligands were used. Although they form weaker bonds, these molecules also preferably bind to the Cd sites. These findings support our interpretation that annihilation with Cd is decreased by the presence of the capping ligands. In fact, the absence of their fingerprint in the ACAR profiles strengthens our claim that the positrons are pushed away from the Cd sites. Indeed, if this were not the case, at least some overlap would be expected with the ligand molecules. Thus, although there is no direct signal from the ligand molecules in the ACAR data, our calculations suggest that they are at least partly responsible for the reduction in the Cd contribution to the spectra.

7.4 Conclusions

We have carried out first-principles calculations on CdSe surfaces to determine the nature of the positron groundstate. To this end, we have followed the approaches we developed in earlier chapters. Calculations with the CMM, in which the background edge is used for the image potential reference plane, predict a positron state in the bulk of the material. The WDA on the other hand, using a screening parameter that reproduced the bulk positron annihilation lifetime, yields a positron surface state which slowly decays in the bulk of the material. The experimental lifetimes, in the range $\tau = 358 - 371$ ps [167], contradict the CMM prediction of $\tau = 259 - 274$ ps, and are somewhat higher than the WDA result of $327 - 333$ ps.

By varying the image potential reference plane position and the screening charge in the CMM and WDA respectively, we found that the experimental lifetimes are reproduced when the positron forms a surface state. In the CMM, the state is strongly confined at the surface and has a non-negligible overlap only with the first couple of layers under the surface. The WDA suggests a significant overlap with the bulk of the material due to the slow decay of the state inside the material.

Our analysis of the orbital annihilation rates for the surface states shows increased annihilation with Se atoms of $\sim 10\%$ relative to bulk, in favour of annihilation with Cd. This is explained by the outwards relaxation of the Se atoms at the surface. Experiments find a much stronger decrease in annihilation with Cd ($4d$) electrons. We attribute this to the presence of the ligands which preferably bind to the Cd sites and push away the positron.

Hence, the combined results reported in Refs. [136, 167, 173, 182] and our calculations, are strongly in favour of positron annihilating from a surface state.

7.A Computational details

Electronic structure calculations presented in this chapter were performed with the PAW method [85] as implemented in VASP [86–88]. A plane wave cutoff of 357 eV was found to be sufficient to converge the quantities of interest. A $11 \times 11 \times 7$ Γ-centered k-grid and two-dimensional grids of comparable density were selected for BZ integration in the bulk and surface calculations, respectively. Exchange and correlation effects in the electronic structure calculations were performed using the PBE functional [65]. Lattice parameters and atomic positions were optimized for the bulk unit cell prior to construction of the surface slab models. In the slab models forces on the atoms were relaxed, keeping lattice parameters fixed. Our slab models contain 12 and 8 atomic layers for the CdSe $(10\bar{1}0)$ and CdSe $(11\bar{2}0)$ surfaces, respectively, which corresponds with thicknesses of 20 Å and 15 Å. Periodic images of the slab are separated by a vacuum of 15 Å.

Positron calculations follow the same procedure as explained in previous chapters. To describe electron-positron correlations, we consider both the CMM, detailed in Sec. 4.3, and the WDA with shell partitioning and sum rule tuning explained in Sec. 3.3.3 and Sec. 3.3.4, respectively. In the shell partitioning scheme, the Cd ($4d^{10}$), Cd ($5s^2$), Se ($4s^2$) and Se ($4p^4$) were taken as the valence electrons. All calculations use the Drummond parameterizations for the homogeneous electron gas [56].

Chapter 8

Summary and Outlook

8.1 Summary

In Chapter 1, we have given a brief introduction to the topic of PAS. We described how positrons, obtained from β decay of a radioactive material or otherwise produced from highly energetic γ rays extracted from a nuclear reactor, are exploited to gain insight into various properties of solid state systems. For instance, the rate with which positrons annihilate in a material is roughly proportional to the electron density, and is thus useful to characterize open volumes. We learned that the photons created in the annihilation process carry information about the electron momentum density in materials. The annihilation radiation is therefore useful both in characterization of the chemical environment of the annihilation site, and for mapping the Fermi-surface of materials. Aside from providing information through their annihilation radiation, positrons can trigger Auger processes as well. Indeed, either through AMPS to the surface, or by creating holes in the occupied electron levels, positrons can generate Auger electrons that provide information about the chemical composition or the electronic structure at the surface of a sample.

The sensitivity of positrons to open volumes has already been exploited to characterize vacancy type defects in metals and semiconductors for several decades. For the same reasons, positrons make a highly sensitive probe for surfaces, as various experiments have repeatedly confirmed. The fact that positrons act as self-seeking probes for open space is convenient on the one hand, but on the other hand often complicates the interpretation of experiments. For this reason, PAS experiments often benefit significantly from guiding first-principles calculations which help with the interpretation of measured data. Bulk solids, including point defects, are quite successfully described in the framework of the 2CDFT with semi-local approximations for the electron-positron correlation. These semi-local approximations are known, however, to fundamentally fail in capturing long-range correlation effects required to describe positron surface states. The common thread through the work presented in this thesis, was to investigate a non-local approach capable of describing these long-range correlation effects correctly.

Chapter 2 dealt with the theory of positrons in solid state systems. Of central importance in the chapter, was the calculation of annihilation characteristics, such as the framework for calculating the electron-positron momentum densities and the positron annihilation lifetimes. We have provided a rather complete derivation starting from the annihilation rate of an isolated electron-positron pair and extending it to the many-body problem relevant in solid state systems. The derivation showed that in the classical limit, electron-positron annihilation properties are determined by the electron-positron contact density, i.e. the probability that the positron resides at the same point in space as an electron. It is worth mentioning that in our derivation we have not made the usual assumption that electron spins in the many-body system are collinear, as such extending the existing theory to deal with non-collinear spin systems. Next, we have shown in some detail how the well-known DFT is extended in the 2CDFT to take into account the effect of the positron. We explained that, in principle, the electron-positron contact density is unobtainable in the framework since it is a two-body quantity and, strictly speaking, the 2CDFT only provides single particle groundstate properties. Generally, though, the annihilation properties can be obtained to good approximation by introducing an enhancement factor which describes the accumulation of the electron density around the positron when it is pinned to a position in space.

In Chapter 3 we started our investigation of the WDA, a non-local functional in which the correlation potential is obtained from the Coulomb interaction of the positron with its screening cloud. We first presented a critical discussion on some aspects of the approach. In particular, we argued that the sum rule, which states that the screening cloud should contain exactly the opposite charge of the positron, is not an exact condition as previously suggested in literature. Instead, it is merely an assumption about the screening properties of the system; one that is realistic for metallic systems, but unlikely to hold for insulators. Our tests with the WDA on a set of elemental bulk materials, showed that the WDA yields poor results for positron annihilation lifetimes without modifications. The problem lies with the fact that the WDA treats all electrons as if they are free electrons. Screening by core and d electrons is therefore severely overestimated, leading in general to a screening cloud which is too delocalized, and as a consequence thereof, an underestimated annihilation rate. By treating core electrons in the LDA instead an important part of the issue was solved. Subsequently, by tuning the sum rule to a value Q, we arrived at an approach with which the experimental lifetimes can be reproduced.

We turned our attention to the description of positron surface states in Chapter 4. At the start of the chapter, we discussed the details of the CMM, a phenomenological model in which the erroneous LDA potential in the vacuum is replaced by the correct image potential. An important parameter in the model is the image potential reference plane z_0, which we showed is hard to determine directly from first-principles calculations. Next, we compared positron workfunctions calculated in the LDA and WDA with experiment. The LDA in general provides an accurate description of the positron state in bulk. Unfortunately, the WDA provides results which are less reliable. Binding energies of positron surface states are well described in the CMM if the image potential reference plane is determined through the Lang-Kohn method. The WDA provides reasonable results in some cases as well, but again not as consistently. Throughout the chapter, our results indicated that changing Q in the sum rule to fit the bulk annihilation lifetime generally does not improve the positron potential. The WDA does provide a qualitative improvement over the CMM by providing a smooth continuation of the potential from bulk into the vacuum. There is also a very limited indication that the description of the contact density is qualitatively improved. On the other hand, we showed that the asymptotic decay of the image potential is incorrect and that positron states calculated in the WDA thus decay too slowly in the vacuum. Despite its current shortcomings, the WDA has the important advantage over the CMM that it does not rely on an ad-hoc correction of the potential in the vacuum region. As a consequence, the former can be applied to complex surface geometries that are inaccessible with the CMM.

Possible applications of PAS in the study of topological surface states were discussed in Chapter 5. We described several experiments that convincingly showed that a positron surface state exists for the TI Bi_2Te_2Se. Positron calculations conducted with the CMM confirmed this interpretation and closely reproduced the binding energy determined from the experiment. After establishing the existence of the surface state, we examined if PAS can provide a useful tool to characterize the topological surface states. A significant overlap between the electron states of interest and the positron indeed indicated this possibility. Calculations of the LCW-map showed that 2D-ACAR experiments should be able to pick up a significant annihilation signal originating from the topological states. Additionally, we demonstrated that PAS experiments should be able to reveal the electronic spin texture at the surface by calculating the magnetic LCW-maps.

An Auger process triggered by holes created in the valence band, termed a VVV process, was the central topic in Chapter 6. From PAES experiments on Cu and graphene deposited on a Cu substrate, where only the latter showed a strong Auger peak at low energies, mechanisms other than the VVV Auger emission were ruled out systematically. Our first-principles positron calculations showed that a positron states exists at the surface of graphene, Cu, and graphene deposited on a Cu substrate. After establishing this requirement for the observation of the VVV process, we turned our attention to the calculation of the lineshape. Based on a model for ion neutralization by Hagstrum, we wrote down a simple model appropriate for a positron annihilation triggered VVV Auger process. The main approximations in the model involve neglecting the Auger matrix elements and introducing a phenomenological function to describe the escape process of excited electrons in the material to the vacuum. All other quantities are determined from electronic structure and positron calculations. The line shape calculated for a free standing graphene layer matched reasonably with the outcome of the PAES measurement, confirming that the VVV process was indeed seen in experiment. In an attempt to improve agreement with experiment, we included cascade effects, in which a single annihilation induced hole triggers multiple Auger electrons, and simple approximations to account for inelastic scattering of Auger electrons in our model. Whereas cascade effects were found to have a negligible effect on the spectrum, inelastic scattering did improve agreement but only if high scattering rates are assumed. Finally, we estimated that the VVV Auger is the dominant channel for decay of holes deep in the valence band, yielding a branching ratio between 65% and 100%.

A long standing debate about the nature of the positron state in colloidal CdSe QDs was resolved in Chapter 7. We presented an overview of the discussion from literature, which showed that it was unclear whether positrons annihilate from the interior, from vacancy type defects in the dots, or from the surface of the particles. New positron annihilation lifetime experiments obtained results that are only consistent with the latter interpretation, however. We presented calculations of the positron state at low index CdSe surfaces using the CMM and WDA and found that the groundstates in these systems are indeed positron surface states. Our analysis of the annihilation rates with Cd and Se electrons reproduced the experimental findings that positrons in CdSe QDs annihilate more often with Se electrons compared to the bulk situation. On a quantitative level, however, the effect in our calculations is not quite as pronounced. This indicates that positrons are pushed away from the binding sites of the ligands to the QDs.

8.2 Outlook

At the start of this thesis, a true first-principles approach applicable to the description of positron surface states was lacking. The work presented here has made some progress on the topic, but further work is definitely required. Nonetheless, we demonstrated that the current state of the theory allows first-principles studies to reliably support experiments. Below, we present some possibly interesting directions to improve the theoretical description of positron surface states.

Our survey of binding energies predicted by the CMM in Chapter 4, as well as accurate binding energy for Bi_2Te_2Se obtained in Chapter 5, shows that the CMM is a useful and accurate model to calculate positron surface states and binding energies for perfect, flat surface geometries. Annihilation properties are somewhat less accurate, due to the lack of a suitable modification of the enhancement factor. We see two important points in which the model can further be improved. The first is to devise a method to calculate the image potential reference plane position z_0 directly from the electronic groundstate. Indeed, currently, the phenomenological methods to determine its value introduce an important uncertainty. In our work, we mentioned that in principle, one can calculate z_0 from the charge density induced by applying a small electrical field perpendicular to the surface. However, this approach does not work for simulations that impose periodic boundary conditions, as most modern electronic structure codes do. A workaround for this problem could significantly boost the reliability of the CMM method. Second, it would be interesting to investigate whether it is possible to come up with a more accurate continuation of the enhancement factor in the vacuum region, rather than abruptly replacing the LDA with the IPM. Such a modification could allow accurate predictions of the annihilation rate and related quantities.

Our work on the WDA revealed several shortcomings of the approach. Though all of them can be traced back to the observation that the assumed non-selective Ps-like pair correlation function is too simple to give an adequate description of the electron pileup around the positron. An important issue, that to some extend can be solved by a partitioning of the electron density, is that all electrons are treated as if they screen the positron charge like free electrons. Further partitioning of the electron density beyond just core and valence, and introducing specific pair correlation functions for each of the components, as done in previous work on the WDA by some authors, is expected to improve the results. At the same time, it introduces many parameters that may undermine the predictive capabilities of the model. Instead, we expect that the best approach might be to calculate a pair correlation function directly from the electronic structure of the material. Indeed, this way the screening properties of the electrons are automatically taken into account, the accuracy of which is controlled by the level of sophistication the pair correlation function is calculated with. Additionally, such an approach is expected to solve the issue with the asymptotic decay of the potential we encountered in Chapter 4. Indeed, by replacing the phenomenological pair correlation function with one derived from the electronic structure, shape approximations are removed and the spreading of the screening cloud over the surface area is expected to be properly described. This should lead to the correct constant in the potential decay far away from the surface.

Although satisfactory agreement of the calculated VVV Auger spectrum with experiment was obtained in Chapter 6, it would nonetheless be interesting to assess the effect of the Auger matrix elements on the line shape. Work in this direction may allow quantitative comparison with experiments.

Finally, it would be interesting to extend our research of the QDs to PbSe. For these nanoparticles, clear effects of different ligands on the electron-positron momentum density were observed. First-principles calculations of the positron surface state and its annihilation properties can help significantly in relating the observed signatures in the momentum density to changes in the structural and electronic properties induced by various ligands. We note, though, that modelling of ligands absorbed on surfaces is likely outside the capabilities of the CMM. Some insights may already be obtained by applying the WDA developed in this thesis, though progress in the accuracy of the functional may be required to allow definite conclusions.

Chapter 9

Samenvatting en vooruitzichten

9.1 Samenvatting

In Hoofdstuk 1, hebben we de lezer een korte inleiding gegeven tot het onderwerp van Positron Annihilatie Spectroscopie (PAS). We beschreven hoe positronen, afkomstig van β verval in een radioactief materiaal of geproduceerd met hoog energetische γ stralen onttrokken uit een nucleaire reactor, gebruikt kunnen worden om inzichten te verwerven in verschillende aspecten van vaste stoffen. Zo is bijvoorbeeld de annihilatie snelheid van een positron ruwweg evenredig met de elektronen dichtheid, wat nuttig is om open volumes te karakteriseren. We zagen dat de fotonen die vrijkomen tijdens het annihilatie proces informatie dragen over de impuls verdeling van elektronen in een materiaal. De annihilatie straling is daarom bruikbaar om de chemische omgeving van de annihilatie site te bepalen, evenals voor het in beeld brengen van het Fermi-oppervlak van materialen. Naast informatie te verschaffen over materialen via de annihilatie straling, zijn positronen ook nuttig om Auger processen te triggeren. Door Auger gemedieerde positronen 'sticking' (AMPS), of door gaten te creëren in bezette elektronen niveaus, kunnen positronen Auger elektronen genereren die informatie dragen over de chemische samenstelling of de elektronische structuur van het oppervlak van een sample.

De gevoeligheid van positronen voor open volumes wordt reeds verschillende decennia gebruikt voor het karakteriseren van vacatures in metalen en halfgeleiders. Verschillende experimenten wijzen uit dat voor diezelfde reden positronen bijzonder gevoelig zijn voor oppervlakken. Hoewel het handig is dat positronen zich gedragen als zelfgeleide projectielen die open volumes opzoeken, is de keerzijde ervan dat dit de interpretatie van het experiment bemoeilijkt. Voor deze reden zijn PAS experimenten vaak sterk gebaat bij ondersteunende eerste principes berekeningen voor de interpretatie van gemeten data. Gebruik makend van semi-lokale benaderingen voor de elektron-positron correlatie, worden bulk materialen en punt defecten behoorlijk accuraat beschreven binnen het kader van de twee-componenten dichtheidsfunctionaaltheory (2CDFT). Van deze semi-lokale benaderingen is echter geweten dat ze fundamenteel falen in de beschrijving van lange dracht correlatie effecten die nodig zijn om positron oppervlakte toestanden te modelleren. De rode draad doorheen dit werk was om een niet-lokale aanpak te bestuderen die in staat is deze lange dracht effecten correct te beschrijven.

In Hoofdstuk 2 hebben we de theorie van elektron-positron annihilatie in vaste stoffen behandeld. Het centrale onderwerp van het hoofdstuk was de berekening van annihilatie eigenschappen, zoals het kader voor de berekening van elektron-positron impuls verdelingen en de positron annihilatie snelheden. Startend van de annihilatie snelheid voor een geïsoleerd elektron-positron paar hebben we de veralgemening naar het veel deeltjes probleem, relevant voor vaste stoffen, gemaakt. Uit de afleiding zagen we dat, in de klassieke limiet, elektron-positron annihilatie eigenschappen bepaald worden door de electron-positron contactdichtheid, dit is de kans dat een positron zich op dezelfde plek bevindt als een elektron. Het is het vermelden waard dat we in onze afleiding niet gebruik hebben gemaakt van de gangbare veronderstelling dat elektronen in het veel-deeltjes systeem colineaire spins hebben, en dat we op die manier de bestaande theorie hebben veralgemeend naar niet-colineaire spin systemen. Vervolgens hebben we in zeker detail getoond hoe de welgekende dichtheidsfunctionaaltheorie (DFT) veralgemeend wordt in de 2CDFT om effecten van positronen in rekening te brengen. We legden uit dat, in principe, de elektron-positron contactdichtheid niet berekenend kan worden in dit kader omdat het een twee-deeltjes grootheid is, en dat strikt genomen de 2CDFT enkel één deeltje eigenschappen levert. Veelal kunnen de annihilatie eigenschappen bij goede benadering echter bekomen worden door een ‘enhancement’ factor te introduceren, die de ophoping van de elektronen dichtheid rond het positron beschrijft wanneer deze zich op een bepaalde locatie bevindt.

In Hoofdstuk 3 zijn we begonnen aan ons onderzoek van de gewogen dichtheid benadering (WDA), een niet-lokale functionaal waarbij de correlatie potentiaal verkregen wordt door de Coulomb interactie tussen het positron en zijn afschermingswolk te berekenen. Eerst gaven we een kritische bespreking van sommige aspecten van de aanpak. In het bijzonder hebben we beargumenteerd dat de somregel, die stelt dat de afschermingswolk een lading bevat die exact tegengesteld is aan de lading van het positron, geen exacte voorwaarde is zoals eerder gesuggereerd in de literatuur. In plaats daarvan is het slechts een veronderstelling over de afschermingseigenschappen van het systeem; één die realistisch is voor metalen, maar waarschijnlijk niet van toepassing is voor isolatoren. Zonder aanpassingen verkregen we in onze testen met de WDA op een verzameling van elementaire bulk materialen povere resultaten voor positron annihilatie leeftijden. Het probleem ligt bij het feit dat de WDA alle elektronen behandeld als vrije elektronen. Afscherming van de positron lading door kern en d elektronen wordt daardoor sterk overschat, wat leidt tot een afschermingswolk die te uitgespreid is, en als gevolg daarvan worden annihilatiesnelheden onderschat. Indien kern elektronen behandeld worden in de lokale dichtheid benadering (LDA) wordt een belangrijk deel van het probleem opgelost. Door verder de somregel aan te passen tot een waarde Q, verkregen we een aanpak waarmee experimentele annihilatie leeftijden gereproduceerd kunnen worden.

De beschrijving van positron oppervlakte toestanden stond centraal in Hoofdstuk 4. Aan het begin van het hoofdstuk, hebben we de details van het gecorrugeerde spiegel model (CMM) besproken, een fenomenologisch model waarin de foutieve LDA potentiaal in het vacuüm vervangen wordt door de correcte beeldlading potentiaal. Een belangrijke parameter in het model is het beeldlading referentie vlak z_0, waarvan we hebben getoond dat het moeilijk direct te bepalen valt uit eerste principes berekeningen. Vervolgens hebben we positron werkfuncties, berekend in de LDA en WDA, vergeleken met experimenten. De LDA geeft in het algemeen een accurate beschrijving van de positron toestand in de bulk van het materiaal. Helaas geeft de WDA minder betrouwbare resultaten. Bindingsenergieën worden goed beschreven in het CMM indien het beeldlading referentie vlak bepaald wordt met de methode van Lang en Kohn. De WDA geeft in bepaalde gevallen eveneens redelijke resultaten, maar opnieuw niet even consistent. Doorheen het hoofdstuk zagen we dat het fitten van de parameter Q in de somregel, om de experimentele bulk annihilatie leeftijden te reproduceren, in het algemeen de beschrijving van de positron potentiaal niet verbetert. Kwalitatief geeft de WDA wel een verbetering ten opzichte van het CMM door een gladde voortzetting van de potentiaal van bulk naar het vacuüm te leveren. Er is ook een zeer beperkte indicatie dat de beschrijving van de contactdichtheid verbeterd wordt in de WDA. Langs de andere kant hebben we getoond dat het asymptotisch afvallen van de potentiaal incorrect is en dat de WDA daardoor positron toestanden voorspelt die te traag afvallen in het vacuüm. Ondanks deze tekortkomingen heeft de WDA het belangrijke voordeel ten opzichte van het CMM dat het niet gebaseerd is op een ad-hoc correctie van de potentiaal in het vacuüm. Als gevolg daarvan kan deze toegepast worden op ingewikkelde oppervlakte geometrieën die niet te beschrijven vallen in het CMM.

Mogelijke toepassingen van PAS in de studie van topologische oppervlakte toestanden werden besproken in Hoofdstuk 5. We beschreven verschillende experimenten die overtuigend aantoonden dat een positron oppervlakte toestand bestaat voor de topologische isolator (TI) $\mathrm{Bi_2Te_2Se}$. Positron berekeningen met het CMM bevestigden deze interpretatie en reproduceerden nauwkeurig de bindingsenergie bepaald uit het experiment. Na het aantonen van het bestaan van de oppervlakte toestand, bekeken we of PAS nuttig kan zijn voor het karakteriseren van de topologische oppervlakte toestanden. Een significante overlap tussen de relevante elektron toestanden en het positron wezen alvast in deze richting. Berekeningen van de Lock-Crisp-West (LCW) map toonden aan dat metingen van de 2-dimensionale correlatie van de annihilatie straling (2D-ACAR) een significant signaal afkomstig van de topologische toestanden zouden moeten kunnen oppikken. Door het berekenen van de magnetische LCW map, toonden we bovendien aan dat PAS experimenten in staat zouden moeten zijn om de elektronische spin textuur aan het oppervlak in kaart te brengen.

Een Auger proces in gang gezet door holtes gecreëerd in de valentieband, een zogenaamd VVV proces, vormde het centrale onderwerp in Hoofdstuk 6. Vanuit positron geïnduceerde Auger elektron spectroscopie (PAES) experimenten op Cu en grafeen op een Cu substraat, waarbij enkel deze laatste een sterk Auger signaal vertoonde bij lage energieën, werden mechanismes anders dan de VVV Auger emissie systematisch uitgesloten. Onze eerste principes positron berekeningen toonden aan dat positron toestanden bestaan aan de oppervlakken van grafeen, Cu, en grafeen op een Cu substraat. Na aantonen van deze vereiste oppervlakte toestanden voor het observeren van het VVV proces, hebben we onze aandacht gericht op het berekenen van de lijnvorm. Gebaseerd op het model van Hagstrum voor ionen neutralisatie, hebben we een eenvoudig model neergeschreven dat van toepassing is op het VVV Auger proces dat in gang gezet wordt door positron annihilatie. De voornaamste benaderingen in het model zijn het negeren van de Auger matrix elementen en het introduceren van een fenomenologische functie die het ontsnappen van elektronen uit het materiaal naar het vacuüm beschrijft. Alle andere grootheden die optreden in het model worden bepaald uit de elektronische structuur en positron berekeningen. De lijnvorm berekend voor een alleenstaande grafeenlaag kwam redelijk overeen met de PAES metingen, wat bevestigd dat het VVV proces inderdaad was waargenomen in het experiment. In een poging om betere overeenstemming te verkrijgen met het experiment, verwerkten we in ons model cascade effecten, waarin een enkele annihilatie geïnduceerde holte meerdere Auger elektronen triggert, en eenvoudige benaderingen om inelastische verstrooiing van Auger elektronen in rekening te brengen. Terwijl cascade effect een verwaarloosbaar effect hadden op het spectrum, vonden we dat in rekening brengen van de inelastische verstrooiing de overeenkomst met het experiment verbeterde, maar enkel indien we hoge mate van verstrooiing veronderstellen. Tenslotte bleek uit schattingen dat het VVV Auger process het dominante kanaal is voor verval van holtes die zich diep in de valentieband bevinden, met een vertakkingsgraad tussen 65% en 100%.

Een reeds lang bestaande discussie over de aard van de positron toestand in colloidale CdSe kwantumdots (QDs) werd beslecht in Hoofdstuk 7. We gaven een overzicht van de bestaande discussie in de literatuur, waaruit bleek dat het niet eenduidig was of positronen annihileren uit het binnenste, vanuit vacatures, dan wel van bij het oppervlak van de deeltjes. Nieuwe experimenten toonden echter aan dat enkel het laatste model consistent is met de gemeten positron annihilatie snelheden. We voerden positron berekeningen uit voor CdSe oppervlakken met een lage index, gebruik makend van het CMM en de WDA, en vonden dat de grondtoestand voor deze systemen inderdaad positron oppervlakte toestanden zijn. Onze analyse van de annihilatie snelheden met Cd en Se elektronen reproduceerden de experimentele bevindingen dat positronen bij CdSe QDs vaker annihileren met Se elektronen in vergelijking met de situatie in bulk. Kwantitatief was het effect echter niet zo uitgesproken in de berekeningen. Dit duidt erop dat positronen weggeduwd worden van de sites waarop liganden binden aan het QD oppervlak.

9.2 Vooruitzichten

Aan de start van deze thesis ontbrak een echte eerste principes aanpak die toepasbaar is voor het beschrijven van positron oppervlakte toestanden. Het werk dat hier gepresenteerd is, heeft een zekere vooruitgang geboekt op dit onderwerp maar verder onderzoek in deze richting is zeker noodzakelijk. Desalniettemin hebben we aangetoond dat de huidige staat van de theorie eerste principes berekening toelaat experimenten te ondersteunen. We beschrijven nu enkele richtingen die mogelijk interessant zijn om te onderzoeken om de theoretische beschrijving van positron toestanden aan oppervlakken te verbeteren.

Ons overzicht van de bindingsenergieën in Hoofdstuk 4 en de accurate bindingsenergie bekomen voor Bi_2Te_2Se, tonen aan dat het CMM een bruikbaar en accuraat model is voor de berekening van positron oppervlakte toestanden en bindingsenergieën voor perfecte, vlakke oppervlakken. Annihilatiesnelheden zijn iets minder accuraat doordat er geen geschikte aanpassing van de enhancement factor bestaat in het vacuüm. We zien twee belangrijke punten waar het model verbeterd kan worden. Het eerste is om een methode te bedenken om de positie van het beeldlading referentievlak z_0 te berekenen direct vanuit de elektronische structuur. De huidige fenomenologische methoden om deze waarde te bepalen introduceren namelijk een belangrijke onzekerheid. We hebben in ons werk vermeld dat het in principe mogelijk is om de waarde van z_0 te berekenen vanuit de lading die geïnduceerd wordt door een klein elektrisch veld aan te leggen loodrecht op het oppervlak. Deze aanpak werkt echter niet in simulaties die periodische randvoorwaarden opleggen, wat in de meeste moderne software pakketten voor elektronische structuur berekeningen het geval is. Een oplossing voor dit probleem kan een belangrijke verbetering van de betrouwbaarheid van het CMM model betekenen. Ten tweede zou het interessant zijn een nauwkeurigere aanpassing van de enhancement factor in the vacuüm te bedenken, in plaats van deze abrupt te vervangen door het onafhankelijk deeltjes model (IPM). Dergelijke wijziging kan nauwkeurigere voorspellingen toelaten van de annihilatie snelheid en gerelateerde grootheden.

Ons onderzoek van de WDA heeft verschillende gebreken van de methode blootgelegd. Al deze gebreken komen voort uit de vaststelling dat de gebruikte niet-selectieve Ps-achtige paar correlatie functie te eenvoudig is om een adequate beschrijving van de afschermende elektronenwolk rond het positron te bekomen. Een belangrijk probleem, dat tot op zekere hoogte kan verholpen worden door het opdelen van de elektronen dichtheid in een kern en valentie partitie, is dat van alle elektronen verondersteld wordt dat ze de lading van het positron afschermen als vrije elektronen. Van meer gesofisticeerde opdelingen van de elektronendichtheid, zoals reeds onderzocht door andere auteurs, kan verwacht worden dat ze de resultaten verbeteren. Tegelijkertijd introduceert zulke aanpak veel parameters, die de voorspellende capaciteiten van het model kunnen ondermijnen. In plaats daarvan verwachten we dat de meest belovende aanpak er één zou kunnen zijn waarbij de paar correlatie functie direct berekend wordt uit de elektronische structuur van het materiaal. Op deze wijze worden de afschermingseigenschappen van de elektronen automatisch in rekening gebracht, en wordt de nauwkeurigheid bepaald door de verfijning van de methode om de paar correlatie functie te berekenen. Bovendien wordt verwacht dat deze aanpak het probleem van de incorrecte asymptotische limiet van de potentiaal in het vacuüm, die we tegenkwamen in Hoofdstuk 4, oplost. Immers, door de fenomenologische paar correlatie functie te vervangen, worden benaderingen in de ruimtelijke vorm van de afschermingslading verwijderd. Als gevolg daarvan, wordt verwacht dat het uitspreiden van de afschermingslading over het oppervlak op een correcte manier wordt beschreven, wat zou moeten leiden tot de correcte limiet voor de potentiaal ver in het vacuüm gebied.

Hoewel we redelijk goede overeenkomst tussen het berekende VVV Auger spectrum en het experiment bekwamen in Hoofdstuk 6, zou het desalniettemin interessant zijn om de effecten van Auger matrix elementen op de lijnvorm te bestuderen. Onderzoek in deze richting zou kwantitatieve vergelijkingen tussen experiment en theorie kunnen toelaten.

Tenslotte zou het interessant zijn ons onderzoek op de QDs uit te breiden naar PbSe. Voor deze nanodeeltjes werden duidelijke effecten van verschillende liganden op de elektron-positron impulsverdeling waargenomen. Eerste principes berekeningen van de positron oppervlakte toestand en gerelateerde annihilatie eigenschappen kunnen aanzienlijk helpen bij het relateren van de geobserveerde veranderingen in de impulsverdeling aan structurele en elektronische veranderingen geïnduceerd door verschillende liganden. We merken echter op dat het modelleren van liganden geabsorbeerd op oppervlakken te complex is om te behandelen met het CMM. De WDA ontwikkeld in deze thesis kan reeds toegepast worden om bepaalde inzichten te verkrijgen in deze systemen, maar voor definitieve conclusies te trekken zijn waarschijnlijk verdere verfijningen van de aanpak noodzakelijk.

Bibliography

[1] F. Tuomisto and I. Makkonen, “Defect identification in semiconductors with positron annihilation: Experiment and theory”, Reviews of Modern Physics **85**, 1583 (2013) (cit. on pp. 1, 3, 32).

[2] P. J. Schultz and K. G. Lynn, “Interaction of positron beams with surfaces, thin films, and interfaces”, Reviews of Modern Physics **60**, 701 (1988) (cit. on p. 1).

[3] C. Hugenschmidt et al., “High-intensity and high-brightness source of moderated positrons using a brilliant γ beam”, Applied Physics B **106**, 241 (2012) (cit. on p. 3).

[4] C. Hugenschmidt et al., “Investigation of positron work function and moderation efficiency of Ni, Ta, Pt and W(100)”, Applied Surface Science **194**, 283 (2002) (cit. on pp. 3, 57).

[5] S. Mukherjee et al., “Auger-Mediated Sticking of Positrons to Surfaces: Evidence for a Single-Step Transition from a Scattering State to a Surface Image Potential Bound State”, Physical Review Letters **104**, 247403 (2010) (cit. on pp. 3, 7, 8, 57, 79, 89, 104).

[6] K. H. Lee et al., “Positron annihilation induced Auger electron spectroscopy studies of submonolayer Au on Cu(100): Direct evidence for positron localization at sites containing Au atoms”, Physical Review Letters **72**, 1866 (1994) (cit. on p. 3).

[7] A. Weiss et al., “Auger-Electron Emission Resulting from the Annihilation of Core Electrons with Low-Energy Positrons”, Physical Review Letters **61**, 2245 (1988) (cit. on pp. 7, 77, 89).

[8] V. A. Chirayath et al., “Auger electron emission initiated by the creation of valence-band holes in graphene by positron annihilation”, Nature Communications **8**, 16116 (2017) (cit. on pp. 7, 8, 89, 104, 109–112).

[9] J. Mayer et al., “Direct observation of the surface segregation of Cu in Pd by time-resolved positron-annihilation-induced auger electron spectroscopy”, Physical Review Letters **105**, 207401 (2010) (cit. on pp. 7, 8).

[10] K. G. Lynn, “Observation of Surface Traps and Vacancy Trapping with Slow Positrons”, Physical Review Letters **43**, 391 (1979) (cit. on p. 8).

[11] A. P. Mills, “Thermal activation measurement of positron binding energies at surfaces”, Solid State Communications **31**, 623 (1979) (cit. on pp. 8, 56, 57).

[12] C. A. Murray and A. P. Mills, “Narrow beam emission of slow positrons from negative affinity surfaces”, Solid State Communications **34**, 789 (1980) (cit. on p. 8).

[13] C. A. Murray et al., “Correlations between electron and positron workfunctions on copper surfaces”, Surface Science **100**, 647 (1980) (cit. on pp. 8, 57).

[14] K. G. Lynn and H. Lutz, “Slow positrons in single-crystal samples of Al and Al-Al$_x$O$_y$”, Physical Review B **22**, 4143 (1980) (cit. on pp. 8, 57).

[15] R. J. Wilson and A. P. Mills, “Positron and positronium emission from tungsten (111)”, Physical Review B **27**, 3949 (1983) (cit. on pp. 8, 56, 57).

[16] K. G. Lynn, “Observation of the Amorphous-to-Crystalline Surface Transition in Al-Al$_x$O$_y$”, Physical Review Letters **44**, 1330 (1980) (cit. on p. 8).

[17] K. G. Lynn et al., “Measurement of the Positron Surface-State Lifetime for Al”, Physical Review Letters **52**, 1137 (1984) (cit. on pp. 8, 59, 62, 70, 71).

[18] K. G. Lynn et al., “Positron or Positroniumlike Surface State on Al(100)?”, Physical Review Letters **54**, 1702 (1985) (cit. on p. 8).

[19] T. Tachibana et al., “Positron-annihilation-induced ion desorption from TiO$_2$ (110)”, Physical Review B **89**, 201409 (2014) (cit. on p. 8).

[20] A. C. L. Jones et al., “Angle-Resolved Spectroscopy of Positronium Emission from a Cu (110) Surface”, Physical Review Letters **117**, 216402 (2016) (cit. on p. 8).

[21] S. F. Mukherjee et al., “Predominance of multielectron processes contributing to the intrinsic spectra of low-energy Auger transitions in copper and gold”, Physical Review B **84**, 155109 (2011) (cit. on pp. 8, 55, 56, 89, 90, 104).

[22] R. M. Nieminen and M. J. Puska, “Positron Surface States on Clean and Oxidized Al and in Surface Vacancies”, Physical Review Letters **50**, 281 (1983) (cit. on pp. 9, 54, 59, 60, 86).

[23] R. M. Nieminen et al., “Comment on the Positron Surface-State Lifetime”, Physical Review Letters **53**, 1298 (1984) (cit. on pp. 9, 59, 87).

[24] K. O. Jensen and A. B. Walker, “Non-local positron-electron density functional theory and the positron surface state”, Journal of Physics F: Metal Physics **18**, L277 (1988) (cit. on pp. 9, 32, 35, 38, 48).

[25] A. Rubaszek, “Electron-positron enhancement factors at a metal surface: Aluminum”, Physical Review B **44**, 10857 (1991) (cit. on pp. 9, 31, 33, 35–38, 40, 48, 54).

[26] A Rubaszek et al., “Electron-positron annihilation characteristics at a metal surface: simple metals”, Journal of Physics: Condensed Matter **5**, 8195 (1993) (cit. on p. 9).

[27] A. Rubaszek et al., “Nonlocal electron-positron correlations in solids within the weighted density approximation”, Physical Review B **58**, 11285 (1998) (cit. on pp. 9, 33, 35, 43, 44, 48).

[28] A. Rubaszek et al., “Non-Local Electron-Positron Enhancement Factors in Solids”, Acta Physica Polonica A **95**, 652 (1999) (cit. on pp. 9, 31, 43).

[29] A. Rubaszek et al., “Electron-positron correlations in silicon”, Physical Review B **61**, 10100 (2000) (cit. on p. 9).

[30] A. Rubaszek et al., “Nonlocal effects in the electron-positron interaction in metals”, Physical Review B **63**, 165115 (2001) (cit. on pp. 9, 33, 43).

[31] A. Rubaszek et al., “Understanding electron-positron momentum densities in paramagnetic chromium”, Physical Review B **65**, 125104 (2002) (cit. on p. 9).

[32] M. Thomson, *Modern particle physics* (Cambridge University Press, 2013) (cit. on pp. 12, 16).

[33] B. Barbiellini, *New Directions in Antimatter Chemistry and Physics*, edited by C. M. Surko and F. A. Gianturco (Springer Netherlands, Dordrecht, 2001), pp. 127–150 (cit. on p. 12).

[34] V. B. Berestetskii and E. M. Lifshitz, *Quantum Electrodynamics* (Pergamon Press, 1982) (cit. on p. 12).

[35] M. D. Harpen, “Positronium: review of symmetry, conserved quantities and decay for the radiological physicist.”, Medical physics **31**, 57 (2004) (cit. on p. 13).

[36] R. A. Ferrell, “Theory of positron annihilation in solids”, Reviews of Modern Physics **28**, 308 (1956) (cit. on p. 14).

[37] G. G. Ryzhikh and J. Mitroy, “Positron annihilation profiles for HPs and He(^{3}S^e)e$^+$”, Journal of Physics B: Atomic, Molecular and Optical Physics **32**, 4051 (1999) (cit. on p. 14).

[38] A. Bansil and M. Lindroos, “Importance of Matrix Elements in the ARPES Spectra of BISCO”, Physical Review Letters **83**, 5154 (1999) (cit. on pp. 15, 84).

[39] M. Neupane et al., “Oscillatory surface dichroism of the insulating topological insulator Bi_2Te_2Se”, Physical Review B **88**, 165129 (2013) (cit. on pp. 15, 77).

[40] B. Robertson, “Introduction to Field Operators in Quantum Mechanics”, American Journal of Physics **41**, 678 (1973) (cit. on pp. 15, 16).

[41] I. Makkonen et al., “Enhancement models of momentum densities of annihilating electron-positron pairs: The many-body picture of natural geminals”, Physical Review B **89**, 041105 (2014) (cit. on pp. 17, 29).

[42] V. Callewaert et al., “Positron surface state as a spectroscopic probe for characterizing surfaces of topological insulator materials”, Physical Review B **94**, 115411 (2016) (cit. on pp. 17, 18, 54, 56, 60, 63, 75, 77).

[43] S. Berko and J. Zuckerman, “Polarized Positron Annihilation in Ferromagnets”, Physical Review Letters **13**, 339 (1964) (cit. on pp. 18, 76, 83, 84).

[44] J. A. Weber et al., “Spin-Resolved Fermi Surface of the Localized Ferromagnetic Heusler Compound Cu_2MnAl Measured with Spin-Polarized Positron Annihilation”, Physical Review Letters **115**, 206404 (2015) (cit. on pp. 18, 83, 84).

[45] M. Springborg, *Methods of Electronic-Structure Calculations* (John Wiley & Sons Ltd, 2000) (cit. on pp. 20, 21).

[46] C. Hugenschmidt et al., “Positron Beam Characteristics at NEPOMUC Upgrade”, Journal of Physics: Conference Series **505**, 012029 (2014) (cit. on p. 22).

[47] P. Hohenberg and W. Kohn, “Inhomogeneous Electron Gas”, Physical Review B **136**, B864 (1964) (cit. on p. 24).

[48] E. H. Lieb, “Density functionals for coulomb systems”, International Journal of Quantum Chemistry **24**, 243 (1983) (cit. on p. 24).

[49] U. V. Barth and L. Hedin, “A local exchange-correlation potential for the spin polarized case. I”, Journal of Physics C: Solid State Physics **5**, 1629 (1972) (cit. on p. 24).

[50] A. K. Rajagopal and J. Callaway, “Inhomogeneous Electron Gas”, Physical Review B **7**, 1912 (1973) (cit. on p. 24).

[51] W. Kohn and L. J. Sham, “Self-consistent Equations Including Exchange and Correlation Effects”, Physical Review **140**, 1133 (1965) (cit. on pp. 24, 28).

[52] B. Chakraborty and R. W. Siegel, “Electron and positron response to atomic defects in solids: A theoretical study of the monovacancy and divacancy in aluminum”, Physical Review B **27**, 4535 (1983) (cit. on pp. 24, 86).

[53] E. Boroński and R. M. Nieminen, “Electron-positron density-functional theory”, Physical Review B **34**, 3820 (1986) (cit. on pp. 24, 28, 29, 36–39, 86).

[54] R. M. Dreizler and E. K. U. Gross, *Density Function Theory* (Springer-Verlag, 1990) (cit. on p. 26).

[55] N. W. Ashcroft and D. N. Mermin, *Solid State Physics* (1976) (cit. on p. 27).

[56] N. D. Drummond et al., “Quantum Monte Carlo Study of a Positron in an Electron Gas”, Physical Review Letters **107**, 207402 (2011) (cit. on pp. 28, 29, 33, 34, 36–38, 73, 86, 96, 119, 125).

[57] M. J. Puska et al., “Electron-positron Car-Parrinello methods: Self-consistent treatment of charge densities and ionic relaxations”, Physical Review B **52**, 10947 (1995) (cit. on p. 29).

[58] H. Stachowiak and J. Lach, “Positron-annihilation characteristics in an electron gas from low to high densities”, Physical Review B **48**, 9828 (1993) (cit. on pp. 29, 36).

[59] B. Barbiellini et al., “Gradient correction for positron states in solids”, Physical Review B **51**, 7341 (1995) (cit. on pp. 29, 40–43, 53, 113).

[60] B. Barbiellini et al., “Calculation of positron states and annihilation in solids: A density-gradient-correction scheme”, Physical Review B **53**, 16201 (1996) (cit. on pp. 29, 43).

[61] M. Alatalo et al., “Theoretical and experimental study of positron annihilation with core electrons in solids”, Physical Review B **54**, 2397 (1996) (cit. on pp. 29, 30).

[62] B. Barbiellini and J. Kuriplach, “Proposed Parameter-Free Model for Interpreting the Measured Positron Annihilation Spectra of Materials Using a Generalized Gradient Approximation”, Physical Review Letters **114**, 147401 (2015) (cit. on pp. 29, 37, 39, 40, 53, 119).

[63] B. Barbiellini et al., “Correlation effects for positron annihilation with core and semicore electrons”, Applied Surface Science **116**, 283 (1997) (cit. on p. 30).

[64] V. Callewaert et al., “Application of the weighted-density approximation to the accurate description of electron-positron correlation effects in materials”, Physical Review B **96**, 085135 (2017) (cit. on p. 31).

[65] J. P. Perdew et al., “Generalized Gradient Approximation Made Simple”, Physical Review Letters **77**, 3865 (1996) (cit. on pp. 33, 49, 72, 86, 125).

[66] J. Sun et al., “Strongly Constrained and Appropriately Normed Semilocal Density Functional”, Physical Review Letters **115**, 036402 (2015) (cit. on pp. 33, 48).

[67] O. Gunnarsson et al., “Descriptions of exchange and correlation effects in inhomogeneous electron systems”, Physical Review B **20**, 3136 (1979) (cit. on pp. 33, 43).

[68] N. D. Drummond et al., “First-principles method for impurities in quantum fluids: Positron in an electron gas”, Physical Review B **82**, 035107 (2010) (cit. on pp. 33, 36, 49).

[69] H. Stachowiak, “Electron-positron interaction in jellium”, Physical Review B **41**, 12522 (1990) (cit. on p. 33).

[70] J. C. Kimball, “Short-Range Correlations and Electron-Gas Response Functions”, Physical Review A **7**, 1648 (1973) (cit. on pp. 36, 49).

[71] J. Arponen, “Exact high-density results for the positron correlation energy and annihilation rate in a homogeneous electron gas”, Journal of Physics C: Solid State Physics **11**, L739 (1978) (cit. on p. 37).

[72] W. Brandt and J. Reinheimer, “Theory of Semiconductor Response to Charged Particles”, Physical Review B **2**, 3104 (1970) (cit. on p. 37).

[73] W. Brandt and J. Reinheimer, “Impurity screening in amorphous semiconductors”, Physics Letters A **35**, 107 (1971) (cit. on p. 37).

[74] G. M. Dunn et al., “Positron states in vacancies and voids”, Journal of Physics: Condensed Matter **3**, 2049 (1991) (cit. on p. 38).

[75] J. Kuriplach and B. Barbiellini, “Improved generalized gradient approximation for positron states in solids”, Physical Review B **89**, 155111 (2014) (cit. on pp. 40, 43, 53).

[76] M. J. Puska and R. M. Nieminen, “Defect spectroscopy with positrons: a general calculational method”, Journal of Physics F: Metal Physics **13**, 333 (1983) (cit. on p. 43).

[77] K. O. Jensen, “Local density calculation of positron annihilation in metals”, Journal of Physics: Condensed Matter **1**, 10595 (1989) (cit. on p. 43).

[78] T. Jarlborg and A. K. Singh, “Local-density approach for calculation of electron-positron enhancement in transition metals”, Physical Review B **36**, 4660 (1987) (cit. on p. 43).

[79] F. Plazaola et al., “Positron annihilation in II-VI compound semiconductors: theory”, Journal of Physics: Condensed Matter **6**, 8809 (1994) (cit. on pp. 43, 118, 119).

[80] J. Laverock et al., “Experimental determination of the state-dependent enhancement of the electron-positron momentum density in solids”, Physical Review B **82**, 125127 (2010) (cit. on p. 43).

[81] H. Przybylski and G. Borstel, “Nonlocal density approximation to exchange and correlation in self-consistent bandstructure calculations: Application to Cu”, Solid State Communications **49**, 317 (1984) (cit. on p. 44).

[82] H. Przybylski and G. Borstel, “Nonlocal density approximation to exchange and correlation: Ground state properties of solid copper and vanadium”, Solid State Communications **52**, 713 (1984) (cit. on p. 44).

[83] J. Sun et al., “Accurate first-principles structures and energies of diversely bonded systems from an efficient density functional.”, Nature chemistry **8**, 831 (2016) (cit. on p. 48).

[84] I. G. Buda et al., “Characterization of Thin Film Materials using SCAN meta-GGA, an Accurate Nonempirical Density Functional”, Scientific Reports **7**, 44766 (2017) (cit. on p. 48).

[85] P. E. Blöchl, “Projector augmented-wave method”, Physical Review B **50**, 17953 (1994) (cit. on pp. 49, 72, 86, 87, 125).

[86] G. Kresse and J. Furthmüller, “Efficient iterative schemes for ab initio total-energy calculations using a plane-wave basis set”, Physical Review B **54**, 11169 (1996) (cit. on pp. 49, 72, 86, 95, 125).

[87] G. Kresse and J. Furthmüller, “Efficiency of ab-initio total energy calculations for metals and semiconductors using a plane-wave basis set”, Computational Materials Science **6**, 15 (1996) (cit. on pp. 49, 72, 86, 95, 125).

[88] G. Kresse and D. Joubert, “From ultrasoft pseudopotentials to the projector augmented-wave method”, Physical Review B **59**, 1758 (1999) (cit. on pp. 49, 72, 86, 95, 125).

[89] R. W. G. Wyckoff, *Crystal Structures 1* (Interscience Publishers, New York, 1963), pp. 7–83 (cit. on pp. 49, 72, 119).

[90] J. P. Perdew and A. Zunger, “Self-interaction correction to density-functional approximations for many-electron systems”, Physical Review B **23**, 5048 (1981) (cit. on p. 49).

[91] D. M. Ceperley and B. J. Alder, “Ground State of the Electron Gas by a Stochastic Method”, Physical Review Letters **45**, 566 (1980) (cit. on p. 49).

[92] I. Makkonen et al., “Modeling the momentum distributions of annihilating electron-positron pairs in solids”, Physical Review B **73**, 035103 (2006) (cit. on pp. 49, 73, 87, 96).

[93] A. M. Frolov, “Positron annihilation in the positronium negative ion Ps^-”, Physics Letters, Section A: General, Atomic and Solid State Physics **342**, 430 (2005) (cit. on p. 53).

[94] N. G. Fazleev et al., “Annihilation of positrons trapped at the alkali-metal-covered transition-metal surface”, Physical Review B **52**, 5351 (1995) (cit. on pp. 54, 59, 60).

[95] N. G. Fazleev et al., “Surface states and annihilation characteristics of positrons trapped at the (100) and (111) surfaces of silicon”, Physical Review B **70**, 165309 (2004) (cit. on pp. 54, 56, 60).

[96] N. G. Fazleev and A. H. Weiss, “Surface states and annihilation characteristics of positrons trapped at the oxidized Cu(100) surface”, Journal of Physics: Conference Series **443**, 012038 (2013) (cit. on p. 54).

[97] S. Hagiwara et al., “Positron states at a lithium-adsorbed Al (100) surface : Two-component density functional theory simulation”, Physical Review B **91**, 115409 (2015) (cit. on pp. 54, 60).

[98] S. Hagiwara and K. Watanabe, “Positron States at Li- and O-adsorbed Fe(001) Ferromagnetic Surfaces Studied by Two-Component Density Functional Theory”, Journal of the Physical Society of Japan **85**, 114703 (2016) (cit. on p. 54).

[99] E. M. Gullikson and A. P. Mills, “Positron deformation potential and the temperature dependence of the electron and positron work functions”, Physical Review B **35**, 8759 (1987) (cit. on p. 57).

[100] I. J. Rosenberg et al., “Temperature dependence of the positronium work function”, Physical Review B **35**, 2083 (1987) (cit. on p. 57).

[101] D. M. Chen et al., “Measurement of positron reemission from thin single-crystal W(100) films”, Physical Review B **31**, 4123 (1985) (cit. on p. 57).

[102] P. J. Schultz et al., “Observation of defects associated with the Cu/W(110) interface as studied with variable-energy positrons”, Physical Review B **27**, 6626 (1983) (cit. on p. 57).

[103] G. R. Brandes et al., “Positron Workfunction of Diamond C(100) Surfaces”, Materials Science Forum **105-110**, 1363 (1992) (cit. on pp. 57, 65).

[104] P. Krüger and J. Pollmann, “Dimer Reconstruction of Diamond, Si, and Ge (001) Surfaces”, Physical Review Letters **74**, 1155 (1995) (cit. on pp. 56, 58).

[105] N. D. Lang and W. Kohn, “Theory of Metal Surfaces: Induced Surface Charge and Image Potential”, Physical Review B **7**, 3541 (1973) (cit. on pp. 60, 62, 63, 71).

[106] M. W. Finnis et al., “The interaction of a point charge with a metal surface: theory and calculations for (111), (100) and (110) aluminium surfaces”, Journal of Physics: Condensed Matter **7**, 2001 (1995) (cit. on pp. 60, 63).

[107] R. M. Nieminen and K. O. Jensen, “Charge transfer and positron states at alkali-metal-covered nickel surfaces”, Physical Review B **38**, 5764 (1988) (cit. on p. 60).

[108] A. Kiejna, “Image potential matched self-consistently to an effective potential for simple-metal surfaces”, Physical Review B **43**, 14695 (1991) (cit. on pp. 60, 62, 63, 66, 71).

[109] C. Kittel, *Introduction to Solid State Physics*, 8th ed. (Wiley, 2004), p. 704 (cit. on p. 63).

[110] N. Lang and W Kohn, “Theory of metal surfaces: charge density and surface energy”, Physical Review B **1**, 4555 (1970) (cit. on p. 63).

[111] N. D. Lang and W. Kohn, “Theory of Metal Surfaces: Work Function”, Physical Review B **3**, 1215 (1971) (cit. on p. 63).

[112] P. García-González et al., “Image potential and the exchange-correlation weighted density approximation functional”, Physical Review B **62**, 16063 (2000) (cit. on pp. 68, 72).

[113] P. García-González et al., “Nonlocal WDA functional capable of describing the image potential of a metallic surface”, International Journal of Quantum Chemistry **91**, 139 (2003) (cit. on pp. 68, 72).

[114] M. Z. Hasan and C. L. Kane, “Colloquium: Topological insulators”, Reviews of Modern Physics **82**, 3045 (2010) (cit. on p. 75).

[115] X.-L. Qi and S.-C. Zhang, “Topological insulators and superconductors”, Reviews of Modern Physics **83**, 1057 (2011) (cit. on p. 75).

[116] A. Bansil et al., “Colloquium : Topological band theory”, Reviews of Modern Physics **88**, 021004 (2016) (cit. on p. 75).

[117] P. Roushan et al., “Topological surface states protected from backscattering by chiral spin texture”, Nature **460**, 1106 (2009) (cit. on p. 76).

[118] C. Jozwiak et al., “Widespread spin polarization effects in photoemission from topological insulators”, Physical Review B **84**, 1 (2011) (cit. on p. 77).

[119] F. Kuemmeth and E. I. Rashba, “Giant spin rotation under quasiparticle-photoelectron conversion: Joint effect of sublattice interference and spin-orbit coupling”, Physical Review B **80**, 241409 (2009) (cit. on p. 77).

[120] K. Shastry et al., “Evidence for a positron bound state on the surface of a topological insulator”, Journal of Physics: Conference Series **618**, 012006 (2015) (cit. on pp. 77, 80).

[121] V. Callewaert, “First-principles study of positronium bound states near the surface of topological insulators”, MA thesis (Universiteit Antwerpen, 2014) (cit. on p. 77).

[122] D. G. Lock et al., “Positron annihilation and Fermi surface studies: a new approach”, Journal of Physics F: Metal Physics **3**, 561 (1973) (cit. on pp. 83, 87).

[123] B. Barbiellini et al., “Positron annihilation and positron-electron correlation effects in high-Tc oxides”, Journal of Physics and Chemistry of Solids **56**, 1693 (1995) (cit. on p. 83).

[124] A. Shukla et al., “Momentum density and Fermi surface of $Nd_{2-x}Ce_xCuO_{4-\delta}$”, Physical Review B **53**, 3613 (1996) (cit. on p. 83).

[125] K. E. H. M. Hanssen et al., “Positron-annihilation study of the half-metallic ferromagnet nimnsb: experiment”, Physiscal Review B **42**, 1533 (1990) (cit. on p. 83).

[126] A. Kawasuso et al., “Doppler broadening of annihilation radiation measurements on $3d$ and $4f$ ferromagnets using polarized positrons”, Physical Review B **85**, 024417 (2012) (cit. on pp. 83, 84).

[127] J. Henk et al., “Complex Spin Texture in the Pure and Mn-Doped Topological Insulator Bi_2Te_3”, Physical Review Letters **108**, 206801 (2012) (cit. on p. 84).

[128] S. Basak et al., “Spin texture on the warped Dirac-cone surface states in topological insulators”, Physical Review B **84**, 121401 (2011) (cit. on p. 84).

[129] H. Lin et al., “An isolated Dirac cone on the surface of ternary tetradymite-like topological insulators”, New Journal of Physics **13**, 095005 (2011) (cit. on pp. 84, 86).

[130] L.-L. Wang and D. D. Johnson, “Ternary tetradymite compounds as topological insulators”, Physical Review B **83**, 241309 (2011) (cit. on pp. 84, 86).

[131] L. Fu, “Hexagonal Warping Effects in the Surface States of the Topological Insulator Bi_2Te_3”, Physical Review Letters **103**, 266801 (2009) (cit. on p. 84).

[132] S. B. Dugdale et al., “The Bristol HIDAC 2D-ACAR Spectrometer”, Journal of Physics: Conference Series **443**, 012083 (2013) (cit. on p. 84).

[133] J. C. Campuzano et al., “Fermi surface in $YBa_2Cu_3O_{6.9}$: Evidence from angle-resolved photoemission spectroscopy and positron two-dimensional angular correlation of annihilation radiation”, Physical Review B **43**, 2788 (1991) (cit. on p. 84).

[134] J. Nieminen et al., “Origin of the Electron-Hole Asymmetry in the Scanning Tunneling Spectrum of the High-Temperature $Bi_2Sr_2CaCu_2O_{8+\delta}$ Superconductor”, Physical Review Letters **102**, 037001 (2009) (cit. on p. 84).

[135] T. R. Devidas et al., “Role of Se vacancies on Shubnikov-de Haas oscillations in Bi 2 Se 3 : A combined magneto-resistance and positron annihilation study”, EPL (Europhysics Letters) **108**, 67008 (2014) (cit. on p. 84).

[136] S. W. H. Eijt et al., “Study of colloidal quantum-dot surfaces using an innovative thin-film positron 2D-ACAR method.”, Nature materials **5**, 23 (2006) (cit. on pp. 84, 117, 118, 123, 124).

[137] S. Steiner et al., “Calculation of the magnetic anisotropy with projected-augmented-wave methodology and the case study of disordered $Fe_{1-x}Co_x$ alloys”, Physical Review B **93**, 224425 (2016) (cit. on p. 86).

[138] X.-Q. Dai et al., "Robust surface state of intrinsic topological insulator Bi_2Te_2Se thin films: a first-principle study", Journal of Physics: Condensed Matter **24**, 035502 (2012) (cit. on p. 86).

[139] J. Chang et al., "Density functional study of ternary topological insulator thin films", Physical Review B **83**, 235108 (2011) (cit. on p. 86).

[140] M. Neupane et al., "Topological surface states and Dirac point tuning in ternary topological insulators", Physical Review B **85**, 235406 (2012) (cit. on p. 86).

[141] T. Arakane et al., "Tunable Dirac cone in the topological insulator $Bi_{2-x}Sb_xTe_{3-y}Se_y$", Nature Communications **3**, 636 (2012) (cit. on p. 86).

[142] I. Makkonen et al., "Calculation of valence electron momentum densities using the projector augmented-wave method", Journal of Physics and Chemistry of Solids **66**, 1128 (2005) (cit. on p. 87).

[143] H. D. Hagstrum, "Theory of Auger Ejection of Electrons from Metals by Ions", Physical Review **96**, 336 (1954) (cit. on pp. 93, 95, 114).

[144] H. D. Hagstrum, "Theory of Auger Neutralization of Ions at the Surface of a Diamond-Type Semiconductor", Physical Review **122**, 83 (1961) (cit. on pp. 93, 95, 110).

[145] J. J. Lander, "Auger peaks in the energy spectra of secondary electrons from various materials", Physical Review **91**, 1382 (1953) (cit. on p. 93).

[146] P. E. Blöchl et al., "Improved tetrahedron method for Brillouin-zone integrations", Physical Review B **49**, 16223 (1994) (cit. on pp. 94, 95).

[147] J. Klimeš et al., "Chemical accuracy for the van der Waals density functional", Journal of Physics: Condensed Matter **22**, 022201 (2010) (cit. on p. 96).

[148] J. Klimeš et al., "Van der Waals density functionals applied to solids", Physical Review B **83**, 195131 (2011) (cit. on p. 96).

[149] G. Graziano et al., "Improved description of soft layered materials with van der Waals density functional theory", Journal of Physics: Condensed Matter **24**, 424216 (2012) (cit. on p. 96).

[150] Y. Fukaya et al., "Spacing between graphene and metal substrates studied with total-reflection high-energy positron diffraction", Carbon **103**, 1 (2016) (cit. on p. 96).

[151] B. Partoens and F. M. Peeters, "From graphene to graphite: Electronic structure around the K point", Physical Review B **74**, 075404 (2006) (cit. on p. 97).

[152] O. Leenaerts, "An ab-initio study of the adsorption of atoms and molecules on graphene", PhD thesis (Universiteit Antwerpen, 2010) (cit. on p. 97).

[153] C. Gong et al., "First-principles study of metal–graphene interfaces", Journal of Applied Physics **108**, 123711 (2010) (cit. on p. 101).

[154] M. Van der Donck et al., "Excitons, trions, and biexcitons in transition-metal dichalcogenides: Magnetic-field dependence", Physical Review B **97**, 195408 (2018) (cit. on p. 102).

[155] S. Tougaard, "Low energy inelastic electron scattering properties of noble and transition metals", Solid State Communications **61**, 547 (1987) (cit. on pp. 106, 107).

[156] S. Tougaard, "Universality Classes of Inelastic Electron Scattering Cross-sections", Surface and Interface Analysis **25**, 137 (1997) (cit. on p. 106).

[157] R. H. Ritchie and A. Howie, "Electron excitation and the optical potential in electron microscopy", Philosophical Magazine **36**, 463 (1977) (cit. on p. 106).

[158] M. P. Seah, "Background subtraction: I. General behaviour of Tougaard-style backgrounds in AES and XPS", Surface Science **420**, 285 (1999) (cit. on p. 106).

[159] M. P. Seah et al., “Background subtraction: II. General behaviour of REELS and the Tougaard universal cross section in the removal of backgrounds in AES and XPS”, Surface science **461**, 1 (2000) (cit. on p. 106).

[160] D. A. Shirley, “High-resolution x-ray photoemission spectrum of the valence bands of gold”, Physical Review B **5**, 4709 (1972) (cit. on p. 106).

[161] J. Végh, “The Shirley-equivalent electron inelastic scattering cross-section function”, Surface Science **563**, 183 (2004) (cit. on pp. 106–108).

[162] A. G. Marinopoulos et al., “Ab initio study of the optical absorption and wave-vector-dependent dielectric response of graphite”, Physical Review B **69**, 245419 (2004) (cit. on p. 107).

[163] T. Eberlein et al., “Plasmon spectroscopy of free-standing graphene films”, Physical Review B **77**, 233406 (2008) (cit. on p. 107).

[164] Y. Motoyama et al., “A study of the secondary electron yield of insulator cathodes for plasma display panels”, IEEE Transactions on Electron Devices **48**, 1568 (2001) (cit. on p. 110).

[165] Y. Cho et al., “First-principles study on secondary electron emission of MgO surface”, Journal of Applied Physics **101**, 083710 (2007) (cit. on p. 110).

[166] E. J. McGuire, “K-Shell Auger Transition Rates and Fluorescence Yields for Elements Be-Ar”, Physical Review **185**, 1 (1969) (cit. on p. 112).

[167] W. Shi et al., “Nature of the Positron State in CdSe Quantum Dots”, Physical Review Letters **121**, 057401 (2018) (cit. on pp. 117, 119, 123, 124).

[168] Y. Nagai et al., “Positron confinement in ultrafine embedded particles: Quantum-dot-like state in an Fe-Cu alloy”, Physical Review B **61**, 6574 (2000) (cit. on p. 117).

[169] Y. Nagai et al., “Fermi Surface of Nanocrystalline Embedded Particles in Materials: bcc Cu in Fe”, Physical Review Letters **87**, 176402 (2001) (cit. on p. 117).

[170] Y. Nagai et al., “Irradiation-induced Cu aggregations in Fe: An origin of embrittlement of reactor pressure vessel steels”, Physical Review B **63**, 134110 (2001) (cit. on p. 117).

[171] C. Falub et al., “Electronic structure and orientation relationship of Li nanoclusters embedded in MgO studied by depth-selective positron annihilation two-dimensional angular correlation”, Physical Review B **66**, 075426 (2002) (cit. on p. 117).

[172] M. A van Huis et al., “Positron confinement in embedded lithium nanoclusters”, Physical Review B **65**, 085416 (2002) (cit. on p. 117).

[173] M. Weber et al., “Direct observation of energy-gap scaling law in CdSe quantum dots with positrons”, Physical Review B **66**, 4 (2002) (cit. on pp. 117–119, 124).

[174] S. W. H. Eijt et al., “Electronic coupling of colloidal CdSe nanocrystals monitored by thin-film positron-electron momentum density methods”, Applied Physics Letters **94**, 091908 (2009) (cit. on p. 117).

[175] L. Chai et al., “Surfaces of colloidal PbSe nanocrystals probed by thin-film positron annihilation spectroscopy”, APL Materials **1**, 022111 (2013) (cit. on p. 117).

[176] W. Shi et al., “Ligand-surface interactions and surface oxidation of colloidal PbSe quantum dots revealed by thin-film positron annihilation methods”, Applied Physics Letters **108**, 081602 (2016) (cit. on p. 117).

[177] M. J. Puska et al., “Positron affinities for elemental metals”, Journal of Physics: Condensed Matter **1**, 6081 (1989) (cit. on p. 117).

[178] X. Lan et al., “10.6% Certified Colloidal Quantum Dot Solar Cells via Solvent-Polarity-Engineered Halide Passivation”, Nano Letters **16**, 4630 (2016) (cit. on pp. 117, 118).

[179] C. B. Murray et al., “Synthesis and Characterization of Monodisperse Nanocrystals and Close-Packed Nanocrystal Assemblies”, Annual Review of Materials Research **30**, 545 (2000) (cit. on p. 118).

[180] Y. Gao et al., “Photoconductivity of PbSe quantum-dot solids: Dependence on ligand anchor group and length”, ACS Nano **6**, 9606 (2012) (cit. on p. 118).

[181] L.-W. Wang and A. Zunger, “Pseudopotential calculations of nanoscale CdSe quantum dots”, Physical Review B **53**, 9579 (1996) (cit. on p. 118).

[182] S. K. Sharma et al., “Direct evidence of Cd vacancies in CdSe nanoparticles: positron annihilation studies”, The European Physical Journal B **82**, 335 (2011) (cit. on pp. 119, 121, 124).

[183] R. Krause-Rehberg and H. S. Leipner, *Positron annihilation in Semiconductors: Defect Studies* (Springer, 1999), p. 378 (cit. on p. 119).

[184] J. Y. Rempel et al., “Density Functional Theory Study of Ligand Binding on CdSe (0001), $(000\bar{1})$, and $(11\bar{2}0)$ Single Crystal Relaxed and Reconstructed Surfaces: Implications for Nanocrystalline Growth”, The Journal of Physical Chemistry B **110**, 18007 (2006) (cit. on p. 123).

[185] J. E. Katari et al., “X-ray photoelectron spectroscopy of CdSe nanocrystals with applications to studies of the nanocrystal surface”, Journal of Physical Chemistry **98**, 4109 (1994) (cit. on p. 123).

Publications

1. **V. Callewaert**, K. Shastry, R. Saniz, I. Makkonen, B. Barbiellini, B. A. Assaf, D. Heiman, J. S. Moodera, B. Partoens, A. Bansil, and A. H. Weiss, "Positron surface state as a spectroscopic probe for characterizing surfaces of topological insulator materials", Physical Review B **94**, 115411 (2016).

2. S. W. H. Eijt, W. Shi, A. Mannheim, M. Butterling, H. Schut, W. Egger, M. Dickmann, C. Hugenschmidt, B. Shakeri, R. W. Meulenberg, **V. Callewaert**, R. Saniz, B. Partoens, B. Barbiellini, A. Bansil, J. Melskens, M. Zeman, A. H. M. Smets, M. Kulbak, G. Hodes, D. Cahen, and E. Brück, "New insights into the nanostructure of innovative thin film solar cells gained by positron annihilation spectroscopy", Journal of Physics: Conference Series **791**, 012021 (2017).

3. **V. Callewaert**, R. Saniz, B. Barbiellini, and B. Partoens, "Surface states and positron annihilation spectroscopy: results and prospects from a first-principles approach", Journal of Physics: Conference Series **791**, 012036 (2017).

4. V. A. Chirayath, **V. Callewaert**, A. J. Fairchild, M. D. Chrysler, R. W. Gladen, A. D. Mcdonald, S. K. Imam, K. Shastry, A. R. Koymen, R. Saniz, B. Barbiellini, K. Rajeshwar, B. Partoens, and A. H. Weiss, "Auger electron emission initiated by the creation of valence-band holes in graphene by positron annihilation", Nature Communications **8**, 16116 (2017).

5. **V. Callewaert**, R. Saniz, B. Barbiellini, A. Bansil, and B. Partoens, "Application of the weighted-density approximation to the accurate description of electron-positron correlation effects in materials", Physical Review B **96**, 085135 (2017).

6. H. Hafiz, K. Suzuki, B. Barbiellini, Y. Orikasa, **V. Callewaert**, S. Kaprzyk, M. Itou, K. Yamamoto, R. Yamada, Y. Uchimoto, Y. Sakurai, H. Sakurai, and A. Bansil, "Visualizing redox orbitals and their potentials in advanced lithium-ion battery materials using high-resolution x-ray Compton scattering", Science Advances **3**, e1700971 (2017).

7. W. Shi, **V. Callewaert**, B. Barbiellini, R. Saniz, M. Butterling, W. Egger, M. Dickmann, C. Hugenschmidt, B. Shakeri, R. W. Meulenberg, E. Brück, B. Partoens, A. Bansil, and S. W. H. Eijt, "Nature of the Positron State in CdSe Quantum Dots", Physical Review Letters **121**, 057401 (2018).

Acknowledgements

I want to take the opportunity here to express my gratitude towards many people that have contributed one way or another to my thesis.

First, I would like to thank my promotor Prof. Dr. Bart Partoens for giving me the opportunity to do a PhD in the first place, for allowing me to explore my own ideas, visit collaborators abroad, and facilitating my research in general. My thanks and gratitude towards my promotor Dr. Rolando Saniz for all the efforts related with this research project. For the good guidance, interesting discussions and suggestions, I am thankful to both my promotors. Comments, suggestions and corrections from all members of the jury to the manuscript are gratefully acknowledged.

My sincerest gratitude to Prof. Dr. Bernardo Barbiellini for a variety of reasons. First of all for being at the root of this research project, for bringing us into contact with Dr. Stephan Eijt and Prof. Dr. Alex Weiss, and coordinating the collaborations. Second, for the nice collaboration and many discussions during the entire course of my PhD, and finally for the kind hospitality during my visit to Boston.

An important factor in the success of this PhD, is the initial software kindly provided to me by Dr. Ilja Makkonen, as well as the initial guidance in carrying out positron calculations. Many of the results presented here would not have been possible otherwise. Thanks also for the pleasant past and current collaboration on the positron software. Speaking of software, I also would like to thank Dr. Engelbert Tijskens for help with optimizing the WDA routines in the code, and Nikolas Gorafil for general IT support.

Next, I would like to thank Dr. Stephan Eijt. The kind help at the very start of my PhD helped tremendously in understanding positron annihilation spectroscopy in general, and the experiments in particular. Also for providing the challenging problem of the Quantum Dots to work on; A significant amount of the theory investigated in this work was motivated by this particular problem.

A large part of my PhD study was devoted to modelling experiments carried out by the positron group of Prof. Dr. Alex Weiss at Arlington, Texas, USA. For providing interesting problems, extended discussions and the collaboration in general, I would like to thank Prof. Dr. Alex Weiss, Dr. Varghese Chirayath, Alex Fairchild, and Dr. Karthik Shastry.

Not immediately involved in the work but therefore not less appreciated: Many thanks toward my parents for the support during the course of my PhD. Thanks to Dr. Pieter Muyshondt and Jeroen Mulkers for the enjoyable lunch breaks. Thanks to family, and many other friends for the all the nice moments in the past four years. Last but not least, thank you, Anne, for all the love and support.